AEOLIAN ENTRAINMENT THRESHOLDS IN A DEVELOPING BOUNDARY LAYER

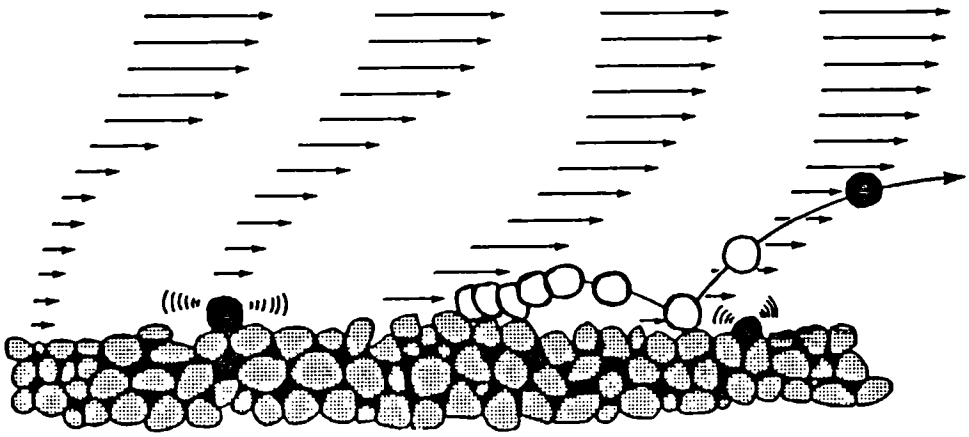

by
Jonathan Jowett Williams BSc

A thesis presented for the degree of
Doctor of Philosophy
in the
University of London

Department of Geography and Earth Science
Queen Mary College

March 1986

To my wife, Jo,

and daughter, Gemma.

Acknowledgements

I would like to thank my two supervisors, Graeme Butterfield and David Clark, for their advice, support and encouragement throughout this research, particularly for their constructive and critical appraisals of the text.

Special thanks to my wife Jo for typing and re-typing numerous manuscripts, for helping with final preparation of this thesis and, most importantly, for her unselfish support, encouragement and self sacrifice throughout the last three and a half years.

Thanks to the technicians from the Department of Aeronautical Engineering (Arthur Fleet, Don Husband, Nevil Kolb, Roger Montague and Ken Taplin) and to technicians from the Department of Geography and Earth Sciences (Dave Armitage, Stan Bartels and Ray Crundwell) at Queen Mary College.

Thanks also to Professor Bruce Atkinson for making the facilities of the Department of Geography and Earth Sciences available to me during the preparation of this thesis.

Finally, thanks to the Natural Environment Research Council for the Research Studentship from October 1982 to October 1985.

Abstract

The aeolian threshold condition is identified as defining the critical state between a static sediment bed and active aeolian transport. Disparities in reported mean threshold shear velocities ($\bar{U}_{*T}$) are attributed to variation in: (a) flow regimes; (b) entrainment criteria; (c) particle characteristics and exposures; and (d) techniques for measurement of $\bar{U}_{*T}$. The relative significance of these factors is assessed for strips and beds of ballotini, aeolian sand, salt crystals and sugar crystals using the controlled, reproducible flow conditions of the developing boundary layer over a flat plate. Such a plate was covered with a non-erosive layer of grains to simulate a flat sediment bed and was positioned in a wind tunnel. $\bar{U}_{*T}$ values were calculated using the momentum integral method. In a separate study, threshold conditions on impervious and permeable beds were compared directly. Analysis of entrainment from strips and beds on the plate shows that the threshold condition is principally determined by a critical degree of overlap between the probability distributions of local shear velocity, $P(U_*)$, and of grain threshold shear velocity, $P(U_{*T})$. Characteristic $P(U_{*T})$ distributions for test materials were determined and two objective definitions of $\bar{U}_{*T}$ were devised. Experimental $\bar{U}_{*T}$ values agree well with published data and are used to resolve the data scatter associated with both 'restricted' and 'universal' threshold curves. Rates of aeolian entrainment over a range of $\bar{U}_{*T}$ values are found to be an inverse exponential function of time and wind speed. Different erosion rates were found to result from skewness of $P(U_*)$ and degree of overlap between $P(U_*)$ and $P(U_{*T})$. Fluid sweeps in the turbulent bursting cycle are considered to be the primary entrainment mechanism. Medium/high-speed cine film gave insight into initiation processes. Grain oscillation due to vortex shedding and initial motion characterized by a progressive rolling and bouncing were observed. Bed permeability was not found to affect aeolian threshold values.

C O N T E N T S

CHAPTER THREE Experimental apparatus

CHAPTER FOUR Aeolian thresholds in a developing boundary layer

CHAPTER SIX Rate of aeolian entrainment from test strips and beds

CHAPTER SEVEN Aeolian thresholds on impervious and permeable test beds

Figures

CHAPTER ONE

CHAPTER TWO

CHAPTER THREE

CHAPTER FOUR

CHAPTER FIVE

CHAPTER SIX

CHAPTER SEVEN

Tables

CHAPTER ONE

CHAPTER TWO

CHAPTER THREE

CHAPTER FOUR

CHAPTER SEVEN

APPENDICES

Nomenclature and Symbols

A	Bagnold's coefficient, $U_{*T}\ (\rho/\sigma gd)^{1/2}$	
A'	constant	
A_B	area of sediment bed	m^2
A_{BS}	area of susceptible grains remaining	m^2
A_h	Bagnold's coefficient modified for humidity	
A_K	constant	
A_s	cross sectional area of sample	m^2
A_w	Bagnold's coefficient modified for damp sediment	
$A_*1, A_*2, A_*3, A_*4, A_*5$	coefficients	
a	regression coefficient	
a'	numerical constant	
a_m	amplitude	m
B	grain Reynolds number	
B'	roughness function	
B^*	experimental constant	
B_K	constant	
b'	numerical constant	
C_D	drag coefficient	
C_s	coefficient expressing the range of particle sizes in a sample, (Bagnold (1941))	
C^*	mass transport coefficient	
C_{LE}	length of the leading edge of the plate	m
c'	numerical constant	
D	effective roughness height	m
D_f	total drag force	Nm^{-2}
D_p	diameter of pitot-tube	m
D_s	standard grain diameter (250μm)	m

d	particle diameter	m
$\bar{d}$	mean particle diameter	m
d_{max}	maximum particle diameter in a test sample	m
d_{min}	minimum particle diameter in a test sample	m
d_p	particle size distribution in a sample	
E	dimensionless grain entrainment rate	
F	immersed particle weight	kg
$f^*(o)$	function of $\tau_o(x)$	
G^*	coefficient expressing relevant physical properties of particles	
g	acceleration due to gravity	ms^{-2}
H	boundary layer velocity profile shape parameter (δ^*/θ_M)	
h	height difference between manometer limbs recording pitot and static pressures	m
$h\delta$	approximate thickness of the boundary layer	m
I_p	inter-particle forces	Nm^{-2}
K_D	empirical drag coefficient	
K_L	empirical lift coefficient	
K_M	empirical overturning moment coefficient	
k	Von Karmans constant; exponent	
k'	Bagnold's focus (i.e. the height above the surface at which wind speed does not change regardless of increases in the external wind velocity)	m
k^*	constant	
$k_{(perm)}$	permeability of a substance	ms^{-1}
L_f	total lift force	Nm^{-2}
l	characteristic dimensions of a body	m
l_s	thickness of sample	m
M_o	moment	
m	mass of particle	kg

Np	packing coefficient	
n	packing factor	
n'	multiplication factor	
n_f	frequency of vortex shedding from one side of a grain	Hz
n_g	number of grain detachments per unit time	$s^{-1}m^{-2}$
n_o	number of τ_I or τ_T values	
P	pressure	Nm^{-2}
$\bar{P}$	mean pressure	Nm^{-2}
P*	normalized turbulence production rate per unit volume	
P_n	porosity	%
P_o	pitot pressure or dynamic pressure	Nm^{-2}
P_s	static pressure	Nm^{-2}
P_T	total pressure	Nm^{-2}
$P(U_*)$	probability density function for instantaneous bed shear velocity (U_*)	
$P(U_{*T})$	probability density function for threshold bed shear velocity associated with a granular test material (U_{*T})	
Q	dimensionless mass transport rate	
Q_d	discharge	ms^{-1}
q	rate of aeolian transport	$kgm^{-1}s^{-1}$
q'	coefficient	
Re	Reynolds number	
Re*	grain Reynolds number	
Re_x	plate Reynolds number	
Re‡	displacement thickness Reynolds number	
$Re\theta_M$	momentum thickness Reynolds number	
R_h	relative humidity	%
Rs	surface roughness factor	
r	grain radius	m

S	Strouhl number	
S_A	angle between wind direction and slope	Degrees
Sc	salt content	mg g^{-1}
T	turbulence factor (Chepil, 1959)	
T'	characteristic 'burst' frequency	Hz
T_*	temperature	Celcius
Tr	tunnel ratio index	
t	time	sec
t_{LE}	thickness of the leading edge of the plate	m
U	wind velocity in x direction	ms^{-1}
$\bar{U}$	mean wind velocity in x direction	ms^{-1}
U_∞	free stream wind velocity	ms^{-1}
$\bar{U}_\infty$	mean free stream wind velocity	ms^{-1}
$\bar{\bar{U}}_\infty$	arithmetic mean free stream wind velocity required to erode an entire test strip	
$U_{(max)}$	wind velocity just sufficient to erode completely a test strip or bed	ms^{-1}
$U_{(min)}$	wind velocity just below U_T	ms^{-1}
U_F	terminal velocity of a grain	ms^{-1}
U_T	threshold wind velocity	ms^{-1}
$\bar{U}_{100}$	mean fluid velocity at 100cm above the bed	ms^{-1}
$\bar{U}(y)$	mean wind velocity at height y	ms^{-1}
U_*	shear velocity	ms^{-1}
$\bar{U}_*$	mean shear velocity	ms^{-1}
$\bar{U}_*'$	mean shear velocity during sand transport	ms^{-1}
U_{*I}	instantaneous shear velocity	ms^{-1}
U_{*T}	threshold shear velocity	ms^{-1}
$\bar{U}_{*T}$	mean threshold shear velocity	ms^{-1}
$\bar{\bar{U}}_{*T}$	arithmetic mean shear velocity associated with complete erosion of a test strip	ms^{-1}

$\bar{U}_{*T(max)}$	maximum mean threshold shear velocity	ms^{-1}
$\bar{U}_{*T(min)}$	minimum mean threshold shear velocity	ms^{-1}
$\bar{U}_{*T(50)}$	mean threshold shear velocity required to erode 50% of a strip	ms^{-1}
U_{*Th}	threshold shear velocity modified by humidity	ms^{-1}
U_{*Tr}	threshold shear veloicty modified by a rough surface	ms^{-1}
U_{*Ts}	threshold shear veloicty modified by a slope	ms^{-1}
$U_{*T(SALT)}$	threshold shear veloicty modified by salcrete	ms^{-1}
U_{*Tw}	threshold shear veloicty modified by sediment moisture	ms^{-1}
U_{*v}	threshold shear velocity for grain oscillation	ms^{-1}
u'	fluctuating wind velocity component in x direction	ms^{-1}
v'	fluctuating wind velocity component in y direction	ms^{-1}
v_d	volume of petri-dish	m^3
v_p	volume of pore water in a sample	m^3
W	particle weight	kg
w_c	water content (% by weight)	%
w_b	weight of ballotini sample	kg
w_d	weight of large petri-dish	kg
w_l	weight of glass lid	kg
w_q	weight of petri-dish, water and glass lid	kg
w_{tb}	weight of petri-dish, lid and ballotini	kg
w_{ts}	weight of petri-dish, lid and saturated ballotini	kg
w_w	weight of water held in sample pore spaces	kg
x	distance downwind from the leading edge of the plate	m
Y_A	percentage of bed area uneroded	%
Ys	percentage of strip area uneroded	%
y	height above the surface	m
y+	dimensionless distance from the boundary, $y\bar{U}_*/\nu$	
y'	grain projection height	m
z_o	roughness length	m

α'	coefficient expressing the upward displacement of the drag force	
β	manometer inclination angle	Degrees
γ	local slope angle	Degrees
ΔP	pressure gradient	$Nm^{-2}m^{-1}$
δ	thickness of the boundary layer	m
δ^*	boundary layer displacement thickness	m
δd_p	particle size distribution in a sample	
δ_{sub}	thickness of the viscous sublayer	m
ε	Reynolds stresses	
η	ratio of lift and drag force on a grain to lift and drag forces on a bed of grains	
η_c	dimensionless coordinate	
θ	Shields parameter	
θ_T	Shields criterion	
θ_M	boundary layer momentum thickness	m
λ	net volume of sand grains contained in unit volume near the sand surface	m^3
λ'	wavelength	m
μ	absolute fluid viscosity	$Ns\ m^{-2}$
ν	kinematic viscosity, μ/ρ	m^2s^{-1}
Ξ	Yalin's parameter	
ρ	fluid density	kgm^{-3}
ρ_B	bulk density	kgm^{-3}
ρ_m	manometer fluid density	kgm^{-3}
σ	particle density	kgm^{-2}
σ_p	RMS of pressure fluctuations	Nm^{-2}
σ_u	RMS of velocity fluctuations	ms^{-1}
$\sigma_{\tau I}$	standard deviation of τ_I distribution associated with turbulent flow	Nm^{-2}
$\sigma_{\tau T}$	Standard deviation of τ_T distribution associated with a granular test material	Nm^{-2}

τ	shear stress	Nm^{-2}
$\bar{\tau}$	mean shear stress	Nm^{-2}
τ_I	instantaneous shear stress	Nm^{-2}
$\bar{\tau}_I$	average value of instantaneous bed shear stress	Nm^{-2}
τ_T	threshold shear stress for a given grain	Nm^{-2}
$\bar{\tau}_T$	mean threshold shear stress	Nm^{-2}
$\bar{\bar{\tau}}_T$	arithmetic mean threshold shear stress associated with complete erosion of a test strip	Nm^{-2}
$\tau_o(x)$	local skin friction	Nm^{-2}
Ψ	dimensionless entrainment parameter	
ϕ	angle of grain repose	Degrees

CHAPTER ONE

INTRODUCTION

1.1 Introduction

The last two decades have witnessed the emergence of specialised studies in geomorphology which attempt to explain landforms by analysing and interpreting the dominant physical and chemical processes operating in the environment. To achieve this, geomorphologists have increasingly used the theoretical and experimental techniques of the physicist and the engineer to develop pragmatic models of environmental systems and processes. In general, most geomorphological studies have been conducted in the field, and overall there has been a reluctance on the part of many geomorphologists to undertake process studies in controlled laboratory conditions. This has arisen largely from the scale of problems associated with establishing relationships between landforms and landforming processes in the laboratory. In certain circumstances, however, it is often more revealing to examine fundamental geomorphological processes using carefully controlled experiments, as they permit a detailed assessment of the significant variables in isolation from each other.

Some examples of geomorphological processes previously studied in the laboratory are: arid zone weathering (Griggs, 1936); aeolian processes (Bagnold, 1941); soil erosion (Chepil, 1956, 1958a); mass-movement (Van Burkalow, 1945); glaciers (Lewis and Miller, 1955); drainage basins (Schumm, 1973); and Martian aeolian processes (Greeley and Iversen, 1985). Results from such studies have aided our understanding of the processes acting in the natural environment which would otherwise have remained elusive.

Unlike some geomorphological processes, fluid and sediment

transport phenomena are particularly amenable to theoretical analysis and laboratory experimentation. The majority of research on aeolian transport has been undertaken using specially designed wind tunnels which allow transport processes to be studied in detail (e.g. Bagnold (1941), Chepil (1945a,b,c), Belley (1964), Kadib (1965), Lyles and Krauss (1971), Dolgilevich and Vasili'yev (1974), Greeley et al. (1980a,b). Fundamental to all aeolian transport processes is the concept of a 'threshold of particle motion'. Simply, if the force supplied to a granular surface by wind shear exceeds a critical level, aeolian entrainment will occur and transport of material will ensue. Present knowledge of aeolian threshold conditions is derived from a large number of inter-disciplinary studies concerned with the interactions between non-cohesive particles and fluids. In addition to direct studies of aeolian processes, significant contributions to the understanding of entrainment thresholds and processes have been made from the fields of fluid mechanics, fluvial geomorphology, soil erosion mechanics, sedimentology, geology and, most recently, from studies of geomorphological processes on other planets (e.g. Mars and Venus). The improved knowledge of aeolian processes these studies have provided has aided the development of physically realistic models of aeolian entrainment and transport and has generally served to improve our knowledge of the global aeolian system.

The importance of the threshold condition is stressed by Kalinske (1942) who states that "one of the most important problems relating to sand movement by wind (or water) is the determination of the conditions for initial movement", Kalinske (1942, p.65). Before considering the aeolian threshold condition in more detail it is useful to place it in the context of the global aeolian system, illustrated schematically in Figure 1.1.

The force driving the 'aeolian transport machine' is derived from net solar radiation. Differences in latitude and albedo, and the influence of oceans and large scale topography, give rise to global temperature variations which provide the energy disequilibrium necessary for atmospheric wind circulation. In addition, a net rotation component is imparted to the atmosphere by the spin of the earth. Frictional interactions between the moving earth surface and the circulating atmosphere cause the lower kilometre of the atmosphere to slow down. This region of retarded flow is termed the 'atmospheric boundary layer' and air motions within it are significantly influenced by large scale topography and surface characteristics (Blom and Wartena, 1969). Close to the surface, however, local changes in roughness quickly affect the properties of the atmospheric boundary layer wind. The air flow very close to the surface is sometimes referred to as the 'internal boundary layer' to distinguish it from the much larger scale atmospheric boundary layer. In the case of a sand surface, each individual grain, although embedded in the internal boundary layer, is also surrounded by its own thin layer of retarded flow which interacts with the internal boundary layer and gives rise to a net downwind force on the grain when the wind blows (see 1.4).

As the wind speed over a bed of grains is increased, a point will be reached when the shear force imparted by the wind just balances the forces resisting motion, and a condition termed the 'aeolian threshold' is reached. Generally, the force applied by the wind is described by the mean surface shear stress ($\bar{\tau}$), or mean shear velocity $\bar{U}_*$ defined as $(\bar{\tau}/\rho)^{1/2}$ where ρ = fluid density ($1.23 kgm^{-3}$ for air). Once the applied force of the wind exceeds the characteristic threshold value for a given granular material, sediment transport will

occur. Bagnold (1941) identified three distinct modes of aeolian transport on the evidence of wind tunnel experiments and field observations in the Libyan desert. These are 'suspension', 'saltation' and 'creep' (or 'surface traction load'). Each of these aeolian transport modes is discussed in detail in 1.3.1. In general, most aeolian grains lie within the size range of 150μm to 710μm (Bagnold, 1941).

The threshold condition therefore acts as a limiting factor of fundamental significance in the global aeolian system, as no transport, deflation or deposition is possible until the threshold is exceeded. Precise knowledge of the processes controlling the threshold of aeolian entrainment is, therefore, essential to understanding the operation of the aeolian system. Figure 1.1 also includes a simplified account of the various sources of aeolian particles (after Pettijohn et al. (1972) and Greeley and Iversen (1985)). Interactions between the wind and large masses of aeolian particles give rise to the familiar bedform hierarchy (Wilson 1972) and other related aeolian landforms. A brief summary of the main types of aeolian landform is given in Table 1.1. This summary includes bedforms composed of loose aeolian particles and erosional features caused by saltation bombardment.

Anyone interested in finding the minimum wind speed required for sediment motion is immediately faced with a fundamental problem. Although there are many published theoretical and empirical expressions at their disposal, it is unlikely that any two will predict the same threshold wind speed and even more unlikely that the predicted values will accord with reality in any given situation. In many respects this problem stems from the diverse ways in which aeolian threshold conditions

have been defined and measured. Generally, aeolian thresholds are expressed in terms of the mean shear stress acting on a flat bed of uniform, contiguous particles at the point of entrainment. Recent advances in the understanding of flow conditions above granular beds (e.g. Grass, 1970) suggest that this parameter is unrepresentative of the forces acting on single grains, and that to talk of 'mean threshold shear stress' is an over-simplification of a complex situation.

The major objective of this study was, therefore, to reconcile the differences in reported aeolian threshold values by investigating the factors widely regarded as being fundamental controls of incipient sediment motion in air. A summary of these factors in given in Table 1.2 under the following headings: sediment properties; surface properties; properties of the wind; and external factors. Paramount amongst these are the characteristics of the wind, the particle size and the particle shape although other factors listed in Table 1.2 became highly significant in certain situations. In laboratory studies of aeolian phenomena, it is sometimes desirable to be able to simulate the atmospheric boundary layer. However, simulation of this kind of shear flow is extremely difficult to achieve in practice. Armitt and Counihan (1968) list three conditions that must be satisfied for accurate similitude. These are: the preservation of geometric similarity; the reduction of the surface roughness in proportion with the geometric scale; and the preservation of aerodynamically rough flow. Work by Cermak and Arya (1970) suggest that the size of wind tunnel required to satisfy these conditions would be prohibitive and note the additional problems associated with simulating the temperature gradients of the atmospheric boundary layer in a realistic manner. Detailed accounts of the temperature, velocity and turbulence structure of the atmospheric

boundary layer are given by Sutton (1949), Monin (1962), Plate (1971) and Panofsky (1974). The most intractable problem associated with atmospheric boundary layer simulation is the simultaneous generation of the velocity profile and turbulence in scale with surface roughness (Owen and Zienkieuvicz, 1957; and Lloyd, 1967).

Laboratory studies of aeolian threshold conditions and transport processes are usually conducted in purpose-built wind tunnels. In general these '<u>aeolian tunnels</u>' have long working sections to produce semi-natural flow conditions and to facilitate the study of aeolian transport processes (e.g. saltation and creep) and development of small scale bedforms (e.g. ripples). Table 1.3 gives details of the lengths, widths and heights of the working sections of some wind tunnels used in the past for aeolian studies. Tunnels that were used for studies of aeolian threshold conditions are indicated by the asterisk. The tunnel ratio index (Tr) given in Table 1.3 is defined as tunnel length divided by the square root of the tunnel cross sectional area and serves as a useful index for comparisons between tunnels. The range of Tr values between 53.3 (Belley, 1964) and 6.39 (Bacharov, 1972) reflects the differences in wind tunnel design and suggests that precise flow conditions in these tunnels are likely to differ significantly from each other, and are probably unique for each given tunnel design. The data shown in Table 1.3 would therefore appear to offer one possible reason for the variation in reported values of aeolian threshold.

In general, most wind tunnel designs aim to simulate the characteristics of the natural wind on a sediment bed. In reality, however, the flows in many of the wind tunnels described in Table 1.3 are likely to have all the characteristic features of fully developed

turbulent pipe flow by the time they reach the test bed of aeolian particle and are thus likely to have a turbulence structure that is significantly different from that of natural wind over a sand surface. Flow characteristics in such working sections change continually from tunnel intake to exhaust and thus may profoundly affect the initial motion of particles on the tunnel floor. This effect was noted by Bagnold (1941) who observed that particles sited just downstream of the tunnel intake were extremely reluctant to move even though the same velocity setting was sufficient to initiate transport further downwind (Bagnold, 1941, p.32). Bagnold also noted that increasing the wind speed in the tunnel shifted the point of initial entrainment further upwind (Bagnold, 1941, p. 33). On the basis of this evidence, Bagnold identified the intensity of flow turbulence as being a crucial factor in determining aeolian threshold conditions. Subsequently, this observation has been confirmed by Kalinske (1942), Neill and Yalin (1969), Grass (1970), Lyles and Krauss (1971), Lyles and Woodruff (1971), Miller et al. (1977), and Greeley et al. (1984).

In order to evaluate further the significance of flow turbulence on aeolian thresholds, it was considered necessary in this investigation to devise a method of creating a range of controlled and reproducible flow regimes characterised by different levels of turbulence intensity. The development of the boundary layer along a flat plate immersed in a moving fluid has been extensively studied and, given certain conditions, its characteristics can be readily predicted using a number of well documented solutions to the boundary layer flow equations. The characteristics of the flow close to the surface of such a plate change continuously in the stream-wise direction from laminar flow near the leading edge to turbulent flow at some distance downstream. (An account

of the developing boundary layer on a flat plate is given in Chapter 2). The use in this study of a large flat plate in air has, therefore, provided the opportunity for investigation of aeolian thresholds in a continuum of flow regimes on the surface of the plate.

The majority of the experimental work reported in this thesis used a specially designed flat plate in a large blow-down wind tunnel. The surface of the plate was covered with a non-erosive layer of test material (see below) to simulate a natural, flat sediment bed. The boundary layer on the surface of the plate was, therefore, forced to develop over a rough surface. By placing loose test grains on the surface of the plate at selected positions and by gradually increasing the wind speed, it was possible to determine the threshold flow conditions associated with a given test material and boundary layer flow regime. The actual flow conditions at the surface could be replicated whenever and wherever required thus providing control of the flow regime at any position on the plate. In the event, the ability to vary flow characteristics at will proved to be particularly informative with regard to the investigation of aeolian threshold conditions. A detailed account of the design of the plate and the experimental investigations of aeolian threshold conditions is given in Chapters 3 to 6.

The test particles used were selected after a thorough review of possible materials and included glass beads ('ballotini'), aeolian dune sand, sugar crystals and salt crystals. Carefully sieved, these materials gave test samples in three major size ranges. These were: 710-600μm; 355-300μm; and 180-150μm. In addition, a 1.7-1.4mm range of ballotini was also studied during preliminary work. The standardization of particle size in this way enabled later comparison between different

granular materials in the same size range and thus permitted an assessment of particle shape effects on both the boundary layer characteristics and the threshold condition.

Most studies of aeolian thresholds are conducted in turbulent boundary layer flow and thus shear stress can be calculated using the Von Kármán-Prandtl logarithmic velocity distribution law (see below). In the case of the experimental plate, however, flow conditions over the majority of the length of the plate do not conform to this law and thus it was necessary to use an alternative technique. After a review of likely methods (2.6), surface shear stress was calculated using the momentum integral method which considers boundary layer momentum losses in friction with the plate surface. This technique provided an assessment of mean surface shear stress and thus permitted direct comparison between the experimentally determined threshold conditions on the plate and the threshold conditions determined by other workers using other shear stress measurement techniques.

1.2 Essential definitions and concepts

The study of particle motion in fluids by researchers from a wide range of scientific disciplines has given rise to a degree of confusion in the literature regarding both the conception and definition of sediment transport phenomena. Central to all models of particle motion in fluids is the concept of a 'threshold of movement' as considered above. If the fluid and sediment interactions are analysed within a systems framework, this state represents the crossing of a systems threshold and the changes that result are irreversible for all practical purposes. Thus, conditions just slightly less than those

required for actual sediment motion are termed 'threshold conditions'. The threshold condition may be thought of as representing the minimum energy level of the aeolian transport 'machine'. At wind speeds below the threshold, no sediment transport occurs and thus the threshold marks a critical boundary between an active (and therefore geomorphologically significant) environment and a static environment. Shields (1936) described the threshold condition as being 'critical', whilst Bagnold (1941) used the term 'fluid threshold' to describe the flow conditions at the point of particle motion. Recently, the term 'static threshold' has been used by Greeley and Iversen (1985) in place of Bagnold's term. Throughout this thesis, however, the conditions for incipient aeolian transport are simply referred to as being 'threshold conditions'.

Threshold conditions for non-cohesive particles in air have been studied by a large number of research workers. The classic work by Bagnold (1941) describes the fundamental physics of initial grain motion in terms of basic fluid and grain parameters. Similar fundamental work on soil erosion thresholds was carried out by Chepil (1945a,b,c, 1959), Smerdon and Beasley (1961) and Woodruff and Siddoway (1965). More recent work on the aeolian threshold condition is reported by Lyles and Krauss (1971), Bisal (1973), Gillette et al. (1980, 1982) and Logie (1982). In addition, the NASA missions to Mars, Mariner 4 (1965), Mariners 6 and 7 (1969), Mariner 9 (1971-1972), the Viking mission (1976-1979), together with the Soviet orbiters, (Mars 3 (1971) and Mars 5 (1974)), provided conclusive evidence of aeolian processes on the planet's surface. Speculation of the likely aeolian threshold conditions in the thin cold atmosphere and reduced gravity on Mars led to a series of publications in the mid 1970s and early 1980s. These include: Arvidson (1972); Wood et al. (1974); Greeley et al. (1974, 1976, 1980a); Iversen et al. (1975,

1976); Pollack et al. (1976); and Miller and Komar (1977). In addition, evidence of aeolian processes on Venus were recognised and studies of likely threshold conditions on the surface of that planet were published by Greeley et al. (1980b, 1984) and Greeley and Marshall (1985).

A less familiar, but nevertheless significant, sediment state prior to entrainment was identified by Bisal and Nielsen (1962). In flow conditions just below the threshold, particles are observed to undergo rapid oscillatory motion. In such a state they are extremely sensitive to minor perturbations in the local bed shear stress and only slight increases in flow velocity will induce entrainment. Such particles are described as being at the '<u>oscillatory threshold</u>' (Azizov, 1977).

A third critical fluid shear velocity is associated with particles in saltation. Bagnold (1941) found that, once set in motion, a saltating grain population could be maintained by wind shear velocities less than the 'fluid' threshold. However, at a wind shear velocity value around 20% lower than the 'fluid' threshold for a given material, Bagnold found that wind is no longer able to sustain saltation and transport suddenly ceases. Bagnold used the term '<u>impact threshold</u>' to describe this critical flow state which reflects the balance between the energy supplied by the wind and the energy losses associated with saltating grains striking the bed. In addition, Bagnold also acknowledged the critical value of the wind shear required to move <u>all</u> the particles in a sediment characterised by a range of grain sizes. The wind shear velocity required to achieve this state was defined as the '<u>ultimate threshold</u>'.

The relationship between grain size and threshold wind shear

velocity was originally determined experimentally by Bagnold (1941). The resulting curves for both the 'fluid' and 'impact' thresholds are illustrated in Figure 1.2. For grain sizes larger than approximately 0.2mm, threshold wind shear velocity increases at a rate proportional to the square root of grain diameter. However, this 'square root law' does not hold for grains smaller than 0.2mm and at a critical diameter of approximately 0.08mm, Bagnold (1941) found that $\overline{U}_{*T}$ began to increase with decreasing particle size. This increase in $\overline{U}_{*T}$ was attributed to changes in the local flow conditions and to interparticle-cohesion effects. An account of these effects is given in Chapter 5 where the relationships between fluid and grain parameters at the threshold are examined in detail.

The concept of a threshold condition is, however, only really applicable to a single grain or a geometric arrangement of identical particles. In such circumstances, sediment motion will only occur <u>en masse</u> at the threshold if the shear stress is applied equally over the entire bed area. In reality, however, even the most closely graded natural sediments are present in non-uniform assemblages and possess a variety of sizes, shapes, specific gravities and surface morphologies. Further, the apparently random fluctuations in bed shear stress through time and space in turbulent flow necessitate the introduction of a stochastic element into the definition of threshold conditions for natural sediments.

To overcome the problems associated with heterogeneous bed sediment and variable flow turbulence, investigators have been forced to devise experimental criteria for initial sediment motion. The criteria are based on an 'observable degree of bed motion' and are considered to

represent the threshold condition. The accuracy of threshold measurements is, therefore, controlled by the subjective judgement of an observer who must correctly identify a defined degree of bed motion. A large number of threshold criteria have been proposed in the literature. These range from 'displacement of the first grain' (Neill, 1967) at one extreme, to 'general bed movement' (Chepil, 1959) at the other. A summary of reported threshold criteria ranging between these two extremes is given in Table 1.4.

A more objective definition of threshold conditions was developed by Neill and Yalin (1969) and Yalin (1972). Using statistical arguments they showed that

$$E = \frac{n_g}{A_B t}\left(\frac{\rho d^5}{(\sigma-\rho)g}\right)^{1/2} \qquad 1.1$$

where

$$E = f\left(\frac{\rho \bar{U}_*^2}{(\sigma-\rho)gd}, \frac{\bar{U}_* d}{\nu} = Re^*\right)$$

and

E	= dimensionless entrainment rate	dimensionless
n_g	= number of grain detachments per unit time per unit area	$s^{-1}m^{-2}$
A_B	= area of sediment bed	m^2
t	= time	s
ρ	= fluid density	kgm^{-3}
d	= particle diameter	m

σ	= particle density	kgm^{-3}
g	= acceleration due to gravity	ms^{-2}
ν	= kinematic fluid viscosity (μ/ρ)	m^2s^{-1}
μ	= absolute fluid viscosity	$Ns\ m^{-2}$
$\bar{U}_*$	= mean shear velocity	ms^{-1}
Re*	= grain Reynolds number	dimensionless

The value of $(\rho d^5/(\sigma-\rho)g)$ is set by the material under investigation. Adjustment of the parameters in $n_g/A_B t$ then allows a constant E value to be set for any sediment by simply altering the flow velocity. Neill and Yalin (1969) suggest a practical lower limit of 1×10^{-6} for values of E. However, despite the elegance of this statistical definition of the threshold condition, it is still necessary to measure n_g interactively to enable appropriate flow adjustments to be made during threshold determinations. A detection system designed to achieve this objective was first proposed by Greeley et al. (1976) and was subsequently developed by Nickling and Eccleston (1980) and Logie (1981, 1982). In this system, a light beam from a 5mW helium-neon LASER is reflected back and forth across the sediment bed using a system of mirrors. Particle movement is then detected using high resolution photodiodes which are able to measure any LASER beam interference caused by particles in motion. Greeley et al. (1976, 1980) and Iversen and White (1982) used a high resolution close-circuit television camera in conjunction with the LASER photocell system to monitor particle motion. In addition, an electrostatic detector was incorporated in the detection apparatus to monitor the movement of small particles. However, only a small percentage of the bed surface is scrutinized using these remote detection systems so it is probable that inaccuracies as great as those associated with direct observations of the bed were incurred.

The problems associated with measuring the forces acting on individual particles at the threshold have forced workers to express threshold conditions in terms of the mean shear stress or shear velocity at the fluid/sediment boundary. The shear velocity is a measure of the velocity gradient in the boundary layer close to the surface (i.e. the rate of increase in velocity with height). The velocity gradient gives rise to a shear stress throughout the boundary layer and this is manifest at the surface as drag. In the case of wind blowing over a fixed sand surface in adiabatic conditions, mean shear velocity $\bar{U}_*$ (ms^{-1}) may be expressed in the form

$$\bar{U}_* = \frac{\bar{U}(y)k}{\ln(Y-D/Z_o)} \qquad 1.2$$

$\bar{U}(y)$	= wind velocity at height y	ms^{-1}
k	= Von Karmans constant ($\approx$0.4)	dimensionless
y	= height above the surface	m
D	= effective roughness height	m
Z_o	= roughness length	m

Equation 1.2 is known as the Von Kármán-Prandtl logarithmic velocity distribution law and is useful in describing the wind velocity distribution for undisturbed, thermally stable turbulent boundary layer flow (e.g. the stable surface wind). (The derivation of equation 1.2 is given in Francis (1969)). Using equation 1.2, therefore, it is possible to determine the value of $\bar{U}_*$ over a given granular surface from a single mean wind velocity measurement at height y, provided D/Z_o is known or can be estimated. Thus by gradually raising the wind velocity

over a bed of sediment and determining the condition of initial particle motion, it is possible to estimate the threshold shear velocity for the experimental material using this equation. Many studies of aeolian threshold conditions have used similar experimental techniques in both the laboratory wind tunnel and the field to obtain a measure of the mean threshold shear velocity, $\bar{U}_{*T}$ for a given sediment (e.g. Bagnold (1941); Belley (1964); Lyles and Krauss (1971)).

1.3 Aeolian thresholds and transport mechanisms

1.3.1 Modes of aeolian transport

A schematic diagram of the aeolian transport modes identified by Bagnold (1941) is given in Figure 1.3 and includes suspension, saltation and creep.

(a) Suspension Particles held aloft for long periods by the turbulent motion of the atmosphere are likely to be transported away from their source of origin in suspension. In air, only particles smaller than approximately 40μm are susceptible to this mode of transport and such fine material is often transported many hundreds of kilometers by the lower atmospheric flows, only returning to earth in anticyclonic conditions or as precipitation nuclei. Peterson and Junge (1971) estimate that 500×10^6 tonnes of dust (i.e. particles smaller than or equal to 20μm) enter the atmosphere in one year on a global basis and the vast loess deposits that cover 10% of the Earth's surface bear witness to the importance of this transport mode.

(b) Saltation Saltation (derived from the Latin Saltare - 'to leap')

was a term first used by McGee (1897) to describe the bouncing or leaping motion of particles as they are transported in a zone of limited vertical extent from their point of entrainment. Particles too large to enter suspension are transported by this process which is often manifest as the familiar 'sand cloud' extending little more than half a metre or so from the surface during windy conditions over unconsolidated sediments. In exceptional conditions, however, saltation heights can reach 20m (d=125 μm) and instances have been recorded of 2mm grains attaining heights of 6m, Pitty (1977, p. 206). Quantitatively, saltation is the most important mode of aeolian transport, Wilson and Cooke (1980).

The importance of this aeolian transport mode is reflected by the number of studies of saltation in air. These include Bagnold (1941), Kawamura (1951), Zingg (1953), Belley (1964), Williams (1964), Owen (1964), Kadib (1965), Horikawa (1959), Horikawa and Shen (1960), Nemoto et al. (1969), Tsuchiya (1970), Tsuchiya and Kawata (1972), Gerety and Slingland (1982, 1983), Jensen and Sørensen (1982, 1983), and Greeley et al. (1983). Bagnold (1941) states that the saltation load accounts for 75% of the total material moved by the wind. Chepil (1945c) puts this figure higher at between 75% and 95% whilst Ishihara and Iwagaki (1952) estimate that the saltating grain population accounts for between 84% and 95% of all the material transported.

Saltation significantly alters the characteristics of the boundary layer wind owing to momentum transfer processes. Bagnold (1941) found that the saltation layer greatly increased the effective aerodynamic roughness height and this was manifest as a substantial reduction in wind speed near the surface due to the additional drag of saltation. A number of authors including Bagnold (1941), Owen (1964),

White and Schulz (1977) and Tabler (1980) have derived expressions to describe the effect of the saltation layer on the wind profile near the surface. The equation given by Bagnold (1941) for mean shear velocity during sand transport $\bar{U}_*'$ is a modified version of equation 1.2 and takes the form

$$\bar{U}_*' = \bar{U}(y)/(1/0.4)\ln(y/k')+(\bar{U}_T/\bar{U}_*) \qquad 1.3$$

In this equation, the term k' is known as Bagnold's 'focus', i.e. the height above the surface at which wind speed does not change regardless of increases in the external wind velocity above the threshold, $\bar{U}_T$.

(c) Creep (or surface traction load). Particles too large to enter into saltation are frequently transported under the action of saltation bombardment. In this process, descending saltating grains strike individual grains on the bed from behind and the net transfer of momentum is often sufficient to knock the grain a short distance downwind. (Bagnold (1941) states that a high-speed grain in saltation is able to move a grain more than 200 times its own weight). Creep accounts for between a quarter and a fifth of total aeolian transport as it operates at a much lower rate than saltation, (Bagnold (1941, p. 34)).

It is clear from the preceding discussion that none of these aeolian transport processes can operate unless aeolian threshold conditions are exceeded. The relationship between aeolian thresholds and aeolian transport is illustrated schematically in Figure 1.4. This figure shows that as wind speed is increased, particles begin to oscillate sporadically. Further increases in the wind speed give rise to incipient grain motion. If these entrained grains are sufficiently

energetic then the processes termed 'avalanching' occur (see Figure 1.3) whereby more and more grains are set into saltation by a chain reaction of impacts between entrained grains and the bed, provided that the mean wind shear velocity remains above the impact threshold. Once saltation is established, small particles will be ejected into suspension by the impacting grains, and by the same process, large grains not moved by the direct wind shear will be pushed along the surface (i.e. creep). As these processes continue, a stage will be reached when the energy supplied to the mobile grain population just balances the solid shear resistance and an equilibrium transport condition is attained.

Owen (1964) showed that aeolian transport is likely to be in dynamic equilibrium with a given wind owing to the reduction in the surface shear stress applied by the wind as the amount of material in transport increases. Owen argued that this reduction in wind shear must be reflected by a corresponding decrease in the momentum of the saltating grain population and hence a reduction in the transfer of momentum to the bed during saltation collisions. The reduction in wind shear acts as a negative feedback mechanism whereby the rates of saltation, creep and suspension transport are reduced. As fewer grains are now in motion, the wind shear again increases and by a positive feedback mechanism, additional material is entrained by the force of the wind and by increasingly energetic collisions between saltating grains and the bed. By these feedback mechanisms, the aeolian transport system is maintained in a state of dynamic equilibrium with the local boundary layer wind, (Figure 1.4).

1.3.2 Classification of transport processes

Greeley and Iversen (1985) classify the three processes of aeolian transport using arguments based on the terminal velocity and the threshold shear velocity associated with a given sediment. The terminal velocity, U_F represents the maximum theoretical velocity a particle will attain by acceleration under gravity in air. For a spherical particle, U_F is given by

$$U_F = (4\sigma g d/3\rho C_D)^{1/2} \qquad 1.4$$

where C_D = drag coefficient

In turbulent air flow, the value of the vertical component of fluctuating velocity is approximately equal to the shear velocity, U_*, Bagnold (1941, p. 65). Using experimental evidence, Iversen et al. (1976) argued that transport of material in suspension will occur when U_F is greater than the threshold shear velocity, U_{*T}. Thus the boundary between suspension and saltation transport for any granular material is defined as being when U_F/U_* is equal to unity. Greeley and Iversen (1985) incorporate the threshold shear velocity U_{*T} in a similar expression to define the saltation and suspension transport modes so that

$$\frac{U_F}{U_*} = \frac{U_F}{U_{*T}} \Bigg/ \frac{U_*}{U_{*T}} = 1 \qquad 1.5$$

The ratio of terminal velocity to threshold shear velocity and the ratio of wind shear velocity to threshold shear velocity may be used

as arbitrary guides to the mode of sediment transport in terms of suspension and saltation. This is illustrated more clearly in Figure 1.5 where U_F/U_{*T} is plotted against particle diameter. Figure 1.5 shows that when U_F/U_{*T} is smaller than 1, the dominant transport mode is suspension and when U_F/U_{*T} is greater than 1, particles are transported by the saltation process. This theoretical definition is, however, limited to non-cohesive, homogeneous particles. In practice, real sediments display a range of particle sizes and shapes and thus both the saltation and suspension transport modes operate simultaneously. Further, the definition does not account for inevitable interactions between the saltating grain population, the bed load and the changes in wind shear velocity caused by saltation transport. In the case of real sediments therefore,

$$\frac{U_F}{U_{*T}} = f(\sigma, C_s, G^*, \rho, \nu, T, Rs) \qquad 1.6$$

where

C_s = coefficient expressing the range of particle sizes in a sample: C_s=1.5 for nearly uniform sand; C_s=1.8 for naturally graded sand, i.e. typical aeolian dune sands; and C_s=2.8 for sand with a wide size distribution, Bagnold (1941, p.67) — dimensionless

G^* = coefficient expressing other relevant particle properties (e.g. shape, cohesion) — dimensionless

T = turbulence factor (e.g. Chepil (1959), equation 1.20) — dimensionless

Rs = surface roughness factor — dimensionless

1.4 Forces acting on a single particle at the threshold condition

A particle exposed to a fluid shear layer, such as a boundary layer, experiences a force that may be resolved into a lift force, normal to the oncoming flow, and a drag force parallel to it, (Nemenyi, 1940). Forces resisting these fluid forces include gravity and cohesive forces between particles. Howard (1977) describes the threshold condition for a single grain as being "when the fluid forces, including drag and lift, exert an overturning moment on the grain equal to the cohesion between particles and the stabilising moment exerted by gravity", Howard (1977, p. 853). The forces acting on a single grain poised at the threshold are illustrated in Figure 1.6 and are discussed in detail below.

1.4.1 The drag force

In theoretical considerations and experimental determinations of the drag force on particles on both air and water, it is usual to consider only total drag because of the problems associated with assessing its components. Studies by Bairstow (1925), Casey (1935), Nemenyi (1940), Einstein and El-Samni (1949), Ford (1957), Chepil (1958a), Coleman (1967, 1972), O'Neill (1968), Garde and Sethuraman (1969), Marshall (1971), Wooding et al. (1973) and Coleman and Ellis (1976) have examined the total drag force for both individual particles and loose granular beds. In theoretical treatments by Goldman et al. (1967) and O'Neill (1968), simple fluid and particle parameters are combined to express the total drag force D_f in low grain Reynolds number flows by:

$$D_f = 1.7005\ (6\pi\rho d^2 U_*^2/4) \qquad 1.7$$

D_f = total drag force $\qquad Nm^{-2}$

A more general expression for the total drag force was developed by Coleman (1972) and Coleman and Ellis (1976) for a grain Reynolds number range of 130 to 13,200. Their equation takes the form

$$D_f = K_D \rho U_*^2 d^2 \qquad 1.8$$

where K_D = empirical drag coefficient (see Table 1.5)

1.4.2 The lift force

The lift force acting on a particle in shear flow is generated by the acceleration of flow over the top surface of the particle. By Bernoulli's principle, an acceleration of fluid gives rise to a reduction in fluid pressure along the streamlines and hence a lifting force. Prior to the work by Coleman (1967), studies of the lift force were conducted in 'rough' flow regimes characterised by grain Reynolds number values, Re* greater than 70. Work by Einstein and El-Samni (1949), Chepil (1958a) Saffman (1965), Cheng and Clyde (1971) and Bagnold (1974) indicated positive lift forces away from the bed. Potential flow analysis for objects close to or in contact with a solid surface by Jeffreys (1929), Benedict and Christensen (1972) and Nath and Yamamoto (1974) also confirmed this general result. In all cases, it was reported that the lift force quickly reduced to zero once an object was displaced a small distance from the surface.

Coleman (1967) and O'Neill (1968) examined the magnitude and direction of the lift force in a range of flow conditions and found them to be dependent on Re*. In further studies, Watters and Rao (1971) and Askoy (1973) recorded both positive and negative lift forces in a range

of flow conditions. In a detailed study by Davies and Samad (1978), positive lift was recorded at Re* values greater than 5 whilst negative lift was measured for Re* values smaller than 5. The negative lift was attributed to flow beneath the particles and thereby suggests that bed porosity may be a significant factor in determining the magnitude of the lift force in certain flow conditions. In addition, Willetts and Murray (1981) and Mutlu-Sumer (1984) suggested that the configuration of the bed has a significant effect on the strength of the lift force and found that the lift force increased markedly with greater bed roughness. Measurements of the lift and drag forces on hemispheres by Chepil (1958a) indicated that the lift force was approximately 4/5 of the drag force. Similarly, Einstein and El-Samni (1949) found the lift and drag forces to be of the same order of magnitude in given flow conditions. In contrast, Askoy (1973) found the lift force to be only 1/7 of the total drag force. However, their studies were highly artificial and were conducted in turbulent flows characterised by relatively high grain Reynolds numbers (500 to 7,000). These studies cannot, therefore, be related directly to the forces acting on typical aeolian sand grains at the threshold of movement.

The most widely used expression to describe the lift force, L_f, was developed by Einstein (1950) and is based on an empirical coefficient of lift and a constant, A'.

$$L_f = K_L \rho \frac{U^2}{2} A' d^2 \qquad 1.9$$

where K_L = empirical lift coefficient — dimensionless

U = fluid velocity — ms^{-1}

A' = constant

Rubinov and Keller (1961) included a Reynolds number term in their expression for the lift force and Coleman (1972) expresses the lift force in terms of the shear velocity. Hence

$$L_f = K_L \rho U_*^2 d^2 \qquad 1.10$$

In low grain Reynolds number flows, equation 1.10 takes the form

$$L_f = 0.8077 \rho U_*^2 d^2 Re^*, \quad \text{Iversen et al. (1976)} \qquad 1.11$$

1.4.3 Forces resisting motion

A particle at rest on a bed of similar grains will only move when the local components of drag and lift exceed the forces resisting motion. Some of the resisting forces are illustrated in Figure 1.6 and include the gravity force and the forces of inter-particle cohesion. General studies of the various cohesive forces which resist particle motion include work by Corn (1966), Smalley (1970), Iversen et al. (1976), Greeley and Leach (1978), Nickling and Eccleston (1981) and Nickling (1984).

The gravity force or relative particle weight for a spherical particle is given by

$$\frac{\pi}{6} d^3 (\sigma - \rho) g \ , \qquad \text{Bagnold (1941)} \qquad 1.12$$

or, for any particle shape by

$$gm(\sigma-\rho)/\rho \ , \qquad \text{Ford (1957)} \qquad 1.13$$

where m = particle mass kg

The force acts through the centre of gravity and pulls the grain downward towards the bed. The most significant cohesive forces acting on particles greater than 80μm in diameter in air are the surface tension forces that result from attraction between particles and the entrapped capillary and pore water in the grain interstices. The effect of moisture on aeolian threshold values was noted by Bagnold (1941) and has since been investigated by Gimmingham (1955), Chepil (1958b), Belley (1964), Bisal and Hsieh (1966), Azizov (1977) and Logie (1982).

Other inter-particle forces include London-Van der Waals forces, electrostatic forces, gravitational forces and forces between adsorbed films. It should be emphasised, however, that these forces are only significant for particles smaller than 80μm. In special cases, additional cohesive forces may result from physical and chemical binding due to micro-organisms (e.g. bacteria and fungal hyphae), organic polymers (e.g. polysaccharide gums), and soluble salts (e.g. NaCl, KCl).

The investigation of forces acting on particles at the threshold of motion has made possible the development of equations which express threshold conditions in terms of the fluid and particle parameters and these are now considered.

1.5 Theoretical and empirical expressions for aeolian entrainment thresholds

Expressions for aeolian entrainment thresholds have been developed either by considering the forces acting on grains at the threshold of movement (1.4), or by empirical means using wind tunnels and field techniques. Nearly all the expressions so derived have some degree of inherent empiricism and most only apply for limited ranges of grain sizes and in a limited range of fluid flow conditions.

Historically, Brahms (1957) first recognised the relationship between the critical threshold velocity and particle weight. The relationship was expressed as a 1/6 power law in the form

$$U_T = k^* W^{1/6} \qquad 1.14$$

where k^* = constant

W = particle weight kg

Subsequent research into the forces acting on particles at the threshold of motion has shown that the relationship described by Brahms is oversimplified. A major advance in the understanding of thresholds was provided by Shields (1936) who combined particle and fluid parameters, shear stress and the acceleration due to gravity in the dimensionless relationship given in equation 1.15.

$$\theta = \frac{\bar{\tau}}{(\sigma-\rho)gd} = \frac{\rho \bar{U}_*^2}{(\sigma-\rho)gd} = f\ Re^* = \frac{\bar{U}_* d}{\nu} \qquad 1.15$$

where	θ	= Shields parameter	dimensionless
and	$\bar{\tau}$	= mean shear stress	Nm^{-2}

The functional relationship between θ and Re^* at the threshold of particle motion was found using empirical methods. The data were found to lie roughly on a curve (i.e. 'Shields curve') when plotted in the form $\log\theta_T$ against $\log Re^*$. The term θ_T, often referred to as 'Shields' criterion', represents θ values at the threshold of motion. Although Shields' relationship was originally derived from studies of incipient motion in water, it is equally applicable to aeolian entrainment as it is a dimensionless value and it has been used to good effect by Miller et al. (1977). However, despite the apparent elegance of this expression it suffers from several inherent deficiencies and these are discussed at length in 5.2.2(a).

White (1940) considered the forces acting on a bed of spherical particles at the threshold and developed an expression which accounted for particle arrangement and the angle of grain repose.

$$U_{*T} = [\alpha' Np \frac{\Pi}{6} (\sigma-\rho) g d \tan\phi/\rho]^{1/2} \qquad 1.16$$

where	α'	= coefficient (see below)	dimensionless
	Np	= packing coefficient	dimensionless
	ϕ	= angle of grain repose	degrees

The coefficient α' is used to account for the upward displacement of the effective drag force as it does not act through the centre of gravity of the particle in shear flow. Using empirical

studies, White was able to simplify equation 1.16 to the form

$$U_{*T} = [0.18(\sigma-\rho)d \tan\phi/\rho]^{1/2} \qquad 1.17$$

Bagnold (1941) considered the forces acting on a grain at the threshold of movement and derived an expression for U_{*T} based on simple grain and fluid parameters and the acceleration due to gravity, (Bagnold, 1941, p. 85).

$$U_{*T} = A\left[\frac{(\sigma-\rho)gd}{\rho}\right]^{1/2} \qquad 1.18$$

where A = Bagnold's coefficient dimensionless

In common with other coefficients in fluid dynamics, the value of Bagnold's coefficient A is found to vary with the state of the flow and sediment sorting. In this case, the most appropriate measure of flow characteristics is the grain Reynolds number, Re*. The numerical value of A is found to increase as Re* values fall below 3.5. At Re* values above 3.5, the coefficient A assumes a near constant value of 0.1 in air. However, a range of A values is reported in the literature and these are summarized in Table 1.6. The discrepancies between the A values presented in Table 1.6 arises for four reasons: (a) the use of different entrainment criteria by the various authors gives rise to inconsistency and ambiguity; (b) the surface packing of the loose particles used in the experiments was probably variable; (c) the technique used by authors to determine U_{*T} varies between experiments; and (d) flow conditions were probably variable. Further discussion of Bagnold's coefficient is given below (5.2.3).

Kawamura (1951) considered the immersed grain weight, the angle of grain repose and the net volume of sand grains contained in the unit volume near the sand surface to express threshold shear velocity as:

$$U_{*T} = \Pi^{1/6}(6\lambda)^{1/3}(\tan\phi)^{1/2}\,[(\sigma-\rho)/gd]^{1/2} \qquad 1.19$$

where λ = net volume of sand grains contained in unit volume near the sand surface m^3

In a theoretical consideration of the balance of moments for particles at the threshold of motion, Chepil (1959) developed an expression for U_{*T}.

$$U_{*T} = [0.66gd(\sigma-\rho)\tan\phi\eta/\rho(1+0.75\tan\phi)T]^{1/2} \qquad 1.20$$

where

η = packing factor = $\dfrac{\text{Drag and lift on the topmost grain moved by the wind}}{\text{Drag and lift on the whole bed}}$

T = turbulence factor = $\dfrac{\text{Maximum lift and drag on the bed}}{\text{Mean lift and drag on the bed}}$

Chepil's equation includes a term η which accounts for the ratio of lift and drag forces acting on a single grain to that acting over the whole bed and in addition introduces a new term T to express the degree of local flow turbulence. Data from White (1940) suggests a value of 0.1 for η. However, Chepil (1959) states that a more appropriate value for η is 0.21 and in an exhaustive study by Lyles and Krauss (1971), the value of η was shown to be dependent upon the particle size. Lyles and Krauss (1971) express values for η using a regression equation in the form

$$\eta = 0.342 - 0.132 \ln(r) \qquad 1.21$$

where r = particle radius m

The inclusion of the turbulence factor T in equation 1.20 acknowledges the importance of the distribution of shear velocity fluctuations in turbulent flow near a rough boundary. Chepil (1959) defines T in terms of boundary layer pressure fluctuations about the mean so that

$$T = (3\sigma_p + \bar{P})/\bar{P} \qquad 1.22$$

where σ_p = root mean square of pressure fluctuations Nm^{-2}

$\bar{P}$ = mean pressure Nm^{-2}

In practical terms, however, pressure fluctuations which occur with the magnitude and frequency of those associated with boundary layer shear flows over natural surfaces (e.g. sand) are extremely difficult to measure accurately (Kraichnan, 1956; Clyde and Einstein, 1966; Blake, 1970; Willmarth, 1971, 1975). In view of this difficulty, Lyles and Krauss (1971) considered fluctuations in flow velocity in lieu of pressure changes as velocity is inherently easier to measure. Hence, for practical purposes, equation 1.22 becomes:

$$T = \left[1 + 3\left(\frac{\sigma u}{\bar{U}(y)}\right)^2\right] \qquad 1.23$$

where σ_u = root mean square of velocity fluctuations ms^{-1}

The right hand term of equation 1.23 is squared because pressure (or

drag) is proportional to U^2. Lyles and Krauss (1971) found that T increased as surface roughness increased owing to the functional relationship between the longitudinal turbulence intensity (i.e. $\sigma_u/\bar{U}(y)$) and the surface roughness.

Greeley and Iversen (1985) consider a sphere in contact with a bed of identical spheres and equate the moments about the downstream point of contact. They derive an expression for the drag force D_f acting on the sphere at the threshold.

$$D_f = 0.445\left(\frac{\Pi}{6}\sigma g d^3 - L_f\right) \qquad 1.24$$

Greeley and Iversen (1985) assume that D_f at the threshold is equal to the surface shear stress ρU_{*T}^2 times the exposed area of the sphere $\Pi d^2/4$. Hence

$$U_{*T} = \left[\frac{[0.445(2/3)\eta]\,\sigma g d}{[1+0.85(0.445\Pi T\rho}\right]^{1/2} \qquad 1.25$$

If Chepil's (1959) values for η and T are substituted (0.21 and 2.5 respectively), the Bagnold coefficient, A, is found to have a value of 0.134.

Greeley and Iverson (1985) argue that at the threshold of motion, the forces acting on a particle are in equilibrium about a point of contact P. These forces and their respective moment arms are illustrated in Figure 1.7. In the condition of equilibrium, the summation of moments about P gives

$$D_f a' + L_f b' + M_o = Wb + I_p c' \qquad 1.26$$

where M = moment

I_p = interparticle forces Nm^{-2}

a', b' and c' = numerical constants dimensionless

Expressions for D_f and L_f were given in equations 1.8 and 1.10 respectively. In addition, Coleman and Ellis (1976) show that

$$M_o = K_M \rho U_*^2 d^3 \qquad 1.27$$

where K_M = empirical overturning moment coefficient

Greeley and Iversen (1985) state that the moment arm lengths a, b and c (Figure 1.7) are proportional to the diameter of the particles, i.e. $a = a_1 d$, $b = b_1 d$, $c = c_1 d$. By substituting equations 1.8, 1.10 and 1.27 into equation 1.26, it is possible to derive an expression for Bagnold's (1941) coefficient A (equation 1.18). Hence,

$$\left[\frac{(\Pi b_1/6)[1+(6c_1/\Pi b_1)Ip/\sigma g d^3]}{K_D a_1 + K_M + b_1 K_L}\right]^{1/2} = \left[\frac{U_{*T}^2 \rho}{\sigma g d}\right]^{1/2} = A \qquad 1.28$$

Experimental and theoretical values for the force coefficients K_D, K_M and K_L are given in Table 1.5. Coleman (1967) derived theoretical expressions for a_1 and b_1 (from which c_1 may be derived) for a single sphere at rest on a bed of identical spheres. The geometrical arrangement of the supporting particles gave this sphere the maximum possible projection height and thus the greatest exposure to the flow. The values for a_1, b_1 and c_1 therefore reflect the minimum

threshold value. By assuming that the cohesive force between particles is zero, Greeley and Iversen (1985) developed an expression for Bagnold's coefficient for cohesionless particles by substituting the equations derived by Coleman (1967) into equation 1.28. Hence

$$A = [(\Pi/24)/[(K_D/(2)^{1/2} + (3)^{1/2}K_M + K_L/4)]^{1/2} \qquad 1.29$$

When appropriate values from Table 1.5 for K_D, K_M and K_L are substituted into equation 1.29, Bagnold's coefficient A assumes a value of 0.104 in flows characterised by Re* greater than 70. Thus equation 1.29 is in good general accord with the experimentally determined values of A given in Table 1.6.

An expression for threshold shear velocity which includes the interparticle forces I_p is given by Iversen et al. (1976), and is based on the preceding discussion of forces acting on a particle at rest on a bed of identical particles.

$$U_{*T} = A_*1 \left[\frac{\sigma g d}{\rho} \left(\frac{1+A_*2I_p/\sigma g d^3}{1+A_*3Re^*}\right)\right]^{1/2} \qquad 1.30$$

The coefficient A_*1, A_*2 and A_*3 are unknowns as they are a function of unknown particle geometry and fluid force coefficients.

All the preceding expressions for threshold shear velocity have considered only a flat, horizontal homogeneous bed of contiguous particles. In reality, such assemblages of sediments are rare and more commonly mixtures of particle sizes, surface slopes and moisture contents occur. A number of expressions have therefore been developed to account

for the effect of these additional variables on aeolian threshold values.

It was noted by Chepil and Woodruff (1963) and Iversen et al. (1973), that the inclusion of large, non-erodible roughness elements in a sediment effectively increased the value of U_{*T} for that sediment. Iversen et al. (1973) and Lyles et al. (1974) investigated this effect in detail and found a functional relationship between U_{*T} and the ratios of (i) roughness height to roughness element spacing, and, (ii) the area covered by the roughness elements to the total surface area. By considering drag, lift and overturning moments acting on particles in flow characterised by Re* values greater than 70, Iversen et al. (1976) derived an equation which incorporated both the effects of non-erodible roughness elements and interparticle forces. Hence

$$U_{*Tr} = A_*4\left[\frac{\sigma g d}{\rho}\left(\frac{1+0.0314d^{0.837}/\sigma g d^{2}}{1+A_*5[\ln(1+d/2z_o)]^{2}}\right)\right]^{1/2} \qquad 1.31$$

where U_{*Tr} = rough surface threshold shear velocity ms^{-1}

and A_*4, A_*5 = coefficients dimensionless

Iversen et al. (1976) found that the value of the coefficients A_*4 and A_*5 were 0.257 and 0.221 respectively, using 29 data points and two surface roughness configurations. Logie (1982) also studied the effect of non-erodible roughness elements on U_{*T} values. It was found that U_{*T} values were lowered if the proportion of non-erodible roughness elements on the bed fell below 6% of the total bed area. Conversely, a cover of more than 6% actually raised U_{*T} values owing to shelter effects. The 6% cover value was termed the 'inversion point' and was reported as having no effect on U_{*T} values. Greeley and Iversen

(1985) suggest that the recorded increase in U_{*T} values due to the inclusion of non-erodible roughness elements may be related to the ratio of particle diameter to equivalent roughness height, Z_o. Greeley and Iversen give an approximate fit to the data from Lyles et al. (1973) and Iversen et al. (1973, 1976) as

$$U_{*TR} = U_{*T}2\left(\frac{d}{Z_o}\right)^{-1/5} \qquad 1.32$$

Equation 1.32 has no universal validity as it is based on data derived from a limited number of surface roughness configurations (Greeley and Iversen, 1985).

Vanoni (1975) developed a simple expression to account for the effects of slope on U_{*T} values. The expression is essentially the same as that given by Bagnold (1941), (equation 1.19) and takes account of both local slope angle and the angle of grain repose.

$$U_{*Ts} = \frac{A\ (\sigma-\rho)d}{\rho}\ \text{Cos}\,\gamma\,(\tan\phi - \tan\gamma) \qquad 1.33$$

where U_{*Ts} = slope modified threshold shear velocity ms^{-1}

and γ = local slope angle degrees

Vanoni's (1975) equation only considers conditions when the wind blows at 90^o to the maximum slope angle and is therefore only applicable in a limited number of situations.

In an attempt to expand the general applicability of equation 1.33, the effect of slope on U_{*T} values and the relationship between

slope angle and prevailing wind direction were investigated by Howard (1977). Slope angle, particle diameter and the angle between wind direction and the slope were included in an expression for slope modified U_{*T} values.

$$U_{*Ts} = F^2 d[(\tan^2\phi\cos^2\gamma - \sin^2 S_A)^{1/2} - \cos S_A \sin\gamma] \qquad 1.34$$

where F = immersed particle weight i.e. $B^*[g(\sigma-\rho)/\rho]^{1/2} ms^{-1}$

B^* = experimental constant dimensionless

S_A = angle between the wind direction and the slope degrees

Moisture in a given sediment has the effect of increasing the magnitude of the interparticle forces, I_p and thus raising U_{*T} values. Belley (1964) also suggests that the presence of water between surface grains may effectively reduce the surface roughness and thereby make grain extraction more difficult. This effect may be particularly significant when atmospheric moisture is deposited on the surface as dew. The effect of moisture on U_{*T} values was expressed by Belley (1964) in terms of a modified value for Bagnold's coefficient A (equation 1.18).

$$A_w = A(1.8+0.6 \log_{10} W_c) \qquad 1.35$$

where A_w = modified value of Bagnold's coefficient to account for a damp sediment dimensionless

W_c = water content (% by weight) %

Hence from equation 1.18

$$U_{*Tw} = A(1.8+0.6 \log_{10} W_c) \left[\frac{(\sigma-\rho)gd}{\rho}\right]^{1/2} \quad 1.36$$

where U_{*Tw} = threshold shear velocity for damp granular material ms^{-1}

Similar work was undertaken by Logie (1982) who measured the threshold shear stress values associated with artificially moistened sands. The results were the same as those derived by Belley (1964) and were expressed in the form

$$U_{*Tw} = U_{*T} q' \quad 1.37$$

where q' = coefficient $(1.8+0.6 \log_{10} W_c)$

The effect of atmospheric humidity on aeolian entrainment thresholds was examined by Belley (1964), Azizov (1977), Knottnerus (1978, 1980) and Logie (1982). Belley's work resulted in an expression to account for the dampening of a sedimentary surface by a moist atmosphere.

$$A_h = A(1+0.5 R_h/100) \quad 1.38$$

where A_h = modified value of Bagnold's coefficient to account for atmospheric humidity — dimensionless

and R_h = relative atmospheric humidity — %

Hence from equation 1.18

$$U_{*Th} = A(1+0.5\ R_h/100)\ \left[\frac{(\sigma-\rho)gd}{\rho}\right]^{1/2} \qquad 1.39$$

where U_{*Th} = threshold shear velocity for a damp atmosphere ms^{-1}

Knottnerus (1980) found that the threshold velocity of coarse grain soil was raised by only 5.6% at R_h values of 50%. However, at R_h values of 95%, U_{*T} values were found to be 32% higher than those determined in a dry atmosphere.

The action of certain soluble salts on sedimentary surfaces leads to the formation of a resistant surface crust. Boughey (1957) and Morton (1957) recognised that the process of crust formation in both unconsolidated sands and cultivated soils acted in such a way as to increase the mechanical strength of the surface layers and hence raised the threshold shear stress value for entrainment. These crusts were termed salcrete by Yasso (1966) and their effect on U_{*T} values have been assessed by Lyles and Schrant (1971), Svasek and Terwindt (1974), Pye (1980), Nickling and Eccleston (1981) and Nickling (1984). Lyles and Schrant (1971) found that soils treated with NaCl solutions became more resistant to wind erosion owing to an increase in interparticle forces, I_p. Svasek and Terwindt (1974) also suggest that lime and/or iron may be important particle bonding agents, particuarly in areas near the coast. In more detailed studies Nickling and Eccleston (1981) and Nickling (1984) assessed the effect of NaCl and KCl solutions on U_{*T} values for soil. They derived a modified Bagnold expression (equation 1.18) in the form

$$U_{*T(salt)} = A\left[\frac{(\sigma-\rho)gd}{\rho}\ (0.97 \text{ exp. } 0.1031\ Sc)\right]^{1/2} \qquad 1.40$$

where $U_{*T(salt)}$ = modified threshold shear velocity due to salcrete ms^{-1}

Sc = salt content mg salt per gm soil

1.6 Comparisons between various theoretical and empirical expressions for aeolian entrainment thresholds

In this section, five predictive equations for the aeolian entrainment threshold are examined in detail: (a) White (1940), equation 1.17; (b) Bagnold (1941), equation 1.18; (c) Chepil (1959), equation 1.20; (d) Belley (1964), equation 1.39 and; (e) Logie (1982), equation 1.37. These expressions were chosen because they are frequently used to determine U_{*T} for a given sediment and appropriate values for the various terms in the equations are unambiguous and easily assessed. Further, the expressions developed by Chepil (1959), Belley (1964) and Logie (1982) incorporate terms to express turbulence, atmospheric humidity and sediment moisture respectively and thus enable a relative assessment of these crucial factors in the context of aeolian thresholds.

Using these predictive equations, U_{*T} values were calculated for a range of grain diameters (0.2mm to 1.8mm). Particle and air densities were assumed to be $2.65 \times 10^{3} kg\ m^{-3}$ and $1.23 kg\ m^{-3}$ respectively, and the angle of grain repose, ϕ, was taken as being 20^{o}. The resulting U_{*T} values are presented in Tables 1.7 to 1.10. Table 1.7 presents U_{*T} values calculated using the equations of White (1940) and Bagnold (1941). In Table 1.8, U_{*T} values derived from Chepil's (1959) theoretical equation are presented. Values for η were

calculated using the regression equation suggested by Lyles and Krauss (1971), equation 1.21, and two values of T are considered (i.e. 0.2 and 3.0). U_{*T} values illustrating the effect of atmospheric humidity (Belley, 1964) are presented in Table 1.9 for R_h values of 90% and 30%, and in Table 1.10, the effect of moisture in the sediment (Logie, 1982) is shown for sediment moisture contents of 30% and 10%. Predicted values of U_{*T} were then plotted against grain diameter (square root scale) in Figure 1.8.

The form of the graphs in Figure 1.8 suggests that smaller and smaller particles require progressively reduced U_{*T} values to induce incipient motion in air. In reality, however, experimental evidence shows that the relationship between threshold shear velocity and particle size (i.e. $U_{*T} = f(d)^{1/2}$) shown in Figure 1.8 does not hold as particle size falls below about 0.2mm (see Figure 1.2). In fact, U_{*T} values are found to increase quite markedly for d smaller than 80μm so that the same U_{*T} value applies to 0.5mm and 0.01mm quartz grains (Figure 1.2, Bagnold (1941, p. 88)). Therefore, all the predictive equations examined in this section must be considered only valid for particles larger than 0.2mm.

The U_{*T} values calculated using White's (1940) expression, equation 1.17, were based on a grain repose angle of 20^{o}. This angle reflects the approximate repose angle associated with a geometric arrangement of particles in the form of a single grain poised on three others. Particles supported on such triangular geometry are the most susceptible to entrainment as they project furthest into the wind. Thus the U_{*T} values presented in Table 1.7 represent the most likely minimum entrainment threshold shear stress for a flat bed of homogeneous

particles with variable packing geometry. Different grain support geometry results in different angles of grain repose and therefore give rise to a range of U_{*T} values despite similarity in all other aspects of the sediment sample. Thus, the relationships between U_{*T} and $(d)^{1/2}$ in Figure 1.8 for White's equation represent only one of many possible relationships which are governed by the configuration of bed particles.

The U_{*T} values calculated using equation 1.18 (Bagnold, 1941), are larger than those deduced from White's equation. This discrepancy results from considering the minimum grain repose angle in equation 1.17 (i.e. 20^{o}). Bagnold's equation (equation 1.18) does not account for different degrees of grain exposure to the air flow and thus gives rise to what appears to be mean U_{*T} values for a given particle size. Consequently, the line labelled 'Bagnold (1941)' in Figure 1.8 lies above the line labelled 'White (1940)'.

Equation 1.20, Chepil (1959), takes account of the intensity of air turbulence over a bed of loose grains at the threshold. In this case, the effect of turbulence is represented by a numerical variable T (equation 1.23) and is found to have a minimum value of zero in laminar flow and a maximum value of approximately 3.5 in well developed turbulent flow. U_{*T} values presented in Table 1.8 were calculated using T values of 0.2 and 3.0 and thus reflect aeolian entrainment thresholds in laminar/transitional and turbulent flow respectively. It is clear from the lines labelled 'Chepil (1959)' in Figure 1.8 that U_{*T} values are considerably influenced by the intensity of flow turbulence. The implications of this finding on aeolian entrainment thresholds are far reaching and are explored in the experimental investigations reported in

Chapters 4, 5 and 6 of this thesis.

The effect of atmospheric humidity on U_{*T} values was expressed by Belley (1964), equation 1.39. Lines in Figure 1.8 labelled 'Belley (1964)' show U_{*T} values for sediment at relative humidity values of 30% and 90%, and illustrate that moist atmospheric conditions may result in a significant increase in U_{*T} values for any given particle size. Similarly, U_{*T} is raised if the sediment is damp, Logie (1982), equation 1.37. The lines labelled 'Logie (1982)' reflect sediment moisture contents of 3% and 10% and suggest that U_{*T} values are raised significantly by the effect of even low moisture levels. This increase in U_{*T} values reflects an increase in inter-particle cohesion and results from the attractive forces between water in grain interstices and the exposed particles on top of the sediment bed. However, the predictive equations derived by Belley (1964) and Logie (1982) were derived using different incipient motion criteria and different boundary layer flow regimes and thus the predicted U_{*T} values are entirely governed by sets of unique experimental data. It is not possible, therefore, to assess whether the predicted increase in U_{*T} values results entirely from genuine moisture effects or from differences arising from the experimental techniques used by Logie (1982). It is likely that they may be attributed to the joint action of both.

1.7 Threshold conditions and aeolian transport modelling

Central to all studies of aeolian phenomena is the rate at which material is transported by the wind. Many theoretical and empirical expressions have been developed to predict aeolian transport rates using fundamental wind and sediment parameters. This section reviews briefly

some of the mass transport expressions used to predict the movement of non-cohesive aeolian material in given wind conditions. The fundamental physical parameters controlling the movement of sand by wind were identified by Bagnold (1941) who considered the loss of air momentum in the boundary layer due to the saltating grain population. He found that the rate of transport (q) was proportional to the cube of the wind shear velocity and that the constant of proportionality was a function of the particle size distribution. Using aeolian transport rate data derived from wind tunnel and field measurements, Bagnold (1941) derived an empirical mass transport equation to fit his experimental data in the form

$$q = C_s\left(\frac{d}{D_s}\right)^{1/2} \frac{\rho U_*^3}{g}, \quad \text{Bagnold (1941, p. 105)} \qquad 1.41$$

where D_s = standard grain diameter (250μm)

Equation 1.41 is very misleading as it suggests that aeolian transport will occur at wind shear velocity values below the threshold value. The term U_* in equation 1.41 might be said to represent the shear velocity in excess of the threshold and thus expresses the competence of the wind to transport material but this is an oversimplification.

Greeley and Iversen (1985) combine the terms in equation 1.41 to obtain a dimensionless aeolian transport rate expression in the form

$$Q = qg/\rho U_*^3 \qquad 1.42$$

where Q = dimensionless mass transport rate

Greeley and Iversen (1985) suggest that Q is probably a function of several fluid and sediment parameters and stress that the lack of accurate and reliable aeolian threshold and transport rate data have restricted the development of appropriate expression and models for the transport process. Greeley and Iversen (1985) suggest that Q is best expressed in the form

$$Q = \frac{qg}{\rho U_*^3} = f(\delta d_p,\ U_*/U_{*T},\ \sigma/\rho,\ U_F/U_{*T},\ Rs) \qquad 1.43$$

where d_p = particle size distribution of sample m

The functional relationship described in equation 1.43 shows that U_{*T} is likely to be a crucial parameter in any realistic aeolian transport rate model. The significance of aeolian threshold conditions is reflected by the inclusion of a threshold term in many published aeolian transport equations. A summary of some of the most widely used aeolian transport expressions, listed in chronological order of their development, is given in Table 1.11. This table includes only a selection of the mass transport equations developed since the work of Bagnold (1941), and includes only those expressions which incorporate terms for threshold wind velocity (U_T) or threshold shear velocity (U_{*T}). Each equation in Table 1.11 simply represents the best-fit expression to a set of unique transport data derived by the author. The number and variety of these expressions reflects the problems associated with deriving equations able to predict the rate of aeolian transport in a range of conditions. The differences in predicted transport rates are illustrated in Figure 1.9 which shows the rates of aeolian transport predicted by selected empirical and semi-empirical equations. Clearly

these formulae give widely different transport rates despite there being close similarities in grain size and wind shear velocity. The disparity between the results of these authors may be attributed to a variety of factors including the inaccurate assessment of the threshold shear velocity, differences in the methods used to measure wind shear velocity and the use of heterogeneous sediments. Further, some expressions lump saltation and creep together whilst others treat the two processes separately. Kalinske (1942), Nemoto et al. (1969), Adriani and Terwindt (1974), Bressolier and Thomas (1977), Berg (1983), and Willetts (1983) suggest that other variables such as particle shape, atmospheric humidity and sediment moisture, vegetation influences, salcretes, the thermal stability of the boundary layer, temperature and slope are also significant factors affecting the rate of aeolian transport.

The differences between published data also reflect a more fundamental problem. It is clear from Figure 1.9 that little further progress in the understanding and modelling of aeolian transport is likely to be made using empirical techniques. In view of the divergent physical parameters used in expressions for aeolian transport rates, Jensen and Sørensen (1982, 1983) argue that progress will only be made in the field of aeolian transport by mathematical modelling of the working physical processes. They advocate a statistical modelling approach and have made considerable progress towards developing a stochastic model of saltation. Similarly, Grass (1970) suggests that threshold conditions and initial particle motion in open channel flow can be defined in terms of the statistical interaction between the distribution of the fluctuating component of bed shear stress and the distribution of threshold shear stress values ascribed to particles in a given sample (see 2.5.3). In view of the divergent aeolian transport models developed

using empirical techniques it appears that further advancement in the understanding of aeolian transport will only be achieved by the development of physically realistic models of entrainment, creep, saltation and suspension.

1.8 Summary

Following a review of the literature, the aeolian threshold condition is identified as being a fundamental parameter in the global aeolian system. It marks the boundary between a geomorphologically active environment and a static environment and no mass transport, deposition, deflation or mechanical erosion is possible until the threshold condition is exceeded. The initial motion of aeolian material is controlled by the sediment properties, the characteristics of the sediment surface, the properties of the surface wind and a range of external factors. Although a number of other factors become significant in certain situations, the principle factors controlling incipient grain motion in air are identified as being: the characteristics of the local boundary layer flow regime (especially the intensity and the spatial and temporal frequency of variation in bed shear stress); the size of the grains; and the aerodynamic shape particles present to the flow.

Past studies of aeolian thresholds have been largely conducted in wind tunnels with markedly different working section dimensions. Flow conditions in such tunnels are likely to be substantially different from natural atmospheric winds close to a sediment bed and they probably differ between one tunnel and the next, particularly with respect to the turbulent characteristics of the flow. It has been shown that differences in flow turbulence profoundly affect the aeolian threshold

condition and thus measurements of U_{*T} taken in these different boundary layer flow regimes are probably unique to an individual author and his methods. Differences in experimental flow regimes are, therefore, likely to account for some of the variation associated with published aeolian threshold values.

As grains do not move en masse when the threshold condition is exceeded, it has been necessary in previous research to specify a subjective criterion of incipient bed motion and relate this condition to a measurement of average bed shear velocity. Differences in entrainment criteria used by various authors and their failure to identify correctly and consistently a defined degree of bed motion is identified as being a likely source of error in past aeolian threshold measurements. In addition it is likely that the different techniques used by authors to determine the U_* value associated with a given boundary layer flow regime also account for part of the variation in reported U_{*T} values.

By considering the forces acting on grains, and by use of empirical techniques, a large number of expressions have been developed in past research to predict aeolian entrainment thresholds in a range of conditions. Often the assumptions on which these are based do not apply in all situations and their predictive accuracy is limited by the precision of the experimental methods from which they are derived. Similarly, past empirical modelling of aeolian transport by saltation and surface creep has given rise to a number of predictive mass transport equations. In order to apply these equations, however, it is essential to know the characteristic threshold conditions associated with the given granular material. Failure to assess threshold conditions correctly has probably contributed to the large variation in rates of mass transport

predicted by the different models for identical material under identical wind regimes.

It is suggested that the developing boundary layer on a flat plate in air provides ideal flow conditions in which the interactions between granular material and wind at the threshold of motion may be studied. By placing carefully selected test materials with uniform characteristics at selected positions on the surface of a suitable experimental plate in a wind tunnel it is suggested that threshold conditions and particle entrainment may be studied in a continuum of controlled and reproducible boundary layer flow regimes. Such studies should, therefore, allow an assessment of the relative influences on aeolian thresholds of factors identified in this Chapter as potentially the most significant controls of incipient grain motion in air.

Table 1.1 Simplified summary of major aeolian landforms.

I BEDFORMS				
	RIPPLES	DUNES	DRAA	TOPOGRAPHIC DUNES
Wavelength	$\lambda' = 0.5 \times 10^{-3}$–25m	$\lambda' = 3$–600m	$\lambda' = 300$–5500m	$\lambda' = 3$–600m
Amplitude	$a_m = 10^{-4}$–10^{2}m	$a_m = 0.1$–100m	$a_m = 20$–450m	$a_m = 0.1$–100m
Types	Normal ripples Megaripples Fluid drag ripples	Transverse dunes Longitudinal dunes Parabolic dunes Dome dunes Star dunes Reversing dunes (A) Simple dunes (1 dune type) (B) Compound dunes (2 or more dunes of the same type) (C) Complex dunes (2 or more dunes of different types	Simple draa Compound draa Complex draa	Climbing dunes Falling dunes Echo dunes

II EROSION AND OTHER FORMS			
	VENTIFACTS	YARDANGS	OTHER FEATURES
Length	3×10^{-3}–3m	Very variable	Sand shadows and drifts
Height	-	Some 200m high and 20km long	Sand sheets and streaks
Types	Prolate Oblate Triaxial Ellipsoidal Irregular		

Table 1.2 Factors controlling aeolian entrainment thresholds (after Cooke et al., 1982).

Sediment Properties	Surface Properties	Properties of the Wind	External Factors
1. Size	1. Large scale surface geometry (bedforms)	1. Turbulence (ratio of instantaneous to mean surface shear stress ($U_{*I}/\bar{U}_{*}$)	1. Gravity
2. Density	2. Small scale surface geometry (individual grain exposure)	2. Surface shear force	2. Precipitation
3. Shape	3. Surface length (i.e. distance from shelter)	3. Characteristic Reynolds number	3. Temperature
4. Surface morphology	4. Surface roughness		4. Pressure
5. Sorting	5. Slope		5. Humidity
6. Cohesive forces	6. Salcrete and other crusts		6. Degree of shelter or exposure
	7. Vegetation: (a) residue (b) height (c) orientation (d) density (e) fineness (f) cover		7. Biographical factors

Author	Length, L(m)	Width, w(m)	Height, h(m)	Tr = $L/(w.h)^{1/2}$
Chepil and Milne (1939)	8.7	1.08	1.23	7.5
Chepil and Milne (1941)	3.6	0.5	0.5	7.2
*Bagnold (1941)	9.14	0.305	0.762	18.9
*Zingg (1942)	17.07	0.527	0.527	32.3
*Zingg and Chepil (1950)	17.07	0.91	0.91	18.7
*Znamenskiy (1958)	4.3	0.3	0.3	14.3
*Horikawa (1960)	18.29	0.305	0.39	53.0
Dyunin (1963) (a)	6.8	0.15	0.15	45.3
(b)	8.6	0.30	0.32	27.8
(c)	21.0	0.42	0.50	45.8
Uil'yams (1963)	9.15	0.35	0.35	26.1
Johnson (1963)	30.9	1.22	0.76	32.2
*Belley (1964)	30.48	1.22	0.268	53.3
*Chiu (1967)	21.7	1.83	0.914	16.8
Bacharov (1972)	4.45	0.5	1.0	6.3
*Butterfield (1972, unpublished)	4.0	0.3	0.3	13.3
*Lyles, Schrandt and Schmeidler (1974)	16.46	1.52	1.93	9.6
*Iversen et al. (1974, 1976) and Greeley et al. (1974, 1977)	11.5	1.1	1.2	10.0
Seppala and Linde (1978)	4.0	0.6	0.6	6.6
*Gillette (1978a, b) - Portable	2.5	0.15	0.15	16.6
*Logie (1981, 1982)	7.5	0.34	0.34	22.1
Murphy (1985, unpublished) - Portable	4.0	0.3	0.3	13.3
WADA tunnel (West Australian Department of Agriculture)-in Painter.D., (1985)-Portable	7.0	1.5	unknown	unknown
*Williams (1985, unpublished (see Ch.7))	3.0	0.16	0.16	18.8

* Tunnels used in aeolian threshold studies

Table 1.3 Summary of wind tunnel dimensions used in studies of aeolian processes

Definition of threshold criteria	Author
1. "The condition for a single particle to be first displaced"	Neill (1967, p.46)
2. "Minimal fluid threshold" (i.e. 1 grain in motion)	Chepil and Woodruff (1963, p.211)
3. "Movement of a single grain"	Lyles and Krauss (1971, p.564)
4. "Several grains moving"	Gilbert and Murphy (1914, p.264)
5. "The instant when a few grains here and there begin to be dislodged	Bagnold (1941, p.85)
6. "Conditions .... where a few grains move"	White (1970, p.152)
7. "Scattered particle movement"	Rathburn and Guy (1967, p.107)
8. "Critical movement"	Vanoni (1964, p.4)
9. "Weak movement"	Kramer (1935, p.801)
10. "Initial motion"	Tison (1953, p.22)
11. "Continuous movement of grains"	Gillett et al. (1982, p.9003)
12. "The wind speed at which continuous motion starts without impact from upwind"	Greeley and Iversen (1985, p.71)
13. "Maximal fluid threshold" (i.e. all grains in motion)	Chepil and Woodruff (1963, p.211)
14. "General bed movement"	Chepil (1959, p.251)

Table 1.4 Reported threshold criteria for air and water.

Investigator	K_D	K_L	K_M	Re*	Fluid
Goldman et al. (1967) and O'Neill (1968)	8.01		0.74	<0.45	Theoretical
Saffman (1965)		0.808Re*		<0.45	Theoretical
Coleman and Ellis (1976b)	5.44			0.95	Hydroxyethyl-cellulose solution
Coleman (1972) and Coleman and Ellis (1976a)	15.42			130-13,200	Water
Einstein and El-Samni (1949)		2.42		3600	Water
Chepil (1958a)	3-4.7	2-2.5		1000-1400	Air

Table 1.5 (K_D), (K_L) and moment (K_M) values for a spherical particle in laminar and turbulent boundary layer shear flows (from Greeley and Iversen, 1985, p.73).

A	FLUID	AUTHOR
0.18 - 0.22	water	Shields (1936)
0.1	air	Bagnold (1941)
0.09 - 0.11	air	Chepil (1945b)
0.12	air	Zingg (1953)
0.17 - 0.20	air (using mean particle diameter)	Lyles and Krauss (1971)
0.19 - 0.23	air (using minimum particle diameter)	Lyles and Krauss (1971)
0.11	air	Iversen et al. (1977)

Table 1.6 Reported values for the Bagnold coefficient, A (equation 1.18).

Particle diameter d x 10^{-6}m	$\bar{U}_{*T}$, ms^{-1} White (1940) (equation 1.17) ($\phi = 20^{o}$)	$\bar{U}_{*T}$, ms^{-1} Bagnold (1941) (equation 1.18)
1800	0.50	0.62
1600	0.48	0.58
1400	0.44	0.54
1200	0.41	0.50
1000	0.37	0.46
800	0.34	0.41
600	0.28	0.36
400	0.24	0.29
200	0.16	0.21

Table 1.7 Predicted threshold shear velocity values derived using White (1940), and Bagnold (1941) (σ=2.65x10^{-3}kg m^{-3}; ρ=1.23 kg m^{-3}).

Particle diameter $d \times 10^{-6}$m	Ratio of lift and drag on a grain to lift and drag on a bed of grains, η (equation 1.21)	$\bar{U}_{*T}$ for stated turbulence factor value, ms^{-1}	
		T=0.2	T=3.0
1800	1.26	0.85	0.22
1600	1.28	0.81	0.21
1400	1.30	0.77	0.19
1200	1.32	0.71	0.18
1000	1.34	0.66	0.16
800	1.37	0.59	0.15
600	1.41	0.51	0.13
400	1.47	0.42	0.10
200	1.56	0.32	0.08

Table 1.8 Predicted threshold shear velocity values for two turbulence intensity values (T), derived using Chepil (1959), (equation 1.21) ($\sigma=2.65 \times 10^{3} kg\ m^{-3}$; $\rho=1.23 kg\ m^{-3}$).

Particle diameter, $d \times 10^{-6}$m	$\bar{U}_{*T}$ for stated relative humidity values, ms^{-1}	
	R_h = 90% (A_h=0.145)	R_h = 30% (A_h=0.115)
1800	0.89	0.71
1600	0.84	0.67
1400	0.78	0.63
1200	0.73	0.58
1000	0.66	0.53
800	0.60	0.47
600	0.51	0.41
400	0.42	0.33
200	0.30	0.24

Table 1.9 Predicted threshold shear velocity values for two atmospheric humidity values derived using Belley (1964), (equation 1.39) (σ=2.65x10^{3}kg m^{-3}; ρ=1.23kg m^{-3}).

Particle diameter, $d \times 10^{-6}$m	$\bar{U}_{*T}$ for stated sediment moisture content values, ms^{-1}	
	W_c=3%	W_c=10%
1800	1.29	1.48
1600	1.21	1.39
1400	1.13	1.29
1200	1.04	1.20
1000	0.96	1.10
800	0.86	0.98
600	0.75	0.86
400	0.61	0.86
200	0.44	0.50

Table 1.10 Predicted threshold shear velocity value for damp sediment derived using Logie (1982) (σ=2.65x10^{3}kg m^{-3}; ρ=1.23kg m^{-3}).

Author	Aeolian transport rate expression
Bagnold (1941)	$q = 5.2 \times 10^4 (U(y)-U_T)^3$
Kawamura (1951)	(i) $q = \frac{\rho U_*^3}{g} C^*[1+(U_{*T}/U_*)^2][1-(U_{*T}/U_*)]$ (ii) $q = \frac{2.78\rho}{g} (U_*-U_{*T})(U_*-U_{*T})^2$
Dyunin (1954)	(i) $q = \frac{\rho U^3}{g} c^*(1-U_T/U)$ (ii) $q = \frac{\rho U^3}{g} C^*(1-U_{*T}/U_*)^3$
Kuhlman (1958)	$q = \frac{\rho U^3}{g} C^*[1-(U_T/U)^3]$
Owen (1964)	$q = \frac{\rho U_*^3}{g}[0.25+0.33(U_{*T}/U_*)(U_F/U_{*T})][1-(U_{*T}/U_*)^2]$
Kind (1976)	$q = \frac{\rho U_*^3}{g} C^*[1-(U_{*T}/U_*)^2]$
Maegley (1976)	(i) $q = \frac{\rho U_*^3}{g} C^*(d/D_S)^{3/4}[1-(U_{*T}/U_*)^2]$ (ii) $q = \frac{\rho U_*^3}{g} C^*(d/D_S)^{3/4}[1-(U_{*T}/U_*)^{13.27}]$
Lettau and Lettau (1978)	$q = \frac{\rho U_*^3}{g} C^*(1-U_{*T}/U_*)$
White (1979)	$q = \frac{2.61 U_*^2}{g}[1-(U_{*T}/U_*)][1+(U_{*T}^2/U_*)]$
Iversen et al. (1976), Schmidt (1982)	$q = \frac{\rho U_*^3}{g} C^*(U_F/U_{*T})[1-(U_{*T}/U_*)]$

C^* = mass transport coefficient = $\frac{qg}{\rho U_*^3}\left[\frac{D}{d}\right]^{1/2}$ dimensionless

D_S = reference particle diameter i.e. 250μm m

$U(y)$ = wind velocity at a specified height, y ms^{-1}

U_T = threshold wind velocity ms^{-1}

Table 1.11 Theoretical and empirical aeolian transport rate expressions incorporating a threshold term (after Greeley and Iversen ,1985).

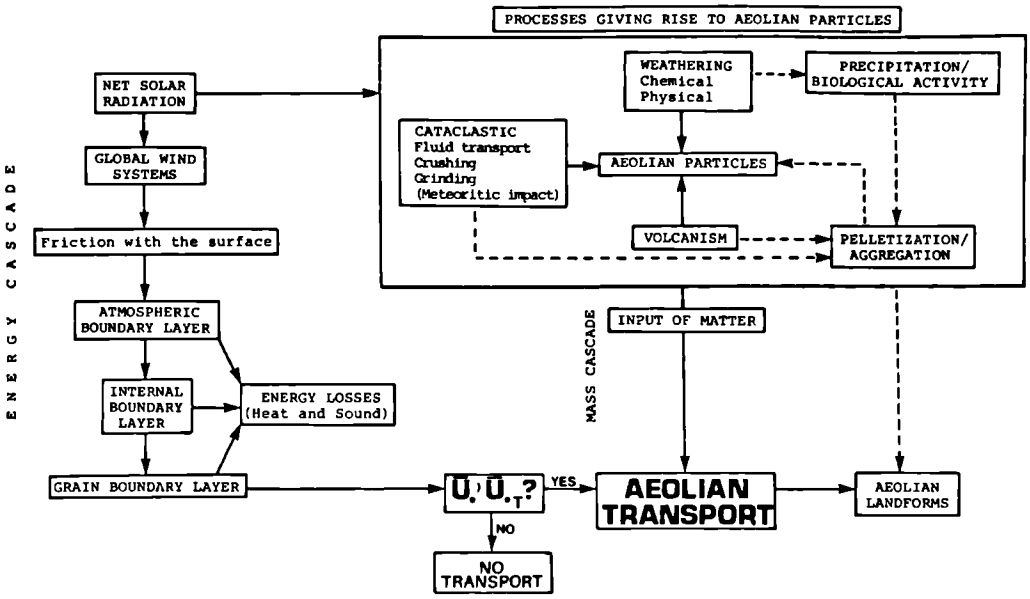

Figure 1.1 Global aeolian system (after Pettijohn 1972, and Greeley and Iversen, 1985).

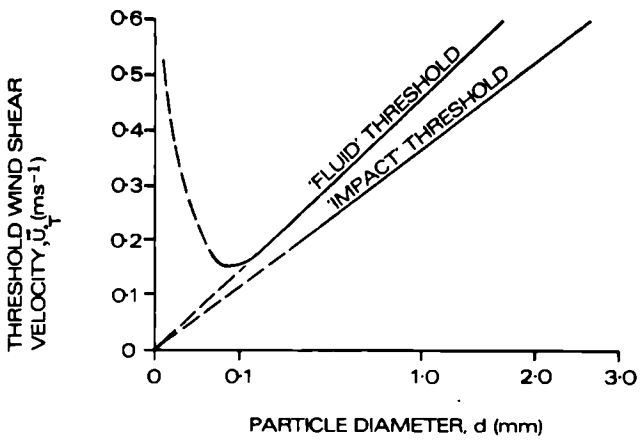

Figure 1.2 Threshold curves for sand (after Bagnold, 1941).

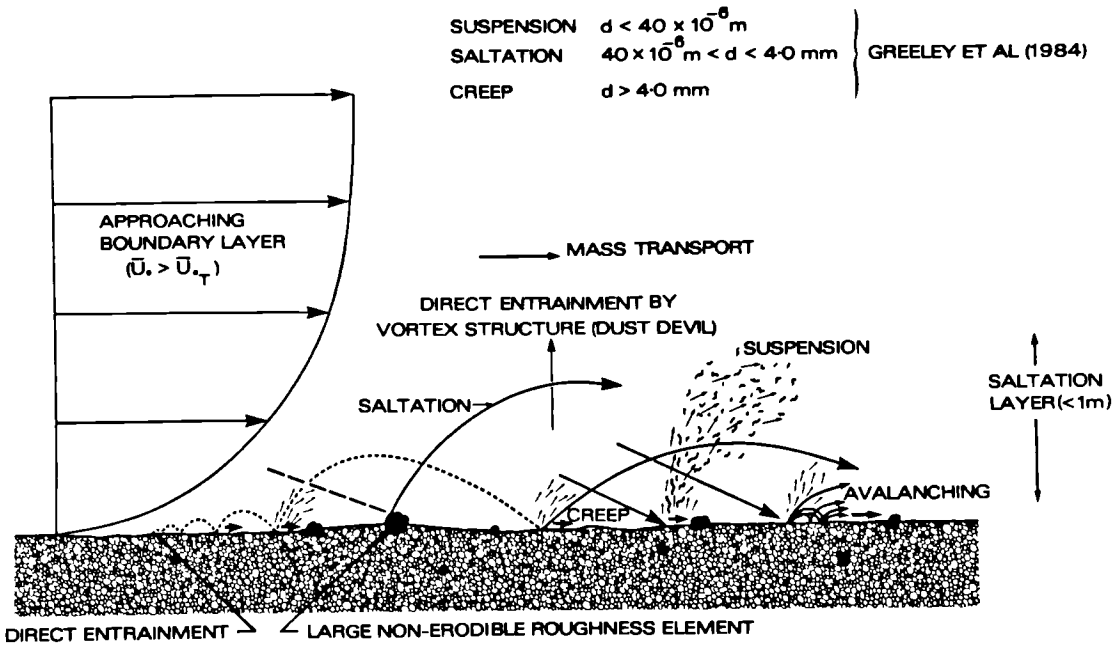

Figure 1.3 Processes of aeolian transport.

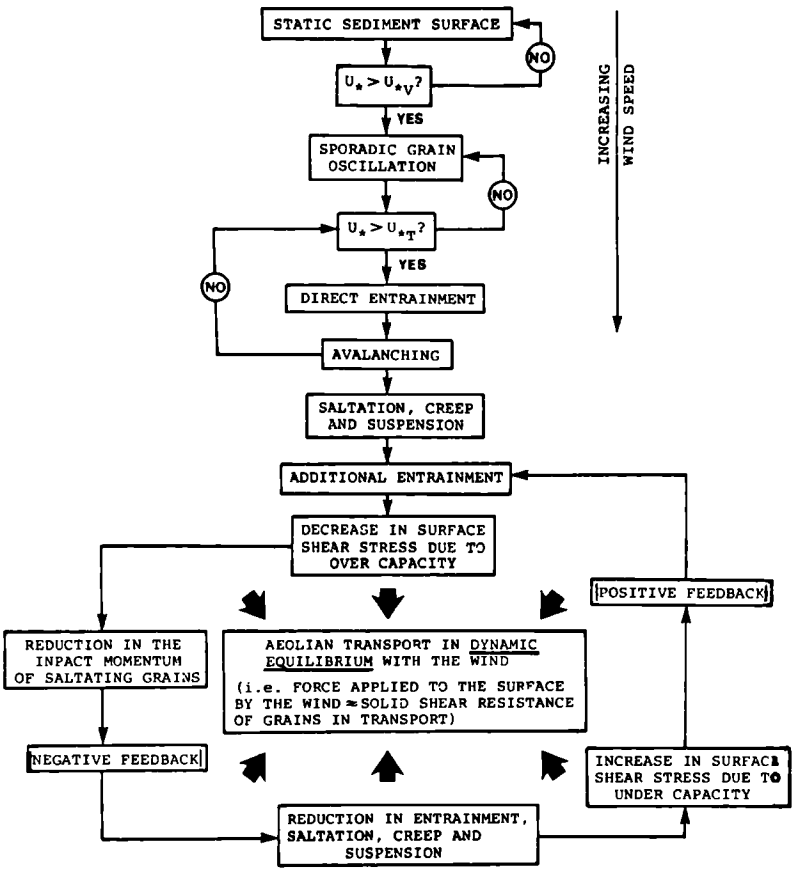

Legend
U_* = Wind shear velocity.
U_{*V} = Threshold shear velocity for grain oscillation.
U_{*T} = Threshold shear velocity for grain motion.

Figure 1.4 Schematic representation of the relationship between aeolian threshold conditions and aeolian transport.

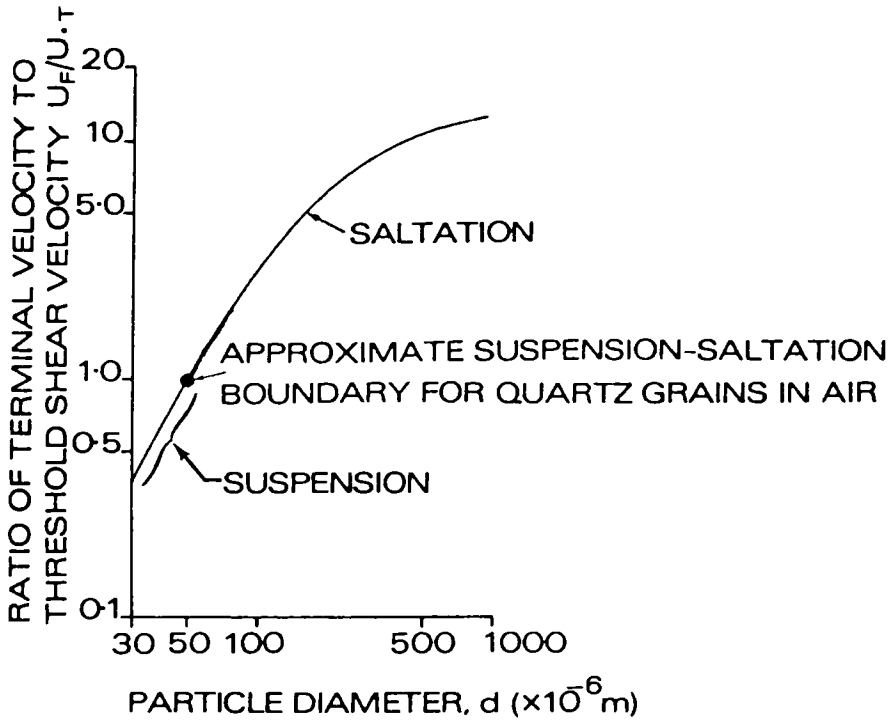

Figure 1.5 Processes of aeolian transport defined by the ratio of terminal velocity to threshold shear velocity, (σ/ρ=2160; g=9.81ms^{-1}; ν=14.6x10^{-6}m^{2}s^{-1}), (after Greeley and Iversen, 1985, p.70).

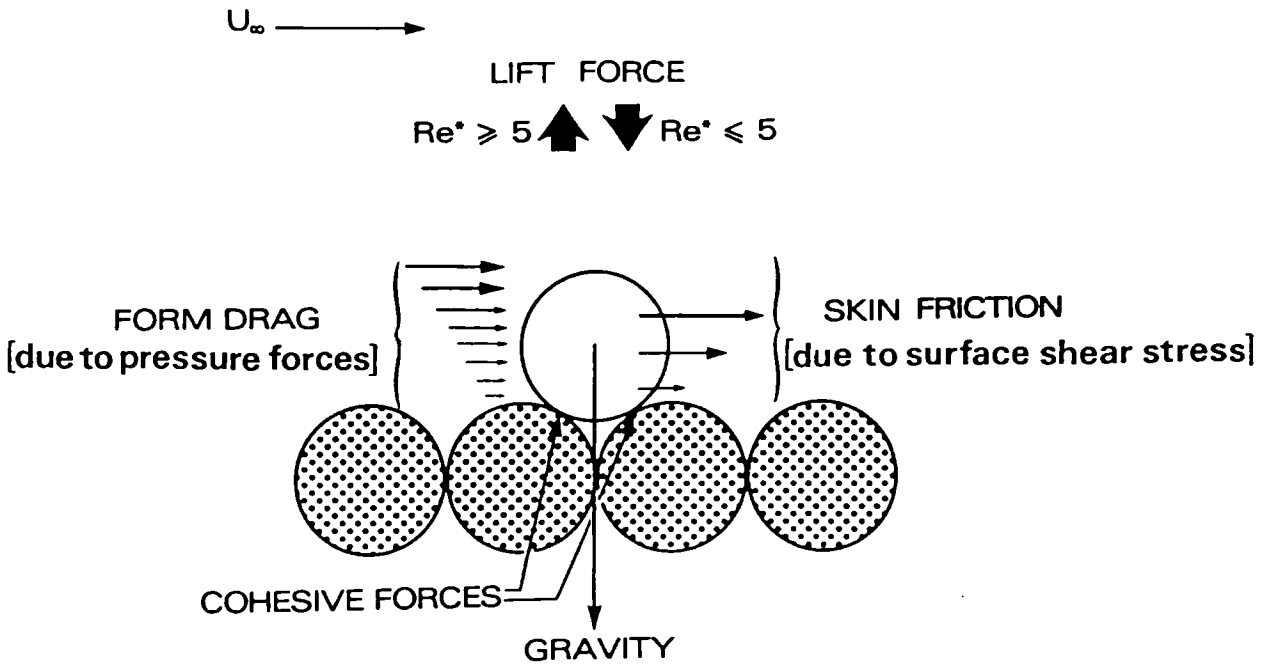

Figure 1.6 Forces acting on a single grain at the aeolian threshold.

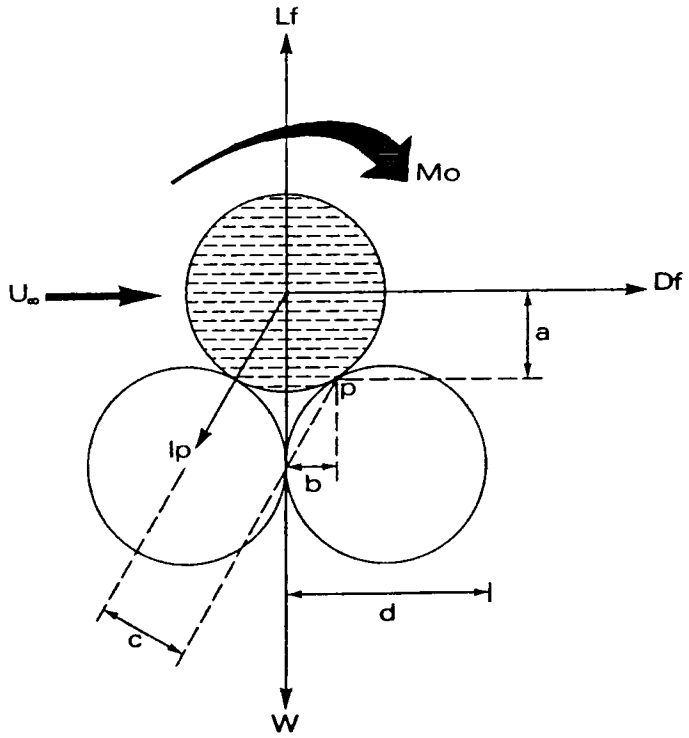

AT THE THRESHOLD CONDITION : Dfa + Lfb + Mo = Wb + lpc

Figure 1.7 Forces acting on a single grain and the respective moment arms at the aeolian threshold condition (after Greeley and Iversen, 1985, p.71)

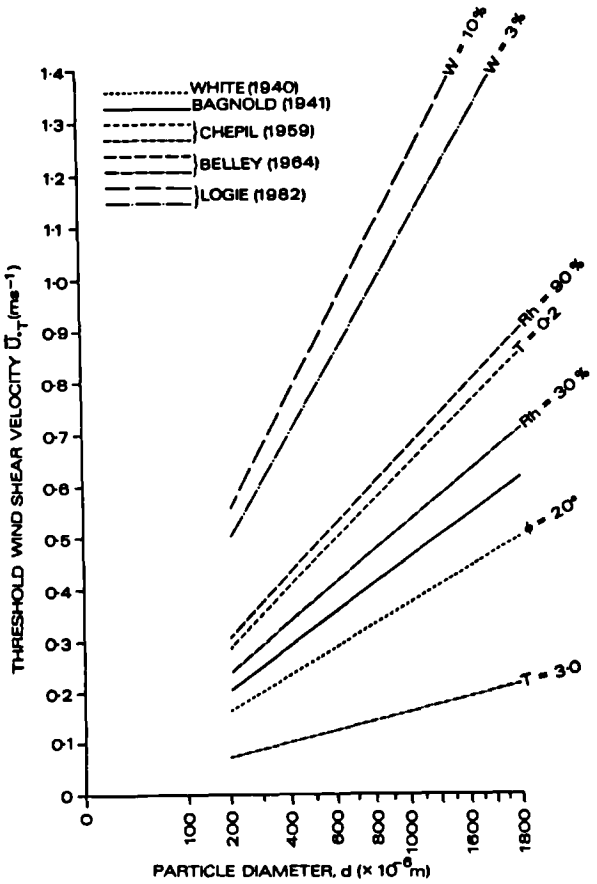

Figure 1.8 Predicted aeolian threshold shear velocity values using equations of various authors.

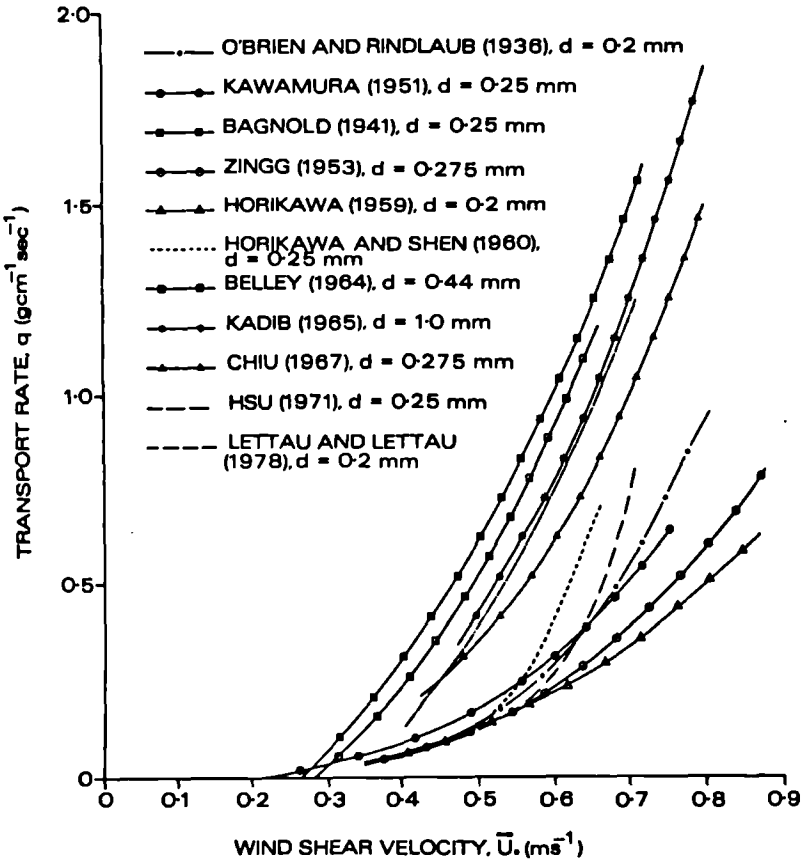

Figure 1.9 Rate of aeolian transport predicted by selected aeolian transport equations.

CHAPTER TWO

The boundary layer and the measurement of shear stress

2.1 Introduction

Aspects of the developing boundary layer on an aerodynamically smooth flat plate have been extensively studied and a number of solutions to the equations describing its development and characteristics are well documented. Examples are to be found in Blasius (1908), Burgers (1924), Van der Hegge-Zijnen (1924), Hanson (1930), Dryden (1934, 1936), Nikuradse (1942), Tillman (1946), Carrier and Lin (1948), Janour (1951), Kuo (1953), Imai (1957), Kraichnan (1956), Boly and Friedman (1959), Messiter (1970) and Stewartson (1974). Despite this extensive treatment, none of these studies consider the developing boundary layer over an aerodynamically rough surface such as the granular covering on the experimental plate described in Chapter 1. In such a case, the characteristics of the developing boundary layer can only be assessed by making careful measurements of the flow. From such data it is possible to derive a good deal of information about the nature and characteristics of the local boundary layer regime on the plate using well documented theoretical and empirical studies. Such information may then in turn be related to corresponding observations of aeolian entrainment at a given location on the experimental plate surface. In order to be able to interpret these observations and measurements it is necessary to understand the structure and characteristics of different boundary layer flow regimes found over the surface of such a plate.

Three flow regimes may be identified over a flat plate. These are:

(a) laminar flow near the leading edge;

(b) a region of transitional flow; and

(c) turbulent flow.

Detailed discussions of laminar, transitional and turbulent boundary layer flows are given in Sections 2.3, 2.4 and 2.5 respectively. In these, particular emphasis is given to those aspects of the flow regime most likely to play a direct role in the processes of entrainment of aeolian grains.

Entrainment thresholds of aeolian grains are generally related to the direct force applied by air, and conventionally this force is assumed to be represented by the mean shear stress at the boundary. Thus, to ensure the studies using the experimental flat plate could be meaningfully compared with other work, it was necessary to adopt this conventional approach. Techniques devised to measure the local shear stress acting on a body in air are many and varied. In Section 2.6 therefore, the techniques most widely used in aeronautical engineering and in aeolian process studies are reviewed and a detailed theoretical account of the momentum integral method chosen for the calculation of shear stress in this study is presented.

2.2 The developing boundary layer along a flat plate at zero incidence

At the boundary between a moving fluid (e.g. air) and a solid (e.g. the surface of a flat plate) fluid elements do not 'slip' over the solid surface no matter what external flow conditions prevail, (within the range of pressures and temperatures for which the fluid may be treated as a continuum). A velocity gradient therefore exists between the surface and the unimpeded free stream air above the plate surface. The narrow region occupied by the retarded flow is called the 'boundary layer' and it consists of a comparatively thin sheet of decelerated fluid.

In common with many other fluid flow regimes, the characteristics of boundary layer flow may be described by the dimensionless ratio known as the Reynolds number, Re, (Reynolds, 1883). The Reynolds number is defined as

$$Re = \text{inertial forces/viscous forces} = \frac{U_\infty l \rho}{\mu} = \frac{U_\infty l}{\nu} \qquad 2.1$$

where U_∞ = free stream fluid velocity ms^{-1}

l = characteristic dimension of a body m

μ = absolute fluid viscosity Nsm^{-2}

The Reynolds number is a convenient way to express the characteristics of any fluid motion using readily determined flow variables. In physical terms it expresses the dominance of either viscous or inertial forces in the flow. The term l in equation 2.1 represents the characteristic dimension of a body which may be, for example, the radius of a pipe or the diameter of an aeolian sand grain. In the case of a flat plate, l may be taken as being the downwind distance from the leading edge (x). Thus the appropriate Reynolds number describing flow conditions on the plate is given by

$$Re_x = \frac{U_\infty X}{\nu} \qquad 2.2$$

'Laminar' boundary layer flow is characterised by smooth, steady streamlines and any tendency for mixing between layers of the flow is vigorously damped down by strong viscous action. Such flows on a flat plate are defined by low Reynolds numbers (typically Re_x smaller than 10^5) owing to the dominance of viscous forces. As Re_x values

increase above 10^5, the laminar streamlines become unsteady, and wave-like or oscillatory motions evolve in the boundary layer flow. Such motion can no longer be damped down by viscous forces, and at a critical value of the Reynolds number the oscillatory motion breaks down completely and the flow in the boundary layer is then characterised by apparently chaotic motion with a considerable random component. Such flows are described as being '<u>turbulent</u>' and are associated with relatively high Reynolds numbers owing to the dominance of inertial forces, (typically Re_x greater than 10^6). The process giving rise to the breakdown of laminar flow is called transition and flows described by $3.5x10^5<Re_x<10^6$ (Schlichting, 1979), are termed '<u>transitional</u>' flows. The breakdown of laminar flow results from shear stresses between fluid layers. These stresses act in such a way as to increase the vorticity of the boundary layer flow in a downwind direction. In other words, as the Reynolds number (Re_x) increases, inertial forces become increasingly dominant and the break-up of streamlines into chaotic motion can no longer be resisted by viscous action.

A flat plate placed in an air flow therefore has a range of Re_x values along its surface governed by the free stream velocity (U_∞), the kinematic viscosity of air (ν) and the distance from the leading edge (x). The value of Re_x therefore increases from zero at the leading edge (i.e. x=0) to a value $U_\infty x/\nu$ at a distance x along the plate. The progressive increase in Re_x values downwind of the leading edge reflects the changing flow characteristics of the boundary layer on the plate. To illustrate this more clearly, Figure 2.1(a) shows the development of a two dimensional boundary layer along the upper and lower surfaces of a flat plate at zero incidence, (the vertical scale has been greatly exaggerated to show the development clearly). In Figure 2.1(b),

the shear stress measured at the upper surface of the plate (τ) and the Reynolds number associated with the plate (Re_x) are plotted against distance from the leading edge of the plate (x).

Figure 2.1(a) shows that the air approaching the plate has a constant velocity U_∞. However, the air in contact with the plate has zero velocity (the velocity of the plate) because of the no-slip condition which characterises continuum flows. It therefore follows that a velocity gradient must exist between the air in contact with the plate and the free stream. Downwind of the leading edge, air close to the surface is subjected to a retarding force caused by the viscous stresses associated with the velocity gradient dU/dy (where y is the height above the surface) and the viscosity of the fluid. As this air moves downstream of the leading edge it will continue to be acted upon by viscous stresses and as a consequence it will continue to decelerate. This slower moving layer of air near the boundary will retard the adjacent air of the free stream and thus the boundary layer thickness will increase downwind of the leading edge. As the velocity difference between the free stream and the surface remains constant, this increase in the boundary layer thickness results in a reduction of the velocity gradient dU/dy. The shear stress at the surface (τ) is a function of dU/dy. Thus the shear stress must be relatively large near the leading edge where the velocity gradient is steep. As the boundary layer thickens downwind of the leading edge, the velocity gradient becomes less steep and consequently a reduction in τ occurs (Figure 2.1(b)).

At a certain distance (x) from the leading edge, flow in the laminar boundary layer becomes unstable and turbulent spots develop close to the surface. These disturbances are swept downwind spreading and

eventually coalescing, to give a turbulent boundary layer flow downwind of a transition region. This change in dominant flow regimes is indicated by the critical Re_x value ($Re_x > 2x10^5$) shown in Figure 2.1(b). In turbulent flow, mixing of the free stream flow with the retarded flow in the boundary layer is vigorous and the velocity gradient $[\partial U/\partial y]_o$ near the surface of the plate now becomes greater than that associated with the laminar boundary layer upstream of the transition point. Consequently shear stress at the surface increases (Figure 2.1(b)). The turbulent boundary layer thickens more rapidly than the laminar boundary layer owing to the more efficient mixing between regions of high and low velocity air. Like the laminar boundary layer, this thickening gives rise to a downstream reduction in the mean velocity gradient at the surface $[\partial U/\partial y]_o$. The corresponding decrease in surface shear stress is shown in Figure 2.1(b). Figure 2.1(a) also indicates that a viscous sublayer develops downwind from the transition point on the plate. This region of flow close to the surface is dominated by viscous forces and consequently has different properties from the rest of the turbulent boundary layer. A detailed discussion of the viscous sublayer is given in 2.6.

2.3 The laminar boundary layer

2.3.1 General characteristics

In laminar boundary layers, air flow proceeds in streamlines almost parallel to the surface and may be visualized in terms of statified layers of air which slide over one another as a result of the velocity gradient between the surface and the free stream flow. At the surface, the velocity is zero owing to the condition of no-slip that must

exist at a solid boundary in continuum flow. This condition is brought about by molecular adhesion between the boundary and the layer of air directly adjacent to it (i.e. 'the adsorbed bed layer'). In the region close to the boundary, the increase in velocity is linear and may be expressed in the form:

$$\frac{U}{U_*} = \frac{U_* y}{\nu} \qquad 2.3$$

where U is the air velocity, U_* is the friction velocity (defined as $(\tau/\rho)^{1/2}$), y is distance normal to the boundary and ν is the kinematic viscosity ($14.8 \times 10^{-6} m^2 s^{-1}$ for air at $20^{o}C$ and 1 atmosphere).

If the air molecules moved in straight paths parallel to the surface, then the motion of the layers of air would be entirely independent of one another. However, molecules move in random motion and thus constantly stray from one air layer to the next. This molecular transfer between air layers constitutes a steady force and faster moving layers tend to drag slow ones along and slower layers resist the motion of the faster ones. This actively generates a shear stress within the fluid which is found to be proportional to the velocity gradient. Thus:

$$\tau \propto \frac{dU}{dy} \qquad 2.4$$

The constant of proportionality is termed the absolute viscosity μ, hence:

$$\tau = \mu \frac{dU}{dy} \qquad 2.5$$

As the boundary layer thickens downwind, the velocity gradient dU/dy decreases and results in a reduction in the surface shear stress. As no mixing occurs between the free stream air and the laminar boundary layer, the rate of growth of the latter along a surface is determined by the retarding ability of molecular activity alone.

The flow in a laminar boundary layer is described by the boundary layer equation of motion, equation 2.6. This equation describes the relationship between momentum, pressure and shear stress within the boundary layer in the form

$$U'\frac{\partial U'}{\partial x} + v'\frac{\partial U'}{\partial y} = -\frac{1}{\rho}\frac{\partial P}{\partial x} + \frac{1}{\rho}\frac{\partial \tau}{\partial y} \qquad 2.6$$

A numerical solution to this equation was obtained by Blasius (1908) for the case of flow with zero pressure gradient along a smooth flat plate. The Blasius solution gives the velocity distribution in a laminar boundary layer as illustrated in Figure 2.2. The scales $y(Re_x)^{1/2}$ and U/U_∞ represent the relative distance from the boundary and the relative velocity, respectively.

The downwind persistence of a laminar boundary layer is largely governed by the Reynolds number as given in equation 2.2. If the surface is smooth, the free stream flow is steady and uniform, and the streamwise pressure gradient is zero, laminar boundary layer development will continue downwind of the leading edge of the plate up to Re_x values of approximately 3×10^6 (Schlichting, 1979, p. 143).

Laminar boundary layers may also be found over granular surfaces in air provided that the grains are small enough. In the case of air flow over grains, the flow is more appropriately expressed in terms of the grain Reynolds number, Re*, which is a dimensionless ratio characterising the surface roughness. Re* is defined as

$$Re^* = \frac{U_* d}{\nu} \qquad 2.7$$

where d is the grain diameter. Flow characterised by Re* smaller than 3.5 is said to be aerodynamically 'smooth' and the boundary layer air is able to pass over individual grains without becoming turbulent. As flow proceeds along such a surface, the laminar boundary layer thickens and becomes increasingly insensitive to the surface roughness. At a certain distance, however, and considerably earlier than in the case of a smooth surface, natural instability again gives rise to transition, and the laminar boundary layer flow breaks up into chaotic turbulent motion.

2.3.2 Aeolian entrainment in a laminar boundary layer

It is clear from the discussion in the preceding section that shear stresses induced at the surface by laminar boundary layer flow are distributed equally over a given area. It therefore follows that a bed of homogeneous particles exposed to such a flow regime would tend to move en masse when the shear stress reached a critical value. However, if the bed consists of a haphazard arrangement of particles, characterised by a range of particle sizes and geometric arrangements, it is likely that some grains will be more susceptible to entrainment than others, partly by virtue of their exposure to the flow and partly by virtue of their less secure seating on the underlying grains.

2.4 Transition from laminar to turbulent boundary layer flow

2.4.1 Transition over 'smooth' surfaces

A diagrammatic representation of transition from laminar to turbulent boundary layer flow on a smooth flat plate is shown in Figure 2.3. White (1974) identifies six distinct flow stages in the transition process (labelled A to F in Figure 2.3).

(a) A region extending a distance x downwind of the leading edge in which the boundary layer is laminar.

(b) At a distance x along the plate, the Reynolds number, Re_x, reaches a critical value and the laminar flow becomes unstable owing to progressive downwind thickening of the boundary layer. In this region the laminar boundary layer develops two dimensional Tollmein-Schlichting waves (Schlichting, 1979, p. 483) which progressively increase in amplitude in a downwind direction.

(c) Further downwind, Tollmein-Schlichting waves induce additional flow disturbances which are manifest as unstable three dimensional waves and vortices.

(d) The resulting local concentration of high vorticity gives rise to sporadic bursts of turbulence termed turbulent spots.

(e) Turbulent 'spots' develop in regions where the turbulent velocity fluctuations are large. These 'spots' act as sites of intense turbulence production and are found to migrate and spread out their disturbance zone downwind from their point of origin, (Elder, 1960).

(f) Turbulence generated by these spots tends then to coalesce and gives rise to a fully turbulent boundary layer. It must be

stressed, however, that only the regions labelled (A), (B) and (C) are amenable to theoretical analysis and that the processes and mechanisms giving rise to the development and growth of turbulent spots are less clearly understood than the processes in other regions.

Three factors have been identified which affect transition in the boundary layer on a solid surface such as a flat plate (Schlichting, 1979). These are as follows:

(a) the pressure distribution in the external flow (a rising, downwind pressure tends to hasten transition whilst a falling, downwind pressure gradient tends to delay transition and in severe, adverse pressure gradients, boundary layer flow separation may occur);

(b) roughness and surface imperfections (see below); and

(c) free stream turbulence, (any turbulent fluctuations in the approaching free stream flow will increase the likelihood of early transition).

The process and mechanisms of transition in the boundary layer on a flat plate have been studied by Burgers (1924), Van der Hegge Zijnen (1924), Hansen (1930) and Dryden (1934; 1936; 1956). In general it has been found that over smooth plates with sharp leading edges placed in airstreams characterised by low turbulence, transition occurs in the Reynolds number range $3.5 \times 10^5 < Re < 3 \times 10^6$. Transition is shown prominently by a sudden increase in the thickness of the boundary layer and a corresponding decrease in the value of the boundary layer velocity profile shape parameter H (the ratio of the displacement thickness, δ^* to the momentum thickness, θ_M, see 4.5.1(c)). Schubauer and Klebanoff (1955) calculated the value of this

parameter and found $H \approx 2.6$ in laminar boundary layers and $H \approx 1.4$ in turbulent boundary layers. The region of transition may, therefore, be assumed to lie in the range $2.6 < H < 1.4$. Analysis of boundary layer velocity profiles can, therefore, be used as an indication of whether the boundary layer flow regime is laminar, transitional or turbulent.

Emmons and Bryson (1952), Schubauer and Klebanoff (1955), Dhawan and Narasimha (1957) and Hinze (1975) showed that the process of transition is intermittent and that its major characteristic is an irregular sequence of laminar and turbulent regions. The regions of turbulence are generally termed turbulent spots and their development and growth has been extensively studied by McCormick (1968), Wygnanski et al. (1976), Cantwell et al. (1978), Wygnanski (1981), Perry et al. (1981) and Browand et al. (1983). Turbulent spots have been observed by these workers to occur suddenly in the transition region and to travel downwind as a wedge-shaped region of intense turbulence. Thus turbulent spots may be considered as being the first manifestation of turbulence in the transition region.

2.4.2 Transition over 'rough' surfaces

As the experimental plate used in this study was covered with contiguous, granular material, it is also necessary to consider briefly the likely effects of surface roughness on the transition process. Studies of transition over rough surfaces have been undertaken by Schiller (1932), Goldstein (1936), Tani et al. (1940), Fage and Preston (1941) and Feindt (1957). The presence of roughness elements on the surface of the plate favours transition in the sense that transition will

occur at a lower critical Reynolds number over a rough surface than over a smooth surface under otherwise identical conditions. This condition is brought about by the shedding of vortices from individual roughness elements. These vortices tend to coalesce in the downwind direction thereby giving rise to turbulence close to the surface in the laminar boundary layer. If these disturbances are small enough they may not necessarily induce transition providing the laminar boundary layer is stable. If, however, the disturbances are large and the resulting turbulent wake lies beneath an unstable laminar boundary layer, transition to turbulent flow will quickly ensue. Further consideration of transition over rough surfaces is given in 4.5.2.

2.5 The turbulent boundary layer

2.5.1 General characteristics

The turbulent boundary layer is characterised by highly distorted streamlines where individual elements of air are subjected to chaotic, random motion. Thus velocity at any point in the boundary layer is constantly changing. The mean velocity profile for a turbulent boundary layer is shown in Figure 2.4. In Figure 2.4(a) relative distance from the boundary (yU_*/ν) is plotted against relative velocity (U/U_*) using linear scales to illustrate the physical shape of the average velocity profile. Three zones are labelled on the diagram: (a) the viscous sublayer; (b) the logarithmic velocity distribution zone; and (c) the outer region. This does not, however, necessarily imply that there is a strong demarcation between zones as it can be seen in Figure 2.4(a) that there is a smooth transition of velocity from the surface to the free stream. To clarify this, Figure 2.4(b) shows the relative

distance from the boundary on a logarithmic scale so that the velocity distribution in the viscous sublayer and the logarithmic velocity distribution zone may be more clearly seen.

The viscous sublayer is found to extend less than $50\nu/U_*$ from the boundary, Ecklemann (1974). In this thin layer, shear stresses are transmitted to the surface entirely through the action of molecular viscosity (Bakewell, 1966). The velocity distribution in this zone is described by the relationship given for laminar boundary layer flow, equation 2.3. Above this zone, the velocity distribution obeys a logarithmic law in the form sometimes called the 'von kármán-Prandtl' law, namely:

$$\frac{U(y)}{U_*} = A_K \ln\left(\frac{y}{Z_o}\right) + B_K \qquad 2.8$$

where A_K and B_K are experimentally determined constants. The velocity distributions described by equations 2.3 and 2.8 are sometimes called the 'law of the wall' and meet at a yU_*/ν value of 11.84. It is clear from the range of experimental data shown in Figure 2.4(b) that in the zone $5 < yU_*/\nu < 30$, neither equation correctly defines the velocity distribution. This zone is called the buffer region.

In the wake region above the logarithmic velocity distribution zone, the velocity distribution is described by the velocity defect law which applies to a zone extending from $y/\delta > 0.1$ to the free stream. The velocity defect law may be expressed in the form

$$\frac{U_\infty - U}{U_*} = f\frac{y}{\delta} \qquad 2.9$$

where δ = thickness of the boundary layer m

This functional relationship is illustrated in Figure 2.4(c). In this figure, the range of experimental data is shown by the shaded area around a solid line representing the mean value of all the experimental data. Over a wide range of Reynolds numbers ($10^5 < Re < 10^7$),

the velocity profile in this region may be approximated by the equation:

$$\frac{U}{U_\infty} = \left[\frac{y}{\delta}\right]^{1/7} \qquad 2.10$$

The relationship described by equation 2.10 is often termed the 1/7 power law for turbulent boundary layers and may be usefully applied to deduce the rate of turbulent boundary layer growth and surface shear stress on a smooth surface.

Above the viscous sublayer, the mixing action of turbulence causes small masses of fluid to be swept back and forth in a direction transverse to the mean air flow. Thus, as a small mass of air is swept away from the low velocity zone adjacent to the sublayer into a higher velocity zone further out in the flow, the mass has a retarding effect on the higher velocity flow. Similarly, when a mass of fluid originating further out in the flow is swept towards the boundary it has an effect on the lower velocity fluid much like shear stress and tends to cause acceleration of the lower velocity fluid. Thus, although this mixing

process is essentially a momentum exchange phenomenon, it has the same effect on the mean boundary layer flow as a shear stress and is thus termed 'apparent shear stress' or 'Reynolds stresses' and may be expressed in the form

$$\varepsilon = -\rho\overline{u'v'} \qquad 2.11$$

where ε = Reynolds stresses and u' and v' are the fluctuating velocity components in the x and y directions respectively. Hence the shear stress in a turbulent boundary layer is expressed as

$$\tau = \mu + \varepsilon \frac{dU}{dy} \qquad 2.12$$

where $\mu \ll \varepsilon$

The action of momentum exchange in a turbulent boundary layer provides a means of vigorous air mixing between regions of low average velocity and regions of high average velocity. Consequently, the entrainment of external flow is more rapid and turbulent boundary layers thicken along a body at a faster rate than laminar boundary layers.

Shear stress in laminar boundary layers results from molecular activity and acts on a surface in a relatively simple way. Turbulent boundary layers, on the other hand, are extremely complicated and in order to understand the interaction between turbulent shear stresses and loose granular material it is necessary to understand the mechanism of turbulence production and its manifestations in the boundary layer. This point is stressed by Grass (1983) who stated that "an essential precursor to any rational study of the wide ranging and frequently dominant effects

of flow turbulence of sediment transport phenomena, is a comprehensive knowledge and understanding of the characteristics and mechanics of boundary layer turbulence itself", Grass (1983, p.3).

2.5.2 The structure of the turbulent boundary layer and the mechanisms of turbulence production

As a detailed discussion of turbulent shear flow is outside the scope of this research, this section presents no more than a brief outline of the structure of turbulent boundary layers and the mechanisms of turbulence production reported in a broad literature. It is emphasised that the turbulent boundary layer is highly complicated and most analyses of its characteristics do not consider air flow over rough surfaces at Reynolds number values typical of aeolian entrainment thresholds. Thus interpretation of reported observations of turbulent boundary layers must be viewed with caution in the context of this research project.

The investigation of turbulence production in the boundary layer reported by Laufer (1954) and Klebanoff (1956) is summarized in Figure 2.5, where the normalized turbulence production rate per unit volume P^* is plotted against the relative distance from the wall (y/δ). Klebanoff (1956) states that approximately 80% of the total turbulence production is accounted for in the inner region of the boundary layer and that the remaining 80% of the boundary layer thickness generates only 20% of the total turbulence. This dominance of the inner region in turbulence production was clearly demonstrated by Favre et al. (1966) who showed that a turbulent boundary layer could be 'relaminarized' by removing the inner region using slight suction. They argued that if the outer region

dominated turbulence production then removal of the inner region would simply bring the fluctuations of the outer region closer to the wall. However, removal of the inner region by suction greatly reduced the level of turbulence and they concluded that the inner region must be responsible for the creation and maintenance of turbulence within the boundary layer. Similarly, studies of the turbulent boundary layer by Kline et al. (1967), Kim et al. (1968) and Grass (1971) confirm that the majority of turbulence is generated in the inner region and suggest that the entire structure of the boundary layer is governed by events within this narrow zone.

In 2.4 it was shown that the velocity distribution of the inner and outer regions of a turbulent boundary layer obey quite different laws, (i.e. the 'law of the wall' and the velocity defect law). The observations of Klebanoff (1956) and Kline et al. (1967) suggest that this difference may be due to the differences in turbulence production rates at different levels in the boundary layer. Indeed Kline et al. (1967) state that "the structure of any turbulent flow reflects the local balance of production, transport and dissipation of turbulent kinetic energy" (Kline et al., 1967, p. 741). In attempts to understand the mechanisms which create and maintain turbulence, several authors have proposed physically realistic models which relate the large and small scale eddy structures and the momentum transfer mechanisms in turbulent flow to the mean velocity field. These models have evolved along two lines:

a) a statistical approach, (e.g. the stationary or eddy model, (Townsend, 1956; 1961)), and the wave models, (Phillips, 1967; and Landahl, 1967) and

b) a deterministic approach (e.g. instability models, Einstein and Li, 1956; Rundstadler et al., 1963; Schraub and Kline, 1965; Black, 1966; Kline et al., 1967).

At the present time, the deterministic approach has the greatest support in the research community, particularly in view of models recently proposed by Cantwell (1979, 1981) and Head and Bandyopadhyay (1981) (see below).

One of the most recent theories concerning the structure of the turbulent boundary layer was proposed by Cantwell (1979, 1981). In this model, the large and small scale turbulent motions in the boundary layer are seen as coherent features that can be identified in the mean flow characteristics. The term coherent in this context refers to flow configurations of definite and reproducible size, shape and persistence time, (Allen, 1985). The coherent features appear to be hierarchical with temporal and spatial scales related to flow properties. The theory unifies many different observations of turbulent shear flow (including the boundary layer case) and suggests that turbulent motion is not composed of small fluid parcels in chaotic random motion but of definite structures which interact in a very complicated way. The coherent features identified in a turbulent boundary layer on a smooth surface are illustrated in Figure 2.6. These include large scale eddies (L), typical eddies (l), energetic near-wall eddies (b) and streamwise vortices (λ). The scale of these features is given in Table 2.1 where length (x), height (y), width (z), convection velocity (C) and persistence distance (X) are given. These data were collated by Gyr (1983) from a wide range of sources (Table 2.2) and were found to scale with the variables U_*, ν, δ and U_∞. Although Cantwell's (1981) model classifies the observed

features in a turbulent boundary layer, it does not suggest the internal structure of the coherent features and the ways in which the features are likely to interact with each other in a range of flow situations. Further, many of the investigations from which the data were taken were conducted using water at low to moderate Reynolds numbers. An excellent review of the condition sampling techniques used to identify coherent features in the boundary layer is given by Antonia (1981).

A model of the turbulent boundary layer over a rough surface was suggested by Gyr (1983). The model is illustrated in Figure 2.7 and in many respects it is similar to that proposed by Cantwell (1981) for smooth surfaces, Figure 2.4. However, the scale of the coherent features are essentially unknown owing to the limited number of studies of turbulent boundary layers over rough surfaces (e.g. Baines, 1950, 1951; Moore, 1951; Hama, 1954; Chanda, 1958; Robertson and Martin, 1966; O'Loughlin and Annambhotla, 1969; Grass, 1970, 1971; Jackson, 1976; Sabot et al., 1977; Mulhearn, 1978; Mulhearn and Finnigan, 1978; Mueller and Studerus, 1979; Raupach, 1981; Gyr, 1983). Large scale eddies are shown with typical eddies, (Falco, 1977), riding on their backs. The energetic near-wall eddies identified over smooth surfaces are absent (or undetected) over rough surfaces and longitudinal streamwise vortices arise as a result of vortex shedding from individual roughness elements on the bed. Each large eddy is visualized as inducing the ejection of low-speed fluid from between particle interstices (Grass, 1971) in an event cycle termed a 'burst'. The removal of low-speed fluid from near the boundary results in a sideways sweep to relatively high velocity fluid and the cycle then repeats itself. Further discussion of bursting is given below, where an outline of the Stanford bursting model (Kline et al. 1967) is given.

Although the models of Cantwell (1981) and Gyr (1983) suggest that turbulence in the boundary layer is ordered in some way, they do not explain the formation and structure of the coherent features in the mean flow field.

Recent studies by Head (1978, 1979) and Head and Bandyopadhyay (1981) of the turbulent boundary layer in air with zero pressure gradient have considered vortex loops to be the fundamental structure in a turbulent boundary layer. These ideas were stimulated by earlier suggestions by Theodorsen (1952) and Black (1966, 1968). Head and Bandyopadhyay (1981) view the turbulent boundary layer as consisting of many stretched vortex loops which are essentially straight over a substantial proportion of their length and are inclined to the surface at approximately 45^{o}. The length of the vortices is only limited by the thickness of the boundary layer. Head and Bandyopadhyay (1981) found that the characteristics of the vortex loops were dependent on the Reynolds number, and it was observed that loops tended to stretch and elongate as the momentum thickness Reynolds number was increased. By observing vortex loops in a range of flow conditions, (500 smaller than $Re_{\theta M}$ smaller than 17500), Head and Bandyopadhyay (1981) identified three loop 'types' as shown in Figure 2.8. These are 'loops', 'elongated loops' and 'elongated hairpins', all of which are thought to be similar in character to the vortices proposed by Theodorsen (1952), Bakewell and Lumley (1967), Tu and Willmarth (1966), Townsend (1970) and Perry et al. (1981). These vortex structures are seen as the fundamental constituents of eddies and, on average, constitute the coherent features defined by Cantwell (1981), (Figure 2.6) and Gyr (1983) (Figure 2.7).

The model of a turbulent boundary layer proposed by Head and

Bandyopadhyay (1981) is illustrated in Figure 2.9. The model was developed from evidence obtained during flow visualization studies in air and is therefore more appropriate to the present study than either of the models proposed by Cantwell (1981) and Gyr (1983) where water flows of low to moderate Reynolds number are considered. Turbulence generation is thought to occur near the boundary and takes the form of readily distinguishable vortex pairs which apparently erupt at random and diffuse outwards to the free stream. The presence of such vortices in turbulent fluid motion was noted by Kuchemann (1965) who described them as being the "sinews and muscles of fluid motions" Kuchemann (1965, p.4). Shear stresses give rise to stretching of these vortices which then combine in extremely complex arrays to form coherent features such as large scale eddies and typical eddies. The degree of vortex stretching or elongation is primarily governed by the Reynolds number, (Figure 2.8). Essentially the model proposes a diffusion transport process where fluid is moved from areas of high mean vorticity to areas of low mean vorticity via energetic vortices. The outer region is visualized as consisting of many highly elongated hairpin vortices at high Reynolds numbers (>2000) and isolated, slightly elongated vortex loops at low Reynolds numbers (<< 800). Head and Bandyopadhyay (1981) noted that the 'legs' of the vortex loops often diffused into each other in a complex process which resulted in the cancellation of their respective vorticity. In the case of the vortex tips, however, no such mechanism exists for the destruction of transverse vorticity. This suggests that at very high Reynolds numbers, only the tips of vortex loops survive with significant vorticity in the outer regions of the boundary layer. Head and Bandyopadhyay (1981) and Grass (1982) suggest that the slowly rotating motion associated with the large scale eddy structures in the outer region of a turbulent boundary layer may simply be the manifestation of the enclosed fluid circulation

around the surviving vortex tips. These vortices interact with the free stream air and thereby cause the growth of the turbulent boundary layer. The violent eruptions of turbulent fluid near the surface reported by Head and Bandyopadhyay (1981) are, therefore, seen as the primary mechanism of turbulence production and propagation.

The process giving rise to violent erruptions of turbulent fluid has been widely observed over smooth surfaces in air and water by Runstadler et al. (1963), Schraub and Kline (1965), Kline et al. (1967), Uzkan and Reynolds (1967), Kim et al. (1968), Corino and Brodkey (1969), Kaplan and Laufer (1969), Nychas et al. (1973), Offen and Kline (1974), Winant and Browand (1974), Smith (1978), Blackwelder (1978), Paturi and Brodkey (1978), Blackwelder and Ecklemann (1979) and Smith and Metzler (1983). Observations over rough surfaces by Grass (1971), Sumer (1974), Jackson (1976), Nakagawa and Nerzu (1977), Dinkelacker (1979), Sumer and Deigaard (1981) and Chambers et al. (1983) are much less extensive, but evidence suggests that violent bed eruptions also occur over granular surfaces. The processes giving rise to turbulent bursting phenomenon near the boundary are not fully understood as they are highly complicated, difficult to measure and hard to visualize. Kline et al. (1967), using water as the working fluid and an imaginative combination of hydrogen bubble flow visualization and hot wire anemometry (described in Schraub et al., 1964), studied the bursting process in the turbulent boundary layer above a smooth wall. They observed that low speed fluid collected in randomly spaced, streamwise streaks close to the boundary. These streaks were subjected to periodic uplift and breakup and thereby gave rise to intense turbulence generation as they mixed with the higher velocity fluid above the boundary. This ejection of low momentum fluid from close to the boundary was followed by an inrush of high momentum

fluid or 'sweep'. This random process was observed to proceed in a cyclic fashion and is often referred to as the 'Stanford' bursting model. Four stages are recognised by Kline et al. (1967) and are illustrated in Figure 2.10. These are:

1) A low-speed streak lifts from the wall and thereby establishes an inflexinal (unstable) instantaneous velocity profile in the boundary layer flow near the wall.
2) The low-speed fluid begins to oscillate owing to general instability in the inner region caused by the mass of low speed fluid and the associated shear stresses it generates.
3) The oscillatory motion is selectively amplified and stretching of the streak occurs in the shear flow near the boundary.
4) Finally, oscillation reaches a critical point and the motion terminates in break up of the streak. In other words, low speed fluid is trapped between regions of high speed fluid and under the action of counter rotating vortex pairs on either side (Blackwelder, 1978) has nowhere to go but outwards where local flow disruption gives rise to turbulence generation close to the boundary.

This sequence of events appears to be a universal feature of turbulent boundary layer flows and is thought to be responsible for the generation of most of the turbulence in the turbulent boundary layer and to be dominant in momentum transfer processes between the inner and outer regions (Uzkan and Reynolds, 1967). The removal of low-speed fluid from the wall allows relatively high speed fluid from further out in the boundary layer to 'sweep' in. Corino and Brodkey (1969) and Grass (1971) have identified these sweeping events as also being important with

regard to triggering turbulence and hence shear stress generation. Fluid sweeps are described by Grass (1982) as being "well ordered, quiescent and almost laminar", Grass (1983, p.5) in contrast to the highly disturbed flow associated with bursts. The bursting cycle appears to occur at random and its frequency is governed by the Reynolds number, the pressure gradient and the characteristics of the boundary (i.e. smooth or rough). Grass (1982) noted that bursts appear to influence the entire depth of the boundary layer.

The mechanism of longitudinal vortex formation (and hence the collection of low speed fluid streaks) in the viscous sublayer was initially proposed by Lighthill (1963) and is reported in Kline et al. (1967). Subsequently Brown and Thomas (1977) and Coles (1978) have proposed that vortex formation results from some instability mechanism and gives rise to the randomly distributed counter-rotating eddy pairs observed by Bakewell and Lumley (1967) and shown in Figure 2.10. Viscous sublayer instability and ensuing periodic breakdowns (or 'bursts') were also recognised by Einstein and Li (1956) and Black (1968) as being significant events leading to the generation of boundary layer turbulence. Head and Bandyopadhyay (1981) recognised the burst cycle in air using smoke flow visualization techniques. Their observations infer that the occurrence of burst is equated with the lifting and stretching of vortex loops from the surface. Rapid elongation of the loops then occurs in the steep velocity gradient near the boundary and violent mixing ensues. Additional vortices are then generated and extend to the free stream fluid. It is not clear, however, whether the loops in the viscous sublayer result from a concentration of streamwise vorticity (as suggested by Lighthill, 1963) or a warping of the transverse vorticity. It could conceivably result from the joint action of both.

The occurrence of bursts is apparently not confined to the inner region of a turbulent boundary layer. Observations and measurements by Fiedler and Head (1966), Imaki (1968) and Kaplan and Laufer (1969) also suggest that bursting occurs in the outer region. In a review paper, Kovasznay (1970) states that bursts in the outer region are found to be highly correlated with the large scale motions of the inner region and suggests large scale bursting events in the outer region may be regarded as the 'footprints' of the small eddies in the inner region. Kovasznay (1970) visualised a reverse cascade of eddies beginning with the frequent small scale events near the wall which either grow or coalesce to produce the large scale eddies which compose the outer region of the turbulent boundary layer. These ideas are comparable with the turbulent boundary layer model proposed by Head and Bandyopadhyay (1981).

2.5.3 Aeolian entrainment in a turbulent boundary layer

In the case of a laminar boundary layer, shear stress at the surface is distributed fairly evenly over a given area and therefore the total drag on, for example, a bed of homogeneous granular material, is carried approximately equally by all the individual grains. In a turbulent boundary layer, however, shear stress is found to fluctuate both spatially and temporally and can result in momentary concentrations of high shear stress well above the mean at random positions on the bed. The distribution of instantaneous shear stress over a given surface is governed by the turbulence structure of the boundary layer. Therefore, in order to understand the interaction between wind and grains at velocities near the threshold of particle motion, it is necessary to utilise existing knowledge of turbulent boundary layer structure in the context of aeolian entrainment.

This section, therefore, briefly considers the implications for thresholds of entrainment by airstreams of the descriptive account of the structure and characteristics of the turbulent boundary layer given in 2.5.2. Saffman (1977), in a discussion of turbulence, likens the search for a universal theory of turbulence to the search for a chimera, and suggests that individual flows should be dealt with on their own merits. In other words, a boundary layer structure and turbulence production model valid for one situation may not necessarily apply to others. The literature dealing with the flow of air over rough, granular surfaces is extremely sparse. It is therefore necessary to interpret and deduce the likely flow characteristics over such surfaces from the investigations of boundary layer flows which use a range of working fluids, boundary conditions and Reynolds numbers. Most of these studies have examined turbulent boundary layers in water where flows were sub-critical, incompressible, steady, quasi-uniform, free from sedimentary particles and less than one metre deep (Merceret, 1972). Great caution must therefore be exercised to ensure that the results from such studies are appropriately interpreted in the context of aeolian entrainment.

The studies by Kline et al. (1967), Grass (1971) and Head and Bandyopadhyay (1981) leave little doubt that the events of the burst cycle constitute a significant mechanism in the transfer of fluid and the generation of turbulent energy (or shear stress) in a turbulent boundary layer, irrespective of the surface roughness or working fluid. A more detailed discussion is given in Chapter 4 in analyses of data arising in this project from investigations of aeolian entrainment in a developing boundary layer on the experimental plate.

Although the concept of coherent structures in turbulent

boundary layers cannot be used to describe aeolian entrainment in a strictly deterministic manner, it can be used as a model for visualising the likely flow characteristics at the threshold of particle motion. A diagrammatic representation of the major coherent structures over rough boundaries was proposed by Laufer (1975), (Figure 2.11). In this model the small scale vortices are shown riding up, around and over the large scale eddies. These give rise to uplift of low momentum fluid which tends to collect in passive reservoirs between and possibly beneath the particles (Grass, 1971). The associated burst is embedded within the large eddy structure and its breakup results in the generation of high local shear stresses. The burst is then followed by a sweep of relatively high momentum fluid and the random cycle then repeats itself. Owing to the high shear stresses generated during the bursting and sweeping cycles, it is therefore likely that such events trigger incipient motion of susceptible particles on the bed. The importance of bursting events is stressed by Jackson (1976) who states that "bursting promotes the entrainment of more and coarser sediment than tractive forces alone can accomplish", Jackson (1977, p. 531). However, it is generally thought that sweeping events are more effective than bursts in regard to grain entrainment.

Sumer (1974) found that bursts were the dominant events responsible for setting particles into saltation, whereas Grass (1971) reported that sweeps tended to set particles into a sliding motion along the bed. As the number of burst and sweep events occurring over a given time are approximately the same it is probably unnecessary to distinguish between the two events in describing overall transport. This may not be true in all cases, however, as Nakagawa and Nerzu (1977) suggest that sweeping events may become increasingly dominant in terms of local shear

stress production as the surface roughness increases. Thus the spatial distribution and frequency of sweeping events over different surface roughnesses may give rise to differences in entrainment processes. However, evidence from the studies of entrainment presented in Chapter 4 indicates that this is unlikely.

Bursting events give rise to momentary values of shear stress well in excess of the mean and at a frequency related to the flow Reynolds number. Thus as the Reynolds number of flow over a loose granular surface is increased a stage will be reached when the instantaneous shear stresses are large enough to result in incipient motion of the bed material.

For a given surface, this Reynolds number will have a characteristic burst frequency T' which may be used as a criterion for incipient motion providing T' can be determined. This criterion of entrainment was first proposed by Vanoni (1964) following a study of fine sediments (0.102 mm) in water. Vanoni (1964) found that when T' is smaller than 0.1 H_z, the entrainment rate was negligible, whereas general bed movement was observed when T' is greater than 1.0 H_z. On the basis of experimental evidence Vanoni suggested that entrainment threshold conditions were represented by 0.33 smaller than T' smaller than 1.0 H_z. Sutherland (1966), on the other hand, suggested that critical conditions are reached when T is smaller than or equal to 2.0 H_z at any given position on the bed.

A useful criterion to define incipient motion in air, therefore, appears to be the frequency of bursting events. However, as such events generate relatively high shear stresses at random over a given surface

(Kline et al., 1967; Grass, 1971), the entrainment of grains is controlled to a large extent by the statistical distribution of shear stress over that surface and thereby renders such a definition impracticable. Further, Gyr (1983) argues that assumptions made regarding the relationship between bursting events and entrainment "rest on shakey ground", Gyr (1983, p. 8) as even the basic mechanisms of bursting events are not well understood. Gyr (1983) suggests that typical eddies (or the wakes shed by individual upstream particles) may also be responsible for the generation of high instantaneous shear stresses which are able to entrain material with the same efficiency as bursts.

On the basis of the preceding discussion, it appears that the incipient motion in granular bed material is determined by the entrainment susceptibility distribution of grains on the bed and the distribution of local instantaneous shear stresses applied to the bed by the fluctuating flow. Incipient motion therefore appears to be characterised by the movement of the most susceptible particles by the highest shear stresses generated during the passage of coherent features in the background flow. Thus each grain in a sample may be ascribed a certain threshold shear stress value which, if exceeded, will result in entrainment.

Grass (1970) measured the magnitude of instantaneous threshold bed shear stresses associated with samples of fine Mersey sand and found that in a given flow regime the distribution was dependent upon the particle size distribution, particle shape and density and the relative exposure of grains to the flow. In addition, the distribution of instantaneous bed shear stresses for turbulent flow over rough surfaces

was also presented. The distribution of these bed shear stresses (i.e. bursts and sweeps) was found to be governed by the mean bed shear stress, the fluid density and kinematic viscosity and the geometric arrangement of bed particles. Compte-Bellot (1963), Schraub and Kline (1965), Kemp and Grass (1967), Clark (1968), Grass (1970), Eckelmann and Reichardt (1972) and Blinco and Simons (1974) all showed that the distribution of instantaneous bed shear stress was positively skewed.

Grass (1970) suggested that at the threshold of motion, particles with the lowest characteristic critical shear stress values (i.e. the most susceptible grains), are entrained by the highest instantaneous shear stress event which occurs in the characteristic shear stress distribution applied to the bed by turbulent boundary layer flow. If the probability distribution of threshold bed shear for an aeolian sand sample with a Gaussian particle size distribution is plotted with instantaneous bed shear stresses using the same axes (Grass, 1970), it is possible to define the threshold condition for the aeolian sand in an objective way.

Figure 2.12(a) shows that when these probability distributions are separated along the shear stress axis, no entrainment occurs as the peak bed shear stresses associated with the turbulent air flow are less than the minimum threshold bed shear stresses. If wind speed is increased to a critical level, the probability distribution of instantaneous bed shear stresses shifts to the right along the abscissa and a condition is reached where peak bed shear stresses are just below minimum threshold bed shear stresses for the aeolian sand (Figure 6.12(b)). In such flow conditions, the particles on the bed most susceptible to entrainment are at the threshold of motion. Further

increases in wind velocity give rise to the conditions illustrated in Figure 6.12(c) where the two probability distributions are shown to overlap. In these circumstances the grains susceptible to erosion by the peak bed shear stresses will be entrained and subsequently transported by the wind. The implications of this fundamental relationship between instantaneous bed shear stress and threshold bed shear stress are crucial in the context of the present study and are discussed in more detail in later chapters.

2.6 The measurement of surface shear stress

2.6.1 Introduction

In studies of incipient motion, investigators have generally been concerned with the determination of average shear stress over an area of sediment. Such measurements have been found to give a fairly good indication of the flow conditions likely to give rise to a certain degree of particle motion for a given range of materials and particle sizes. However, the presence of the highly energetic coherent structures in turbulent boundary layers suggests that these average conditions may be unrepresentative at the scale of single grains as the shear stresses associated with bursting and sweeping events may give rise to localised instantaneous shear stresses in excess of 2.5 times the mean shear stress (Grass, 1970, p. 629). It was suggested in 2.5.3 that such events probably give rise to the local shear forces necessary for particle entrainment, thus a measurement of the threshold shear stress at the scale of single grains would appear to be a more appropriate measure of threshold flow conditions. However, because of the random occurrence of such events in time and space, the difficulties associated with measuring

extremely localised shear and an inability to know precisely which event will cause a given grain to move, it is impossible to determine the instantaneous threshold shear stress directly. At present it appears that the only solution to the problem lies in the statistical relationship between mean and instantaneous shear stress.

The drag on a flat plate with roughness elements on its surface has two components: (a) skin friction; and (b) pressure drag. Hence:

$$\begin{Bmatrix}\text{Boundary drag}\\(\text{profile drag})\end{Bmatrix} = \begin{Bmatrix}\text{Skin friction}\\(\text{viscous drag})\end{Bmatrix} + \begin{Bmatrix}\text{Pressure drag}\\(\text{form drag})\end{Bmatrix}$$ Duncan et al. (1970)

The relative magnitude of the boundary drag components are dependent on Reynolds number. In low Re flow viscous stresses predominate, and skin friction dominates over pressure drag, whereas high Re flow bodies, such as sedimentary particles, induce flow separation, and higher pressure drag results (see Figure 1.7).

In the study of incipient motion on the experimental flat plate, however, the measurement of the boundary drag components was unnecessary as incipient motion is governed by the sum total of skin friction and pressure drag forces. A number of techniques devised to measure boundary drag were evaluated with a view to determining the most suitable method for use with the experimental plate. The methods used to determine shear stress may be considered under two catagories: (a) 'direct' methods; and (b) 'indirect' methods.

2.6.2 'Direct' methods

A method of shear stress measurement often employed in aeronautical and hydraulic engineering involves mounting an object so as to allow limited free movement under the action of local drag forces. In aeolian entrainment studies the object could be a single sand grain or bed of grains. Using electrical or mechanical means, the drag can be measured directly. Considerable difficulty is generally encountered as the forces involved are usually very small and care must be taken to ensure that the mounting apparatus does not interfere with flow around the object. Examples include the "floating shear tray" apparatus devised by Zingg (1952) and the drag balance methods reported by Lynch and Brackley (1974) and Mulhearn and Finnigan (1978).

The relationship between drag and the rate of heat transfer to the surroundings was exploited in the method described by Ludweig and Tillman (1949). Simply:

$$\frac{dT_*}{dt} = C_D^{3/2} \qquad 2.13$$

where T_* = temperature Celsius

Similarly, the heated element used by Leipmann and Skinner (1954) and the thin-film heat transfer gauge by Bellhouse and Schultz (1966) have enabled the measurement of boundary drag using the heat transfer relationship (equation 2.13). Such techniques require precise calibration owing to heat conduction to the surrounding and are therefore not generally applicable. As a considerable amount of sophisticated

equipment is required for accurate drag measurements using 'direct' methods, they were considered to be inappropriate for measurements of shear stress on the experimental flat plate used in this investigation.

2.6.3 'Indirect' methods

(a) Von Kármán-Prandtl log law

The velocity distribution within the 'inner region' of a turbulent boundary layer over a rough surface was described in section 2.5.1 by equation 2.8, i.e.

$$\frac{U(y)}{U_*} = A_K \ln\left[\frac{y}{Z_o}\right] + B_K \qquad (2.8)$$

In flows characterised by grain Reynolds numbers, Re^* greater than 70, flow and surface friction are independent of the Reynolds number as shear stresses are almost entirely derived from the pressure drag associated with eddy shedding processes by individual roughness elements. As the form drag due to the eddying wake behind bluff bodies is relatively insensitive to the Reynolds number, the constants in the velocity distribution relationship (equation 2.8) assume constant values for Re^* greater than 70. In such conditions A_K=2.5 and B_K=8.5 and the flow is referred to as "fully developed roughness flow" (Duncan et al., 1970, p. 327). In flows characterised by $5 < Re^* < 70$, the value of the constant B varies as a function of Re^* and in flow regimes where Re^* smaller than 5, B_K assumes a value of 5.5. Such flow is termed "hydraulically smooth" and is characterised by the immersion of roughness elements in the viscous sublayer which therefore

have no effect on the flow.

In general, aeolian studies are undertaken in fully developed roughness flow because all naturally erosive winds are fully turbulent (Chepil and Woodruff, 1963). By using a form of equation 2.8 it is possible to determine the surface shear stress or shear velocity, U_*, using the appropriate surface roughness parameter, Z_o, and a single velocity measurement taken at a known height from the boundary, providing it falls within the "inner region" of the turbulent boundary layer. However, as this method is only applicable to fully developed roughness flow it was not possible to use a form of the logarithmic velocity distribution equation to determine shear stress on the experimental flat plate because the flow conditions associated with the developing boundary layer at any point on the rough plate surface were essentially unknown.

Field observations of marine sediment transport in uni-directional currents led Sternberg (1972) to develop a simple technique to estimate bed shear stress based on the quadratic stress law equations given by Bagnold (1963). If the fluid velocity at 100 cm above the bed is known, then

$$\bar{\tau} = 3 \times 10^{-3} \rho \bar{U}_{100}^2 \qquad 2.14$$

where $\bar{U}_{100}$ = Mean fluid velocity at 100 cm above the bed ms^{-1}

Equation 2.14 is only applicable in turbulent boundary layer flow in water, and the numerical coefficient is empirically determined for average marine conditions.

(b) Inner region total pressure measurements

A widely-used technique for determining shear stress in aeronautical and hydraulic engineering involves pressure measurements within the viscous sublayer and inner region of the boundary layer. The method devised by Stanton et al. (1920) used a fine surface pitot probe which extended no more than a few hundredths of a millimetre above the surface. The tube was therefore well immersed in the viscous sublayer and the total head reading of the tube minus the static pressure was then simply related to the velocity gradient at the wall and hence the shear stress. However, the relationship between the measured pressure difference and shear stress cannot be easily predicted on theoretical grounds alone and the tube must therefore be calibrated. Great accuracy and technical precision is required for the reliable measurement of shear stress by this method which limits the range of its practical application (Fage and Faulkner, 1930).

Preston (1954), using an argument based on the inner velocity law (or "law of the wall") developed a similar instrument to measure shear stress. A detailed account of the operation, calibration and limitations of the Preston tube method is given by Patel (1965). The inner region velocity law may be expressed as

$$\frac{U}{U_*} = f\left(\frac{yU_*}{\nu}\right) = Re^* \qquad 2.15$$

Preston argued that since the flow of the "inner layer" is described by equation 2.15, then it must be a region described by ρ, ν, τ and a suitable length. Thus if a fine pitot probe of diameter D_p is placed

in contact with the boundary so that it is well immersed in the "inner region" flow, then the measured difference between the static pressure, P_s and the pitot pressure P_o must be dependent on ρ, ν, τ and D_p. Hence

$$P_s - P_o = f\{\rho, \nu, \tau \text{ and } D_p\} \qquad 2.16$$

where D_p = diameter of pitot tube m

Preston showed that the functional relationship in equation 2.15 can be expressed as

$$\frac{(P_s - P_o) D_p^2}{\rho\nu^2} = f\left(\frac{\tau D_p^2}{\rho\nu^2}\right) \qquad 2.17$$

Using empirical techniques, Preston found that for the boundary layer on a flat plate, equation 2.16 takes the form

$$\text{Log}_{10}\left[\frac{\tau D_p^2}{4\rho\nu^2}\right] = -1.366 + 0.877\ \text{Log}_{10}\left[\frac{(P_s - P_o) D_p^2}{4\rho\nu^2}\right] \qquad 2.18$$

Thus it is possible to determine shear stress, τ, using simple fluid parameters and a single pressure measurement. However, equation 2.18 applies only to the boundary layer flow over a smooth plate and is therefore not applicable to the rough surface of the plate in the present experiments. Even if it were possible to solve the functional relationship described by equation 2.16 for the case of the rough plate, it would still be difficult to site a fine pitot tube in a representative way due to the vigorous interaction of particle wakes. The use of such a

technique on the experimental plate, therefore, seems to be impracticable.

(c) Momentum integral method

The relationship between momentum, pressure and shear stress within the boundary layer are described by the boundary layer equation of motion, equation 2.6. Von Kármán (1921) argued that a relationship must therefore exist between the overall rate of momentum flux, the shear stress and the pressure gradient across a section of the boundary layer. By integrating equation 2.6 with respect to y, from the surface (y=0) to the outer edge of the boundary layer (y≈δ), Von Kármán was able to derive an expression to describe the relationship between momentum flux, shear stress and pressure gradient. The expression is called the momentum integral equation and detailed accounts of its derivation are given by Thwaites (1960), Duncan et al. (1970) and Schlichting (1979).

Duncan et al. (1970) derived a useful approximation of the momentum integral equation given by equation 2.19.

$$\frac{d}{dx}\left[\int_{y=0}^{y=h\delta} \rho U^2 dy\right] \delta x - U_\infty \frac{d}{dx}\left[\int_{y=0}^{y=h\delta} \rho U dy\right] \delta x = -\frac{h\delta dP}{dx} - \tau \qquad 2.19$$

$$+ \text{ residual terms of order } \delta x^2$$

where $h\delta$ = approximate thickness of the boundary layer m

Equation 2.19 describes the relationship between the momentum flux, shear stress and pressure gradient. However, the most useful form of the momentum integral equation describes this relationship in terms of two

other parameters: (i) the displacement thickness, δ^* and; (ii) the momentum thickness, θ_M.

(i) Displacement thickness, δ^*

In the boundary layer, the volume flow per unit width over a vertical distance δy is given by $U\delta y$. Were the flow not retarded through friction (i.e. the velocity of the flow in the boundary layer is the same as the free stream velocity), then the value of the flow per unit width over the same vertical distance would be $U_\infty \delta y$. Thus the reduction in the total flow caused by friction may be expressed as

$$\int_{y=0}^{y=\infty} (U_\infty - U)dy \qquad 2.20$$

Theoretically, the boundary layer extends to infinity. For most practical purposes, however, integration of equation 2.20 proceeds from y=0 to a height where the boundary layer flow velocity is approximately equal to the free stream velocity. In physical terms, expression 2.20 may be interpreted as a fluid flow rate deficit within the boundary layer. Dividing this by the free stream velocity gives a distance, which in turn may be interpreted as a distance by which the external flow is displaced away from the surface by the retarded flow in the boundary layer. This distance is termed the displacement thickness, δ^* and is defined as

$$\delta^* = \frac{1}{U_\infty} \int_{y=0}^{y=\infty} (U_\infty - U)dy \qquad 2.21$$

For the purposes of calculating the physical value of δ^* however, equation 2.21 is generally expressed in the form

$$\delta^* = \int_{y=0}^{y=\delta} (1-U/U_\infty)dy \qquad 2.22$$

(ii) The momentum thickness

The momentum of a small fluid element in a boundary layer is defined as $\rho d_y U$, where dy is the thickness of the element. In the absence of the boundary layer, the momentum of the same element would be $\rho dy U_\infty$. If the fluid density is constant, the total reduction in flow momentum in the boundary layer may be expressed as

$$\int_{y=0}^{y=\infty} \rho(U_\infty - U)Udy \qquad 2.23$$

The loss of momentum due to friction in the boundary layer is equivalent to the momentum of free stream flow which extends a vertical distance θ_M. Hence

$$(\rho U_\infty \theta_M)U_\infty = \int_{y=0}^{y=\infty} \rho(U_\infty - U)Udy \qquad 2.24$$

Equation 2.24 expresses the vertical extent of free stream flow with a momentum flux exactly equal to the momentum deficit in the retarded boundary layer flow. For computational simplicity, θ_M may be defined as

$$\theta_M = \int_{y=0}^{y=\delta} \frac{U}{U_\infty}\left(1-\frac{U}{U_\infty}\right)dy \qquad 2.25$$

Using the expressions for δ^* and θ_M given in equations 2.22 and 2.25 respectively, it is possible to express the momentum integral equation in the form

$$\tau = \frac{d}{dx}\left(\rho U^2 \theta_M\right) + \frac{dU_\infty}{dx}\rho U_\infty \delta^* \qquad 2.26$$

If the pressure gradient dP/dx is zero, then equation 2.26 reduces to the form

$$\tau = \frac{d\theta_M}{dx}\rho U_\infty^2 \qquad 2.27$$

Equation 2.27 may be used to calculate the shear stress at any chosen position on the boundary and may therefore be usefully applied to calculate surface shear stresses on the experimental plate in this investigation. To achieve acceptable accuracy a number of conditions must be satisfied and a number of sources of error must be eliminated. These include the following:

(a) The pressure gradient along the plate must be zero.

(b) The flow must be two dimensional; any cross-flow will also transfer momentum and therefore render the results inaccurate.

(c) The velocity profile measurements, necessary for the calculation of δ^* and θ_M must be accurate and give sufficient profile resolution.

(d) There must be no interference with the boundary layer flow by the side walls or roof of the wind tunnel.

Using boundary layer velocity profile measurements, the momentum thickness may be determined for various streamwise stations on the experimental plate using equation 2.25. The value of θ_M is then plotted against the streamwise distance along the plate (x) and a smooth, 'best fit' curve is placed through the data points. The gradient of the resulting curve ($d\theta_M/dx$) is then determined at a chosen streamwise distance and substituted into equation 2.27 to obtain surface shear stress. Thus there is a 'smoothing' effect inherent in the deduction of $d\theta_M/dx$ from discrete measurements of θ_M on the plate. A detailed account of the computational procedures used to calculate surface shear stress from velocity profiles on the flat plate is given in 4.3.3.

Table 2.1 Scale of coherent structures in a turbulent boundary layer on a smooth wall (after Cantwell, 1981; and Gyr, 1983).

Data sources given in Table 2.2

Coherent structure	length scale	convection velocity C_j	persistence distance x_j	Life time x_j/C_j
Sublayer structure: Streamwise vortices, λ_i (1)	ν/U_*	U_∞	λi	λ_i/U_∞
	λ_x=1000 (200-2000)			
	λ_y=15 (10-25)	$C_j<<1$ (2)	1 (2)	>> 1 (2)
	λ_z=80 ± 20			
Energetic near-wall eddies, b_i (3)	ν/U_*	U_∞	δ	δ/U_∞
	b_x=20-40 60-100(P)	0.65 ± 0.05	0.5-1.5	0.33-0.98 (2)
	b_y=15-20	0.2 (P)		0.1-0.3 (2)
	b_z ?>$b_{x,y}$			
typical eddies, Re dependent l_i (4)	ν/U_*	U_∞	ν/U_*	ν/U_*U
	l_x≈200			
	l_y≈100	0.8-0.9	≈1000	1100-1250 (2)
	l_z≈100-200			
Large eddies, Re dependent L_i (5)	δ	U_∞	δ	δ/U_∞
	L_x≈1-2		1.6-2	1.8-2.5 (2)
	L_y≈0.8	0.8-0.9 at (y-0.8δ)	50-70+	60-85 (2)
	L_z≈0.5-1			
Shear layer events, i.e. bursting and sweeping (6)	δ	U_∞	δ	δ/U_∞
	S_x≈0.05-0.1			
	S_y≈0.6	0.7-0.9	0.5	3.5-4.5
	S_z≈0.1			

(P) = from pressure measurements
\+ = large discrepancy depending on the method of measurement

Table 2.2 Data sources used to determine the scale of coherent structures in a turbulent boundary layer on a smooth wall (after Cantwell , 1981 ; and Gyr , 1983).

Structure	AUTHORS
(1)	Bakewell and Lumley (1967), Blackwelder (1978), Blackwelder and Eckelman (1979), Cantwell et al. (1978), Grass (1971), Gupta et al. (1971), Kim et al. (1971), Kline et al. (1967), Kovasznay et al. (1970), Lee et al. (1974), Oldaker and Tiederman (1977), Praturi and Brodkey (1978), Willmarth and Yang (1970).
(2)	Gyr (1983)
(3)	Brown and Thomas (1977), Cantwell et al. (1978), Corino and Brodkey (1969), Dinkelacker et al. (1977), Kline et al. (1967), Praturi and Brodkey (1978), Sabot et al. (1977), Smith (1978).
(4)	Cantwell (1981), Falco (1977), Kovasznay et al. (1970), Savas (1979), Smith (1978), Wygnanski and Champagne (1973), Zilberman et al. (1977), .
(5)	Brown and Thomas (1977), Cantwell et al. (1978), Coles and Barker (1975), Dinkelacker et al. (1977), Falco (1977), Head and Bandyopadhyay (1978), Kovasznay et al. (1970), Praturi and Brodkey (1978), Sabot et al. (1977), Savas (1979), Smith (1978), Willmarth and Wooldridge (1962), Zakkay et al. (1978), Zilberman et al. (1977).
(6)	Brown and Thomas (1977), Coles and Barker (1975), Falco (1977), Kim et al. (1971), Kline et al. (1967), Kovasznay et al. (1970), Lu and Willmarth (1973), Narayanan and Marvin (1978), Rao et al. (1971), Sabot et al. (1977), Smith (1978), Zakkay et al. (1978).

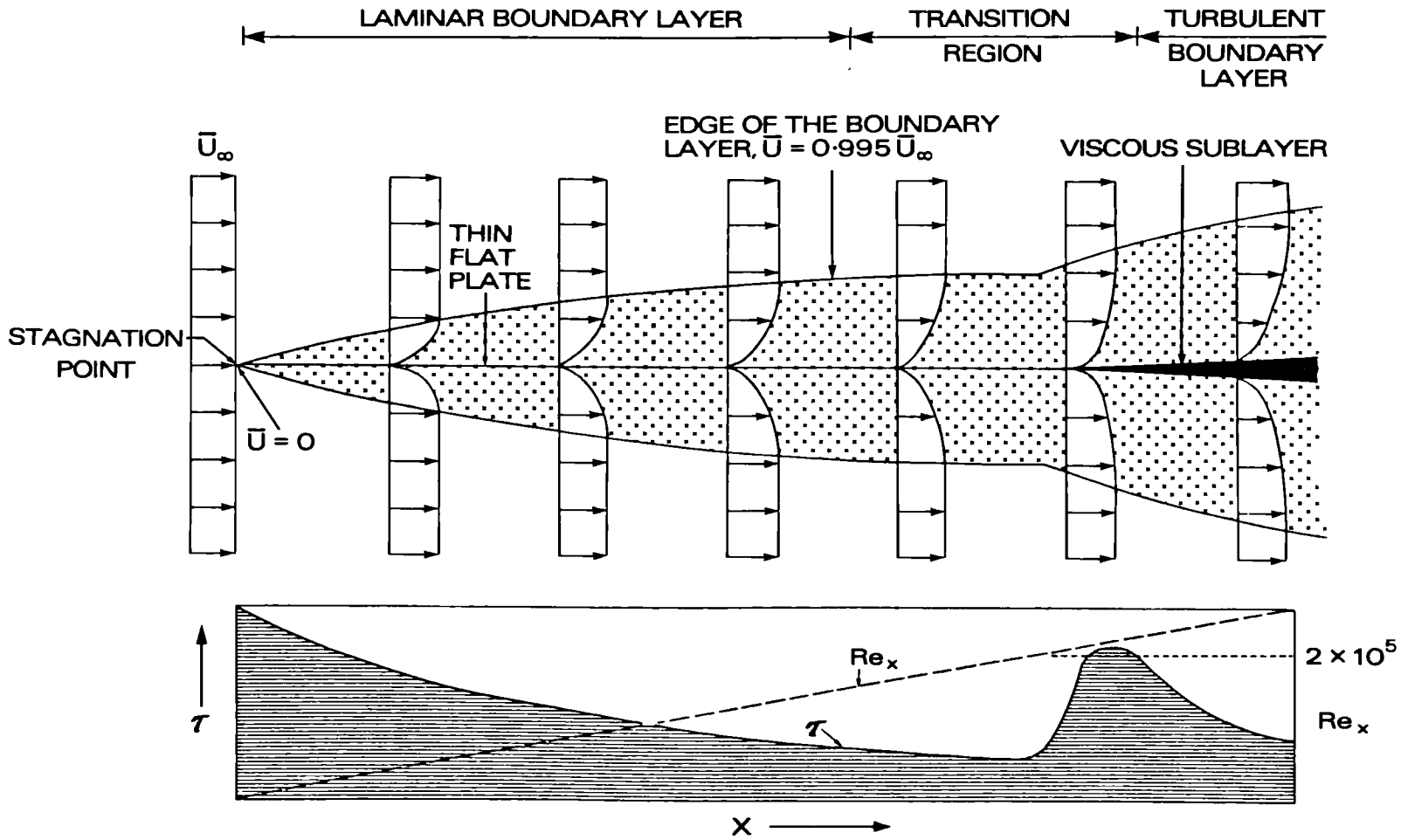

Figure 2.1 Developing boundary layer on a flat plate.

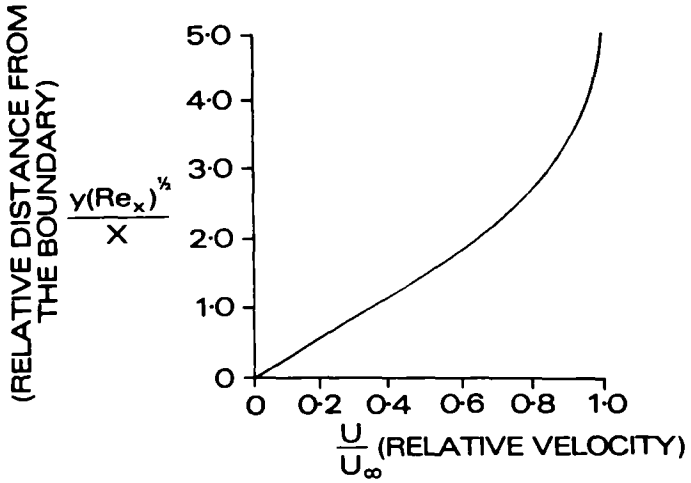

Figure 2.2 Laminar boundary layer.

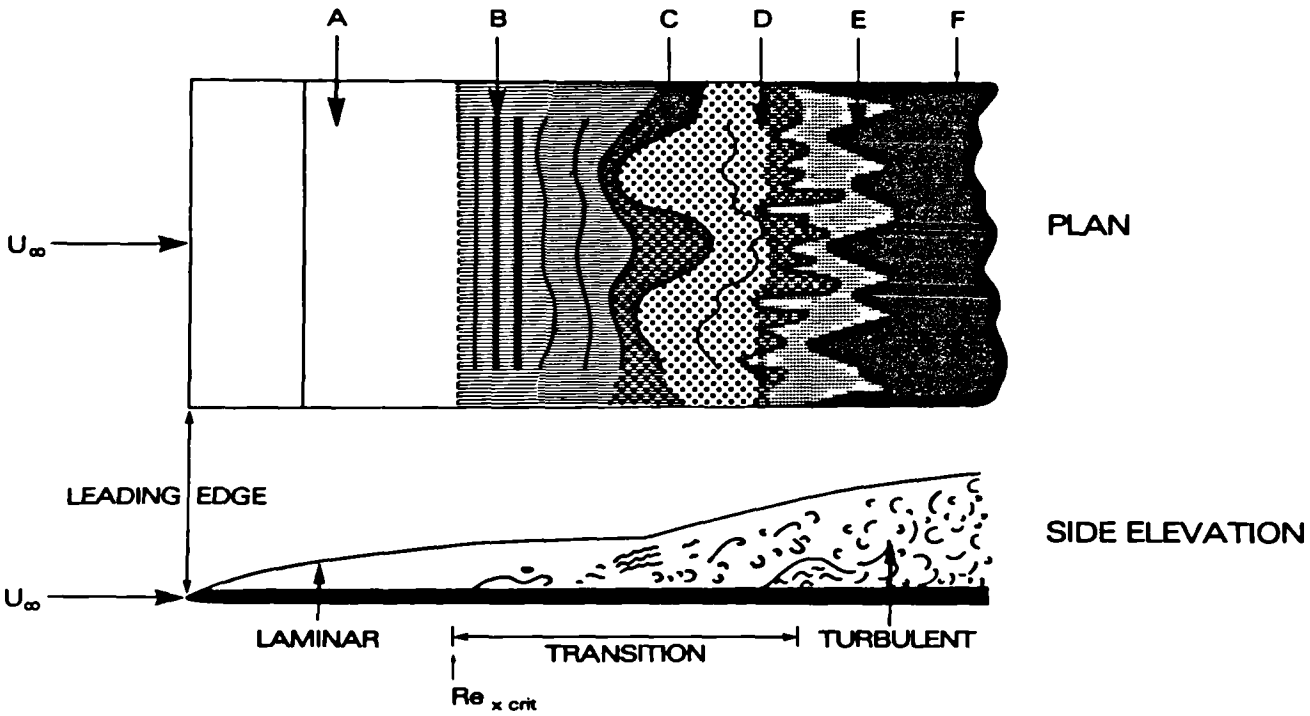

A Stable, laminar boundary layer flow.

B Laminar boundary layer flow with two dimensional Tollmien-Schlichting waves.

C Development of laminar three dimensional waves and vortices.

D High local vorticity gives rise to bursts of turbulence.

E Turbulent spots form in places where the turbulent velocity fluctuations are large.

F Turbulent spots coalesce to give a fully turbulent boundary layer.

Figure 2.3 Transition from laminar to turbulent boundary layer flow on a flat plate in air (flow stages after White, 1974).

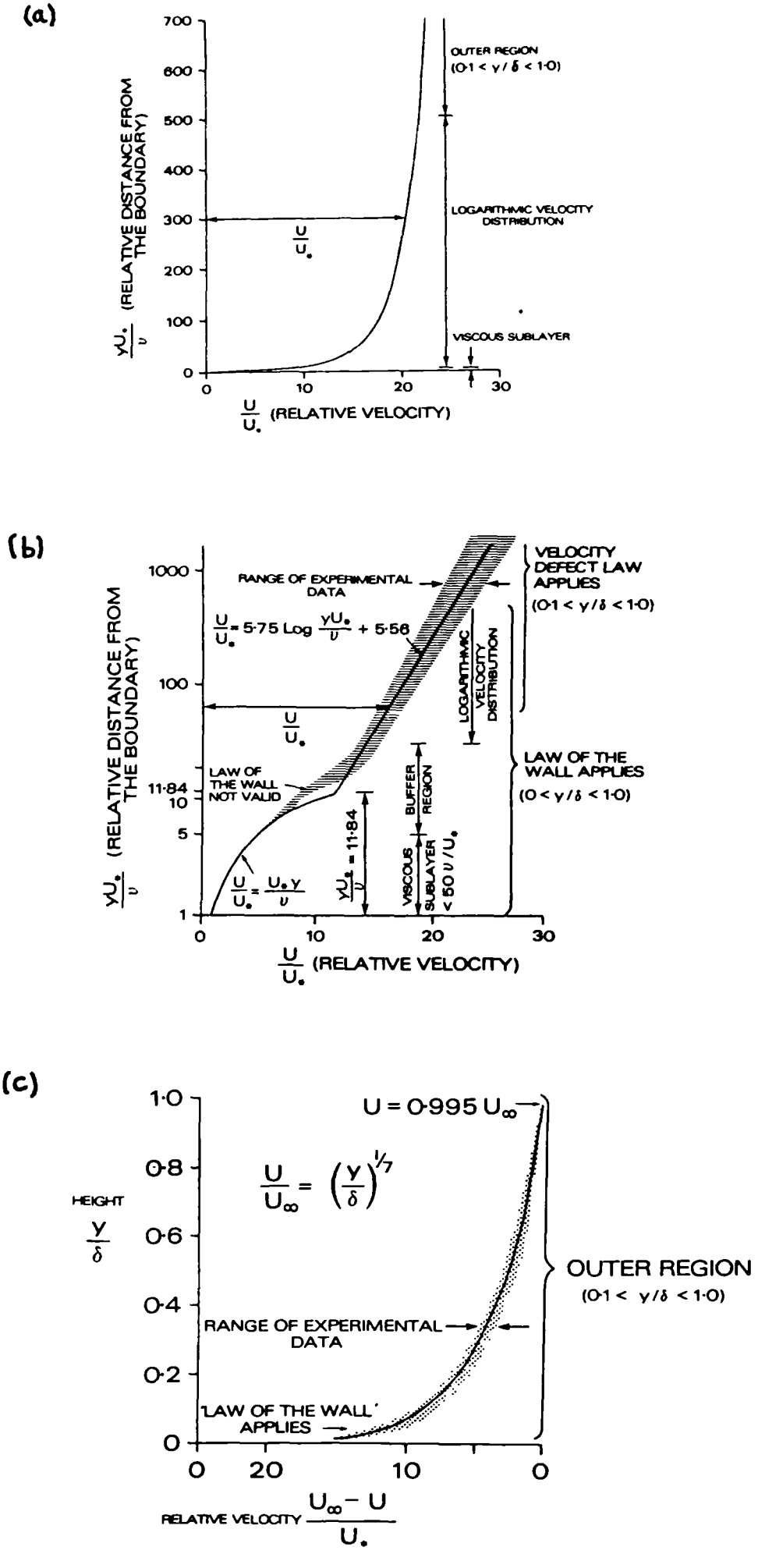

Figure 2.4 Turbulent boundary layer.

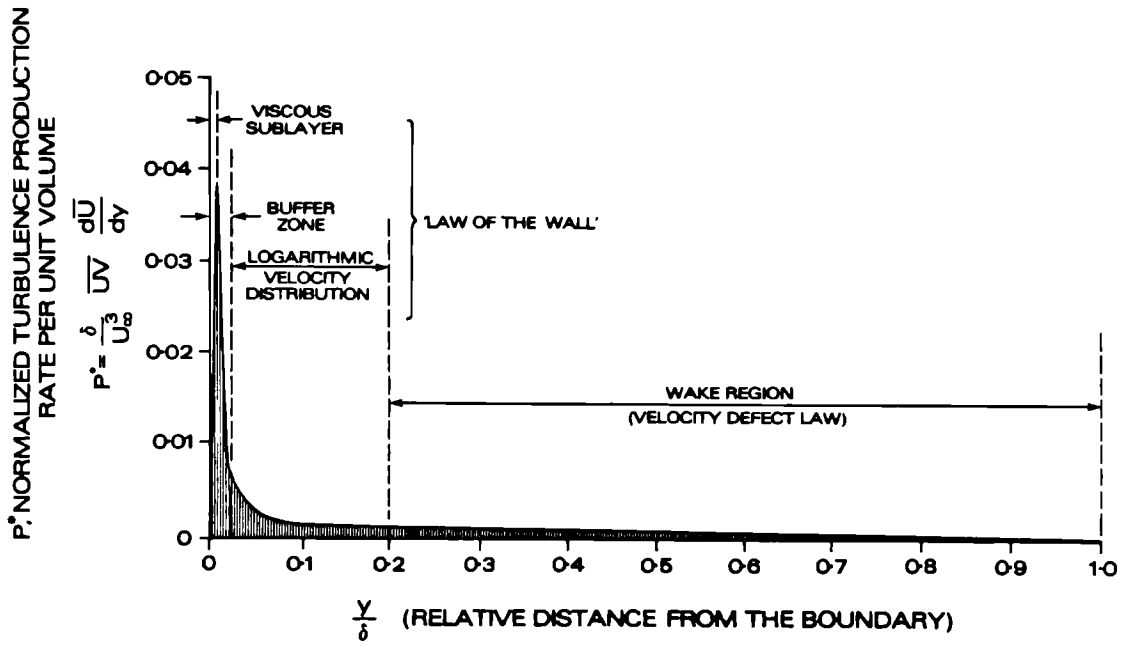

Figure 2.5 Turbulence production in a boundary layer (after Klebanoff, 1956).

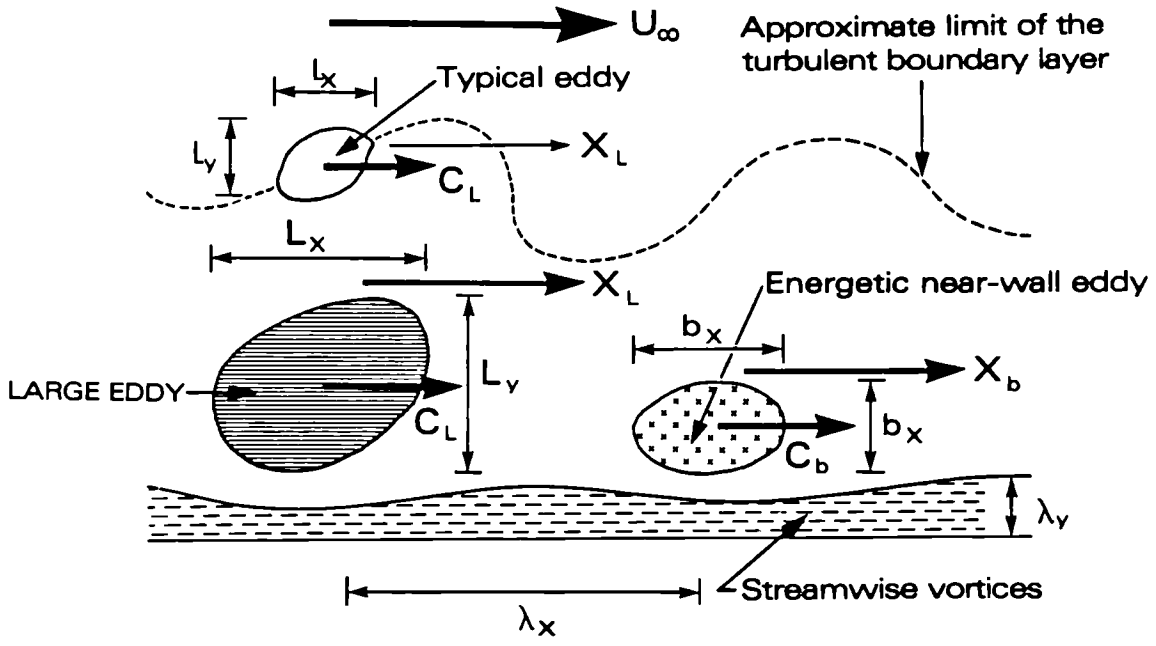

L	Large scale eddy	y	Height
l	Typical eddy	z	Width (not shown)
b	Energetic near-wall eddy	C	Convection velocity
λ	Streamwise vortices	X	Persistence distance
x	Length		

Figure 2.6 Coherent features in a turbulent boundary layer (scales in Table 2.1), (after Gyr, 1983).

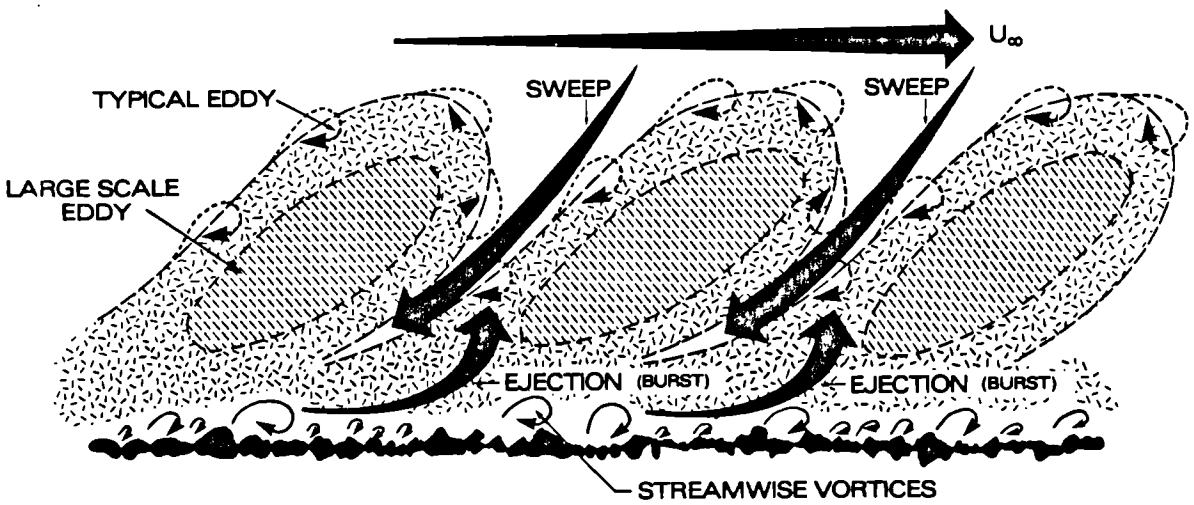

Figure 2.7 Schematic representation of a turbulent boundary layer (rough surface) (after Gyr, 1983).

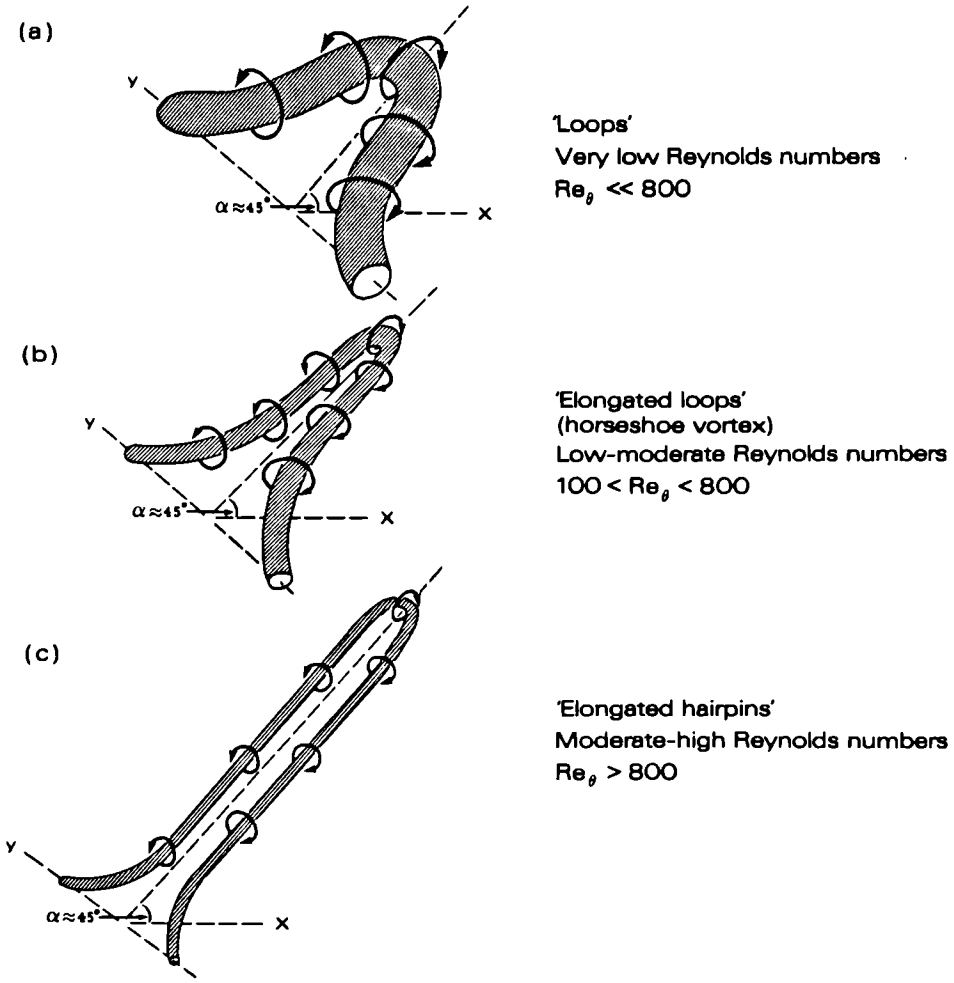

Figure 2.8 Vortex loop structures in a turbulent boundary layer (after Head and Bandyophadyay, 1981).

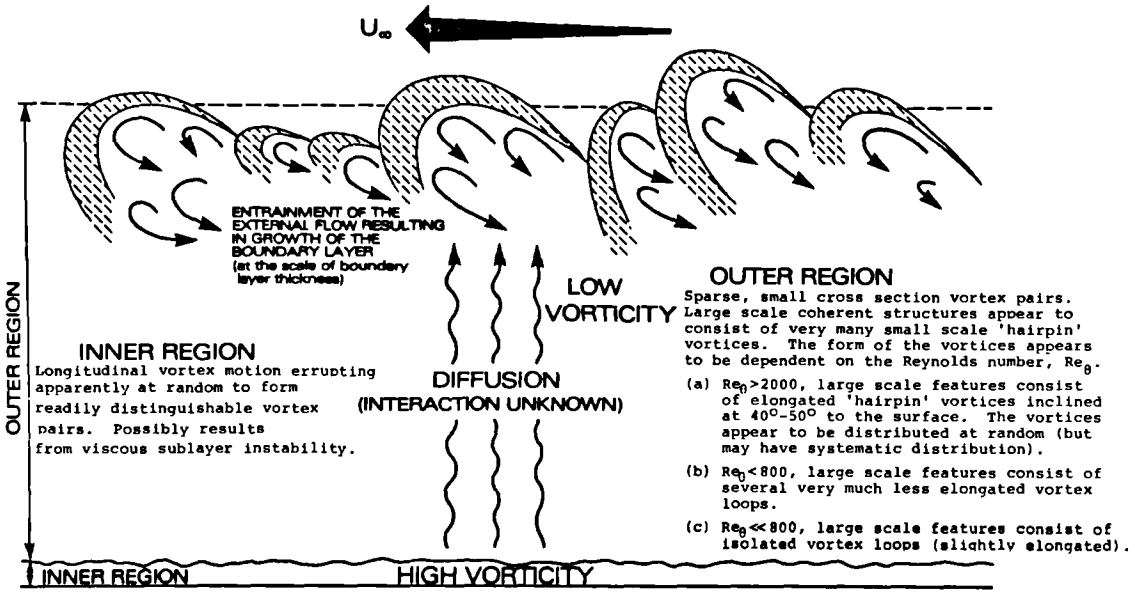

Figure 2.9 Model of a turbulent boundary layer (after Head and Bandyophadyay, 1981).

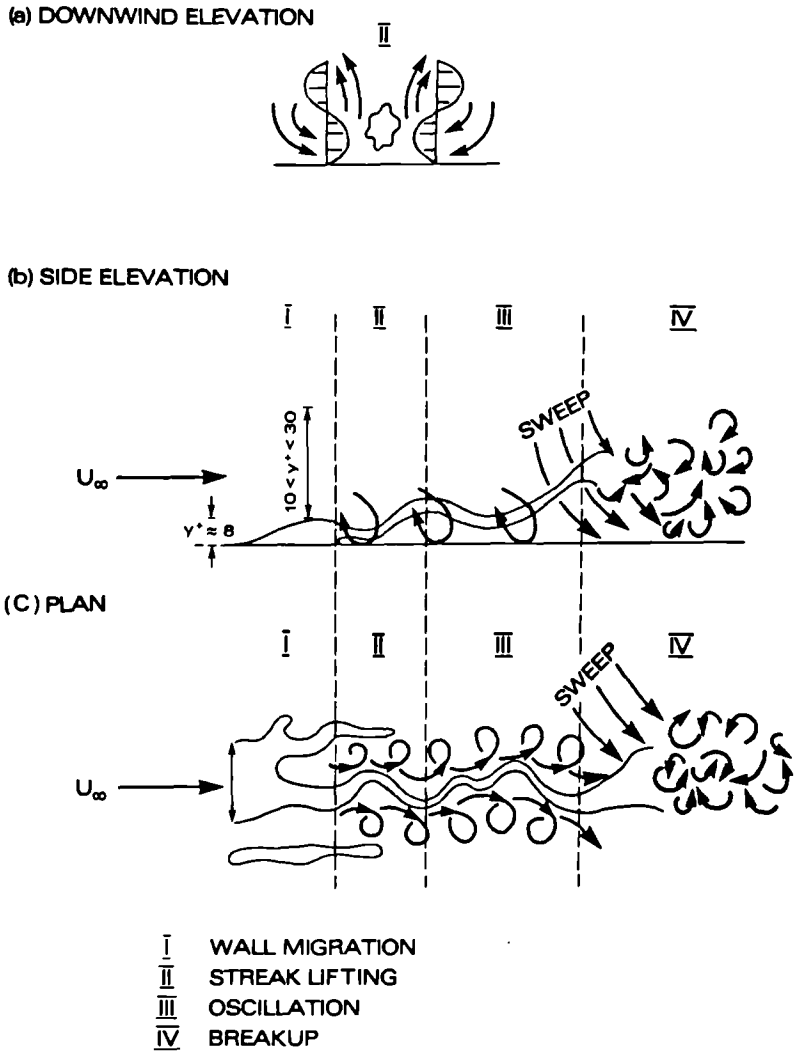

Figure 2.10 The 'Stanford' bursting model (after Kline et al., 1967).

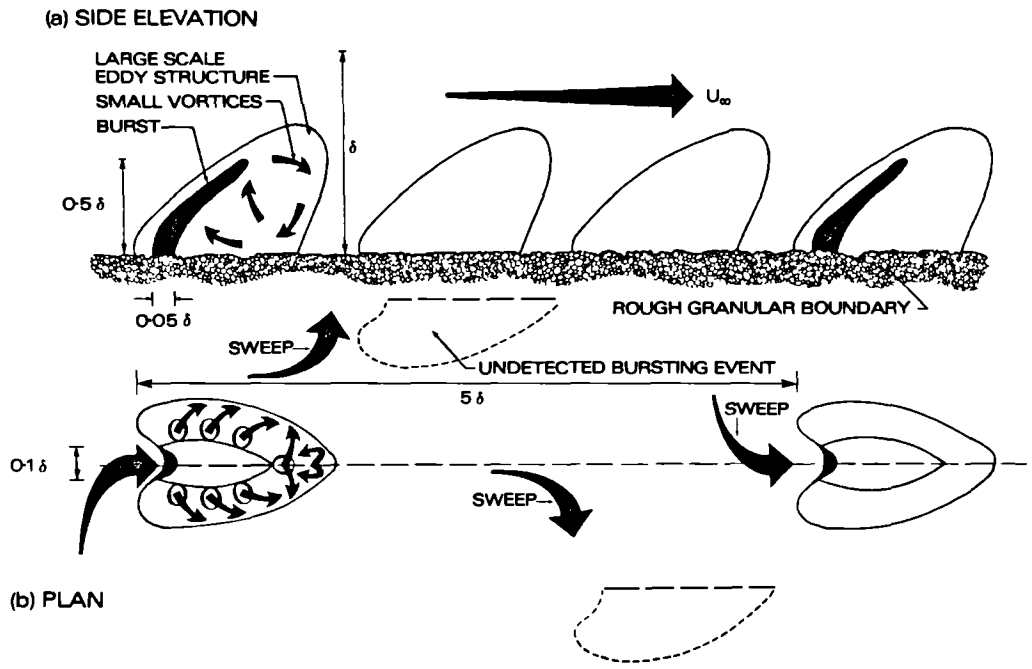

Figure 2.11 Major coherent structures on rough boundaries (after Laufer, 1975).

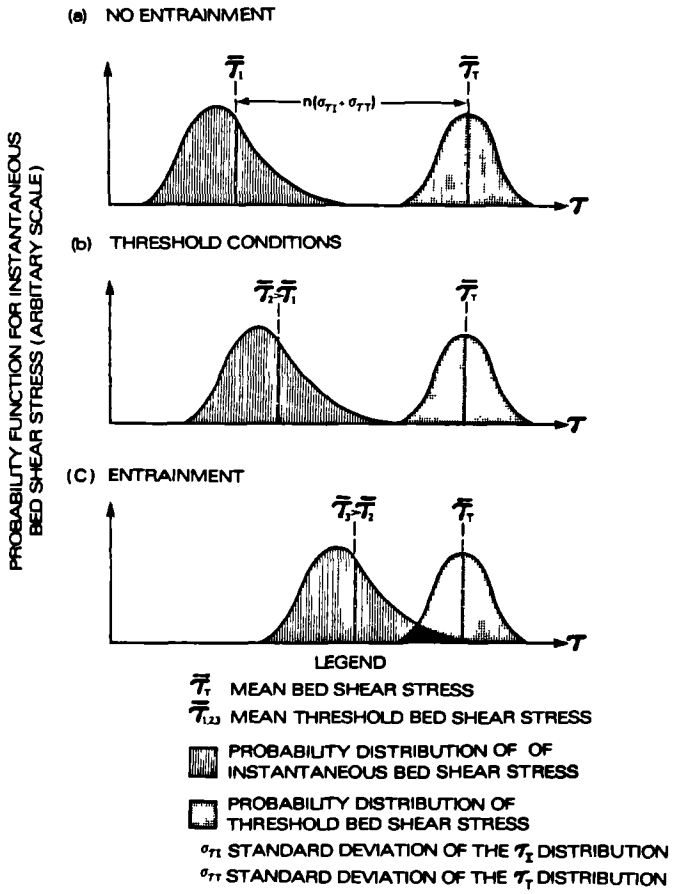

Figure 2.12 Aeolian threshold conditions in a turbulent boundary layer (after Grass, 1970).

CHAPTER THREE

Experimental apparatus

3.1 Introduction

In Chapter 1 it was considered that owing to the controlled and reproducible nature of the developing boundary layer on a flat plate in air, observation and measurement of initial grain motion on the surface of a suitable plate using carefully designed experiments would elucidate certain aspects of aeolian thresholds and entrainment processes associated with loose granular materials. In this chapter, the design and construction of a large experimental plate and its subsequent installation into the working section of a blow-down wind tunnel are described. Once installed, certain characteristics of the developing boundary layer on the whole length of the plate were examined using (a) velocity profile measurements taken at selected study sites, and (b) a flow visualization technique to examine in detail flow conditions near the leading edge of the plate.

This chapter also describes the selection and preparation of uniform granular test materials. Each of these materials were fixed to the surface of the plate in a flat layer, one grain diameter in thickness, using a specially developed technique described in this chapter. Test material fixed in this way allowed simulation of a natural, flat sediment bed and provided the necessary support for loose test grains laid on this surface in subsequent investigations. A preliminary examination of the boundary layer characteristics over this type of 'rough' surface is also reported in this chapter.

3.2 The experimental flat plate

The working configuration of the flat plate used in this

research is shown in Figure 3.1. It consists of three separate sections: (a) the leading edge section; (b) the working surface; and (c) the tail section.

3.2.1 Leading edge section

Flow approaching the leading edge of the plate is brought to rest at the stagnation point, where the pressure is higher than the atmospheric (or static) pressure. Downwind of the stagnation point, round the surface of the leading edge, the static pressure drops and flow accelerates in the pressure gradient. Owing to the condition of "no slip" at the solid/air interface, and to the effects of air viscosity, a laminar boundary layer will grow downwind from the front of the leading edge and pass through transition to fully turbulent flow at some distance back along the plate (see 2.2). It is important to shape the leading edge of the plate in such a way that static pressure falls steadily, with distance, from the value at the stagnation point to the free stream value over the working surface of the plate. If the leading edge is too blunt, with a discontinuity of curvature at the junction between the leading edge and the working surface, the pressure tends to fall below the free stream value. This results in a region of adverse rising static pressure which may give rise to flow separation, particularly if the boundary layer is still laminar. The curved leading edge must, therefore, be sufficiently slender and any discontinuities of curvature must be avoided. The latter aim is achieved by using a cubic equation of the form

$$y = t_{LE} \left[1-(x/c_{LE})^3\right]^{1/2} \qquad 3.1$$

to generate a suitable shape. The term t_{LE} in equation 3.1 represents half the thickness of the leading edge of the plate, and c_{LE} represents its length.

For $0 < x < c_{LE}$, equation 3.1 gives a curve similar to a half eclipse, but differing from it in that both the curvature and the slope fall to zero at x=0. The curvature of the leading edge section thus blends with the flat working surface of the plate in the required manner. Sufficient slenderness is given to the nose by choosing an appropriate value of t_{LE}/c_{LE}. In this instance, the value chosen was 1/5 and the resulting curve is shown in Figure 3.2.

Using a template shaped according to equation 3.1, the leading edge was shaped from a single piece of fine-grained hardwood. Three pressure tappings were installed on the leading edge to monitor the position of the stagnation point (Figure 3.1). Further explanation and description of their use is given in 3.2.3 where the construction and operation of the tail section of the plate is described. The surface finish of the leading edge was critical as any blemishes or irregularities would adversely affect the downwind development of the boundary layer. To achieve this, five coats of paint were applied to the leading edge section and these were sanded down at each painting stage using fine grade wet and dry abrasive paper. Final smoothing of the leading edge surface with flour grade paper gave a very smooth surface free from any marks likely to affect the air flow (see 3.4.4(b)).

3.2.2 The working surface

The working surface of the prototype plate was constructed from

hardboard and was supported from beneath using numerous close-spaced hardboard strips. However, this working surface proved to be unsatisfactory as slight ridges and depressions were present over the entire surface, and detailed pitot-tube array measurements of the boundary layer velocity profiles (see below) indicated that the flow was laterally disturbed. An alternative form of working surface was therefore needed as any cross-flow on the surface of the plate invalidated the use of the momentum integral equation for calculating surface shear stress (see 2.6.3(c)). After careful consideration of alternatives, a sheet of 6mm thick plate glass was used (Figure 3.1). This provided a flat and completely smooth surface which was unaffected by changes in humidity etc. The surface was also resistant to abrasion and was easily cleaned with solvents. A slight disadvantage was its weight which made the plate more difficult to handle. The glass working surface was supported from beneath using the same hardboard strips as before and its height was adjusted so that it blended smoothly with the leading edge section. The small gap at the junction between the glass working surface and the leading edge (Station A) was filled with 'Tetrion' filling compound and carefully smoothed. Despite the slight flexing movements of the plate as it was manoeuvred in and out of the wind tunnel, the filler remained in place and the joint remained undisturbed throughout all the experiments reported below. An assessment of flow across this junction is also given below.

3.2.3 The tail section

It is critically important that the flow stream lines approaching the plate should arrive at the leading edge parallel to the working surface. If this is not the case, a displaced stagnation point

is likely to result which could give rise to flow separation just downwind of the leading edge. To ensure this did not occur a tail section was joined to the plate by hinges (Figure 3.1). Raising or lowering of the tail section from the horizontal position induced a slight alteration of the pressure distribution on the upper and lower surfaces of the plate and thus enabled the position of the stagnation point to be adjusted. This effect was monitored using three pressure tappings on the leading edge (described above, Figure 3.1). Two pressure tappings, sited on the upper and lower surfaces of the leading edge, indicated the static pressure as the flow accelerated away from the stagnation point. If the stagnation point was on the precise centre-line of the plate, these two pressures were equal as air flow was directed equally over both the upper and lower surfaces of the plate. Adjustment of the tail to the appropriate position above or below the horizontal achieved this condition. The tapping on the plate centre line recorded a maximum pressure value when the above condition was reached.

The effect of tail adjustments on both the external flow and the boundary layer on the leading edge section of the plate is shown diagramatically in Figure 3.3. Figure 3.3(a) illustrates the flow regime when the stagnation point is incident on the centre line of the leading edge section and shows normal downwind laminar boundary layer development. In Figure 3.3(b), however, the effect of a displaced stagnation point is shown and illustrates the laminar separation bubble which is likely to develop in the region of downwind adverse static pressure gradient. Such flow separation results in early flow transition to a turbulent boundary layer regime and thereby negates certain assumptions made concerning the developing boundary layer on the experimental plate and outlined in Chapter 2. To ensure controlled and

reproducible flow conditions further downwind on the working surface of the plate, it was, therefore, essential to adjust the tail elevation correctly. Using pressure measurements from the tappings on the leading edge of the plate, the correct tail angle was found to be 5^{o} above the horizontal position. Further discussion of the effects of tail adjustments on boundary layer velocity profiles is given in 3.4.1.

3.3 Wind tunnel facilities

3.3.1 The wind tunnel

The experimental work using the flat plate was undertaken in a large 'blow-down' wind tunnel. This tunnel, illustrated in Figure 3.4, is an open return type and consists of seven sections. These are a motor section, a divergence section with intermediate gauzes, a settling chamber and contraction sections, a working section and a second diffuser section. Power is supplied to two seven blade fans by two 11.2 kW d.c. electric motors, with a Ward-Leonard set, augmented by a fine adjustment, providing speed control. The experimental plate was positioned in the centre of the wind tunnel working section on runners and was secured in place using screws driven through to the plate from outside the tunnel.

A number of design features made this wind tunnel particularly suitable for the investigation of loose particle entrainment thresholds using the flat plate. The working section was sufficiently large to accommodate a plate large enough for the study, and permitted the installation of several lighting units necessary for photograhy of the loose material on the surface of the plate. The range of operational velocities was large enough to ensure entrainment of all the materials

studied, and past experience had shown that flow in the working section was smooth and uniform thereby ensuring that the boundary layer developed evenly both across and along the surface of the plate Contraction reference pressure could be monitored using a Betz manometer which permitted quick and accurate checks on any chosen wind velocity setting. In addition, quick release hatches in the floor and roof of the working section gave easy access to the plate, and the sectional roof allowed the inclusion of a perspex window for viewing and vertical photography of the plate surface during the experiments described below.

All the loose material entrained from the surface of the plate was ejected from the rear of the diffuser section and most could be collected for re-use using a sediment catcher (see below). Further, this open-return wind tunnel obviates the need for a special particle settling chamber and screens to prevent material from entering into the general circulation. This is particularly important in experimental determinations of aeolian thresholds as any circulating grains would collide with the test bed and any ensuing ejection of particles would give rise to an inaccurate measurement of threshold conditions.

3.3.2 The sediment catcher

During initial trials it became apparent that test material blown from the diffuser could not be re-used if it was allowed to fall to the floor and become contaminated with dirt and dust particles. Further, loose ballotini on the laboratory floor constituted a hazard. It was necessary, therefore, to devise a method of recovering grains for re-use. A preliminary attempt involved placing a butter muslin screen across the exit from the diffuser to catch the blown material. However,

this was found to be unsatisfactory as the exhaust flow was restricted to such an extent that the threshold erosion velocities associated with test materials (see below) could not be attained. Therefore, a parachute design made from butter muslin was devised which allowed air to flow relatively 'cleanly' out of the tunnel. Owing to the momentum of the entrained particles, deflection of the flow around the sides of the parachute did little to deflect their path and the majority were caught. Particles collected in this way were immediately ready for re-use and reduced the amount of sieving time required for replacement of spent grains. A few of the smallest particles escaped capture, but these did not consititute a significant loss. The working configuration of the sediment catcher is illustrated in Figure 3.5. It was found that the collection of sediment was made more efficient when a few weights were placed in the bottom of the catcher, although precise reasons for this could not be deduced.

3.4 Flow on the 'smooth' plate

3.4.1 Measurement of wind velocity

In most of the experimental work, it was necessary to record the wind velocity at a number of heights within the boundary layer close to the surface of the plate and to record the free stream wind velocity associated with the unimpeded flow outside the boundary layer. After considering the merits and disadvantages of several instruments, pitot-tube arrays (or pitot-combs) were selected as being the most appropriate. Two pitot-tube arrays were used and these consisted of seven pitot-tubes arranged vertically up to maximum height of 25.4mm (pitot-tube array 1) and 98.5mm (pitot-tube array 2). The spacing

between pitot-tubes in the array (Table 3.1) was chosen so as to provide more detailed information on the wind velocity in the lower portion of the boundary layer where the velocity gradients are steepest (see Chapter 2). A further refinement was to flatten horizontally the pitot-tubes nearest to the surface so that they gave a closer approximation to a point velocity measurement. Static pressure was measured using a single static pressure probe which was off-set slightly from the pitot-tube array and located at 50mm above the surface. Two annotated photographs of pitot-tube arrays deployed on the surface of the plate are shown in Figure 3.6(a).

Each of the probes in an array was connected to the limbs of an inclined multi-tube alcohol manometer, (see Figure 3.6(b)) using plastic tubing. Pitot-tube pressures caused the alcohol to be forced down the tube whilst the static pressure probe drew alcohol up the tube. The resulting height differences due to static and pitot pressures are related to the mean wind velocity by equation 3.2.

$$\overline{U} = \left(\frac{\rho_m g h \sin\beta}{1/2\rho} \right)^{1/2} \qquad 3.2$$

where ρ_m = manometer fluid density — kg m^{-3}

h = height difference between manometer limbs recording static and pitot pressures — m

β = manometer inclination angle — degrees

For convenience, a simple computer program was used to calculate wind velocity using the relationship in equation 3.2. The program, given

in Appendix A1, allows for changes in air density caused by variations in air temperature and pressure. For additional accuracy, the density of the manometer fluid (alcohol) was also adjusted for the variations in ambient temperature which occurred during experimental investigations. Changes due to variations in air humidity were neglected as the influence is negligible. Further discussion of wind velocity measurement using pitot-tubes may be found in 4.5.1.

3.4.2 Effect of tail adjustment on the boundary layer

In a preliminary study, the effects on the local boundary layer velocity profiles caused by adjustments of the tail section were investigated. The velocity profiles were measured at 1400, 1500 and 1600mm downwind from the junction between the leading edge section and the working surface of the plate (Station A) for tail positions 2^{o}, 4^{o} and 6^{o} above and below the horizontal position, using the pitot-tube arrays described above. The data are presented in Figure 3.7 where dimensionless velocity ($\bar{U}/\bar{U}_{\infty}$) is plotted against distance above the surface of the plate (Y). These velocity profiles are grouped according to tail displacement above or below the horizontal position, and demonstrate clearly the changes in the thickness of the boundary layer brought about by different tail alignments. At tail positions below the horizontal, the boundary layer is shown to be significantly thicker than the boundary layer associated with tail positions above the horizontal. These differences are thought to result from the formation of a laminar separation bubble on the leading edge section caused by changes in the pressure distribution on the upper and lower surfaces of the plate (i.e. the stagnation point was not incident on the centre line of the leading edge of the plate, Figure 3.3). This simple study, therefore, confirmed

that the tail section was a suitable device for controlling flow over the upper and lower surfaces of the plate. Using the stagnation and static pressure tappings on the leading edge as described in 3.2.3 above, the tail angle was set and securely clamped.

It was obviously essential to ensure that, once set, the tail section did not move. To test this, the free stream wind velocity was set to a value found by experiment to be greater than the maximum threshold velocity associated with the largest test material, (i.e. $26ms^{-1}$ for 1.7-1.4mm ballotini). At this wind speed, the tail was found not to move, providing the locking mechanism (Figure 3.1) was tight. In the subsequent experiments reported in Chapters 4 and 6, the tail inclination angle was regularly checked. Minor adjustments were found to be necessary on only two occasions when the tail was accidentally knocked during installation of the plate into the working section.

3.4.3 Static pressure in the boundary layer

Use of the momentum integral method to calculate the mean surface shear stress on the surface of the plate (see 2.6.3(c)) requires that there is a zero downwind static pressure gradient associated with the developing boundary layer. In order to assess whether or not this was the case, static pressure measurements were made at 16 equally spaced positions downwind from Station A. Static pressure was found to be constant at all stations less than 1300mm (Station B) downwind from Station A. At measurement stations just downwind of Station B, static pressure was found to decrease slightly whilst at sites further than 1400mm downwind of Station A, the static pressure was found to fall

significantly. It is thought likely that these changes in static pressure were brought about by the tail section of the plate (see above). Consequently, all experimental work using loose test material on the surface of the plate was restricted to a region extending no more than 1300mm downwind of Station A.

3.4.4 Developing boundary layer on the plate

In order to investigate the streamwise and spanwise flow regime on the smooth plate surface, several sets of velocity profile measurements were taken using the pitot-tube arrays. In addition, a flow visualization technique was also used to examine the details of flow over the leading edge of the plate and the working surface immediately downwind. This flow visualization technique gave a visual impression of air flow across the junction of the leading edge and the working surface of the plate (Station A) and allowed assessment of whether or not flow separation occurred in this critical region.

(a) Using boundary layer velocity profiles

Two boundary layer velocity profile measurement stations were established on the surface of the plate: the junction between the leading edge and the working surface of the plate (Station A); and 1300mm downwind of Station A (Station B). During all velocity measurements, the free stream wind speed was held constant at $5ms^{-1}$. Velocity profiles were measured at various spanwise positions at each of the measurement stations on the surface of the plate. The results are presented in Table 3.2 and are illustrated in Figures 3.8 and 3.9.

In Figure 3.8 the X, Y and Z axes represent dimensionless velocity ($\bar{U}/\bar{U}_\infty$), the height above the surface (Y) and the spanwise position of each velocity profile taken at a given measurement station, respectively. The profiles at Station A indicated that the boundary layer was laminar in this region (see 2.3.1) and that no significant spanwise flow anomalies were present. At 1300mm downwind of Station A (i.e. Station B), the form of the boundary layer velocity profile indicates that flow was turbulent in this region (see 2.5.1) and like profiles measured at Station B showed little spanwise variation. Over this distance the boundary layer thickness, δ, increased from 5.7mm at Station A to 16.0mm at Station B. In Figure 3.9, data from Table 3.2 are plotted to show clearly the spanwise differences in the form of the boundary layer velocity profile curves measured at Stations A and B. In Figures 3.9(a) and 3.9(b), (laminar and turbulent boundary layer flow respectively), the mean velocity profile is shown by the dashed line. The shaded area enclosed by solid lines either side of the mean represents the limits of spanwise profile variation recorded at these measurement stations and indicates that the spanwise characteristics of the developing boundary layer on the plate do not differ significantly at these two measurement stations. These measurements were repeated three times on separate occasions in order to assess the ability of the plate apparatus to replicate a given boundary layer flow regime. On no occasion were significant differences detected.

Strips of loose test material laid normal to the wind on the surface of the plate at any position between Stations A and B would, therefore, be exposed to virtually the same boundary layer flow regime along their entire width. Thus, in subsequent experiments it was necessary to measure only one boundary layer velocity profile in the

centre of the plate in order to determine the characteristics of the boundary layer across the entire width of the plate in any given location on the surface of the plate.

(b) Using flow visualization

The technique of surface flow visualization was best suited to the present study. In this, a mixture of four parts liquid paraffin and one part fluorescent pigment was applied to the leading edge of the plate using brush strokes normal to the airflow. Increasing the wind velocity over the surface of the plate caused the liquid paraffin/pigment mixture to be drawn back by friction. Photographs of the liquid paraffin/pigment layer taken with ultra-violet illumination created a permanent record for later inspection. In this investigation, the free stream wind speed was increased to $23.5ms^{-1}$ and was left at this setting for approximately half an hour. During this time, the liquid paraffin/pigment mixture was slowly drawn downwind across Station A and occupied the region most likely to be affected by flow separation. Figure 3.10 shows such 'visualized' flow patterns on the leading edge and the upwind portion of the working surface of the plate. As the patterns indicate the spatial distribution of surface shear stresses and, therefore, the approximate behaviour of the flow close to the surface, any tendency for the flow to separate on the leading edge would have been made clearly visible as an abrupt pattern boundary using this method. No such tendency was detected (Figure 3.10) provided the angle of the tail was correctly set.

3.5 Selection and initial preparation of experimental particles

In order to simplify the investigation of incipient motion on

the plate it was necessary to limit variations in the size, shape, density and surface characteristics of test particles. By careful control of these grain parameters, and by the use of carefully devised experiments, it was possible to assess the influence of a given grain property upon aeolian threshold values in the controlled and reproducible flow conditions associated with the developing boundary layer on the flat plate. Control of particle characteristics also permitted objective comparisons to be made of the threshold conditions associated with granular materials posessing different physical properties and shapes. After a thorough review of possible test materials, ballotini, aeolian sand, sugar crystals and salt crystals were selected as being the most appropriate.

3.5.1 Ballotini

Solid glass beads or 'ballotini' were found to have a number of advantages which rendered them ideal for use in this study. Ballotini were available in a wide range of sizes and their shape is stated as being within 85% of a true sphere over a large range of sizes (manufacturer's specification). Density variation, due to air inclusion, affected no more than 10% of the particles by volume and those affected particles had density values decreased by not more than 20%. Only 3% of all the particles were found to be broken or angular, and examination under a low power optical microscope showed their surfaces to be relatively smooth with only very slight ridges and pits. At a purely practical level two factors were important; (a) the availability in 25kg bags at a relatively low cost from a local supplier; and (b) the health hazard due to silicosis is negligible as no free silicates are present in ballotini (Military specification, MIL-G-9954A, for abrasive glass

beads). The supplied ballotini were characterised by a fairly wide range of sizes and careful sieving was required to give samples in quarter phi (ϕ) ranges [where $\phi = -\log_2(d_{mm})$] using standard laboratory sieves and Ro-Tap sieving machine. (In this study, particle sizes are generally referred to in micrometres (μm) as this enables direct comparisons to be made with the results of other workers (see Chapter 5)). Initially it was envisaged that the investigation would examine a large number of sizes. However, such an approach was considered to be impracticable given the limited time that the wind tunnel was available. Further, the need for additional studies to assess the effect of particle shape on aeolian thresholds using other selected materials (see below) necessitated the selection of a limited number of size ranges.

The ballotini sizes chosen for this study all fall within the particle size class termed 'sand' by Wentworth (1922). The sub-division of this class, recognised by Bagnold (1941) as 'aeolian sand', embraces the range from 710μm to 150μm. Table 3.3 shows ballotini sizes used in the experiments reported below, and their relationships to the general particle classification by size. Sized used were: 1.7-1.4mm; 710-600μm; 355-300μm; and 180-150μm. Also shown in Table 3.3 are the sand range (Wentworth, 1922) and the 'aeolian sand' sub-division (Bagnold (1941)). The 1.7-1.4mm ballotini fraction lies well outside the 'aeolian' range and would strictly be classed as very coarse sand, (even though Greeley et al. (1984) suggest grains larger than 4.00mm may move in surface creep). In a feasibility study this size fraction was found to be useful for visual assessments of the entrainment process and helped in the design of suitable experiments on the flat plate. It was also useful in extending the range of experimental particle sizes, and in the assessment of certain universal entrainment functions (Chapter 5).

Before undertaking any experimental work it was necessary to remove any broken or angular ballotini likely to affect the uniformity of a sample. By slightly inclining a large sheet of glazed paper and rolling material backwards and forwards it was possible efficiently to separate the near-spherical from the non-spherical grains. It was found necessary to repeat this process several times in order to remove most of the unwanted angular particles. The samples were then thoroughly washed in alcohol to remove any contamination likely to give rise to inter-particle cohesion, and were then oven dried at 110^{o}C for 24 hours. To reduce the likelihood of moisture absorbtion, samples were kept in a dessicator until required for experimental work.

3.5.2 Aeolian sand

Aeolian threshold values reported in the literature are often determined for natural aeolian sands and consequently the direct comparison between data derived from this study using ballotini and existing data sets published in the literature was not possible. To make this comparison possible aeolian sand was collected from sand dunes near Rye, Sussex. After careful washing to remove sea salt contamination and 'floating off' any light organic material, a 180-150μm aeolian sand fraction was separated by sieving to give a second test material.

3.5.3 Sugar crystals and salt crystals

The choice of suitable materials for the planned investigations into the effects of particle shape on incipient motion proved to be rather more problematic. As crystalline materials display a variety of characteristic shapes attention was given to finding suitable particles.

A wide variety of such particles was critically assessed and after careful consideration of several common crystalline materials, common salt crystals and sugar crystals were chosen. The salt had a roughly cubic crystal shape whilst sugar consisted of short prisms. Choice of these two materials was based on the relative simplicity and individuality of the crystal shapes. The sizes used in the study were obtained by sieving to give a 710-600μm range for sugar crystals and 180-150μm range for salt crystals. These size classes corresponded with ballotini ranges and permitted later comparisons between the different materials (see Chapter 5).

A summary of the granular test materials selected for use in this study is given in Table 3.4. In this table the size range, mean diameter, specific gravity and shape of the test materials are given.

3.6 Preparation of the 'rough' plate surface

In previous work on aeolian threshold conditions, a number of authors stress the need to develop boundary layer flows over a representative surface in the long run-up section of conventional 'aeolian' wind tunnels (e.g. Bagnold (1941), Belley (1964), Kadib (1965); see 1.1). Generally the same particles as those used in test beds are advocated as a 'lining' for the tunnel. In view of this convention and in view of the need to rest loose test particles upon a uniform surface of similar grains for support, it seemed logical to cover the entire plate surface with the material under investigation. By ensuring the particles were well secured on the surface of the plate, (i.e. the surface was non-erosive), it was possible to simulate a natural flat sediment bed that was unaffected by the wind. Loose test material placed

on this surface was thus supported by a granular bed with fairly regular geometric properties and was exposed to a developing boundary layer flow regime determined in part by the characteristics of the test surface on the plate.

Development of a suitable method of securing particles to the plate proved to be difficult. It was important to ensure that no single particle protruded above the mean bed level and that the particles were closely packed to provide similar support geometry for the erosive grains placed on top of them in subsequent investigations. Further, the method of adhesion should not produce any surface disturbances such as minor ridges or troughs as these would adversely affect the boundary layer development. In addition, the non-erosive particles on the surface of the plate should not retain any residual 'stickness' from the adhesion process that might adversely affect aeolian threshold values associated with the erosive grains.

A number of adhesives were tested in order to assess their particular suitability for the bonding of ballotini to the plate surface. Tests were conducted on 'off-cuts' from a large 6mm plate glass sheet using a range of ballotini sizes. Where necessary, adhesives were diluted with an appropriate solvent. The results of these trials are summarized in Table 3.5. In addition to the adhesives mentioned in this table, cellulose aerosol paint, cellulose model aircraft 'dope', aerosol lacquer and polyurethane varnish were also tried with varying degrees of success. By experimentation it was found that the adhesive side of 'contact' clear plastic film was extremely effective in securing loose granular materials. The film was available in lengths up to 20m and widths up to 0.45m, and its adhesive side was protected by a waxed paper

backing which could simply be peeled off when required. A technique was therefore developed in which the 'contact' film was secured to the surface of the plate with its adhesive side facing upwards. In this way, a flat, homogeneous bed of non-erosive particles could be created by removing the protective waxed paper backing and pouring granular material over the adhesive surface. This technique is described in detail below and illustrated by annotated photographs in Figure 3.11.

The glass working surface of the plate was painted black so as to achieve the maximum contrast between non-erosive and loose erosive grains on the plate under certain lighting conditions, (determined in a preliminary study). Prior to the application of the clear plastic film, the surface was 'keyed' using flour grade abrasive and thoroughly cleaned with alcohol, (Figure 3.11(a)). A role of clear 'contact' film was then cut to a length extending 180cm from the leading edge of the plate and was cleaned to ensure no particles adhered to its back surface. It was found by experience that even small particles trapped between the film and the glass gave rise to surface blemishes when the film was stuck down on the plate. Similarly, the plate surface had to be painstakingly checked for foreign debris. Any such blemishes on the plate surface would be likely to give rise to localised flow disturbance and may, therefore, have led to inaccurate determinations of threshold conditions.

The pressure tappings, tail section and plate support frame were carefully masked, and Scotch 'Spray Mount' aerosol adhesive was then applied to the leading edge and working surface of the plate in long sweeping strokes to give an even cover. 'Spray Mount' was found to be an ideal adhesive for securing the plastic film to the experimental plate surface as it allowed re-positioning of the film without any significant

loss of adhesion. This was particularly important during the last stages of the plate preparation when it was found necessary to lift the contact film from the plate surface and stretch it slightly to remove small wrinkles (see below). In addition, when it was necessary to prepare the surface of the plate with a different granular material, the 'contact' film was simply peeled off in single sheets and any residual 'Spray Mount' adhesive could be easily removed using white spirit. Before securing the 'contact' film to the surface of the plate, the Spray Mount was left for half an hour during which time the most volatile of the adhesive solvents evaporated. This was found to be necessary as the solvents affected the plastic film causing marked localized expansion which was manifest as small wrinkles which could not be removed by rolling.

After a suitable 'drying' period, the clear 'contact' film was rolled out along the plate, sticky side up. Great care was taken to ensure that bubbles of trapped air were removed by rolling using a rubber print roller (Figure 3.11(b)). After being in contact with the adhesive for approximately 24 hours, a slight overall expansion of the plastic film occurred caused by residual aerosol solvents. The minor ripples this produced were readily removed by lifting the plastic film clear of the plate and stretching it slightly. When laid down and rolled, a smooth flat surface resulted. The smooth, even expanse of the adhesive side of the plastic film was then revealed by carefully peeling off the waxed paper backing (Figure 3.11(c)). The chosen sediment was then spread across the surface and rolled down under a light pressure (Figure 3.11(d)). Excess was removed by tipping the plate and gently tapping the surface. Further rolling improved particle adhesion and packing. A close-up photograph of the geometric packing of test particles on the

plastic film is given in Figure 3.11(e).

The pressure tappings on the leading edge were uncovered and any other masking was removed. The plate was then installed in the wind tunnel and the tail elevation setting was carefully checked using the pressure tappings on the leading edge of the plate (see 3.2.3). Once the tail section was locked into position, the bare area around the pressure tappings was sprayed with Scotch 'Photomount' adhesive to secure the appropriate granular material to this local area. With this process completed, a continuous cover of non-erosive test material extended a distance of 180cm downwind from the leading edge.

Despite some difficulties during its development, this technique provided a highly satisfactory and effective means of producing a uniform, non-erosive granular surface. The applications of the technique are numerous and in Chapter 8 some possibilities for further research using this method are briefly discussed.

3.7 Flow on the 'rough' plate

The flow conditions on the surface of the rough plate were assessed initially using a surface prepared using 1.7-1.4mm ballotini. The prepared plate was installed in the working section of the wind tunnel and pitot-tube array 2 was used to measure the boundary layer velocity profiles at seven study sites downwind of Station A at a constant free stream velocity of $8ms^{-1}$. The results of this study are presented in Table 3.6. Data from Table 3.6 are illustrated in Figure 3.12 where dimensionless velocity ($\bar{U}/\bar{U}_\infty$) is plotted against height above the surface of the plate (Y).

The form of the resulting curves indicates that the boundary layer over this surface was turbulent at these measurement sites (see 2.5.1). Further, Figure 3.12 also shows that the boundary layer thickness δ increases significantly as the downwind distance from Station A increases (e.g. δ = 34mm and 70mm at 100mm and 700mm downwind from Station A, respectively). The rate of boundary layer thickening over this surface is much greater than that recorded on the smooth surface (3.4.4(a)) and reflects the considerable aerodynamic roughness associated with the 1.7-1.4mm ballotini. Spanwise measurements of the boundary layer velocity profile on this surface taken at 100mm and 700mm downwind of Station A did not reveal any significant variation in spanwise flow characteristics (data not given). A more detailed investigation of the developing boundary layer on the prepared surface of the plate is given in Chapter 4.

3.8 Summary

The design and construction of an experimental flat plate apparatus to be used in the study of aeolian entrainment thresholds is described. The plate was installed in a large blow-down wind tunnel and preliminary tests were conducted to assess the characteristics of the developing boundary layer on the upper surface of the plate. These included measurements of boundary layer velocity profiles at selected study sites and a flow visualization technique used to assess flow characteristics close to the leading edge of the plate. When the tail section of the plate was set at the appropriate angle, the boundary layer on the plate was shown to develop in a manner similar to that described in 2.2 and no significant spanwise variations in the developing boundary layer were detected at any of the study sites. Repetition of these

measurements showed that the boundary layer charactistics could be replicated at any chosen study site on the surface of the plate. The flow visualization study showed that flow separation did not occur in the critical region close to the leading edge of the plate, provided that the tail section angle was correctly set. Static pressure in the boundary layer was found to be constant over the majority of the length of the plate and thus validated the use in subsequent experimental studies of the momentum integral equation (2.6.3(c)) to determine shear stress at a given location on the surface of the plate. Further, the flow visualization study did not detect any anomalous cross-flows which, if present, would invalidate certain assumptions necessary for use of the momentum integral equation.

The careful selection and preparation of granular test materials for use in subsequent experiments limited the variability of grain characteristics normally associated with natural sediments and thereby simplified subsequent investigations. A special technique to secure these test materials to the surface of the plate was devised which used the adhesive side of 'contact' plastic film. Preliminary measurements of the boundary layer velocity profile at selected sites on a surface prepared using 1.7-1.4mm ballotini showed that the boundary layer developed in a manner similar to that described in 2.2 and no significant spanwise variation was detected. The surface of the plate prepared in this way produced a homogeneous and non-erosive flat sediment bed of contiguous particles with negligible permeability. As a result it provided a test surface which, when used in studies of aeolian threshold conditions, effectively reduced the number and complexity of interacting variables which had to be considered.

	Probe elevation above the surface of the plate (mm)	
Probe number	Pitot-tube array 1	Pitot-tube array 2
1	0.2	0.6
2	2.2	4.7
3	4.3	9.7
4	5.8	19.2
5	8.4	39.0
6	16.0	69.1
7	25.4	98.5

Table 3.1 Mean vertical elevation of pitot-tubes above the surface of the plate (mm), (see also Figure 3.6).

Table 3.2 Boundary layer velocity profile data over the smooth plate surface at Stations A and B at distances (mm) right (R) and left (L) of the plate centre (free stream wind velocity = $5ms^{-1}$).

(a)

Height above the surface of the plate	$\bar{U}/\bar{U}_\infty$ values at STATION A, (the junction between the leading edge and the working surface of the plate)				
y mm	300R	150R	CENTRE	150L	300L
2.2	0.62	0.58	0.70	0.61	0.60
4.3	0.97	0.97	0.98	0.96	0.98
5.8	1.00	1.00	1.00	1.00	1.00

(b)

Height above the surface of the plate	$\bar{U}/\bar{U}_\infty$ values at STATION B (1300mm downwind from Station A)						
y mm	300R	200R	100R	CENTRE	100L	200L	300L
2.2	0.38	0.41	0.35	0.53	0.37	0.46	0.43
4.3	0.60	0.63	0.55	0.71	0.54	0.64	0.63
5.8	0.69	0.72	0.68	0.81	0.65	0.75	0.74
8.4	0.82	0.87	0.81	0.90	0.78	0.87	0.87
16.0	1.00	1.00	1.00	1.00	1.00	1.00	1.00

φ	cm	μm		SIZE CLASS
-8.0	25.6	-		BOULDERS
-6.0 to -8.0	6.4 to 25.6	-		COBBLES
-1.0 to -6.0	0.2 to 6.4	-		PEBBLES
-1.0	-	2000		
-0.75		1700		
-0.50		1400		
-0.25	-	1180		
0.0	-	1000		
0.25	-	850		
0.50		710		
0.75		600		
1.00	-	500		SAND, after Wentworth (1922)
1.25	-	425		and Pettijohn et al. (1972)
1.50		355	AEOLIAN SAND, BAGNOLD (1941)	
1.75		300		
2.00	-	250		
2.25	-	212		
2.50		180		
2.75		150		
3.00	-	125		
4.00	-	63		
4.0 to 8.0	-	63 to 3.9		SILT
8.0 to 12.0	-	3.9 to 0.24		CLAY

BALLOTINI SIZE RANGES

Table 3.3 Size ranges of ballotini used in the flat plate study and their relation to sediment size classifications.

MATERIAL	SIZE, μm	MEAN DIAMETER $\bar{d}$, μm	SPECIFIC GRAVITY	SHAPE
Ballotini (soda-lime glass)	1700/1400 710/600 355/300 180/150	1550 655 328 165	2.51	Spherical
Sugar ($C_{12}H_{22}O_{11}$)	710/600	655	1.588	Prismatic (monoclinic)
Salt (NaCl)	180/150	165	2.164	Cubic
Aeolian sand (SiO_2)	180/150	165	2.650	Sub-angular/ sub-rounded

Table 3.4 Summary of test material properties.

Table 3.5 Adhesive trial summary.

Adhesive	Ballotini size	Comments
Evo-stick "clear" diluted with xylene	710/600μm and 355/300μm	The necessary dilution produced a volatile mixture with poor adhesive properties. Where firm adhesion occurred, however, particles tended to be grouped and thereby created an uneven surface.
Evo-stick "regular" diluted with xylene	710/600μm	The diluted adhesive was easy to apply but bond strength was poor and adhesion was generally rather patchy.
Araldite Rapid diluted with xylene	710/600μm and 355/300μm	Araldite was readily dissolved in xylene but adhesion was found to be weak despite an even surface finish.
RS components water soluble contact adhesive	710/600μm and 180/150μm	This adhesive gave satisfactory surface bonding and grain packing. However, brush application tended to produce ridges in which grains projected above the mean bed level.
Scotch photo-mount spray	355/300μm and 180/150μm	This aerosol adhesive provided strong bonding and even grain cover on the surface of the plate. However, the prepared surface remained slightly tacky despite a long period of drying and was, therefore, unsuitable for the present study. A further drawback was the high cost of this adhesive.
Gloy studio gum diluted with white spirit	355/300μm	Poor adhesion and a tendency for particles to clump together makes this adhesive wholly unsuitable.

Table 3.6 Boundary layer velocity profiles ($\bar{U}/\bar{U}_\infty$) on 1.7-1.4mm ballotini at distances (x) along the plate, measured using pitot-tube array 2. ($\bar{U}_\infty = 8.0 ms^{-1}$).

Height y	Distance downwind from Station A, x, (mm)						
mm	100	200	300	400	500	600	700
4.7	0.56	0.52	0.50	0.46	0.43	0.41	0.37
9.7	0.70	0.66	0.62	0.59	0.55	0.52	0.50
19.2	0.88	0.84	0.79	0.75	0.72	0.68	0.65
39.0	1.00	1.00	0.99	0.98	0.95	0.90	0.87
69.1	-	-	1.00	1.00	1.00	1.00	1.00

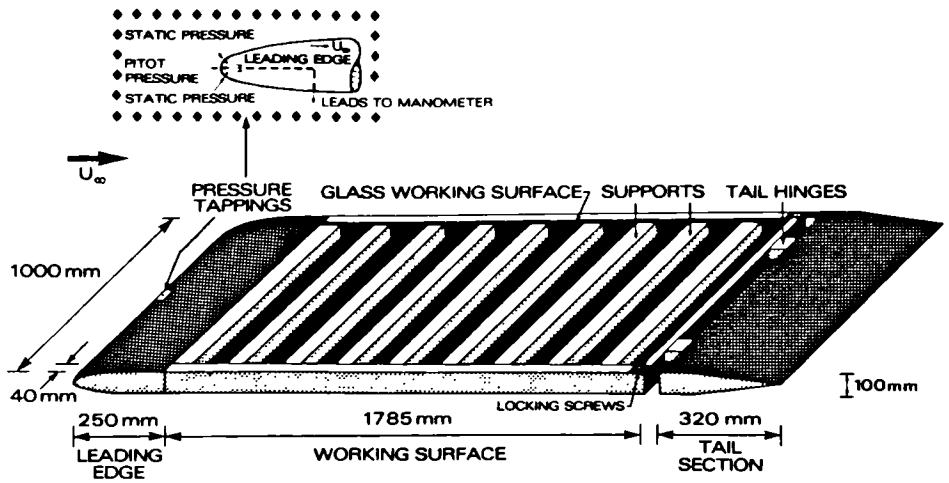

Figure 3.1 Experimental flat plate.

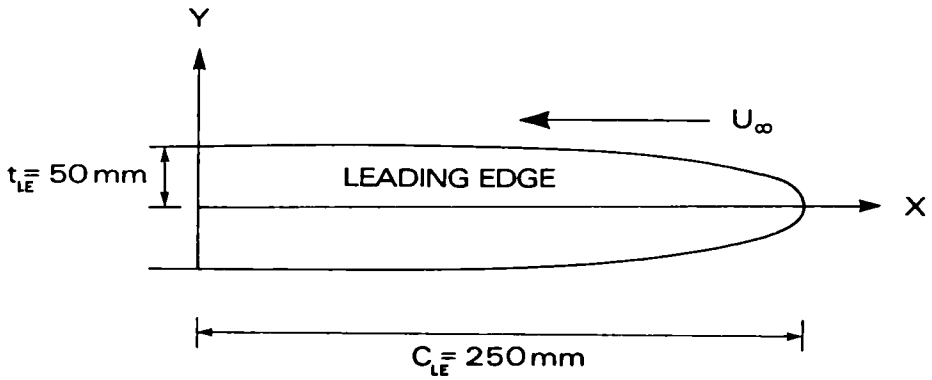

$$y = t_{LE}\left[1 - \left(\frac{X}{C}\right)^{3}_{LE}\right]^{1/2}$$

Figure 3.2 Leading edge of the plate.

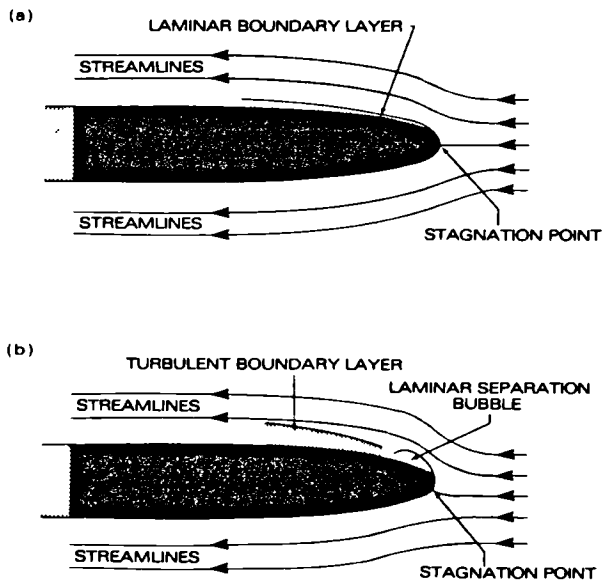

Figure 3.3 Flow on the leading edge of the plate.

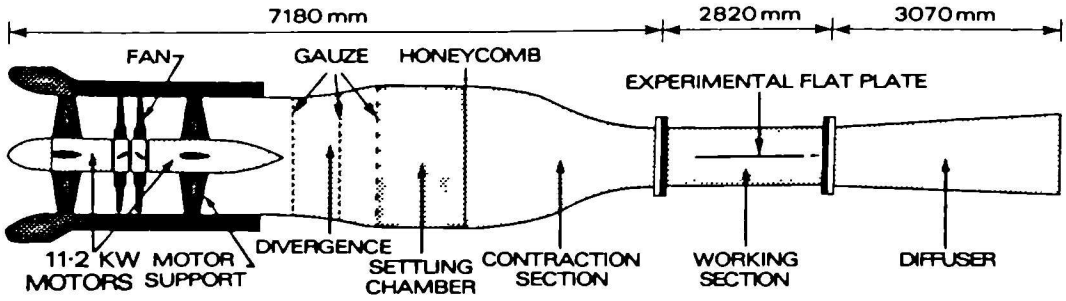

(a) Side elevation; dimensions and components.

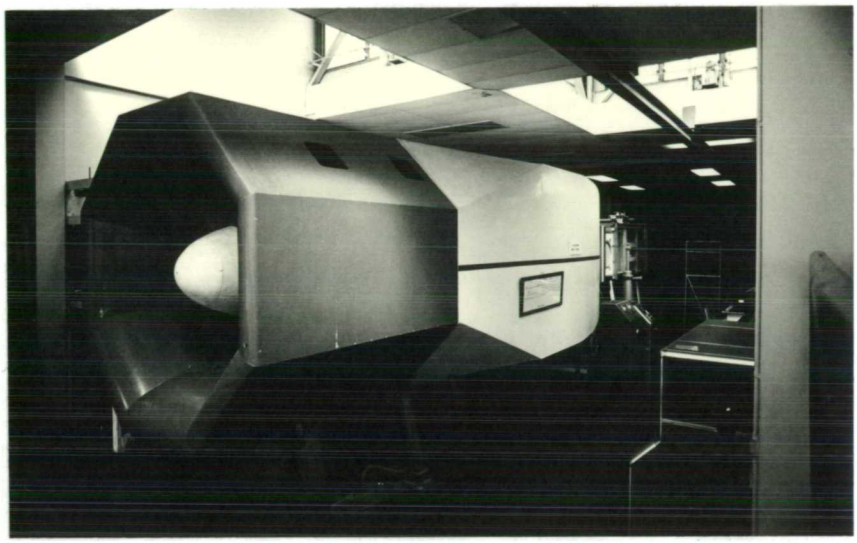

(b) View from tunnel intake.

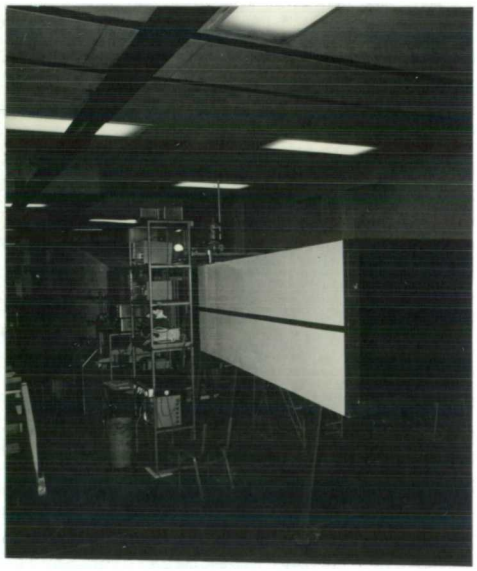

(c) View from diffuser exhaust.

Figure 3.4 Blow-down wind tunnel.

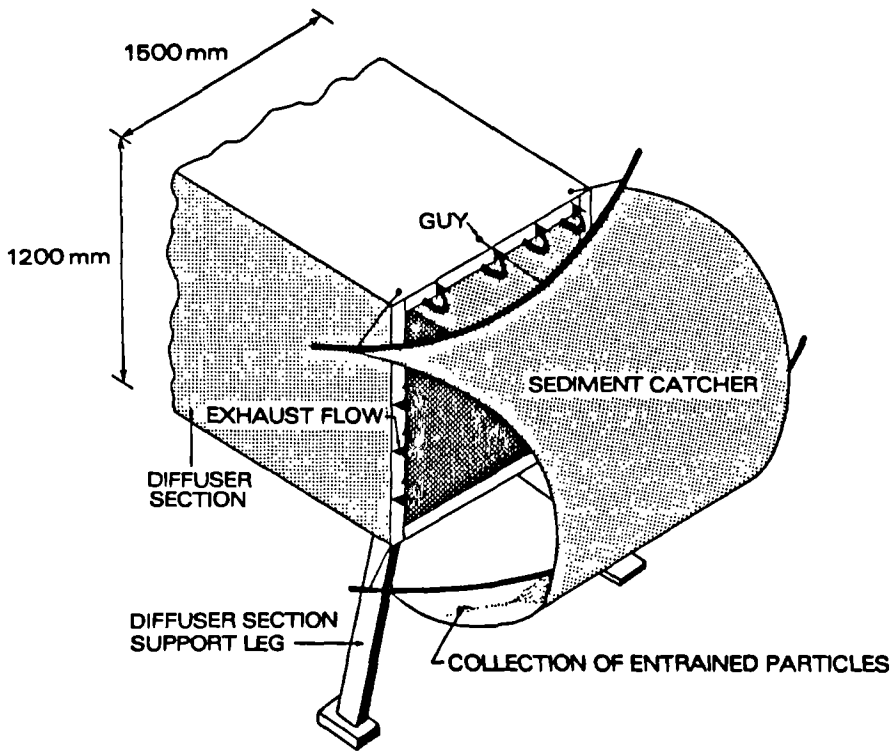

Figure 3.5 Sediment catcher.

Figure 3.6(a) Pitot-tube arrays

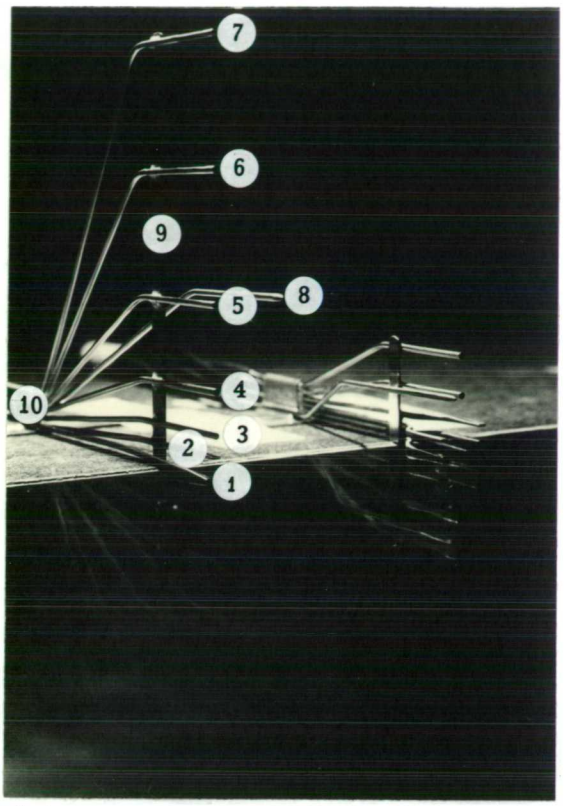

(i) Pitot-tube array 1 (right) and 2 (left)

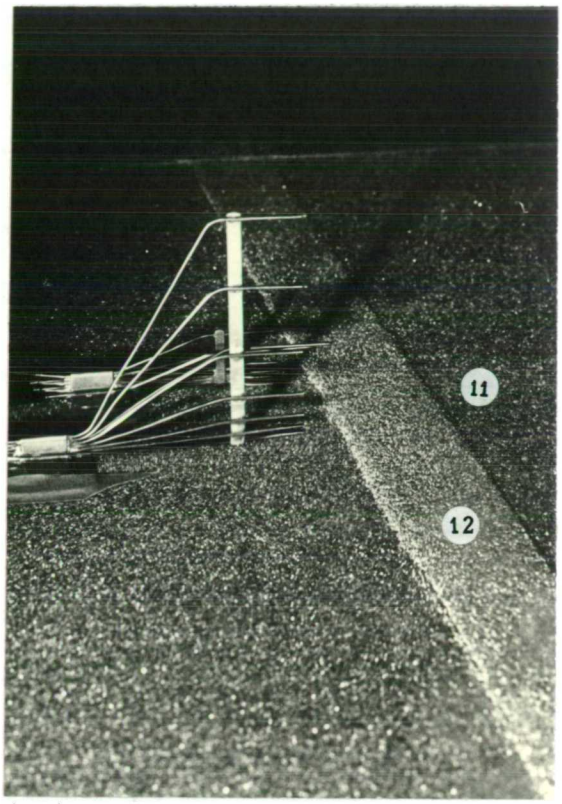

(ii) Pitot-tube arrays behind a strip on the plate

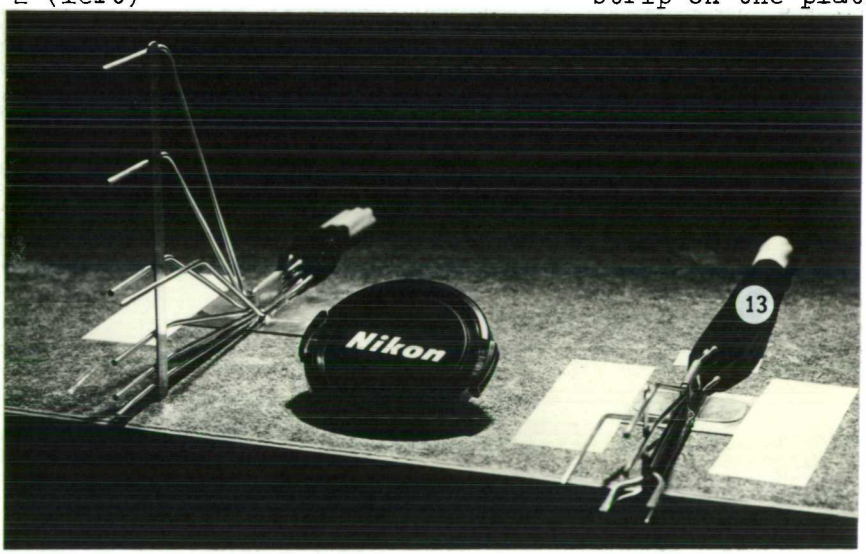

(iii) Pitot-tube arrays 1 (right) and 2 (left)

Legend

1 to 7	Pitot-tubes of pitot-tube array 2 (heights in Table 3.1)
8	Static pressure probe
9	Support column
10	Support base
11	Working surface of the plate covered with 710-600µm ballotini
12	Erosive strip of 710-600µm ball tini
13	Leads to multi-tube manometer (see Figure 3.6(b))

Figure 3.6(b) Multi-tube manometer.

(i) General view.

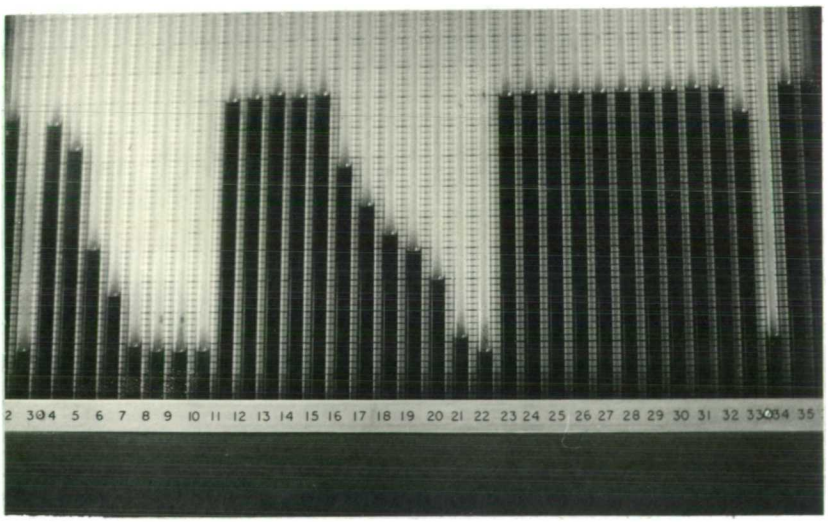

(ii) Typical boundary layer velocity profiles recorded using the multi-tube manometer. (Columns 4 to 10 and 16 to 2 are connected to pitot-tube arrays 2 and 1, respectively. Columns 11 and 3 record static pressure in the boundary layer).

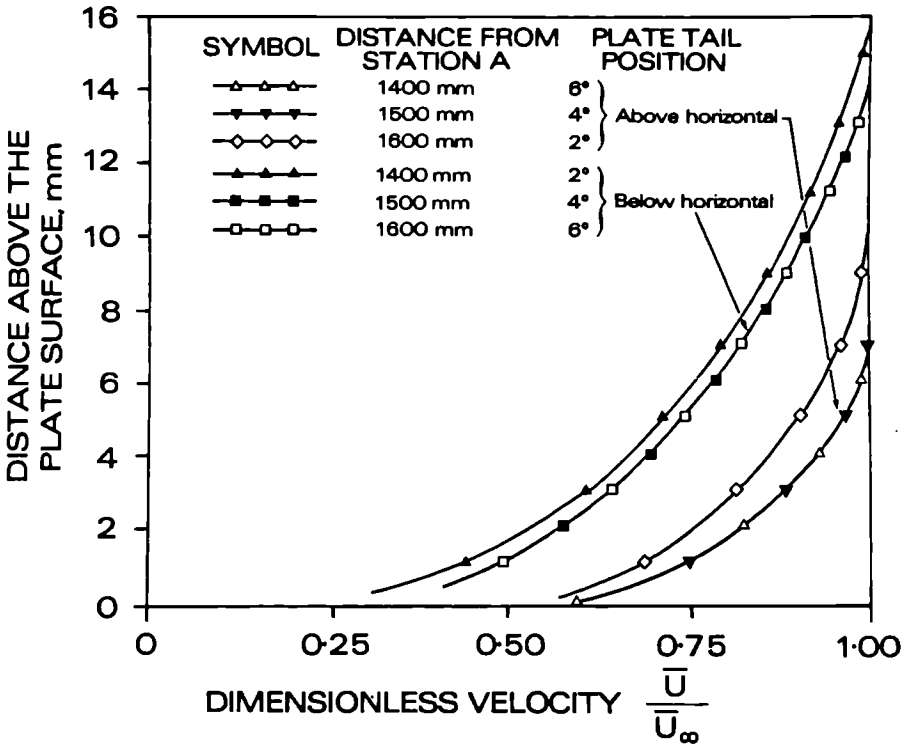

Figure 3.7 Effect of tail elevation on the boundary layer velocity profile.

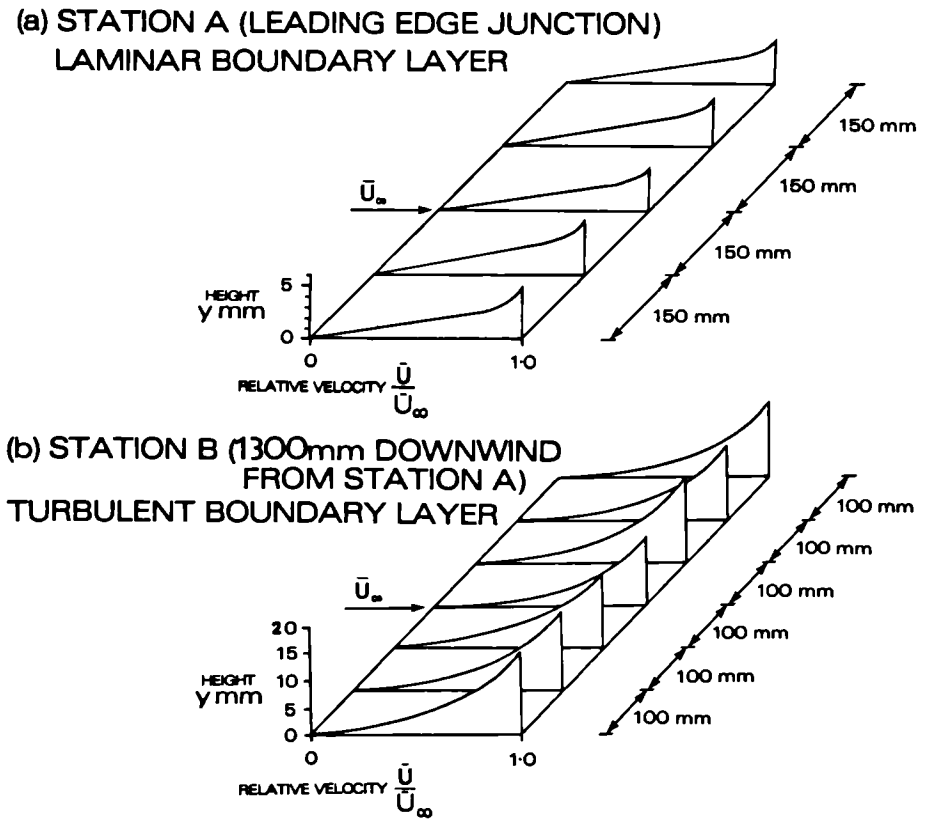

Figure 3.8 Boundary layer velocity profiles at Stations A and B on the 'smooth' plate surface.

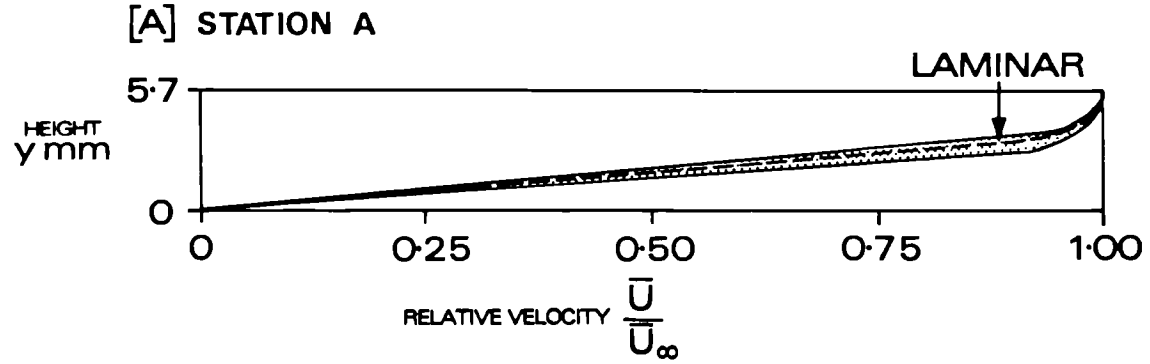

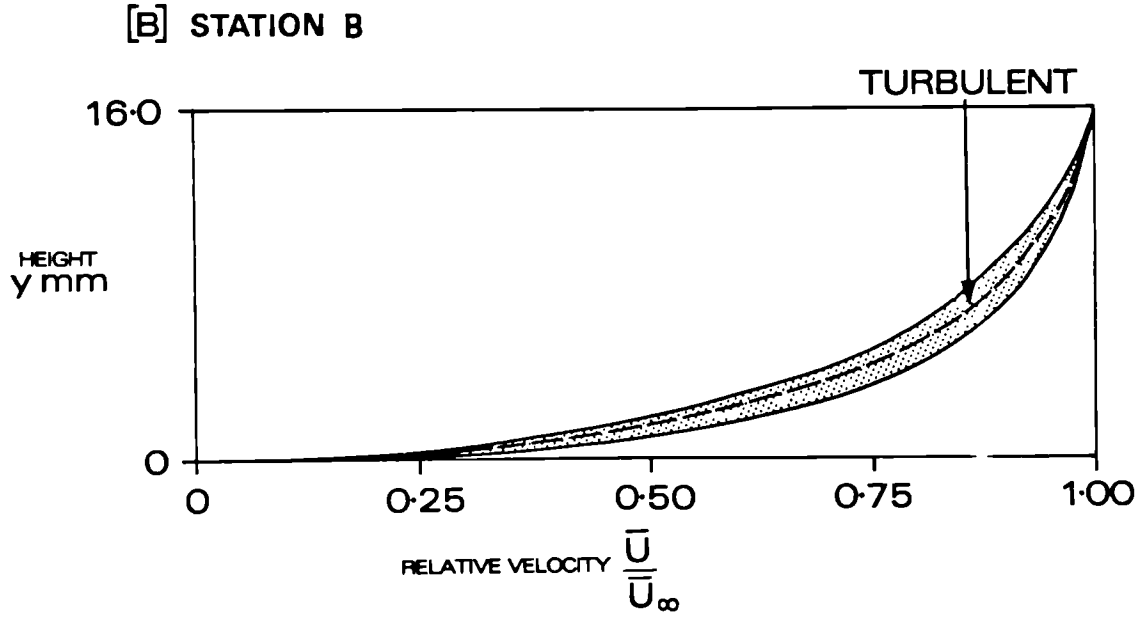

Figure 3.9 Boundary layer velocity profiles at Stations A and B on the 'smooth' plate surface.

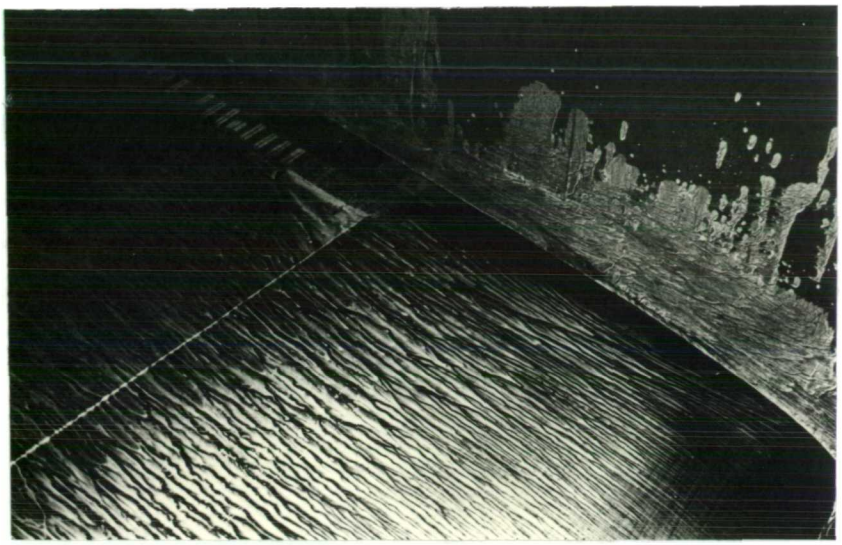

(a) Pattern on the right of the leading edge.

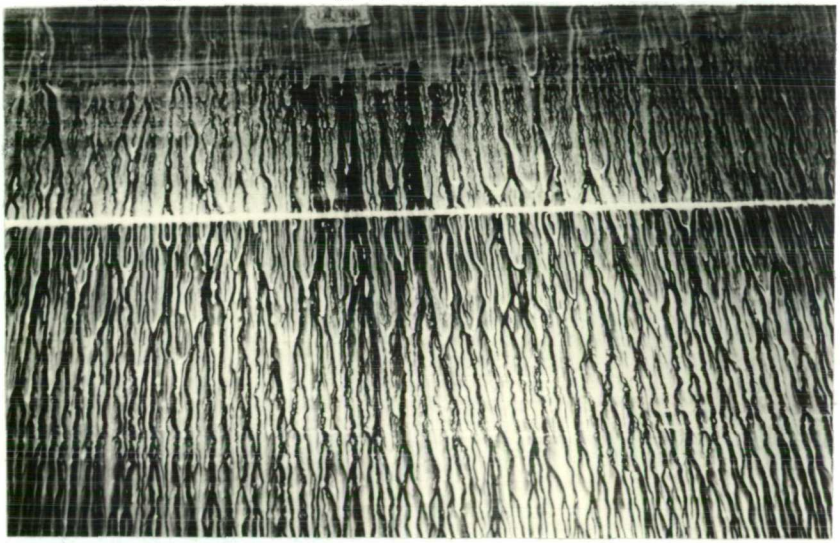

(b) Pattern in the centre of the leading edge.

(c) Pattern on the left of the leading edge.

Figure 3.10 Fl w visualization on the leading edge of the plate using liquid paraffin and flu rescent pigment (U.V. illumination, $\bar{U}_\infty$ = 3.5ms^{-1}).

Figure 3.11 Preparation of the surface of the plate.

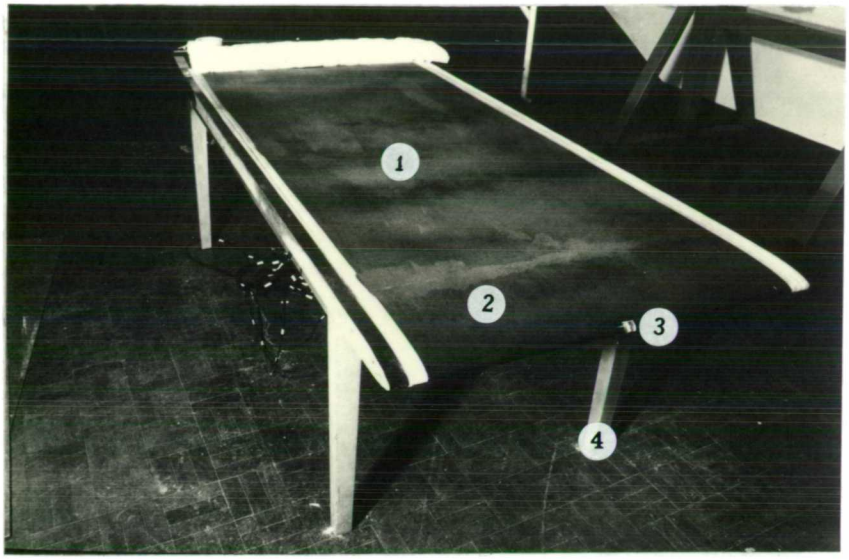

1 Working surface.
2 Leading edge.
3 Pressure tappings.
4 Table to support the plate.

(a) The plate prior to the application of the aerosol adhesive.

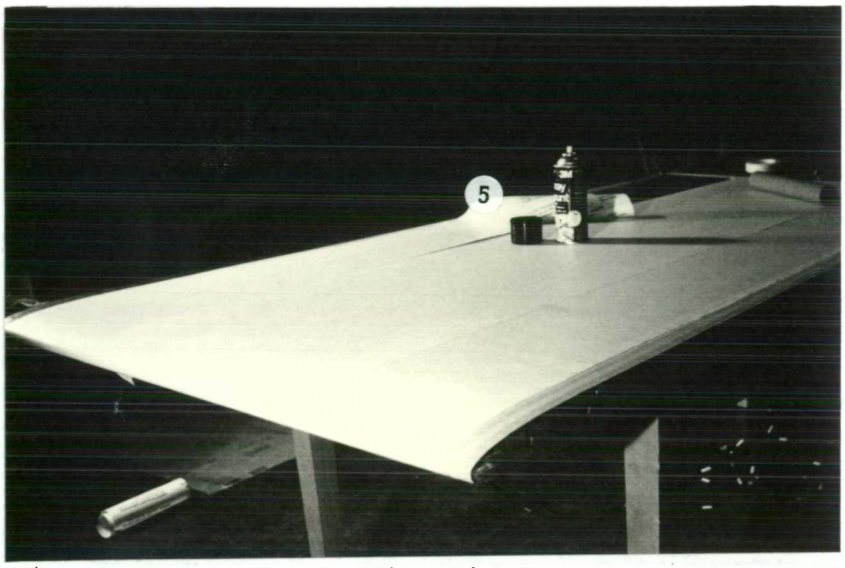

5 'Contact' plastic film on the plate (waxed paper backing still in place).

(b) 'Contact' plastic film fixed to the surface of the plate, sticky side up (waxed paper backing still in place).

6 'Contact' plastic film on the plate (waxed paper backing removed).

(c) Exposed adhesive side of the 'contact' film bef re test material was poured n.

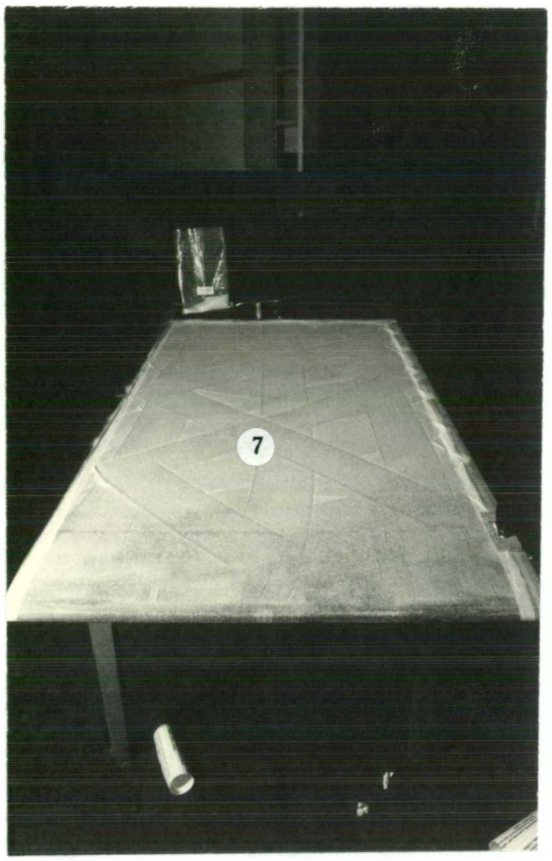

7 Test material

(d) Test material spread out on the surface of the plate (the excess was removed by tipping the plate)

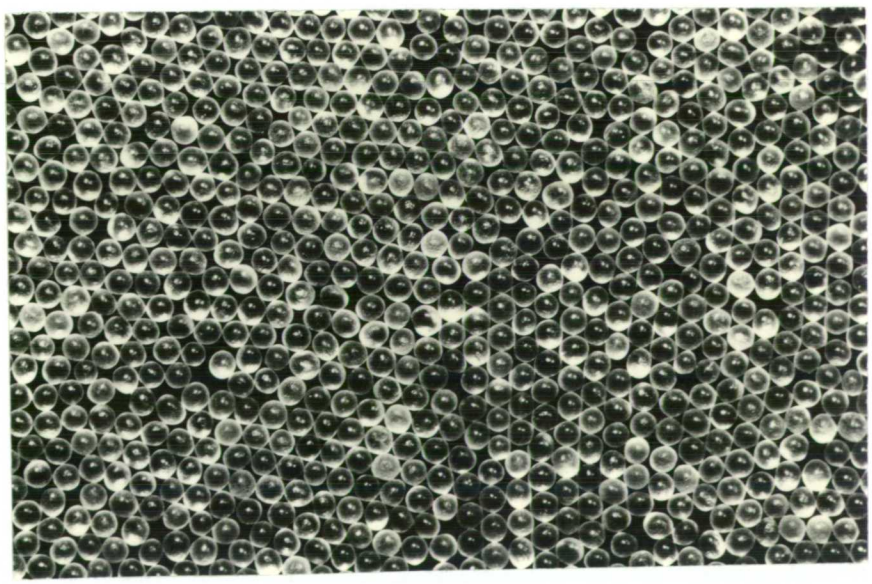

(e) Close-up of the prepared surface of the plate (700-600 μm ballotini)

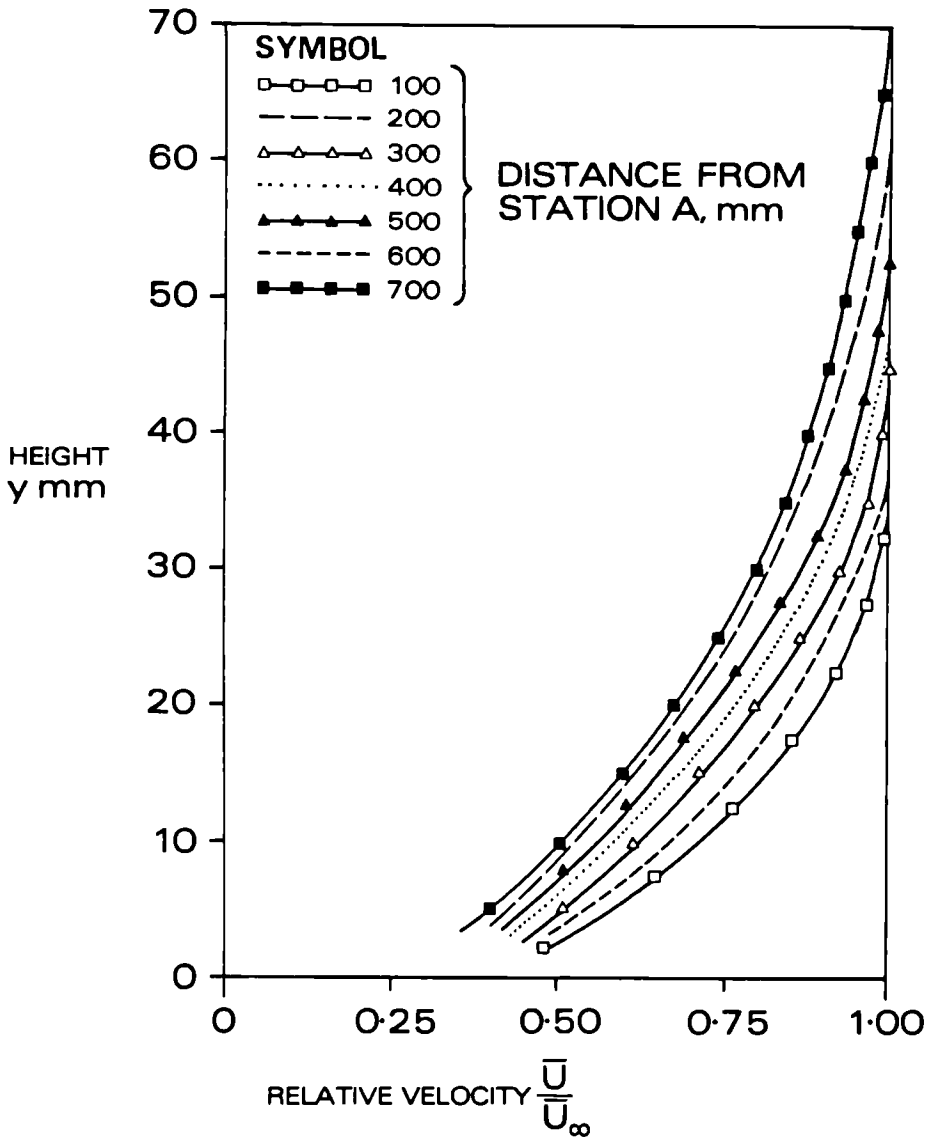

Figure 3.12 Boundary layer velocity profiles on 1.7-1.4mm ballotini at seven stations on the surface of the plate

CHAPTER FOUR

Aeolian thresholds in a developing boundary layer

4.1 Introduction

This Chapter reports a systematic investigation of aeolian entrainment thresholds and entrainment processes using the experimental plate and the range of non-cohesive particles described in Chapter 3 (ballotini, aeolian sand, sugar crystals and salt crystals). The experimental investigations were principally designed to assess the relative significance of the three factors identified in Chapter 1 as being the major contributors to inconsistency and ambiguity in reported values of aeolian entrainment thresholds. These are: the characteristics of the boundary layer flow; the characteristics of the aeolian grains; and the definition of aeolian threshold conditions.

The surface of the plate was covered with a selected material and installed in the blow-down wind tunnel (see 3.6). A narrow strip of the same material was then laid across the surface of the plate close to the junction between the leading edge and the working surface (Station A), and a photograph was taken of this initial strip configuration through a perspex window in the working section roof. The wind velocity was then gradually raised until the entrainment of a few grains occurred. Boundary layer wind velocity profile measurements were then taken to record the local mean threshold flow conditions near the strip at this wind velocity.

Increasing the wind velocity a little more, and allowing the ensuing entrainment of particles from the strip to proceed for a standard 10 minutes, gave rise to the erosion of a portion of the strip. During this erosion time further boundary layer wind velocity profile measurements were taken and visual observations of the entrainment

processes were made. A second photograph of the strip was then taken to record the amount of material removed by the wind at this velocity. Additional increase in the wind velocity resulted in further erosion of the strip during the standard 10 minute erosion time and gave rise to a second strip erosion stage. Subsequent increases in the wind velocity resulted in progressively greater erosion of the strip until after seven or eight stages, little or none of the original strip remained on the surface of the plate. This technique thus provided a photographic record of sequential strip erosion and details of the local boundary layer wind velocity profiles at each erosion stage. The loss of material from the strip was found by analysing the photographs, and the local shear stress was calculated from the boundary layer wind velocity profile data using the momentum integral method (2.6.3(c)). In addition, the analysis of the wind velocity profiles also provided a number of useful parameters to describe and classify the local boundary layer flow regime in the vicinity of a strip. In this way a known degree of strip erosion was related to a known local shear stress and boundary layer flow regime on the plate.

Owing to the changing characteristics of the boundary layer downwind from the leading edge of the plate, (see 2.2), it was possible to study aeolian entrainment thresholds in a range of different flow regimes simply by placing strips of loose material on the surface of the plate at selected distances downwind of the leading edge. The role of boundary layer flows in aeolian entrainment thresholds was assessed in this way using the range of test materials. The problems associated with defining the aeolian entrainment threshold objectively were overcome by considering the range of mean local shear velocities required to erode a strip, thereby accounting for the variations in particle characteristics

and individual grain exposures within a given strip of material. In doing so, it was no longer necessary to detect the motion of the first few grains and the errors associated with incorrect identification of a defined degree of particle movement were eliminated. In the event, the analysis of strip erosion sequences proved to be particularly informative and made it possible to suggest an objective definition of aeolian threshold conditions that depended not only on the properties of the particles themselves but also on the characteristics of the local boundary layer. To aid the analysis of the experimental data, the flow conditions at the scale of single grains were assessed theoretically using an appropriate scaling factor to describe grains at the threshold of motion in relation to dimensionless wind velocity distributions for laminar and turbulent boundary layers. Using these results it was then possible to infer the likely threshold flow conditions at strip sites on the plate.

The wind velocity values derived from pitot-static pressure measurements represent mean values in the boundary layer ($\bar{U}$) and in the free stream ($\bar{U}_\infty$). Similarly, the momentum integral method, used to calculate surface shear stress τ, (and hence shear velocity $U_*, (\tau/\rho)^{1/2}$) also gave mean shear velocity values ($\bar{U}_*$). In the context of aeolian thresholds in transitional and turbulent boundary layers it is crucial to distinguish between $\bar{U}_*$ and its randomly fluctuating instantaneous component, U_{*_I}. (This is unnecessary in laminar boundary layers as the shear velocity is constant). Throughout this chapter only mean shear velocity is considered as it was not possible to measure directly the fluctuating component of shear velocity. In this present study, it was found that a range of $\bar{U}_*$ values was required to erode completely a given test strip on the plate,

and thus it was necessary to distinguish between the minimum, maximum and average shear velocity values associated with strip erosion. As these $\bar{U}_*$ values are associated with varying amounts of aeolian entrainment, they are given the conventional subscript T to indicate threshold conditions. Hence the first grains to move in a strip are characterised by a value $\bar{U}_{*T(min)}$ and the most resistant grains (i.e. the last to be entrained) are associated with a value $\bar{U}_{*T(max)}$. In later data analyses, it was also found useful to refer to the threshold shear velocity associated with the entrainment of 50% of the strip material ($\bar{U}_{*T(50)}$), the arithmetic mean of all the threshold shear velocities associated with erosion of the test strip material ($\bar{\bar{U}}_{*T}$), and similarly, the arithmetic mean of all the free stream wind velocities ($\bar{\bar{U}}_{\infty}$). For clarity, each of these new terms are introduced again at the appropriate point in the text below.

4.2 Experimental procedure

The surface of the plate was covered with one of the materials shown in Table 4.1 using the plate surface preparation technique described in 3.6. The plate was then installed in the wind tunnel and the diffuser section, previously removed to allow access to the working section, was replaced. The sediment catcher was attached to the diffuser exhaust by means of guy ropes (Figure 3.5). Before starting experimental work, the pressure tappings on the leading edge of the plate were checked to ensure the correct adjustment of the tail (3.2.3 and 3.4.2). Using the same material as that on the surface of the plate, a narrow strip (4cm wide) of loose particles was laid across the plate using the technique described in Appendix A2 - see Figure 4.1(a) normal to the wind direction at the selected study site. Great care was taken to ensure the

strip was as uniform as possible, particularly regarding the projection of individual grains above the general strip surface. This task became increasingly difficult for particles smaller than the 600μm. However, it was found that repeated careful rolling gave a uniform and consistent strip with similar geometric properties regardless of the particle size.

Before describing in detail the experimental procedure used to erode the test strips, it is necessary to describe the techniques devised for photographing the strip of particles on the surface of the plate. In addition, it is also necessary to describe use of the pitot-tube arrays (3.4.1) in the measurement of the boundary layer velocity profile above the test strip.

4.2.1 Photography of the strips

To ensure maximum definition and contrast between the test strip and the underlying surface in the final photographs, a number of lighting arrangements were assessed experimentally. Overall illumination was found to give an unsuitable, low contrast negative image in which it was difficult to discriminate between the strip and the plate base layer. It was found that low angle illumination from a strip floodlight positioned inside the tunnel near the leading edge of the plate, lit both the front edge and top of the strip when directed along the plate surface. In this case the rear edge of the strip was defined by a narrow shadow region. Using such lighting conditions it was then possible to produce a negative in which the strip was clearly visible. The use of coloured filters on the camera lens was tried in an attempt to improve contrast but was not found to enhance picture quality significantly. Filters were not used, therefore.

It was necessary to raise the floodlight through the bottom access hatch of the working section for each photograph of the strip. The floodlight was then removed before continuing with the next run. For successful photography, the floodlight needed to be raised half a metre into the working section using a tall light stand. Manoeuvring the light stand in and out of the working section was awkward at first but became easier with practice. As it was only possible to gain access to the working section from below, exact adjustment of the lighting angle was achieved by observing the loose particle strip from above using a mirror. Horizontal and vertical floodlight adjustments could then be made easily to provide optimum lighting conditions for a given strip position on the plate surface.

An Olympus OMlN body with Zuiko 50mm f1.4 lens was used in all the photography. The camera was mounted on a tripod and positioned on top of the wind tunnel working section. In this position photographs could be taken through a perspex window in the tunnel roof. It was essential to ensure planimetric accuracy as the photographs were later used in the calculation of strip area. Accurate film plane alignment was achieved using two spirit levels to make horizontal and vertical adjustments of the camera axes.

4.2.2 Boundary layer wind velocity profile measurements

In order to calculate the local surface shear stress in the vicinity of a strip using the momentum integral method (2.6.3(c)), it was necessary to record detailed velocity profiles above the surface of the experimental plate at positions corresponding to the strip sites. The pitot-tube arrays and a multi-tube alcohol manometer described in 3.4.1

were used to take these measurements. To obtain a satisfactory resolution two pitot-tube arrays were used, one giving fine velocity resolution in the lower levels of the boundary layer and the other able to measure velocity up to 98.5mm above the surface of the plate. Preliminary tests conducted using a pitot-static probe at the rear of the plate and the 'roughest' surface (i.e. 1.7 - 1.4mm ballotini) showed that free stream velocity was attained at vertical distances less than 50mm above the plate at threshold velocities. As the thickness of the boundary layer would not exceed this value over the other test surfaces at threshold velocities, this preliminary measurement confirmed that the topmost probe in the array would always indicate free stream wind velocity.

It was essential that the wind velocity profiles recorded by the pitot-tube arrays were representative of flow conditions in the vicinity of the strips, and that the flow around the pitot-tube arrays did not interfere significantly with the entrainment of grains. Therefore, the siting of the probes was investigated carefully and two possible sites were assessed. These were (i) just upwind of the strip, and (ii) just behind the strip. Although the surface probe gave unuseable readings behind the strip due to strip wake interference, the probe at 2.2mm (pitot-tube array 1) gave virtually the same velocity reading whether upwind or downwind of the strip. Although the pitot-tube arrays gave virtually the same readings when located in either position, the disturbance to the strip when they were located upwind was considered unacceptable. In the event the loss of surface probe readings was considered unimportant as their reliability when taken on the 'rough' plate surface was poor due to local shelter and exposure effects behind grains on the plate. Loss of these surface velocity measurements was not

found to compromise the accuracy of the shear stress calculations. The pitot-tube arrays were accordingly sited just behind the strip.

4.2.3 Erosion of test strips

A strip of test material was laid across the plate near the leading edge (usually at 10cm from Station A) and pitot-tube arrays were positioned centrally just behind its downwind edge. The strip floodlight was then raised into the working section from below and adjusted to give the best possible illumination. A Gossen spot light meter was then used to take a number of light intensity measurements at various positions on the strip and these were used to calculate an average exposure value. As depth-of-field was relatively unimportant in this case, fairly wide lens apertures were chosen (typically f2.8) to ensure a shutter speed of at least 1/250 second and thereby minimise the risk of camera shake. As it was essential for later analyses that the photographs were sharp, the short exposure time was found to be a necessary precaution, despite the firm tripod support.

After checking the alignment of the camera axes, photographs of the particle strip were taken through the perspex window in the tunnel roof. To give a choice of negatives at the printing stage, bracketed exposures one stop either side of the averaged meter readings were taken. The floodlight was then removed and the cover over the bottom tunnel access hatch was secured in place. Working section velocity was then gradually raised in small increments whilst visually observing the strip through the perspex window. The necessary illumination for these observations was provided by a theatrical light directed through a small side window in the working section. At a certain velocity a few

particles were seen to oscillate sporadically. (In the case of particles smaller than 355μm, it was found necessary to use a small telescope to view the details of oscillation through the perspex window in the roof of the working section). A further small increase in velocity resulted in the entrainment of a significant number of particles from the strip. A ten minute period of erosion was given at this velocity setting, during which time average boundary layer wind velocity profile measurements were taken and the tunnel reference pressure was recorded using a Betz manometer. The adoption of a standard ten minute period of erosion was based on observation of an eroding strip in an early feasibility study in which it was noted that after ten minutes at a given wind velocity, erosion had effectively ceased.

The velocity in the working section was then reduced to near zero and the floodlight was re-installed and adjusted. The strip, now showing the first signs of erosion, was then photographed. The floodlight was again removed and the wind velocity in the working section was increased to a value slightly higher than the previous one. This resulted in the entrainment of additional particles from the strip over the ten minute erosion period to give a second erosion stage. Average boundary layer wind velocity profiles and tunnel reference pressure measurements were taken again during this erosion period and, after reducing tunnel velocity and re-installing the floodlight, this second erosion stage was also photographed. The procedure was repeated until little or none of the strip remained on the surface of the plate. Generally this involved six or seven erosion stages per strip. Data collected for a single strip therefore comprised: 1) average boundary layer velocity profiles corresponding to a defined erosion stage of the strip; 2) a photographic record of the erosion sequence; and

3) detailed visual observation of the entrainment processes.

A second strip of particles was then laid across the surface of the plate (usually at 25cm from Station A) and the above procedure was repeated. The erosion of further strips was then recorded at successive distances downwind of Station A. As noted in 3.4.3 above, the furthest downwind distance used was 130cm from Station A. A summary of this experimental procedure is illustrated in Figure 4.1(b).

The plate was then removed from the tunnel and its surface covering was stripped. The leading edge and glass working surface were cleaned with white spirit and alcohol to remove any residual spray mount adhesive. The plate was then re-covered with a different material and was re-installed into the working section of the wind tunnel. The procedure of strip erosion described above was then repeated using this new material. Strip positions on the plate were chosen to correspond with the previous runs. The experimental investigation proceeded in this way using all the test materials and strip positions given in Table 4.1. In some cases, noteably the investigations of aeolian thresholds using 180-150μm ballotini, the number of strip positions examined was increased to provide more detailed information in regions of suspected laminar and transitional flow on the surface of the plate.

4.3 Data extraction and reduction

The experimental investigation of aeolian entrainment thresholds using strips of test material on the plate produced a considerable amount of data in two forms: (a) a photographic record of strip erosion sequences; and (b) boundary layer velocity profile data in the form of

pitot-static pressure measurements. It was necessary, therefore, to extract and reduce the relevant data to provide a manageable quantity of information in a suitable form. This involved: (a) photographic processing of the films; (b) data acquisition from the photographs; and (c) the calculation of surface shear stress and other information boundary layer parameters using the boundary layer velocity profile data. A diagrammatic summary of data acquisition and extraction techniques used in this study is given in Figure 4.1(b).

4.3.1 Photographic processing

The quality of the erosion data ultimately derived depended greatly upon the quality of the photographs from which measurements were to be taken. Much time was therefore devoted to the trials of various photographic materials and processing techniques before the optimum method was selected. Ilford FP4, a medium speed, panchromatic black and white negative film, was used for most of the photographic work. Where lighting conditions were less favourable, such as at the rear of the plate, Ilford HP5 was used and rated at between ASA/ISO 500 and 800 depending on the local light intensity. This increase in film speed ensured that the exposure time was never more than 1/250 second. A detailed account of film processing and negative printing is given in Appendix A3.

4.3.2 Photographic interpretation and data extraction

In general, the strips were clearly visible on the final photographs and their outlines were carefully traced onto dimensionally stable 'estar' drawing film using a 0.2mm ink pen. Under some lighting

conditions (generally encountered at the rear of the plate), the contrast between the strip and the plate base layer on the print was poor and before tracing it onto the drawing film, it became necessary to enhance the strip outline on the photograph using a fine ink pen. It was not uncommon to reject prints at this stage if it was not possible to discriminate accurately between the strip and the base layer. In such cases this problem was usually overcome by reprinting the negative on Ilford 'Ilfospeed' grade 6 paper which gave the maximum possible contrast from a given negative. In special cases, however, poor contrast negatives were contact printed onto lithographic film to produce a straight black and white image, (see Appendix A3).

The area of the strip remaining was found by placing the tracing of the original enlarged photograph onto metric graph paper and manually counting the number of enclosed millimetre squares. The area values were then expressed as a percentage of the uneroded strip area, thus permitting comparison of the relative erosion losses of the various materials in strips at different positions on the surface of the plate.

4.3.3 Calculation of surface shear stress

The technique used to calculate the surface shear stress associated with a strip erosion stage at a given position on the surface of the plate was derived from a form of the momentum integral equation described in 2.6.3(c). Use of this equation required that the pressure gradient along the plate was zero and that no cross-flow occurred on the surface of the plate. Verification that these conditions were met has been given in 3.4 and 3.7.

The pressure measurements taken using the pitot-tube arrays were converted to mean wind velocities so that the local boundary layer mean velocity profile of the boundary layer could be plotted. Owing to the large number of measurements taken during the experimental study, some time was saved by using the computer program given in Appendix A1 to calculate wind velocity from pitot-static pressure measurements. The effects of changes in air temperature and pressure during the experimental runs were accounted for in this program. In addition, correction was also made for the changes in the density of the manometer fluid (alcohol) caused by air temperature variations during the various experimental runs. In general air temperature and pressure varied between $\pm 5^{o}C$, and $\pm 70mb$ respectively.

A summary of the computational procedures used to obtain surface shear stress values is given in Figure 4.2. Mean free stream velocity, $\bar{U}_{\infty}$ above the plate was measured by the pitot probe stationed at 98.5mm above the surface (Pitot-tube array 2). Using this value, the boundary layer velocity profile measurements were reduced to the dimensionless form $\bar{U}/\bar{U}_{\infty}$. The $\bar{U}/\bar{U}_{\infty}$ values were then plotted against height (y) above the surface to give boundary layer velocity profiles similar to those illustrated in Figure 4.2(a). The $\bar{U}/\bar{U}_{\infty}$ against y plots defined the boundary layer thickness δ and were used to determine the boundary layer displacement thickness δ^*. The displacement thickness is defined as

$$\int_{y=0}^{y=\delta} (1-\bar{U}/\bar{U}_{\infty})dy$$

(equation 2.22) and is graphically represented in Figure 4.2(a) as the area beneath the dimensionless velocity profile curve. This area was found by counting the number of graph squares beneath the curve and

applying an appropriate scaling factor. Strictly speaking it is generally unnecessary to calculate the boundary layer displacement thickness to determine the shear stress by the momentum integral method. In this case, however, the displacement thickness proved to be a useful parameter for assessing certain boundary layer characteristics on the plate and is discussed in more detail in 4.5.1(c) and 4.5.2.

Using the graph of $\bar{U}/\bar{U}_\infty$ against y, it was then possible to determine the boundary layer momentum thickness θ_M defined as

$$\int_{y=0}^{y=\delta} \bar{U}/\bar{U}_\infty . (1-\bar{U}/\bar{U}_\infty) dy$$

(equation 2.25). In practice this involved calculating $\bar{U}/\bar{U}_\infty(1-\bar{U}/\bar{U}_\infty)$ for successive heights (y) using the mean boundary layer velocity profile (see Figure 4.2(b)). The $\bar{U}/\bar{U}_\infty(1-\bar{U}/\bar{U}_\infty)$ values were then plotted against y to produce a graph of a form similar to that illustrated in Figure 4.2(c). The momentum thickness is defined as the area beneath the curve and was found by counting the enclosed millimetre graph squares and using the appropriate scaling factor.

Using this technique, each boundary layer velocity profile measured on the surface of the plate during the erosion of the strips was used to calculate the boundary layer momentum thickness at that point on the plate. The relationship between momentum thickness and surface shear stress in zero pressure gradient is defined as $\tau = d\theta_M/dx\ \bar{U}_\infty^2$ (equation 2.27), where x is the distance downwind of the leading edge of the plate. In practice shear stress was calculated by plotting θ_M against x (Figure 4.2(d)) and measuring the gradient of the resulting curve $d\theta_M/dx$, at the selected distance along the plate, x. It was

necessary that each graph of θ_M against x should include only those θ_M values associated with the same mean free stream wind velocity $\bar{U}_\infty$ for any distance x along the plate. Thus sets of θ_M values associated with the same $\bar{U}_\infty$ value were collated before plotting θ_M against x. For a given surface material cover (e.g. 710-600 m ballotini), θ_M against x graphs were used to calculate the mean local shear stress at a position (x) on the plate corresponding to a loose particle strip site. In this way, the shear stress on the plate could be related to a certain degree of strip erosion at a given free stream wind velocity. By plotting a number of θ_M against x curves for the range of free stream wind velocities set during the erosion sequence of a strip, it was possible to deduce the relationship between mean shear stress and the portion of strip remaining for any of the materials tested.

In studies of shear stress along bodies such as the experimental plate, measurement of wind velocity profiles is commonly automated using motorized traversing gear, computers and digitizers (e.g. Greeley et al., 1980a). Fitting curves to boundary layer velocity profiles usually involves use of some form of cubic spline technique and areas beneath such curves are calculated using a numerical quadrature method. The use of manual techniques in this study was felt to be justified in the circumstances as setting up automated data collection systems was considered too time-consuming. The procedure adopted to calculate mean local shear velocity values were considered to be sufficiently accurate for the purposes of interpreting the erosion of strips on the surface of the plate.

4.4 Results

4.4.1 Developing boundary layer characteristics

As the boundary layer flow characteristics at any point on the surface of the plate are governed by the Reynolds number and the nature of the underlying surface, and this in turn controls the local surface shear stress, it is essential that differences in boundary layer development on the range of test surfaces are analysed before commenting on the erosion of strips subjected to a variety of flow conditions. Boundary layer velocity profiles associated with similar free stream wind speeds were selected and used to calculate a number of informative boundary layer parameters. These included: $\bar{U}_\infty$, the mean free stream velocity; δ, the boundary layer thickness; δ^*, the boundary layer displacement thickness; θ_M, the boundary layer momentum thickness; H, a wind velocity profile shape parameter (δ^*/θ_M); $d\theta_M/dx$, the rate of change of momentum thickness; $\bar{\tau}$, the mean surface shear stress; $\bar{U}_*$, the surface shear velocity $(\bar{\tau}/\rho)^{1/2}$; δ_{sub}, the thickness of the viscous sublayer (from $10\nu/\bar{U}_*$) and; $\bar{U}_\infty\delta^*/\nu$, the displacement thickness Reynolds number. The value of these parameters over ballotini and aeolian sand surfaces at various positions on the plate (x) are presented in Tables 4.2 to 4.6. In 4.5.1, these results are examined in detail and used to compare boundary layer characteristics and development over the various test surfaces. A study of boundary layer development over 710-600μm sugar crystals and 180-150μm salt crystals was not possible owing to the limited number of particle strip positions and corresponding velocity profile measurements.

4.4.2 Erosion of the test strips

Data extraction, reduction and analysis related a known degree of strip erosion with a known mean shear velocity and free stream wind velocity. The results of sequential strip erosion for ballotini (1.7-1.4mm, 710-600μm, 355-300μm and 180-150μm), sugar crystals (710-600 μm), sand (180-150μm) and salt crystals (180-150μm) are presented in Tables 4.7 to 4.13, respectively. These tables show the amount of a strip remaining uneroded after the standard ten minute erosion period at any given erosion stage (expressed as a percentage of original strip area), and the corresponding mean shear velocity ($\bar{U}_*$) and free stream wind velocity ($\bar{U}_\infty$) responsible for the observed amount of erosion. Arithmetic mean values of $\bar{U}_*$ and $\bar{U}_\infty$ which reflect the mean shear velocity and mean free stream wind velocity associated with the complete erosion of a strip are also given (i.e. $\bar{\bar{U}}_{*T}$ and $\bar{\bar{U}}_\infty$).

As only three strip positions were investigated using sugar crystals and salt crystals, (Tables 4.12 and 4.13), U_* values could not be calculated using the momentum integral method. Further, the use of a logarithmic profile equation (equation 1.2) was invalidated as a logarithmic velocity distribution could not be guaranteed for each strip position, particularly at locations near the leading edge of the plate. The following method was therefore adopted to estimate shear velocity for these materials. Using data for 710-600μm and 180-150μm ballotini, mean shear velocity $\bar{U}_*$, derived from the momentum integral method, was plotted against mean free stream wind velocity $\bar{U}_\infty$ for strip positions at 10, 85 and 130cm from Station A. These strip positions corresponded to those used for 710-600μm sugar crystals and 180-150μm salt crystals. Using the appropriate graph, it was possible to estimate $\bar{U}_*$ from any

measured $\bar{U}_\infty$ value for a given strip position, and in consequence it was possible to estimate the shear velocity responsible for the observed degree of strip erosion in sugar and salt crystals ($\bar{U}_*$(est)).

Data from Tables 4.7 to 4.13 are illustrated in Figures 4.3 to 4.9 which show the percentage of a given loose particle strip remaining uneroded at any given erosion stage plotted against the corresponding mean shear velocity. Each figure includes a number of graphs to illustrate the relationship between % strip area remaining uneroded and $\bar{U}_*$ at successive strip distances downwind from Station A. In some cases, due to lack of available data, the graphs have been extrapolated to indicate the likely erosion sequence. Such extrapolations are shown by a dashed line. For clarity of presentation, data for 180-150μm ballotini and 180-150μm sand are presented using two graphs (Figures 4.6(a), 4.6(b) and 4.7(a) and 4.7(b) respectively).

Figures 4.10 to 4.16 illustrate strip erosion sequences in outline form at selected positions on the plate. The strip outlines were traced directly from photographs and are arranged in sequence. Each sequence is annotated and shows a numbered erosion stage, the area of strip remaining uneroded (expressed as a percentage), the corresponding mean shear velocity, the flow direction, the material and particle size range, and the position of the strip relative to Station A. Generally, strip erosion sequences at 10 and 130cm from Station A are shown. However, in Figures 4.13 and 4.14 (180-150μm ballotini and sand, respectively), strips at 40 and 55cm from Station A are also included.

4.4.3 Summary of visual entrainment observations

Observations of entrainment processes were made during the entire strip erosion sequence of each test material used. The following comments can be applied to all the test strips over the entire range of positions on the flat plate, with the exception of the 180-150μm salt crystal strip at 10cm from Station A. Using illumination from a theatrical lamp, loose particles in the strips were observed both through a side window and the perspex window in the roof of the wind tunnel working section. Particles smaller than 710-600μm were viewed through a small macro-telescope which provided sufficient magnification to see even the smallest grains in great detail. With the exception of salt crystals in the strip at 10cm from Station A (see below), all particles were observed to vibrate at or near the threshold of movement. This did not, however, necessarily imply imminent entrainment, as often the alignment of grain support geometry was such as to effectively restrain the particle yet still permit rapid, restricted oscillation in the wind. On many occasions it was observed that further increases in wind velocity tended to suppress such movement and the individual grains were physically restrained against each other by the force of the wind. In other instances, particles were seen to move short distances and fall into naturally sheltered sites. In doing so, it was uncommon for them to disturb one or more stationary grains. However, sometimes the impact was sufficient to cause particles to enter saltation in a 'mini' grain avalanche. In the majority of cases it was noted that particles tended to oscillate with greater violence and frequency with increasing distance downwind from Station A.

When the local shear velocity exceeded the threshold value, particles moved downwind along the plate surface. This process was filmed using a 16mm Bolex H16 RX-5 medium high-speed movie camera set at 64 frames per second, and a close-focusing Kern macro-Switar 75mm f1.9 lens capable of giving a macro reproduction ratio of 1:2. The high intensity lighting necessary for filming was supplied by eight quartz-halogen projector bulbs. Panchromatic Ilford HP5 (ISO/ASA 400) black and white film was used and processing was undertaken by a local laboratory. Analysis of the films revealed a number of interesting features associated with the entrainment of particles from the strips. Particles were observed to roll initially over stationary ones and rise a short distance from the bed after colliding with the grains immediately downwind. By doing so, they acquired forward momentum from the faster moving air above the stationary particles, and subsequent collisions were progressively more violent. The height of particle 'bounces' and the distance between collisions with the bed were observed to increase as the particle acquired a greater downwind velocity. The 'bouncing' process continued downwind until the particles appeared to acquire true saltation trajectories at an unmeasured distance downwind. On no occasion were particles seen to rise vertically from the bed in initial entrainment.

Entrained particles from the front of the strip were sometimes involved in violent collisions with loose material at the rear and avalanching ensued. This was more significant in turbulent boundary layer flows where the steep velocity gradient above the bed probably gave rise to higher particle collision velocities. This partially explains why strips in turbulent flows showed a tendency to erode from the back forwards. However, it was thought that grain entrainment from the rear of the strip was brought about by the increase in wind turbulence as flow

encountered the upwind edge of the strip. Towards the rear of the plate, strips were well embedded in the turbulent flow, and by observing the strips, the passage of highly turbulent regions was detected at velocities just below the threshold. In such events, areas of the strip appeared to 'shimmer' as a large proportion of the particles vibrated simultaneously. Raising the velocity resulted in a cessation of such movement as particles appeared to be pressed against the bed by the air flow. Further slight increases gave rise to individual particle oscillation and entrainment.

Salt crystals in a strip positioned at 10cm downwind of Station A were not observed to oscillate during the strip erosion sequence. They were, however, observed to shift their resting positions at wind speeds just below the threshold and in certain instances, this type of motion gave a visual impression of oscillation. Close inspection revealed that some particles changed position in the strip as many as six times before finally succumbing to the local shear stress and moving downwind. Further consideration of this observation is given in 6.5.2 where additional experimental evidence is discussed and reasons for particle oscillation (or lack of oscillation in this case) are suggested.

4.5 Discussion of Results

In this discussion of aeolian entrainment thresholds four aspects of the results presented in 4.4. are considered. These are: (a) the characteristics of the developing boundary layer over the plate; (b) transition from laminar to turbulent flow; (c) theoretical considerations of flow regimes at the scale of single grains; and (d) the sequential erosion of test strips.

4.5.1 Developing boundary layer characteristics

Parameters expressing the development of boundary layers on the rough surface of the plate are summarized in Tables 4.2 to 4.6. From these tables, the characteristics of the boundary layer over four size ranges of ballotini and a single aeolian sand fraction may be seen. As far as possible, free stream wind velocities are similar to enable direct comparison between the various boundary layer parameters. The mean shear velocity values given in Tables 4.2 to 4.6 were sufficient to cause the removal of a significant portion of the strips of ballotini and aeolian sand at the various distances downwind of Station A and are thus representative of aeolian threshold conditions.

The boundary layer characteristics presented in Tables 4.2 to 4.6 were derived from velocity profile measurements using the pitot-tube arrays. Therefore, before discussing these boundary layer parameters, it is necessary to assess the accuracy and reliability of these velocity measurements. In a shear flow such as the boundary layer, the geometry of a pitot-tube causes a slight flow displacement which, unless taken into account, will give rise to errors in the measurement of wind velocity. In the shallow wind velocity gradients of the outer region of a boundary layer the error will be small. However, in the steep velocity gradients associated with the inner region of the turbulent boundary layer readings can be seriously in error (Davies, 1950). In addition, the near-surface wind profile resolution of a given pitot-tube array is governed by the pitot-tube diameter. This problem was overcome to some extent by flattening the three probes nearest the surface so that they gave a closer approximation to a point velocity measurement, and by alternately off-setting them from the central support column. However,

the advantages of improved resolution achieved in this way are probably offset by local flow displacements induced by the modified tube geometry. The pitot-tube diameter is itself of the same order of size as the ballotini (1.5mm) and therefore resolution of the wind velocity profiles at the scale of the individual grain is impossible using these instruments. However, over most plate surfaces, the boundary layer thickness exceeded 4mm (Tables 4.2 to 4.6) so that even in the most unfavourable conditions of thin boundary layer development, it was possible to measure wind velocity at a minimum of two heights and therefore to interpolate a velocity profile. Use of such techniques was only necessary in a restricted region up to 10cm downwind from Station A over the smallest particles, and was not thought to compromise the overall accuracy of the measurements. It was not possible to infer a great deal about the detailed boundary layer structure from the pitot-tube array measurements and therefore the following discussion is restricted to the parameters shown in Tables 4.2 to 4.6.

(a) Free stream wind velocity

The incorporation of external flow into the boundary layer, whether by molecular activity or turbulence, is a fundamental mechanism determining the rate and character of boundary layer development along the plate. It was therefore essential to ensure that the free stream air above the plate was as uniform and free from turbulence as possible, as any disturbances in the free stream wind would be likely to give rise to flow anomalies in the developing boundary layer on the plate. Such disturbances would thus invalidate assumptions made regarding its characteristics. Past experience had shown that the free stream wind was virtually free from any velocity fluctuations and extended to at least

twice the maximum boundary layer thickness before working section roof effects were recorded. Thus the boundary layer on the plate developed beneath a flow of air free from any disturbances likely to disrupt uniform boundary layer development. A low frequency, periodic oscillation in free stream wind velocity was recorded by a pitot-static probe positioned in the centre of the contraction section (Figure 3.4) and was thought to be associated with the recirculation of air from the exhaust of the blow-down wind tunnel. The effect was barely detectable and was not thought to interfere with boundary layer development in any significant way.

(b) Boundary layer thickness

The thickness of the boundary layer, δ over 1.7-1.4mm ballotini ranged between 27.7mm at 10cm from Station A and 47.5mm at 85cm from Station A (Table 4.2). At a similar free stream wind velocity, the boundary layer thickness over 180-150μm ballotini ranged between 4.1mm at 5cm from Station A and 21mm at 85cm from Station A (Table 4.5). These differences, reflecting different aerodynamic roughnesses on the plate, are more clearly demonstrated in Table 4.14 where the rate of boundary layer thickening $d\delta/dx$ along the plate is shown. Tables 4.2 to 4.6 and Table 4.14 show that the thickness of the boundary layer, δ, increases with increasing distance downwind of Station A irrespective of the test material, and that $d\delta/dx$ values decrease with particle size. Variations in rates of boundary layer thickening (Table 4.14) may be attributed to two factors.

Firstly, individual roughness elements shed vortices which increase the general level of boundary turbulence and lead to more

efficient entrainment of the external flow. Roughness elements thus contribute to boundary layer development directly and the degree of turbulence they generate is a function of the roughness height D and the Reynolds number (Re*). The rate of boundary layer thickening is, therefore, greater on a rough surface (e.g. 1.7-1.4mm ballotini) than on smooth surface (e.g. 180-150μm ballotini). Laminar-like flows were detected on the experimental plate over 180-150μm ballotini and aeolian sand and were found to occupy a narrow region extending no more than 40cm downwind from the leading edge of the plate. Beyond this region, transitional and fully turbulent flow dominated. The much slower boundary layer thickening associated with laminar flow over these surfaces contributes to the lower $d\delta/dx$ values reported in Table 4.14.

Secondly, it was noted that the $d\delta/dx$ values for sand were higher than for the same size of ballotini. The difference in particle shape between sand and ballotini is a likely explanation of this result. The geometric arrangement and angularity of sand grains are likely to present a 'rougher' aerodynamic surface to flow and thus promote more rapid boundary layer thickening than the smoother 180-150μm ballotini surface. However, it is also possible that the size distributions associated with these test materials may have been different and may have led to surfaces characterised by different mean particle diameters. The quarter phi sieve interval was too coarse to detect these differences and thus this matter must remain speculative.

Over 180-150μm ballotini, the boundary layer thickness increased rapidly from δ = 9.2mm at 40cm from Station A to δ = 16.1mm at 55cm from Station A (Table 4.5). Transition from laminar to turbulent flow appeared to occur in this narrow region and is reflected by the 57%

increase in δ values. Beyond 55cm, the rate of turbulent boundary layer development was slower than might normally be expected (6.5mm m^{-1}). A similar reduction in turbulent boundary layer thickening was also recorded over 180-150μm sand (Table 4.6). The viscous sublayer was thought to play a part in this phenomenon by sheltering the grains in such a way as to reduce vortex shedding effects which contribute to the general turbulence intensity within the boundary layer. Such a reduction in the turbulence level would reduce the rate of external flow incorporation into the boundary layer and thereby suppress the thickening rate. Further consideration of this phenomenon is given in 4.5.2 and 4.5.3.

(c) Boundary layer displacement thickness and momentum thickness

The physical meaning of the boundary layer displacement thickness δ^* and the momentum thickness θ_M was described in 2.6.3(c) and it is clear that the comments made in 4.5.1(b) regarding the relationship between boundary layer thickness and the surface of the plate may equally be applied to δ^* and θ_M. The ratio of displacement thickness to momentum thickness, (δ^*/θ_M) gives a dimensionless boundary layer shape parameter, H, which may be used to assess boundary layer stability. The range of H values presented in Tables 4.2 to 4.6 lie within the stability limits of 2.3 to 3.5 for laminar flow and 1.3 to 2.2 for turbulent flow (Schlichting, 1979). However, as the boundary layer velocity profiles close to the leading edge of the plate were interpolated from only two mean velocity measurements, there is insufficient data for the calculation of reliable H values. Is is not possible, therefore, to infer much about the condition of the boundary layer from H values at these stations.

4.5.2 Transition from laminar to turbulent flow on the plate

It is clear from the preceding discussion that the boundary layer on the plate has changing downwind characteristics. It is likely, therefore, that the changing threshold conditions on the surface of the plate are related in some way to these changing flow regimes. Therefore, before analysing the strip erosion sequences, it is important to have knowledge of the local flow conditions and in particular to determine whether the flow is laminar, transitional or turbulent at a given strip position on the surface of the plate. Data presented in Tables 4.2 to 4.6 indicate that flow over the majority of the length of the plate was turbulent regardless of the surface roughness, but the precise nature of the flow near the leading edge, particularly over the 180-150μm grains, remained elusive using this method.

The most fundamental criterion for transition from laminar to turbulent flow on the plate is the Reynolds number (Re_x), defined as $\bar{U}_\infty x/\nu$ (equation 2.2), where x is the downwind distance from the leading edge. A value of Re_x greater than about 10^3 for flow over the type of surface covering the plate indicates transitional or turbulent flow. The only real uncertainty over the smallest grain sizes is the extent to which the laminar boundary layer thickens downwind of the leading edge and thereby becomes insensitive to the surface roughness before natural instabilities cause transition. As the value of Re_x rises downwind, the boundary layer becomes increasingly sensitive to disturbances, and whether it undergoes transition or not depends on whether a sufficiently marked disturbance occurs. On the leading edge, the boundary layer is too thin to be unstable and laminar flow will persist for a certain distance downwind of the stagnation point regardless of the surface

roughness. Roughness elements on the surface of the plate shed vortex trails and if propagated a sufficient distance downwind will trigger transition. The size of the roughness elements will determine where this occurs. In the case of the large grain sizes, vortex shedding will be so vigorous that transition to turbulent flow will occur almost immediately as the flow travels downwind of the stagnation point. As grain size becomes smaller, however, laminar flow is able to persist for a greater downwind distance and flow will only undergo transition if roughness elements cause sufficient disturbance or natural flow instabilities give rise to mixing between streamlines.

It is clear, therefore, that a degree of uncertainty is associated with transition from laminar to turbulent flow on the plate and the precise determination of where it occurs is not possible. Keulegan (1938) and Einstein (1950) considered this problem and suggested a criterion based on the thickness of the viscous sublayer assuming turbulent flow, calculated from a measured mean shear velocity. They define the viscous sublayer thickness δ_{sub} as

$$\delta_{sub} = 11.6\nu/\bar{U}_* \qquad 4.1$$

and suggest flow is fully turbulent over a surface in which the roughness element projection height D is greater than $5\delta_{sub}$. Over a rough granular surface, such as that on the plate, D may be taken as being equivalent to the diameter of the particles themselves (Einstein, 1950; and Schlichting, 1979). In Tables 4.2 to 4.6, δ_{sub} and $5\delta_{sub}$ values are given for the range of experimental materials and strip positions used. The $5\delta_{sub}$ values suggest that, in general, particles on the plate are sheltered to some extent by a viscous region. The only

exceptions are the 710-600μm ballotini at 10cm from Station A and the 1.7-1.4mm ballotini at all plate positions. The $5\delta_{sub}$ values therefore suggest transitional or laminar flow over the majority of particle sizes regardless of their position on the surface of the plate.

However, H values (Tables 4.2 to 4.6) derived from measurements of the boundary layer wind velocity profiles suggest that laminar flow was only present over the 180-150μm ballotini and aeolian sand near the leading edge of the plate and that transitional flow only occupied a restricted region along the plate (smaller than 15cm in most cases). This evidence conflicts with the flow regime implied by the $5\delta_{sub}$ values and suggests that in the special conditions on the rough surface of the plate $5\delta_{sub}$ may not be a useful parameter for defining the onset of turbulence. In this case, $5\delta_{sub}$ values probably do not account for the process of vortex shedding by the exposed grains on the leading edge of the plate which may give rise to early transition to turbulent flow if the local flow regime is sufficiently sensitive to such disturbances.

Additional evidence to support the argument above is given by considering a Reynolds number using boundary layer displacement thickness δ^* as the characteristic length scale so that

$$Re\# = \bar{U}\delta^*/\nu \qquad 4.2$$

The Re# values calculated for the boundary layer over the plate are given in Tables 4.2 to 4.6. Schlichting (1979) states that for Re# greater than 950 flow is transitional and becomes fully turbulent at some value of the order of 10^3. The Re# values presented in Tables 4.3 to 4.7 exceed 10^3 in all cases except over 180-150μm ballotini and sand

near the leading edge suggesting, therefore, that laminar-like flow extends for at least 40cm downwind of Station A. Re* values also suggest that transitional flow occupies a region extending between 40cm and 55cm from Station A over these surfaces and that flow downwind of this region is turbulent. The flow, as indicated by Re* values over the other test surfaces appears to be transitional or turbulent by 10cm from Station A.

In the subsequent analysis of the strip erosion sequences it was assumed that the flow over all the test materials with sizes ranging between 1.7mm and 300μm was turbulent. This assumption was based on the evidence provided by the boundary layer wind profile measurements and the calculated Re* values reported above. Flow over particles smaller than 180μm in size was considered to have laminar-like characteristics for at least the first 40cm from Station A. Beyond this distance, flow disturbances, caused by natural boundary layer instability and vortex shedding by upwind grains, resulted in the transition to turbulent flow around 40 to 55cm from Station A.

4.5.3 Theoretical considerations of flow at the scale of single grains on the surface of the plate

Evidence given above has suggested the likely flow regime over a given particle size for any position on the surface of the plate. However, despite this, little is known about the flow characteristics at the scale of single grains in a strip. Knowledge of these conditions may be usefully applied in the analysis of strip erosion sequences as the local flow around grains is likely to determine the forces acting at the threshold of movement. Using hot wire anemometry it may have been possible to measure the details of the flow at the scale of single

grains. However, the procedure is extremely difficult, even over smooth surfaces, as flow interference, radiative exchange and convection effects give rise to errors which must be accounted for. These problems are compounded over rough surfaces such as those on the plate. Therefore, in this investigation, no attempt was made to make such measurements.

An alternative method devised to determine the local flow regime was based on the 'law of the wall' (Chapter 2) which describes the functional relationship between velocity, shear velocity, height above the surface and kinematic viscosity. It is generally expressed in the form:

$$U/U_* = f(yU_*/\nu) \qquad 4.3$$

To utilise this method the functional relationship described by equation 4.3 was solved for both laminar and turbulent boundary layer flows and yU_*/ν was plotted against U/U_*. Appropriate scaling of grain projection height was determined using the expression $Y'\bar{U}_{*T(50)}/\nu$ where the particle projection height is represented by the term y' (see below), and $\bar{U}_{*T(50)}$ represents the mean threshold friction velocity required to entrain 50% of the test material from a strip at a given position on the surface of the plate. Using this expression it is possible to assess the the position of grains in dimensionless laminar and turbulent boundary layers. The solutions to the functional relationship in equation 4.3 were derived for flow on a smooth surface and are therefore not strictly representative of the flow conditions on the 'rough' plate. The calculated position of grains in the boundary layer can, therefore, only be used as a guide and must be interpreted

with caution with regards to the flow on the rough plate surface.

(a) Laminar boundary layer

A solution of the laminar boundary layer equations for flow on a smooth, flat plate was first derived by Blasius (1908) and subsequently developed by Von Karman (1921), Bairstow (1925), Goldstein (1930) and Howarth (1938). Using Howarth's solution (shown in Table 4.15) the following procedure based on that described by Schlichting (1979, p. 136) was adopted to solve the functional relationship described by equation 4.3.

Using a dimensionless co-ordinate, η_c defined as:

$$\eta_c = y\left[\frac{U_\infty}{\nu x}\right]^{1/2} \qquad 4.4$$

a height y was calculated at a given η_c value (using Table 4.15) for a chosen free stream wind velocity, U_∞, and distance along the plate, x. The velocity at height y was then found from the column $f' = U/U_\infty$ by referring across Table 4.15 at the appropriate η_c value. This was repeated for values of η_c up to 2.8 (where $U = 0.995\ U_\infty$) in order to derive a dimensionless laminar boundary layer velocity profile associated with the selected free stream wind velocity. It was then necessary to calculate the shear velocity (U_*) value associated with the velocity profile dU/dy derived from Table 4.15. Local skin friction, $\tau_o(x)$ is defined as:

$$\tau_o(x) = \mu\left[\frac{dU}{dy}\right]_{y=0} = \mu U_\infty\left[\frac{U_\infty}{\nu x}\right]^{1/2} f''(0) \qquad 4.5$$

where $f''(o)$ = function of $\tau_o(x)$, (Howarth, 1938, Table 4.15).

From Table 4.15 $f''(o) = 0.33206$, therefore, $\tau_o(x)$ may be calculated using equation 4.5. Shear velocity U_* is related to the shear stress $\tau_o(x)$ by

$$U_* = \left(\frac{\tau_o(x)}{\rho}\right)^{1/2} \qquad 4.6$$

Thus, with a knowledge of the laminar boundary layer profile, dU/dy and shear velocity U_*, it was then possible to plot the dimensionless parameter (yU_*/ν) against dimensionless relative velocity (U/U_*), (The curve of Figure 4.17) for the laminar boundary layer case.

(b) Turbulent boundary layer

The position of particles in the turbulent boundary layer can similarly be examined using the universal relationship, $U/U_* = f(yU_*/\nu)$. The viscous sublayer close to the surface, like the laminar boundary layer, is characterized by a linear velocity gradient (equation 2.3) i.e.

$$\frac{U}{U_*} = \frac{yU_*}{\nu}$$

Above the sub-layer, the velocity gradient assumes a logarithmic distribution (2.6.3(a)), which was described by equation 2.8, i.e.

$$\frac{\overline{U}}{\overline{U}_*} = A \operatorname{Log}_{10} \frac{y\overline{U}_*}{\nu} + B$$

In the calculation of the turbulent boundary layer velocity profile using a given $\bar{U}_*$ value, values of 2.5 and 5.5 were assumed for the constants A and B, (Ludwieg and Tillman, 1949; and Thwaites, 1960). A graph of $(y\bar{U}_*/\nu)$ against $(\bar{U}/\bar{U}_*)$ for the turbulent boundary layer is presented as the curve in Figure 4.18.

(c) Grain height scaling

The grain support geometry for spheres of radius r can be simplified into two basic geometric configurations: (a) three spheres arranged in a triangle; and (b) five spheres arranged in a pentagon. The triangular configuration gives rise to the maximum projection height above a homogeneous bed of particles and the pentagonal arrangement to the minimum. These two configurations thus represent the extremes of projection height for each size of particle. Ballotini grains in a strip on the rough surface were considered to be supported by both triangular and pentagonal geometry. Grain projection height scaling was calculated using $y'\bar{U}_{*T(50)}/\nu$, where y' is the projection height (maximum height $y'_{max}=1.633r$; minimum height $y'_{min} = 1.0515r$) and $\bar{U}_{*T(50)}$ is the experimentally determined mean threshold shear velocity required to erode 50% of a strip of given grain size at a specified position on the plate. The $\bar{U}_{*T(50)}$ values were read directly from Figures 4.3 to 4.6.

It has been shown that laminar flow is only found near the leading edge of the plate over 180-150μm ballotini and aeolian sand. Thus values of $y'\bar{U}_{*T(50)}/\nu$ were calculated for this size range using $\bar{U}_{*T(50)}$ values measured for strips at 5, 10, 15 and 25cm from Station A. To avoid confusion only values for ballotini were considered. The data for both triangular and pentagonal support geometry are presented in

Table 4.16 and are plotted in Figure 4.17 on the dimensionless laminar boundary layer profile using the $y\bar{U}_*/\nu$ axis.

Individual grain exposure to flow in a turbulent boundary layer was considered by calculating $y'\bar{U}_{*T(50)}/\nu$ values for the following ballotini sizes and strip positions on the plate: (a) 1.7-1.4mm at 10 and 85cm from Station A; (b) 710-600μm at 10 and 130cm from Station A; and (c) 355-300μm at 10 and 130cm from Station A. As turbulent flow was detected over 180-150 m ballotini at 55cm from Station A, $y'\bar{U}_{*T(50)}/\nu$ values for 180-150μm ballotini at 55cm from Station A were also included. The $y'\bar{U}_{*T(50)}/\nu$ values for these strips are given in Table 4.17 and are plotted on the dimensionless velocity distribution graph for a turbulent boundary layer in Figure 4.18 using the $y\bar{U}_*/\nu$ axis. In all cases $y'\bar{U}_{*T(50)}/\nu$ values are calculated for both triangular and pentagonal grain support geometry.

(d) Theoretical flow over test particles on the plate

A number of general comments can be made regarding the dimensionless laminar and turbulent boundary layer velocity distributions depicted in Figures 4.17 and 4.18 respectively. Given the experimentally determined shear velocity values for 180-150μm ballotini, it is likely that grains of this material would lie within the lower region of a laminar boundary layer if the surface of the plate were smooth. However, the experimental plate surface was rough and undoubtedly altered the characteristics of the laminar boundary layer significantly.

Figure 4.17 shows that 180-150μm ballotini near the leading edge of the plate project a good way into the laminar boundary layer in

threshold flow conditions and are therefore likely to induce flow transition. However, in the experimental studies, the boundary layer developed over a surface in which grain projection height was of the order of r and highly exposed grains were only encountered at a strip on the plate. Therefore, it is likely that a laminar boundary layer could develop along the plate as far as a strip, providing the distance of propagation does not exceed that where natural flow instability and cumulative vortex shedding effects give rise to transition. On encountering the test strip, however, it is likely that flow disturbances would be sufficient to cause transition to turbulent flow at a short distance downwind of the strip.

The curve in Figure 4.18 represents the turbulent boundary layer on a smooth surface. The full range of experimental particle sizes are included and threshold conditions at the leading edge and rear of the plate are considered. The most striking feature shown in Figure 4.18 is that all the particles, irrespective of their size or the plate position considered, would lie within the inner region of a standard turbulent boundary layer developed over a smooth surface in flow conditions representative of the threshold.

The major effects of a rough surface in the case of turbulent flow on the plate would be to increase local turbulence by vortex shedding and thus give rise to greater boundary layer thickening for a given Reynolds number. Evidence of this phenomenon was given in 4.5.1(b). Given a rough surface, therefore, it seems likely that particles would also occupy this inner region and be subjected to the high local mean shear stresses associated with the characteristically steep velocity gradient of the turbulent boundary layer. Figure 4.18

indicates that towards the rear of the plate, the smaller particles are sheltered to some extent by the viscous sublayer, where velocity gradients are not as severe. A rough surface would probably not afford so much protection and loose particles, particularly those raised above the mean bed level (i.e. strips), would be subject to rapidly fluctuating shear stresses caused by the intermittent effects of bursting at the sublayer/inner region interface, (2.5.2). The development on the surface of the plate of a viscous sublayer with characteristics similar to that on a smooth surface (Figure 4.18) is unlikely in view of the local Reynolds number (Table 4.2 to 4.6) and the aerodynamic characteristics of the surface itself. Thus, it is likely that any tendency of the viscous sublayer to provide protection to exposed grains greater than 300μm (as suggested in Figure 4.18) is off-set by the generation of vortices from the upwind particles, and by high shear stress events in the inner region of the boundary layer (e.g. bursting and sweeping) which would tend to suppress significant viscous sublayer development over the rough surface.

However, in 4.5.1(b) it was suggested that a viscous sublayer may have developed from the transition point over particles smaller than 180μm in size. Table 4.5 shows that over 180-150μm ballotini, mean threshold shear stress steadily falls with distance from Station A until at 55cm a marked increase was recorded. Downwind of this position U_{*T} values again fall steadily. In 4.5.2 it was suggested that flow upwind of this position was essentially laminar in character and thus at the scale of single grains was characterised by essentially viscous flow near the surface. At a suitable distance downwind of the transition point (55cm in the case of 180-150μm ballotini), the viscous sublayer may have been sufficiently thick to afford some degree of shelter to the grains in the strip and hence a sudden rise in mean threshold shear velocity was

recorded. Further downwind, turbulent flow became dominant and the characteristics of the viscous sublayer were significantly altered by the increased vortex shedding and high shear stress events associated with the turbulent flow. The particles do not appear to be sheltered by the viscous sublayer to the same degree and mean threshold shear stress for 180-150μm ballotini again decreased at sites beyond 55cm from Station A in response to a corresponding increase in instantaneous bed shear stress.

4.5.4 Erosion of test strips

The data presented in Tables 4.7 to 4.13 show that, in general, a larger mean threshold shear velocity ($\overline{\overline{U}}_{*T}$) is needed to entrain particles from strips at the front of the plate than from strips at the rear of the plate. To show this clearly, Table 4.18 summarizes mean threshold shear velocity ($\overline{\overline{U}}_{*T}$) values measured for the range of experimental materials and strip positions on the plate. (In this case, the symbol $\overline{\overline{U}}_{*T}$ represents the arithmetic mean of the range of mean shear velocities ($\overline{U}_{*T}$) required to erode at least 90% of a given strip). This section examines the sequential erosion of the test strips and attempts to explain why the mean threshold shear velocity decreases with increasing distance downwind from the leading edge of the plate. Evidence is provided by the analysis of strip erosion sequences, the boundary layer characteristics on the plate (4.5.1 and 4.5.2) and the theoretical interpretation of flow conditions at the scale of single grains (4.5.3). Interpretation of these experimental results is largely based on the entrainment model proposed by Grass (1970), (see 2.5.2), in which threshold conditions are defined by a small degree of overlap between the probability distribution of the fluctuating bed shear stress component of the boundary layer flow and the probability distribution of

threshold shear stress values ascribed to individual particles in a given granular material.

In 4.5.1 it was shown that the boundary layer characteristics changed continuously downwind from the leading edge of the plate irrespective of the test material on the surface of the plate. It is likely, therefore, that the interaction between loose material and the flow is unique at any point on the surface of the plate. As the resistance of a particle to entrainment is independent of its position on the plate, the same force is required to initiate grain movement at the threshold irrespective of the prevailing flow conditions. Providing, therefore, that the particles are sufficiently uniform, the initiation of grain movement is primarily controlled by the characteristics of the local boundary layer flow regime and, in particular, by the value of the peak instantaneous shear velocity associated with the background flow (2.5.2). This deduction is consistent with the $\overline{U}_{*T}$ values reported by Bagnold (1941), Yalin and Karahan (1979) and Greeley et al. (1980a), who also noted a reduction in the value of $\overline{U}_{*T}$ in response to increasing boundary layer turbulence.

To interpret and analyse the experimental results pertaining to strip erosion presented in 4.4, it is necessary to examine the strip erosion sequences, the corresponding boundary layer flow and to use the visual observations made during the experimental work. In this discussion, reference is made to Figures 4.10 to 4.16 which depict a representation of the actual erosion sequences at selected positions on the plate traced directly from photographs. However, before discussing the results in detail, it is useful to examine the mutual attributes of the erosion sequences illustrated in Figures 4.3 to 4.9 as these reveal

some interesting features that aid assessment of the interaction between loose material and flow at the aeolian threshold.

(a) General results

Each of the asymptotic erosion curves illustrated in Figures 4.3 to 4.9 possess several similar characteristics. The mean shear velocity is shown to increase until a critical value is reached. Slight increases in $\overline{U}_*$ then give rise to the removal of a small percentage of the strip material. This $\overline{U}_*$ value may be thought of as representing the mean aeolian threshold shear velocity, $\overline{U}_{*T}$. Further increases in $\overline{U}_*$ above this $\overline{U}_{*T}$ value give rise to additional entrainment until, at what appears to be a second threshold, erosion of the test strip occurs at an accelerated rate. When the area of the strip falls below approximately 15%, particles are relatively resistant to erosion and quite large increases in $\overline{U}_*$ are generally required for the complete removal of the remaining test material. There are, however, two exceptions to this general description of strip erosion characteristics. These are the erosion curves for 180-150μm ballotini at 5cm and 10cm downwind of Station A (Figure 4.6(a)) which are discussed in detail in 4.5.4(b) below.

In general, the form of the characteristic asymptotic curves showing the erosion of test strips (Figures 4.3 to 4.9) are remarkably similar irrespective of the test material or position on the surface of the plate. All these curves are amalgamated in a single graph (Figure 4.19) by aligning mid-ordinate values (i.e. 50%) of each curve. The upper and lower bounds of curve variation are shown by the dashed lines and the single solid curve depicts the average curve for all test strips. Curves with the steepest mid-point gradient are associated with

erosion of strips on the downwind portions of the plate whilst curves with the shallower gradient are associated with strips positioned close to Station A. The shaded area between the two dashed erosion curves in Figure 4.19 represents the range of shear velocities in excess of the threshold required to erode completely all the test strips studied during this investigation, with the exception of the 180-150μm ballotini strips mentioned above. With strip erosion data in the form of Figure 4.19, it is now possible to compare directly the mutual attributes of the characteristic erosion curves.

In general it is found that the range of shear velocities in excess of the threshold required for complete strip erosion decreased slightly with increasing distance downwind from Station A (Figures 4.3 to 4.9 and Figure 4.19). However, this decrease rarely exceeded $0.1ms^{-1}$ over the entire length of the plate suggesting, therefore, that the characteristic curve associated with strip erosion by threshold wind speeds is essentially the same irrespective of the test material or the position of the strip on the surface of the plate. Consequently, it appears that the loss of strip material, in response to a shear velocity value greater than the threshold, is determined by the characteristics of the strip particles themselves. This result has important implications for the understanding of aeolian threshold conditions and is considered now in the context of threshold ideas of Grass (1970).

Grass (1970) introduced the novel concept that each grain at rest on a bed can be ascribed a specific threshold shear velocity value which, when exceeded, results in entrainment (see 2.5.3). Grass (1970) was able to measure this distribution by determining the local velocity gradient (and hence τ) in the viscous sublayer directly above a grain at

the instant of entrainment. This was achieved by analysing high speed motion picture records of instantaneous hydrogen bubble flow visualization. By repeating these measurements many times he was able to determine the characteristic threshold shear stress distribution associated with a given test sediment. However, this elegant technique cannot be applied to determine the threshold distribution of particles in air for two reasons. Firstly, Grass (1970) only considered hydraulically smooth boundaries (i.e. Re* smaller than or equal to 3.5) where individual grains were well immersed in the viscous sublayer. In threshold flow conditions typical for aeolian sized particles (i.e. d=355μm, Table 3.3) the flow is aerodynamically rough and individual grains project well into the inner region of the turbulent boundary layer (see 4.5.3(d)). Measurement of the instantaneous shear stress associated with grain entrainment in these circumstances is extremely difficult. Secondly, no appropriate flow visualization technique exists for analysing local flow at the scale of single grains in air.

The pattern of sequential erosion of test strips shown in Figures 4.3 to 4.9 and 4.19, however, suggests an indirect method of obtaining the aeolian threshold shear velocity distribution associated with a given material. Using the graphs showing the percentage of strip area remaining uneroded (%A) versus mean shear velocity ($\bar{U}_*$), (Figures 4.3 to 4.9), it is possible to calculate tan ($\%A/\bar{U}_*$) values from the asymptotic curve for small increments of %A. Plotting tan ($\%A/\bar{U}_*$) against $\bar{U}_*$ results in curves with similar characteristics to that for $P(\tau_T)$ given in Figure 2.12. This form of curve not only defines the mean threshold shear velocity ($\bar{U}_{*T}$) associated with a given test material and strip position on the surface of the plate, but also defines the maximum and minimum $\bar{U}_{*T}$ values. In addition, as strip erosion was

allowed to proceed for ten minutes at each velocity setting, each strip erosion stage probably represented the equilibrium configuration with the prevailing flow conditions. In other words, all the susceptible grains were removed during the standard erosion time and only those grains with threshold shear velocities greater than the peak instantaneous shear velocity of the local wind regime remained in the strip.

This argument is illustrated in Figure 4.20 which shows the interaction between the distribution of threshold shear velocity of material in a strip and the changing distributions of shear velocity associated with the local boundary layer flow as wind speed is increased during a strip erosion sequence. The area beneath the threshold distribution curve may be thought of as representing the area of a test strip. If mean shear velocity is increased in equal increments (Figure 4.20) the maximum rate of erosion per increment is observed to occur when 50% of the strip area remains uneroded. Therefore, the reduction in strip area in response to increasing mean shear velocity of the airflow takes asymptotic form illustrated in Figures 4.3 to 4.9. (It is likely that the form of the shear velocity distribution for the boundary layer flow will change in response to the increase in free stream wind velocity at each strip erosion stage owing to the corresponding increase in flow Reynolds number. The increased frequency and intensity of bursting and sweeping events this implies would probably be manifest as an increase in the skewness of the distribution (see below). (For simplicity, this effect is not shown in Figure 4.20). This technique, therefore, provides a simple and effective means of determining the characteristic threshold shear velocity distribution associated with a given test material in a specific boundary layer flow regime on the surface of the plate.

Table 4.18 shows that for particle sizes larger than 180-150μm, $\overline{\overline{U}}_{*T}$ values decrease from a maximum value at the front of the plate to a minimum value at the rear. Further, the rate of reduction in mean threshold shear velocity, $d\overline{\overline{U}}_{*T}/dx$ is greatest over the roughest surfaces and this, therefore, suggests that the underlying surface characteristics are important in determining the boundary layer structure and hence the local mean shear velocity value. The 180-150μm particles also show a reduction in mean threshold shear velocity values over the first 40cm downwind from Station A. However, they differ from the larger grains in that an increase in $\overline{\overline{U}}_{*T}$ values is recorded at approximately 55cm from Station A. Further downwind, $\overline{\overline{U}}_{*T}$ values again fall and reach a minimum value at the rear of the plate (Table 4.5 and 4.6). Possible explanations of this observation were given in 4.5.2, (i.e. particles were probably sheltered in the viscous sublayer).

Using the arguments of Grass (1970), it is also possible to explain why the mean threshold shear velocity associated with a given test material decreases with increasing distance downwind of Station A. Figure 4.21 shows a theoretical distribution of threshold shear velocities for a given test material. As the same force is required to entrain grains irrespective of their position on the plate, the position of this distribution on the U_* axis will remain the same regardless of the strip position considered. As argued above, the measured downwind decrease in mean threshold shear velocity must be accompanied by a corresponding increase in the peak values of the fluctuating shear velocity component. In other words, the distribution of shear velocity becomes increasingly positively skewed as the boundary layer turbulence intensity increases downwind on the plate. The effect of this increasing downwind skewness in the U_* distribution upon interaction with the

threshold distribution is illustrated in Figure 4.21. It is probable that this effect gave rise to the observed downwind reduction in mean threshold shear velocity for a given test material on the surface of the plate.

The graphs in Figures 4.3 to 4.9 also suggest a way to define aeolian thresholds objectively. These figures show that the relationship between the percentage of a given strip area remaining uneroded and shear velocity is approximately linear if the erosion of the first and last 15% of the strip area is ignored. By extrapolating this near linear portion so that it intersects with the lines representing 100% and zero % of the strip area remaining uneroded, it is possible to define several values of $\bar{U}_{*T}$ which may be used as objective entrainment criteria. Figure 4.22 shows the typical relationship found between the percentage of a strip area remaining uneroded and shear velocity, and shows a number of critical $\bar{U}_{*T}$ values which may be defined by the graph.

The $\bar{U}_{*T(min)}$ and $\bar{U}_{*T(max)}$ values represent the mean shear velocity required to entrain the first and last particle in the strip respectively. They can only be determined by observation and, therefore, their accuracy is limited by the skill of the observer or the resolution of a system designed to detect entrainment. The $\bar{U}_{*T(50)}$ value defines the mean shear velocity required to erode 50% of the total strip area. This parameter can only be determined from such a graph and thus it represents an objective definition of the aeolian entrainment threshold giving a specified amount of entrainment. Similarly the extrapolated values $\bar{U}_{*T(100)}$ and $\bar{U}_{*T(0)}$ provide objective definitions of aeolian entrainment. In this case $\bar{U}_{*T(100)}$ represents the incipient aeolian threshold condition where a few grains move, and $\bar{U}_{*T(0)}$ may be thought

of as being close to the ultimate threshold (Bagnold, 1941, p. 93) for a given sample. A less specific definition of the aeolian threshold shear velocity is represented by the arithmetic mean of all the shear velocities recorded during the complete erosion of the strip (i.e. $\bar{\bar{U}}_{*T}$). This definition of threshold, together with measures of dispersion of observed $\bar{U}_{*T}$ values, can be used to account for the whole range of threshold values observed in a test material, and could be used to define mean threshold shear velocities for materials having unusual or skewed distributions of grain size or density. This threshold definition accounts for the whole range of threshold values associated with grains in a given test sample and thus may be useful for defining mean threshold shear velocity values associated with unusual mixtures of grain sizes and densities.

(b) Specific results

1.7-1.4mm ballotini

The sequential erosion of 1.7-1.4mm ballotini strips is presented in Figure 4.3. A reduction in $\bar{\bar{U}}_{*T}$ values from $1.61ms^{-1}$ at 10cm from Station A to $0.69ms^{-1}$ at 85cm from Station A is clearly shown (Table 4.18). Figures 4.10(a) and 4.10(b) show that erosion of strips in this size range proceeded in a similar way regardless of their position on the plate, and that the loss of material was distributed fairly evenly over the entire strip length. As the force required to move a grain is the same irrespective of its position on the plate surface then the local instantaneous shear stress (U_{*I}) at the rear of the plate must be at least two and a half times the magnitude of the measured average shear stress ($\bar{U}_{*}$). This result suggests that mean surface shear velocity is

a relatively insensitive measure of the forces acting on grains at the threshold in turbulent flow conditions as it appears that threshold conditions are more strongly associated with peak fluctuations in U_{*I}. This suggestion is, therefore, consistent with the arguments above.

710-600μm and 355-300μm ballotini

Figures 4.4 and 4.5 which depicts the erosion sequences for strips of 710-600μm and 355-300μm ballotini respectively, also show that $\overline{U}_{*T}$ values decrease with increasing distance downwind of Station A. This downwind reduction in $\overline{U}_{*T}$ probably reflects a corresponding increase in the magnitude of the fluctuating instantaneous shear velocity component, U_{*I}, and is a characteristic feature of a developing turbulent boundary layer.

Figures 4.11 and 4.12 show graphically the strip erosion sequences for 710-600μm and 355-300μm ballotini, respectively. Two different erosion patterns are evident in these figures. Figures 4.11(a) and 4.12(a) (i.e. strips at 10cm from Station A) show that particles were initially entrained from localised areas of the strips. Flow on this region of the plate may still have been transitional and, therefore, probably possessed some of the characteristics associated with laminar flow, particularly on the aerodynamically smoother 355-300μm ballotini. In such conditions, local fluctuations in shear velocity would be smaller than those associated with turbulent flow and thus it is likely that the spatial and temporal distribution of bed shear stress was fairly even over the entire strip width. However, the distinct gaps in the eroding strips (Figures 4.11(a) and 4.12(b)) suggest that this condition was modified in some way and indicate the presence of localised regions of

relatively high shear stress at the surface. It is suggested that these flow anomalies reflect the downwind passage of turbulent spots (2.4.1) which are characteristic of transitional boundary layer flow. In these conditions, turbulent spots would give rise to a 'wedge' of highly turbulent air characterised by instantaneous shear stress values well in excess of the mean. The interaction between test strips and this disturbed flow would probably be manifest as localised regions of erosion over the span of the strips. Figures 4.11(a) and 4.11(b) show that further velocity increases resulted in the formation of additional breaks in the strips until most of the test material was eroded. This is thought to result from both an increase in the spatial and temporal frequency of turbulent spot passage and a the propagation of erosion by flow channelling and acceleration through gaps in the eroding strips.

At 130cm from Station A, (Figures 4.11(b) and 4.12(b)), the erosion sequences were similar to those shown in Figures 4.10(a) and 4.10(b), (i.e. 1.7-1.4mm ballotini). From the evidence of boundary layer velocity profile measurements and Re# values, it was clear that these sequences were associated with turbulent flow. Erosion along the strips was fairly regular, leaving frequent small 'islands' of material which were gradually reduced in size or eroded completely as the wind velocity was increased. Small gaps, which developed along the strips, also apparently channelled the flow and caused grains to be slowly winnowed out.

An additional feature which became increasingly obvious as smaller grains were tested, was that the majority of erosion occurred at the downwind edge of the strip. This is shown well in Figure 4.12(b) for the case of 355-300μm ballotini. Although no substantial evidence is

available it seems likely that the first few upwind grains of the strip acted as a 'fence' and generated additional turbulence at the rear of the strip. This additional turbulence was apparently sufficient to initiate particle entrainment from the downwind edge of the strip. It is also possible that grains entrained from the upwind edge of the strip were involved in violent collisions with strip material a little further downwind and so gave rise to the observed pattern of erosion through the avalanching process. Visual observation of strip erosion, however, indicated that avalanching was a relatively infrequent phenomenon and that most grain entrainment resulted from the direct shear force applied to the strip by the wind.

180-150μm ballotini

The sequential erosion of 180-150μm ballotini strips is shown in Figures 4.6(a) and 4.6(b). These figures show that at 5cm from Station A, mean threshold shear velocity ($\bar{U}_{*T}$) exceeded $1ms^{-1}$. Downwind of this position, $\bar{U}_{*T}$ values slowly decreased and reached a minimum mean value of $0.2ms^{-1}$ at 40cm from Station A. However, as Figure 4.6(b) shows, the mean threshold shear velocity again rose to a value of $0.73ms^{-1}$ at 55cm from Station A and then slowly decreased to a minimum value of $0.23ms^{-1}$ at 130cm from Station A. These results differ markedly in two respects from the erosion sequences recorded for 1.7-1.4mm, 710-600μm and 355-300μm ballotini described above. Firstly, the range of shear velocities required to erode strips at 5cm and 10cm from Station A is significantly larger than that recorded for strips of other test materials and that recorded for strips of the same test material at other positions on the surface of the plate. Secondly, a significant increase in mean threshold shear velocity was recorded for

the strip of 180-150μm ballotini at 55cm downwind from Station A. All the other test materials previously examined showed a consistent decrease in $\overline{\overline{U}}_{*T}$ as strips were tested progressively further downwind. These apparently anomalous results may be explained by considering the characteristics of the developing boundary layer on the 180-150μm ballotini surface, and the influence of external factors such as variable particle cohesion brought about by atmospheric moisture absorption.

The large range of shear velocities required to erode 180-150μm ballotini strips at 5cm and 10cm from Station A suggests that the threshold shear stress distribution associated with particles in these strips was substantially different from that associated with other strips. The increased variance of $\overline{U}_{*T}$ values of grains in this position on the plate cannot be explained with the available experimental data, but it may be speculated that one reason may be the occurrance of a local increase in interparticle cohesion at these sites due to the absorption of moisture from the wind prior to and during these experimental runs.

It is also possible that these results arose as a consequence of a local flow anomaly such as a laminar separation bubble close to the leading edge of the plate. In such conditions, $\overline{U}_{*}$ values determined using the momentum integral method would be completely erroneous and may also have contributed to the anomalous results recorded in this region. At the time of these investigations, these spurious results were not immediately apparent and only detected during subsequent data analysis stages. It was not possible to re-examine the erosion of 180-150μm ballotini strips in this position on the plate owing to constraints on the availability of the wind tunnel facilities.

The initial fall in mean threshold shear velocity with increasing distance downwind of Station A, the sudden rise again at 55cm from Station A and the subsequent reduction in $\overline{U}_{*T}$ values towards the back of the plate may be due in part to the changing downwind characteristics of the developing boundary layer on this surface. In 4.5.1 it was shown that 180-150μm ballotini were sufficiently small to permit extended propagation of essentially laminar flow for at least 40cm downwind of Station A at Reynolds numbers characteristic of threshold conditions for this test material. Downwind of 40cm, the boundary layer was transitional and by 55cm was turbulent. The sudden increase in $\overline{U}_{*T}$ values recorded for the 180-150μm ballotini strip at 55cm downwind of Station A was discussed in 5.4.3 and it was suggested that the viscous sublayer at this point was sufficiently thick to shelter individual grains from the much faster moving air above it. Such shelter effects would obviously increase the mean shear velocity required to initiate motion. The subsequent downwind reduction in $\overline{U}_{*T}$ values recorded for strips at 70, 85 and 130cm from Station A resulted from a downwind increase in peak shear velocity values as the intensity of boundary layer turbulence increased. In this case the interaction between the distributions of bed shear velocity and threshold shear velocity followed the general pattern described in 4.5.4(a).

This explanation is, however, complicated by a shifting of the transition region in response to increases in the wind speed during the strip erosion sequences. As the Reynolds number for the plate ($\overline{U}_{\infty}\ x/\nu$) governs the position of the transition point, increasing the wind speed to erode a further portion of a strip established a new transition region upwind of the previous one. The strip was, therefore, now subjected to a different boundary layer flow regime. Thus, the apparently anomalous

$\overline{U}_{*T}$ values recorded for 180-150μm ballotini strips in transitional boundary layer flow appear to have resulted from the combined effects of (i) varying degrees of viscous sublayer protection, and (ii) changing flow characteristics brought about by an upwind migration of the transition region in response to increases in wind velocity. However, the precise effects of these changes on the erosion of test strips in this region of the plate could not be assessed accurately using the available data and must remain speculative.

The outline diagrams of the erosion sequences for 180-150μm ballotini at 10 and 40cm from Station A are shown in Figures 4.13(a) and 4.13(b) respectively. These figures show that small breaks in the strips were eroded into large gaps by flow channelling, and illustrated the tendency for erosion to proceed from the rear of the strip in the manner described above. This pattern of erosion appears to be indicative of laminar and transitional boundary layer flow regimes and is thought to be caused by the passage of the highly disturbed flow associated with cycles of upwind turbulent spot formation (see above). Figures 4.13(c) and 4.13(d) show the strip erosion sequences at 55cm and 130cm from Station A respectively to be quite distinct from the sequences shown in Figures 4.13(a) and 4.13(b). The former sequences represent the entrainment of particles by fully turbulent flow where, after a certain degree of erosion, small 'islands' of loose material remain. These sequences are similar in character to those shown in Figures 4.10, 4.11(b) and 4.12(b) and described above.

180-150μm aeolian sand

The erosion sequences for 180-150μm aeolian sand strips are

illustrated in Figures 4.7(a) and 4.7(b). Mean threshold shear velocity decreases from 0.69ms^{-1} at 5cm downwind of Station A to 0.36ms^{-1} at 40cm. It then increases to 0.4ms^{-1} at 55cm and subsequently falls to a minimum value of 0.22ms^{-1} at 130cm downwind of Station A in a trend quite similar to that for 180-150μm ballotini. This increase in mean threshold shear velocity at 55cm is again attributable to viscous sublayer shelter as described above. In 4.5.1(b) evidence of a significantly greater rate of boundary layer thickening over the aeolian sand surface was presented. This is thought to be due to the increase in the aerodynamic roughness of the surface at a given Reynolds number and was probably brought about by differences in particle shape and sorting between ballotini and sand. As a result, $\bar{U}_{*T}$ values were found to be consistently lower for 180-150μm aeolian sand than 180-150μm ballotini.

The range of $\bar{U}_{*T}$ values recorded for erosion of 180-150μm aeolian sand at 5cm and 10cm downwind from Station A was not as wide as that for ballotini of the same size at these positions. On the basis of these results, it appears that significant modifications to $\bar{U}_{*T}$ values brought about by absorption of atmospheric moisture and possible flow separation in the case of 180-150μm ballotini are less evident.

710-600μm sugar crystals

The erosion sequences recorded for strips of 710-600μm sugar crystals are illustrated in Figure 4.8. These results cannot be compared directly with those for 710-600μm ballotini owing to differences in particle density (Table 3.4). However, comparison may be facilitated by the use of certain dimensionless expressions which are discussed in Chapter 5. The sequence of strip erosion is similar to that recorded for

ballotini and shows that once the threshold is exceeded, erosion proceeds rapidly in response to relatively small increases in mean shear velocity. Further, as with ballotini, it can be seen that measured threshold shear velocities at the front of the plate are approximately three and a half times as great as those at the rear.

The outline traces of strip erosion for sugar crystals at 10 and 130cm downwind from Station A (illustrated in Figures 4.15(a) and 4.15(b)) show, however, that the pattern of erosion associated with the strips of sugar crystals differs markedly from that recorded for 710-600 μm ballotini. In fact this pattern almost suggests laminar or transitional flow conditions over the entire length of the plate and thereby contradicts evidence from boundary layer velocity profile measurements. This effect is probably associated with moisture absorption by the hygroscopic sugar crystals. Despite the precautions taken to ensure the material was as dry as possible and that experiments were conducted on days of low atmospheric humidity, moisture played a crucial role in raising the mean threshold shear velocity values and caused individual crystals to stick both to themselves and to the bed. Further discussion of this phenomenon is given in Chapter 5.

180-150μm salt crystals

The erosion sequences recorded for 180-150μm salt crystal strips are illustrated in Figure 4.9 and are similar to those already presented and discussed for other materials in this size range. The range of mean threshold shear velocities normally associated with such a spread of strip positions on the plate was, however, greatly reduced in this case, and the strip of salt crystals at 10cm from Station A did not display the

great resistance to erosion recorded for 180-150μm ballotini and sand at this position. It is suggested that the greater erosion susceptibility of salt crystals may be related to differences in particle shape and density, and to undetected flow modifications caused by this surface.

The pattern of erosion shown in Figures 4.16(a) and 4.16(b) is rather confusing and suggests an uneven distribution of flow across the plate. This is particularly true for the pattern shown in Figure 4.16(b) where erosion is apparently biased to the left of the strip. Moisture is again thought to be the dominant factor in determining the erosion pattern of salt strips despite the inclusion of small quantities of desiccant particles. Further discussion and interpretation of these results is given in Chapter 5.

4.6 Summary of experimental results

4.6.1 Developing boundary layer on the plate

The developing boundary layer on the plate was not found to be significantly affected by the flow adjacent to the walls and roof of the working section of the wind tunnel. Values of the boundary layer parameters δ, δ^* and θ_M were found to be governed by Re_x and the surface roughness. Maximum and minimum δ, δ^* and θ_M values were associated with 1.7-1.4mm and 180-150μm ballotini respectively, and the downwind rate of increase in these parameters was found to be greatest over the largest particles and least over the smallest particles. The most rapid downwind increases were associated with the regions of transitional boundary layer flow on the 180-150μm ballotini and aeolian sand surfaces. Values of the boundary layer shape parameter H were

within the stability limits given by Schlichting (1979).

Characteristics of the developing boundary layer on the plate were also assessed using the parameters δ_{sub} and Re♯. These parameters indicate that at threshold wind speeds the laminar boundary layer was restricted to a narrow region extending no more than 40cm downwind from Station A on 180-150μm ballotini and aeolian sand. Over particles greater than 180μm, transition generally occurred very close to the leading edge of the plate so that the boundary layer quickly became turbulent. Transition occurred at around 40cm downwind of Station A over test surfaces smaller than 180μm and transitional flow was found to occupy a region extending between approximately 40cm and 55cm downwind of Station A. Further downwind, the boundary layer over these particles then became turbulent. Strip erosion sequences recorded at sites close to the leading edge of the plate using test material smaller than 710μm and greater than 180μm indicate that transitional boundary layer flow was dominant in a region extending approximately 25cm downwind from Station A.

4.6.2 Theoretical flow conditions at the scale of grains

Dimensionless boundary layer wind velocity profiles were calculated using standard solutions to the functional relationship $U/U_\infty = f(yU_*/\nu)$ for both laminar and turbulent boundary layers. Appropriate grain projection height scaling on the resulting graphs of U/U_∞ against yU_*/ν permitted a theoretical assessment of local threshold flow conditions at the scale of single grains. The results indicate that some degree of viscous sublayer shelter was given to the majority of test particles irrespective of their location on the surface of the plate. It is considered, however, that these theoretical conditions are

unrepresentative of conditions on the surface of the roughened plate where vortex shedding by upwind roughness elements is likely to suppress significant viscous sublayer development. Only in the case of transitional/turbulent flows on 180-150μm surfaces did the results suggest that viscous sublayer protection may have had a significant effect in raising the aeolian threshold value. These theoretical considerations also indicate that at the threshold, grains were likely to be sited well within the inner region of the turbulent boundary layer and were, therefore, exposed to the full force of the fluid inrush cycles associated with turbulence production in this region.

4.6.3 Erosion of test strips

Strip erosion data plotted in the form of the percentage of strip area remaining uneroded versus mean shear velocity gave asymptotic erosion curves. The form of such curves was generally found to be similar irrespective of the test material or position on the surface of the plate. It was also found that the mean threshold shear velocity value for a given test material generally decreased with increasing distance downwind from Station A.

The asymptotic erosion curves are shown to express the range of $\bar{U}_{*T}$ values ascribed to individual particles in a test sample. Plotting tan ($\%A/\bar{U}_{*}$) versus $\bar{U}_{*}$ gives a curve with similar characteristics to those obtained by Grass (1970) for incipient grain motion in water. It is considered that strip erosion provides a suitable method of obtaining the characteristic threshold distribution curve ($P(\bar{U}_{*T})$) for a given sediment in air.

The characteristic erosion curves also provides a means for objectively defining the aeolian threshold condition. This involved extrapolation of the near-linear, central section of the curve to intersect with certain specified ordinate values. In this way, threshold conditions can be defined using any chosen criteria of motion.

Using the entrainment model proposed by Grass (1970), it is shown that the distribution of shear velocity associated with the boundary layer flow ($P(U_*)$) probably became increasingly positively skewed as the Reynolds number (Re_x) increased along the plate. As entrainment is probably instigated by the peak fluctuations in shear velocity, the downwind reduction in mean threshold shear velocity was thought to reflect the changing characteristics of the $P(U_*)$ distribution.

However, in the case of 180-150μm ballotini and aeolian sand the mean threshold shear velocity was found to increase unexpectedly at 55cm downwind of Station A. Downwind of this site, $\overline{U}_{*T}$ values again decrease in the usual manner. Analysis of the local flow conditions revealed that particles were probably sheltered by the viscous sublayer in this region and were thus less susceptible to entrainment. The precise nature of the interactions between this transitional/turbulent boundary layer flow and 180-150μm particles could not be assessed in the present experiments as the increases in wind speed necessary to erode the test strips also changed the characteristics of the local flow regime.

The photographic record of strip erosion revealed some fundamental differences in the patterns of entrainment at different positions on the surface of the plate. At sites close to the leading

edge, large gaps were eroded in the strips in response to relatively small increases in wind speed. It is speculated that these gaps were associated with the passage of turbulent spots. At sites well downwind of the leading edge, entrainment occurred from localized regions of the strip and erosion sites were observed to be distributed fairly evenly across the entire span of the strip. As erosion proceeded, frequent small 'islands' of grains were left which slowly eroded as the wind speed was increased. It is considered that this erosion pattern may reflect the spatial distribution of fluid inrush events.

Investigations into the effects of particle shape on aeolian threshold conditions were inconclusive. The characteristics of the boundary layer on the 180-150μm aeolian sand surface and the associated $\bar{U}_{*T}$ values were found to be significantly different from the boundary layer and $\bar{U}_{*T}$ values measured over the 180-150μm ballotini surface. However, it was not possible to assess whether these differences arose directly from a variation in particle shape or as a result of moisture effects and differences in the distribution of particle sizes within each test material. Sugar and salt crystals proved to be unsuitable materials in these experiments, partly due to the increased cohesive forces acting between particles caused by moisture absorption at even moderate atmospheric humidities, and partly due to the density differences between these materials and ballotini. Consequently, the effect of particle shape on aeolian threshold conditions for these materials cannot be ascertained directly by comparison with results obtained using ballotini.

Particle entrainment, whether by laminar, transitional or turbulent boundary layer flow, was generally preceded by sporadic particle vibration. The particles in strips at the rear of the plate

were observed to oscillate with greater violence and frequency than those near Station A. Entrained particles were observed to enter saltation by a progressive rolling and bouncing motion with grains acquiring greater height and forward velocity at each successive collision with the bed. On no occasion were particles observed to rise vertically from the bed.

4.7 Conclusion

The developing boundary layer on the plate has provided an opportunity to investigate aeolian threshold conditions in a continuum of boundary layer flow regimes using narrow sediment strips at selected study sites on the surface of the plate. The parameters used to analyse the characteristics of the developing boundary layer on the roughened surface of the plate validated the assumptions made in Chapter 2 regarding its characteristics and confirmed that controlled and reproducible flow conditions could be generated at any chosen study site. Experimental evidence shows that the two main factors controlling aeolian threshold values are (i) the characteristics of the local flow regime; and (ii) the mean diameter of the test grains. The effect of particle shape could not be assessed directly owing to differences in particle density. Further, it seems that inter-particle cohesion tended to obscure any differences in aeolian threholds brought about by virtue of shape differences between test grains.

On the basis of evidence presented above, it may be concluded that the downwind reduction in $\overline{\overline{U}}_{*T}$ values reflects a corresponding increase in the instantaneous peak shear velocity. This downwind increase in peak shear velocity values is thought to result from a corresponding downwind increase in the spatial and temporal frequency and

intensity of fluid bursting cycles close to the surface of the plate (as indicated by a downwind increase in the Reynolds number (Re_x), (Corino and Brodkey, 1969; Blackwelder and Eckelman, 1979)).

It is suggested that the entrainment model proposed by Grass (1970) is the most appropriate in the context of aeolian entrainment processes as it considers both the fluctuating component of bed shear velocity and the wide variability in the entrainment susceptibility of individual grains in a sediment bed identified in these investigations. However, in order to predict the aeolian threshold using this model, it is necessary to determine the statistical characteristics of the $P(U_*)$ and $P(U_{*T})$ distributions. In this investigation it was not possible to determine the $P(U_*)$ distribution with the available instruments, nor was it possible to obtain such data from the literature as virtually nothing is known about the spatial and temporal fluctuations of bed shear velocity on rough surfaces in air.

It is found, however, that analysis of strip erosion characteristics provides an effective means of determining the $P(U_{*T})$ distribution in air for any given sediment and position on the plate. The $P(U_{*T})$ distribution obtained in this way is, therefore, specific to both the sediment and the local flow regime. In addition to the technical simplicity of this surrogate method for determination of the $P(U_{*T})$ distribution, it also circumvents some of the problems associated with measuring $P(U_{*T})$ using beds of erosive grains. Grass (1970) and Williams and Kemp (1971) note that at threshold flow velocities, beds of non-cohesive particles were characterised by the growth of elongated surface undulations and, after a period of time, these features induced flow separation and spontaneous ripple formation.

In such conditions it is obviously impossible to take accurate, interactive measurements of the critical shear velocity values associated with the less susceptible grains owing to the changing nature of the local flow regime. This problem does not arise when considering the erosion of test strips on a plate as the test bed is rigid and thus unaffected by any tendency for incipient ripple formation. It is concluded that this method provides an effective means for the determination of $P(U_{*T})$ distributions in air using relatively simple techniques, and is applicable to any mixture of grain sizes, shapes and densities.

The characteristic asymptotic erosion curves associated with the strips can also be used to define a specified degree of aeolian entrainment. In conclusion it is considered that this information could be applied to predict the amount of material likely to be moved at a certain wind speed from a given population of mixed grains, as the curve may be derived for any mixture of grain sizes, shapes and densities. Threshold values determined in this way are also unaffected by changes in the local flow regime induced by shifting bed material, and to a large extent are unaffected by grain avalanching provided that the strip is sufficiently slender.

The theoretical analysis of local threshold flow conditions at the scale of single grains indicates that particles were sited well within the inner region of the turbulent boundary layer and were, therefore, probably exposed to the high shear velocities generated by the fluid inrush cycles associated with bursting processes in this region. On the basis of this evidence it may be concluded that in air, aeolian entrainment is probably accomplished by the high shear velocities

associated with fluid sweeps as the majority of this energy is concentrated at levels where erosive grains are likely to lie.

In the context of the overall objectives of this investigation of aeolian entrainment thresholds, these experiments have revealed that even closely graded particles are characterised by a range of entrainment susceptibilities, and that the aeolian threshold condition is largely controlled by the frequency and spatial distribution of peak shear stress events close to the bed. The primary mechanism giving rise to these high shear stress events is likely to arise from the sweeps of high velocity air which occur during the turbulent bursting cycle. On the basis of the available experimental evidence presented here, the entrainment model proposed by Grass (1970) appears to provide the most satisfactory explanation of aeolian threshold conditions as it accounts for the probablistic nature of entrainment processes revealed by these experiments.

Material		Distance from Station A, cm								
		5	10	15	25	40	55	70	85	130
Ballotini	1.7 to 1.4mm		▒		▒	▒	▒	▒	▒	
	710 to 600μm		▒		▒	▒	▒		▒	▒
	355 to 300μm		▒		▒	▒	▒		▒	▒
	180 to 150μm	▒	▒	▒	▒	▒	▒	▒	▒	▒
Sugar crystals	710 to 600μm		▒						▒	▒
Aeolian sand	180 to 150μm	▒	▒		▒	▒	▒	▒	▒	▒
Salt crystals	180 to 150μm		▒						▒	▒

▒ strip positions studied

Table 4.1 Test materials and strip positions used in the plate experiments.

x, (m)	0.10	0.25	0.40	0.55	0.70	0.85
$\bar{U}_\infty$, (ms^{-1})	16.4	16.3	16.2	15.6	15.5	16.6
δ, x 10^{-3}(m)	27.7	32.8	36.4	40.0	43.0	47.5
δ^*, x 10^{-3}(m)	15.3	16.7	19.9	21.4	22.9	26.8
θ_M, x 10^{-3}(m)	9.2	10.3	12.3	13.1	14.4	17.10
$H=\delta^*/\theta_M$	1.66	1.62	1.62	1.63	1.59	1.57
$d\theta_M/dx$ x 10^{-3}	8.58	4.37	3.59	3.41	2.44	1.36
$\bar{\tau}$, (kg m^{-2})	2.84	1.43	1.16	1.02	0.73	0.46
$\bar{U}_*$, (ms^{-1})	1.52	1.08	0.97	0.91	0.77	0.61
δ_{sub} x 10^{-4}(m)	1.13	1.59	1.77	1.89	2.24	2.81
$5\delta_{sub}$ (μm)	565	795	885	945	1120	1405
$Re\# = \bar{U}_e\delta^*/\nu$ x 10^3	16.9	18.4	21.8	22.6	24.0	30.1

Table 4.2 Boundary layer parameters over 1.7-1.4mm ballotini (symbols defined in text).

x, (m)	0.10	0.25	0.40	0.55	0.85	1.30
$\bar{U}_\infty$, (ms^{-1})	12.8	12.5	12.4	12.5	12.6	12.3
δ, $x10^{-3}$(m)	11.2	15.6	18.5	22.1	27.9	32.3
δ^*, $x10^{-3}$(m)	8.4	8.9	10.5	11.8	14.1	16.2
θ_M, $x10^{-3}$(m)	4.6	4.9	6.10	6.8	8.20	9.60
$H=\delta^*/\theta_M$	1.83	1.81	1.72	1.73	1.71	1.68
$d\theta_M/dx \times 10^{-3}$	11.31	6.14	4.92	3.33	1.59	0.97
$\bar{\tau}$, ($kg\ m^{-2}$)	2.28	1.18	0.93	0.64	0.31	0.18
$\bar{U}_*$, (ms^{-1})	1.36	0.98	0.87	0.72	0.50	0.38
$\delta_{sub} x10^{-4}$(m)	1.26	1.75	1.97	2.38	3.43	4.52
$5\delta_{sub}$ (μm)	630	875	985	1190	1715	2260
Re# = $\bar{U}_*\delta^*/\nu \times 10^3$	7.3	7.5	8.8	9.9	12.0	13.5

Table 4.3 Boundary layer parameters over 710-600μm ballotini (symbols defined in text).

x, (m)	0.10	0.25	0.40	0.55	0.85	1.30
$\bar{U}_\infty$, (ms^{-1})	11.2	11.2	11.2	11.1	10.8	10.2
δ, $x10^{-3}$(m)	4.6	5.2	7.5	13.2	16.6	23.0
δ^*, $x10^{-3}$(m)	1.96	3.34	4.6	5.05	5.95	6.63
θ_M, $x10^{-3}$(m)	0.98	1.67	2.16	2.54	3.27	3.65
$H=\delta^*/\theta_M$	2.01	2.00	2.12	1.99	1.82	1.76
$d\theta_M/dx \times 10^{-3}$	2.39	2.01	1.81	1.39	2.72	0.78
$\bar{\tau}$, (kg m^{-2})	0.37	0.31	0.28	0.21	0.39	0.10
$\bar{U}_*$, (ms^{-1})	0.55	0.50	0.48	0.41	0.39	0.29
$\delta_{sub} x10^{-4}$(m)	3.12	3.43	3.58	4.19	4.40	5.92
$5\delta_{sub}$ (μm)	1560	1715	1790	2095	2200	2960
$Re_\# = \bar{U}_\# \delta^*/\nu \times 10^3$	1.48	2.53	3.5	3.8	4.3	4.6

Table 4.4 Boundary layer parameters over 355-300μm ballotini (symbols defined in text).

x, (m)	0.05	0.10	0.15	0.25	0.40	0.55	0.70	0.85	1.30
$\bar{U}_\infty$, (ms^{-1})	13.70	12.80	12.80	12.5	12.0	12.0	11.2	11.6	11.8
δ, $x10^{-3}$(m)	4.1	5.0	5.9	7.8	9.2	16.1	18.4	19.9	21.0
δ^*, $x10^{-3}$(m)	0.88	1.22	1.51	2.07	3.30	4.33	4.93	5.23	5.63
θ_M, $x10^{-3}$(m)	0.35	0.50	0.64	0.92	1.64	2.21	2.50	2.86	3.11
$H=\delta^*/\theta_M$	2.51	2.43	2.36	2.25	2.01	1.96	1.97	1.83	1.81
$d\theta_M/dx \times 10^{-3}$	4.03	2.43	1.19	0.94	1.41	4.01	3.05	2.72	0.82
$\bar{\tau}$, kg (m^{-2})	0.93	0.49	0.24	0.18	0.25	0.71	0.47	0.45	0.14
$\bar{U}_*$, (ms^{-1})	0.87	0.63	0.44	0.38	0.24	0.76	0.62	0.61	0.34
$\delta_{sub}x10^{-4}$(m)	1.97	2.73	3.90	4.52	7.15	2.26	2.77	2.81	5.05
$5\delta_{sub}$ (μm)	985	1365	1950	2260	3575	1130	1385	1405	2525
$Re\# = \bar{U}_*\delta^*/\nu x10^3$	0.82	1.06	1.31	1.75	2.7	3.51	3.7	4.1	4.5

Table 4.5 Boundary layer parameters over 180-150μm ballotini (symbols defined in text).

x, (m)	0.05	0.10	0.25	0.40	0.55	0.70	0.85	1.30
$\bar{U}_\infty$, (ms^{-1})	13.3	11.3	11.20	11.10	10.6	10.9	10.4	9.9
δ, $x10^{-3}$(m)	4.3	6.0	7.6	9.36	15.9	18.6	20.2	22.1
δ^*, $x10^{-3}$(m)	0.83	1.11	2.14	2.68	3.66	4.58	4.76	4.97
θ_M, $x10^{-3}$(m)	0.36	0.49	1.02	1.51	1.97	2.53	2.77	3.03
$H=\delta^*/\theta_M$	2.31	2.10	2.10	1.77	1.86	1.81	1.72	1.64
$d\theta_M/dx \times 10^{-3}$	1.88	1.27	1.49	1.85	1.66	1.03	0.75	0.83
$\bar{\tau}$, (kg m^{-2})	0.41	0.20	0.23	0.28	0.23	0.15	0.10	0.10
$\bar{U}_*$, (ms^{-1})	0.58	0.40	0.43	0.48	0.43	0.35	0.28	0.29
$\delta_{sub} x10^{-4}$(m)	2.96	4.29	3.99	3.58	3.99	4.91	6.13	5.92
$5\delta_{sub}$ (μm)	1480	2145	1995	1290	1195	2455	3065	2960
Re# = $\bar{U}_* \delta^*/ x10^3$	0.75	0.85	1.7	2.0	2.6	3.4	3.3	3.3

Table 4.6 Boundary layer parameters over 180-150μm aeolian sand (symbols defined in text).

	x, distance from Station A, cm																	
EROSION PERIOD	10			25			40			55			70			85		
	%	$\bar{U}_*$	$\bar{U}_\infty$	%	$\bar{U}_*$	$\bar{U}_\infty$	%	$\bar{U}_*$	$\bar{U}_\infty$	%	$\bar{U}_*$	$\bar{U}_\infty$	%	$\bar{U}_*$	$\bar{U}_\infty$	%	$\bar{U}_*$	$\bar{U}_\infty$
1.	100	0	0	100	0	0	100	0	0	100	0	0	100	0	0	100	0	0
2.	98	1.52	16.4	98	1.08	16.3	98	0.97	16.2	99	0.91	15.6	98	0.77	15.5	99	0.61	16.6
3.	95	1.55	18.2	96	1.11	17.9	97	0.97	17.9	91	0.96	17.3	96	0.79	17.1	91	0.64	18.8
4.	80	1.66	20.3	85	1.19	20.2	87	1.07	20.1	81	1.00	19.5	79	0.84	19.2	70	0.68	20
5.	40	1.72	21.6	61	1.26	21.5	56	1.14	21.6	71	1.00	20.6	13	0.86	20.5	8	0.75	21.6
6.	0	/	25.9	3	1.37	23.1	2	1.23	23.1	6	1.06	22.3	1	0.90	22.7	3	0.78	22.2
7.			/	0	1.41	23.8	0	/	23.8	1	1.09	22.9	0	/	23.9			
$\bar{U}_*, \bar{U}_\infty$ ms^{-1}	-	1.61	20.5	-	1.24	20.5	-	1.08	20.4	-	1.00	19.7	-	0.83	19.8	-	0.69	19.8

Table 4.7 Sequential erosion and associated airflow velocities for 1.7-1.4mm ballotini strips (symbols defined in text).

EROSION PERIOD	x, distance from Station A, cm																	
	10			25			40			55			85			130		
	%	$\bar{U}_*$	$\bar{U}_\infty$	%	$\bar{U}_*$	$\bar{U}_\infty$	%	$\bar{U}_*$	$\bar{U}_\infty$	%	$\bar{U}_*$	$\bar{U}_\infty$	%	$\bar{U}_*$	$\bar{U}_\infty$	%	$\bar{U}_*$	$\bar{U}_\infty$
1.	99	0.99	9.9	99	0.86	10.1	96	0.74	9.2	99	0.58	10.1	99	0.48	10.1	99	0.34	10.1
2.	39	1.21	11.2	97	0.89	11.6	/	/	10.1	/	/	10.7	98	0.49	10.8	98	0.35	10.8
3.	5	1.31	12.1	60	0.98	12.5	51	0.83	11.5	79	0.67	11.5	96	0.49	11.6	97	0.36	11.5
4.	2	1.36	12.8	12	1.05	13.1	19	0.87	12.4	36	0.72	12.5	82	0.50	12.6	90	0.38	12.3
5.	1	/	14.5	0.3	1.11	13.8	2	0.91	13.2	14	0.76	13.1	45	0.53	13.1	57	0.41	13.0
6.							0.3	0.94	13.8	2	0.79	13.9	14	0.54	13.9	26	0.48	13.8
$\bar{\bar{U}}_*, \bar{\bar{U}}_\infty$ ms^{-1}	—	1.22	12.1	—	0.98	12.2	—	0.86	11.7	—	0.70	12.0	—	0.51	12.0	—	0.39	11.9

Table 4.8 Sequential erosion and associated airflow velocities for 710-600μm ballotini strips (symbols defined in text).

EROSION PERIOD	x, distance from Station A, cm																	
	10			25			40			55			85			130		
	%	$\bar{\bar{U}}_*$	$\bar{\bar{U}}_\infty$	%	$\bar{\bar{U}}_*$	$\bar{\bar{U}}_\infty$	%	$\bar{\bar{U}}_*$	$\bar{\bar{U}}_\infty$	%	$\bar{\bar{U}}_*$	$\bar{\bar{U}}_\infty$	%	$\bar{\bar{U}}_*$	$\bar{\bar{U}}_\infty$	%	$\bar{\bar{U}}_*$	$\bar{\bar{U}}_\infty$
1.	97	0.55	11.2	90	0.50	11.2	95	0.42	9.2	95	0.33	8.9	89	0.28	8.9	98	0.19	8.2
2.	84	0.57	12.1	58	0.54	12.0	39	0.45	10.8	51	0.40	10.0	64	0.30	9.3	90	0.25	8.9
3.	55	0.66	13.4	21	0.58	12.8	25	0.48	11.2	39	0.41	10.7	22	0.32	10.2	45	0.28	9.7
4.	19	0.73	14.2	9	0.58	13.8	11	0.50	11.9	22	0.41	11.1	0.3	0.39	10.8	24	0.29	10.2
5.	5	/	14.9	4	/	14.0	5	0.51	12.6	10	0.45	11.9				3	-	10.9
6.	1	/	16.1	0.7	/	14.7										0.4	-	11.5
7.			13.7													0.1	-	12.0
$\bar{\bar{U}}_*, \bar{\bar{U}}_\infty$ ms^{-1}	—	0.63	13.7	—	0.55	13.1	—	0.47	11.1	—	0.40	10.52	—	0.32	9.8	—	0.25	10.2

Table 4.9 Sequential erosion and associated airflow velocities for 355-300μm ballotini strips (symbols defined in text).

	x, distance from Station A, cm																											
	5			10			15			25			40			55			70			85			130		
EROSION PERIOD	%	$\bar{U}_*$	$\bar{U}_\infty$	%	$\bar{U}_*$	$\bar{U}_\infty$	%	$\bar{U}_*$	$\bar{U}_\infty$	%	$\bar{U}_*$	$\bar{U}_\infty$	%	$\bar{U}_*$	$\bar{U}_\infty$	%	$\bar{U}_*$	$\bar{U}_\infty$	%	$\bar{U}_*$	$\bar{U}_\infty$	%	$\bar{U}_*$	$\bar{U}_\infty$	%	$\bar{U}_*$	$\bar{U}_\infty$
1.	100	0	0	100	0	0	100	0	0	100	0	0	100	0	0	100	0	0	100	0	0	100	0	0	100	.0	0
2.	98	-	11.9	97	0.44	11.2	97	0.35	10.5	97	0.29	9.5	66	0.19	9.9	99	0.46	8.7	52	0.53	9.1	71	0.40	8.9	96	0.11	7.9
3.	97	-	12.8	88	0.63	12.8	75	0.4	11.7	95	0.31	10.4	20	0.22	11.1	89	0.64	9.4	29	0.58	10.0	45	0.45	9.4	69	0.18	8.7
4.	80	0.87	13.7	79	0.73	13.9	44	0.44	12.8	10	0.38	12.5	10	0.24	12.0	76	0.7	10.1	20	0.59	10.6	19	0.51	10.4	24	0.29	9.6
5.	40	1.13	14.4	69	0.81	14.9	11	0.52	14.1	2	-	13.4	3	-	12.7	68	0.71	11.1	7	0.63	11.2	6	0.54	11.0	10	0.33	10.3
6.	15	1.29	15.2	34	1.09	16.1	5	0.58	15.0	0.7	0.39	14.5	0.3	-	13.5	24	0.76	12.0	0.6	-	11.9	0.8	0.60	11.6	4	-	10.8
7.	2	1.54	15.9	8	-	17.3	0.2	0.67	16.3	0.2	-	15.6				13	-	12.6	0.3		12.6			12.4	1	0.34	11.8
8.	0.5	-	16.7			18.6											7	-	14.0								13.3
$\bar{\bar{U}}_*, \bar{\bar{U}}_\infty$ ms^{-1}		1.21	14.4		0.74	14.9		0.49	13.4		0.34	12.7		0.22	11.8		0.65	11.1		0.58	10.9		0.50	10.6		0.25	10.3

Table 4.10 Sequential erosion and associated airflow velocities for; 180-150μm ballotini strips (symbols defined in text).

	x, distance from Station A, cm																							
	5			10			25			40			55			70			85			130		
EROSION PERIOD	%	$\bar{U}_*$	$\bar{U}_\infty$	%	$\bar{U}_*$	$\bar{U}_\infty$	%	$\bar{U}_*$	$\bar{U}_\infty$	%	$\bar{U}_*$	$\bar{U}_\infty$	%	$\bar{U}_*$	$\bar{U}_\infty$	%	$\bar{U}_*$	$\bar{U}_\infty$	%	$\bar{U}_*$	$\bar{U}_\infty$	%	$\bar{U}_*$	$\bar{U}_\infty$
1.	100	0	0	100	0	0	100	0	0	100	0	0	100	0	0	100	0	0	100	0	0	100	0	0
2.	97	0.58	13.3	85	0.40	11.3	96	0.31	9.8	90	0.27	9.0	93	0.33	8.7	90	0.27	8.2	94	0.21	8.0	85	0.18	7.7
3.	45	0.7	14.6	56	0.47	12.3	91	0.34	10.5	72	0.29	9.7	86	0.35	9.5	83	0.29	9.0	83	0.22	8.6	44	0.21	8.6
4.	23	0.76	16.0	44	0.49	13.2	56	0.43	11.2	36	0.39	10.5	51	0.40	10.1	50	0.31	9.7	77	0.24	9.2	18	0.24	9.3
5.	6	-	16.7	24	0.53	14.2	44	0.45	11.9	8	0.48	11.1	10	0.43	10.6	10	-	10.3	19	0.28	10.4	0.4	0.29	9.9
6.	1		17.6	8		15.6	18	0.49	12.8	0.2	-	12.4	2	-	11.0	1	0.35	10.9			11.2			
7.				1		17.4	0.5	-	14.2						11.7									
$\bar{\bar{U}}_*, \bar{\bar{U}}_\infty$ ms^{-1}		0.68	15.6		0.47	14.0		0.40	11.73		0.36	10.54		0.38	10.3		0.31	9.6		0.24	9.5		0.23	8.9

Table 4.11 Sequential erosion and associated airflow velocities for; 180-150μm aeolian sand strips (symbols defined in text).

	x, Distance from leading edge, cm								
	10			85			130		
Erosion period	%	$\bar{U}_\infty$	$\bar{U}*$(est)	%	$\bar{U}_\infty$	$\bar{U}*$(est)	%	$\bar{U}_\infty$	$\bar{U}*$(est)
1.	100	0	0	100	0	0	100	0	0
2.	95	9.9	1.1	93	8.5	0 45	98	7.8	0.27
3.	92	10.4	1.11	88	10.1	0.47	16	10.9	0.34
4.	89	11.9	1.13	80	11.4	0.49	3	12.4	0.37
5.	75	13.6	1.16	72	12.7	0.51	2	13.4	0.41
6.	50	14.3	1.22	3	15.1	0.55	1	14.6	0.48
7.	31	15.7	1.25						
8.	17	16.8	1.27						
$\bar{\bar{U}}*$, $\bar{\bar{U}}_\infty$ ms^{-1}	—	13.2	1.18	—	11.6	0.49	—	11.8	0.37

Table 4.12 Sequential erosion and associated air flow velocities for 710-600μm sugar crystal strips (symbols defined in text).

	x, Distance from leading edge, cm								
	10			85			130		
Erosion period	%	$\bar{U}_\infty$	$\bar{U}*$(est)	%	$\bar{U}_\infty$	$\bar{U}*$(est)	%	$\bar{U}_\infty$	$\bar{U}*$(est)
1.	100	0	0	100	0	0	100	0	0
2.	69	6.8	0.24	91	5.4	0.14	90	5.1	0.10
3.	54	6.9	0.25	63	5.5	0.14	69	5.3	0.11
4.	43	7.1	0.26	42	5.6	0.15	46	5.4	0.12
5.	31	7.3	0.27	30	5.7	0.16	27	5.5	0.15
6.	1	8.51	0.32	16	5.7	0.16	14	5.6	0.17
7.				2	5.8	0.17			
$\bar{\bar{U}}*$, $\bar{\bar{U}}_\infty$ ms^{-1}	—	7.35	0.26	—	5.61	0.15	—	5.4	0.12

Table 4.13 Sequential erosion and associated airflow velocities for 180-150μm salt crystal strips (symbols defined in text).

Particle size range	Material	$d\delta/dx$, mm m^{-1}
1.7 to 1.4mm	Ballotini	26.4
710 to 600μm		17.6
355 to 300μm		15.3
180 to 150μm		13.5
180 to 150μm	Aeolian sand	14.2

Table 4.14 The rate of boundary layer thickening $d\delta/dx$ along the plate measured over ballotini and aeolian sand (data from Tables 4.2 to 4.6).

$\eta_c = y \left(\frac{U_\infty}{\nu x}\right)^{1/2}$	$f' = \frac{U}{U_\infty}$	f''
0	0	0.33206
0.2	0.06641	0.33199
0.4	0.13277	0.33147
0.6	0.19894	0.33008
0.8	0.26471	0.32739
1.0	0.32979	0.32301
1.2	0.39378	0.31659
1.4	0.45627	0.30787
1.6	0.51676	0.29667
1.8	0.57477	0.28293
2.0	0.62977	0.26675
2.2	0.68132	0.24835
2.4	0.72899	0.22809
2.6	0.77246	0.20646
2.8	0.81152	0.18401
3.0	0.84605	0.16136

Table 4.15 The function $f(\eta_c)$ for a laminar boundary layer along a smooth, flat plate at zero incidence in zero pressure gradient, (after Howarth, 1938).

Size range mm	Mean particle radius, r 10^{-3}m	y', grain projection height, 10^{-3}m		Distance from Station A, cm											
				5			10			15			25		
		TRIANGLE	PENTAGON	$\bar{U}_{*T(50)}$	$y'\bar{U}_{*T(50)}/\nu$ TRIANGLE	$y'\bar{U}_{*T(50)}/\nu$ PENTAGON	$\bar{U}_{*T(50)}$	$y'\bar{U}_{*T(50)}/\nu$ TRIANGLE	$y'\bar{U}_{*T(50)}/\nu$ PENTAGON	$\bar{U}_{*T(50)}$	$y'\bar{U}_{*T(50)}/\nu$ TRIANGLE	$y'\bar{U}_{*T(50)}/\nu$ PENTAGON	$\bar{U}_{*T(50)}$	$y'\bar{U}_{*T(50)}/\nu$ TRIANGLE	$y'\bar{U}_{*T(50)}/\nu$ PENTAGON
0.18-0.15	0.08	0.14	0.09	0.87	8.23	5.29	0.63	5.96	3.83	0.44	4.16	2.68	0.30	3.59	2.31

Table 4.16 $y'\bar{U}_{*T(50)}/\nu$ values at 5, 10, 15 and 25cm downwind from Station A for triangular and pentagonal support geometry (180-150μm ballotini).

Size range mm	Mean particle radius, r 10^{-3}m	y', grain projection height, 10^{-3}m		Distance from Station A, cm											
				10			55			85			130		
		TRIANGLE	PENTAGON	$\bar{U}_{*T(50)}$	$y'\bar{U}_{*T(50)}/\nu$ TRIANGLE	$y'\bar{U}_{*T(50)}/\nu$ PENTAGON	$\bar{U}_{*T(50)}$	$y'\bar{U}_{*T(50)}/\nu$ TRIANGLE	$y'\bar{U}_{*T(50)}/\nu$ PENTAGON	$\bar{U}_{*T(50)}$	$y'\bar{U}_{*T(50)}/\nu$ TRIANGLE	$y'\bar{U}_{*T(50)}/\nu$ PENTAGON	$\bar{U}_{*T(50)}$	$y'\bar{U}_{*T(50)}/\nu$ TRIANGLE	$y'\bar{U}_{*T(50)}/\nu$ PENTAGON
1.7-1.4	0.78	1.27	0.82	1.52	130.4	84.2	-	-	-	0.61	52.3	33.8	DATA NOT AVAILABLE		
0.71-0.6	0.33	0.54	0.34	0.99	36.1	22.7	-	-	-	-	-	-	0.34	12.4	7.8
0.355-0.3	0.16	0.27	0.17	0.55	10.0	6.3	-	-	-	-	-	-	0.19	3.5	2.2
0.18-0.15	0.18	0.14	0.09	0.63	5.9	3.8	0.46	4.35	2.8	-	-	-	0.11	1.0	0.66

Table 4.17 $y'\bar{U}_{*T(50)}/\nu$ values at 10, 55, 85 and 130cm downwind from Station A for triangular and pentagonal support geometry (using the whole range of ballotini sizes).

Particle size and material	Strip distance from Station A									
	5	10	15	25	40	55	70	85	130	$d\bar{U}_{*T}/dx$ $ms^{-1}cm^{-1}$
1.7-1.4mm ballotini		1.61		1.24	1.08	1.00	0.83	0.69		0.018
710-600μm ballotini		1.22		0.98	0.86	0.70		0.51	0.39	0.006
355-300μm ballotini		0.63		0.55	0.47	0.40		0.32	0.25	0.003
180-150μm ballotini	1.21	0.74	0.49	0.34	0.22	0.65	0.54	0.49	0.25	0.007
180-150μm aeolian sand	0.68	0.47		0.40	0.36	0.38	0.31	0.24	0.23	0.003
710-600μm sugar crystals		1.18						0.49	0.37	0.006
180-150μm salt crystals		0.26						0.15	0.12	0.001

Table 4.18 Arithmetic mean threshold shear velocities $\bar{U}_{*T}(ms^{-1})$ for all test materials and strip positions and the associated rates of downwind $\bar{U}_{*T}$ reduction $d\bar{U}_{*T}/dx$, $ms^{-1}cm^{-1}$.

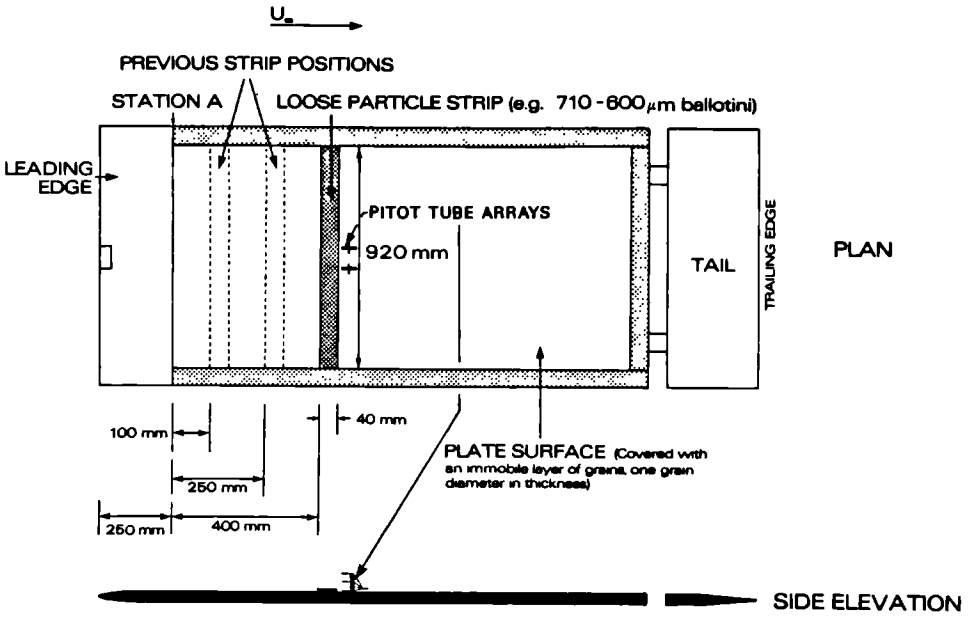

Figure 4.1(a) Location and configuration of test strips on the surface of the plate.

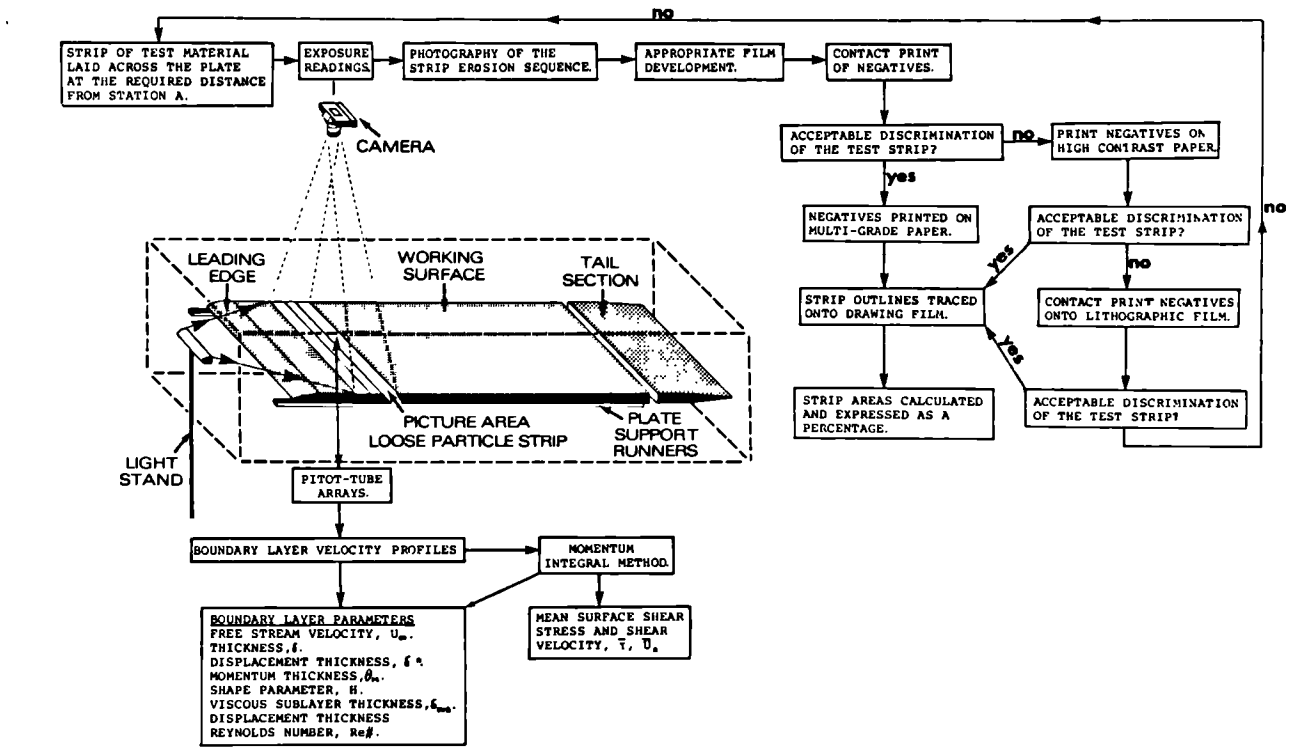

Figure 4.1(b) Summary of data acquisition and extraction techniques.

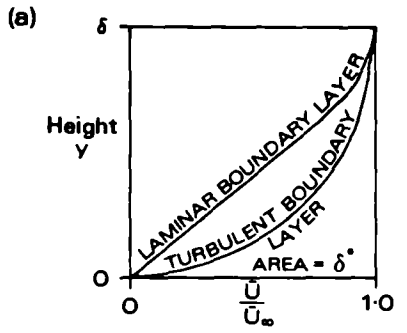

$\bar{U}/\bar{U}_\infty$ versus y is plotted for all boundary layer wind velocity profiles. Boundary layer thickness δ is defined as $y=\delta$ when $\bar{U}=0.995\bar{U}_\infty$. The displacement thickness δ^* is defined as

$$\delta^* = \int_{y=0}^{y=\delta} (1-\bar{U}/\bar{U}_\infty)\,\delta y \qquad 2.22$$

and is represented by the shaded area beneath the graph.

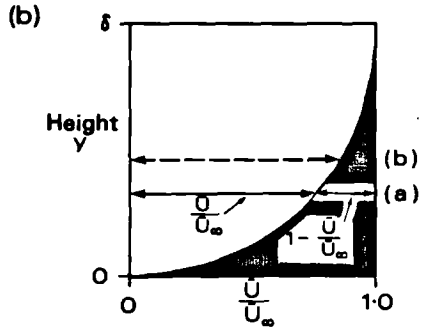

Using the same graph, values of $\bar{U}/\bar{U}_\infty$ times $1-\bar{U}/\bar{U}_\infty$ are calculated at successive heights from $y=0$ to $y=\delta$.

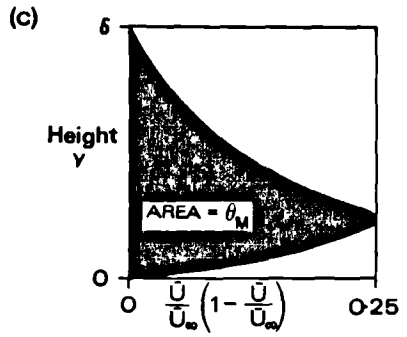

$\bar{U}/\bar{U}_\infty \cdot 1-\bar{U}/\bar{U}_\infty$ values from (b) are plotted against height y. The momentum thickness θ_M is defined as

$$\theta_M = \int_{y=0}^{y=\delta} \frac{\bar{U}}{\bar{U}_\infty}\left(1-\frac{\bar{U}}{\bar{U}_\infty}\right)\delta y \qquad 2.25$$

and is represented by the shaded area of the graph.

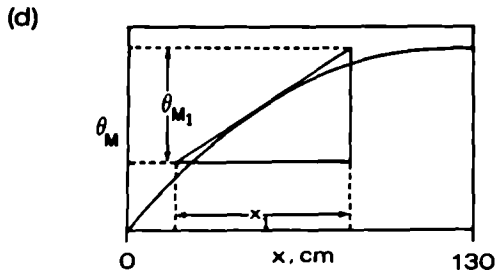

θ values are then plotted against distance from Station A(x). Each θ value must be derived from boundary layer velocity wind profiles taken at the same free stream wind velocity. The gradient of the resulting curve, $d\theta_M/dx$ is related to the shear stress in the case of zero pressure gradient by

$$\tau = \frac{d\theta_M}{dx}\rho\bar{U}_\infty^2 \qquad 2.27$$

Shear stress may then be calculated for any distance, x, from Station A and can be, therefore, related to a known degree of strip erosion at any chosen position on the plate.

Figure 4.2 Calculation of mean surface shear stress in zero pressure gradient by the momentum integral method.

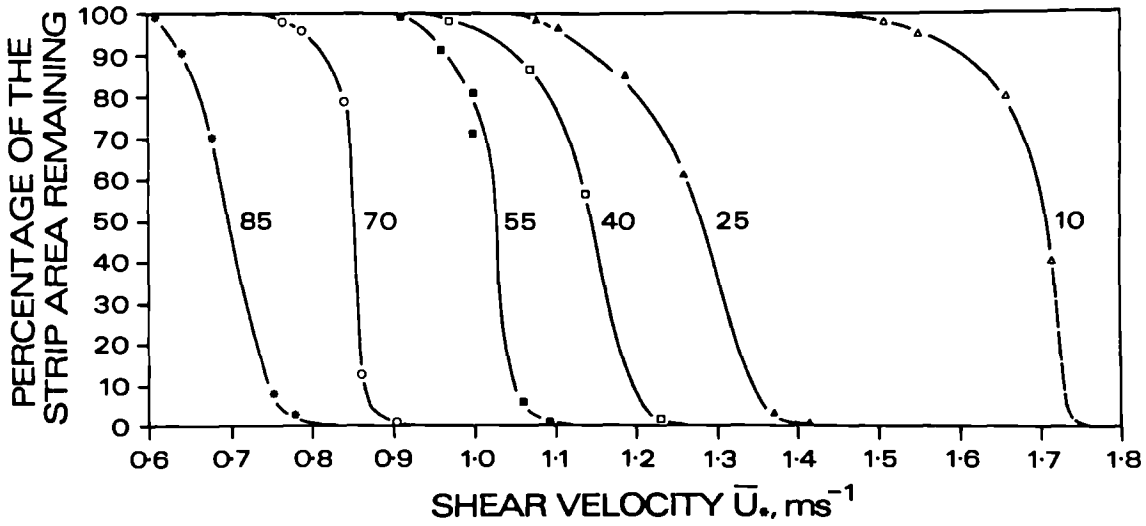

Figure 4.3 Erosion of 1.7-1.4mm ballotini strips.

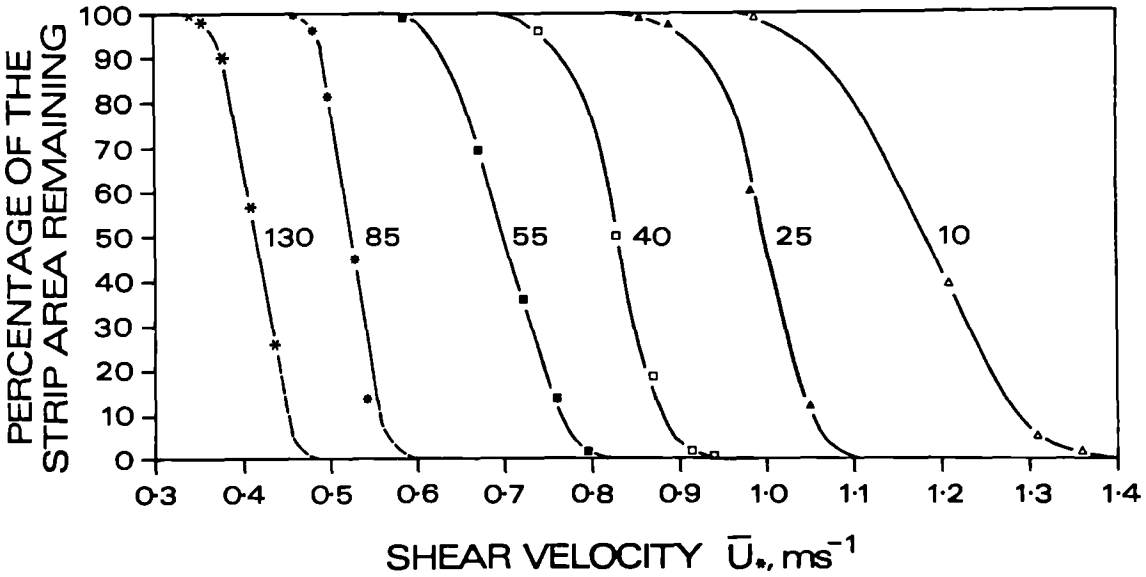

Figure 4.4 Erosion of 710-600μm ballotini strips.

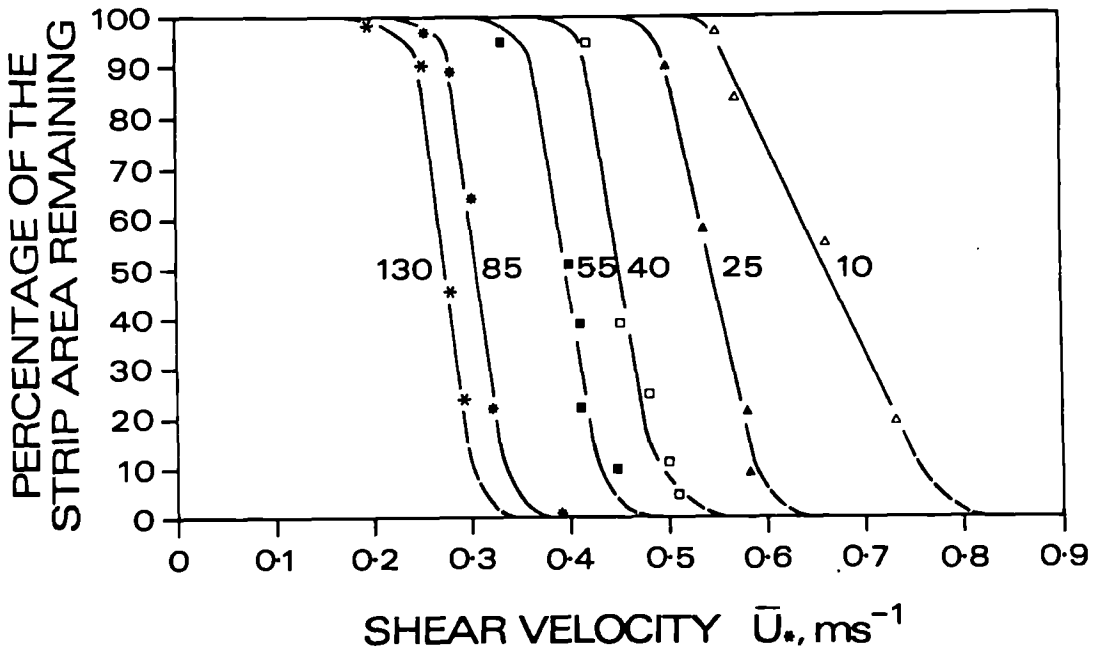

Figure 4.5 Erosion of 355-300μm ballotini strips.

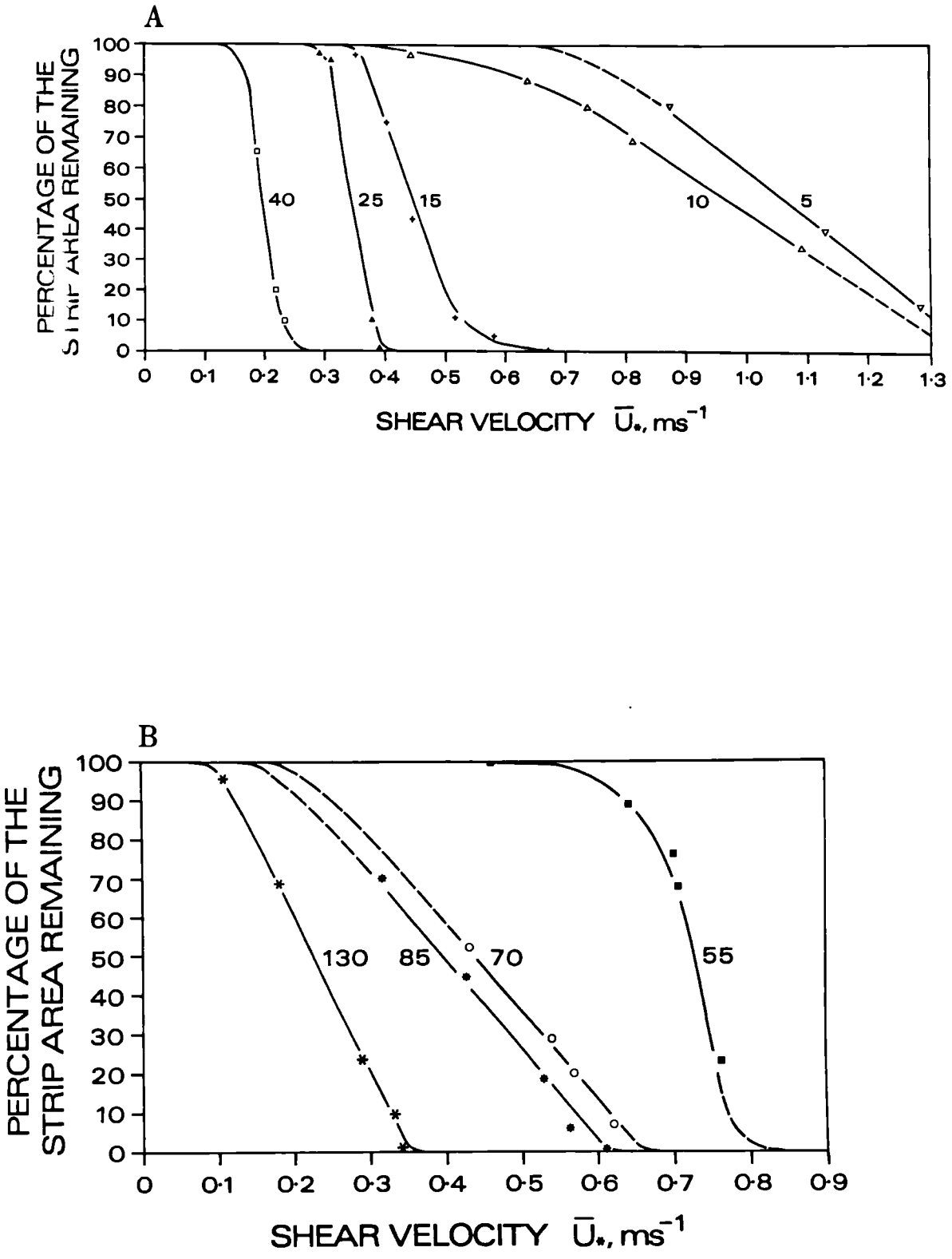

Figure 4.6 Erosion of 180-150μm ballotini strips.

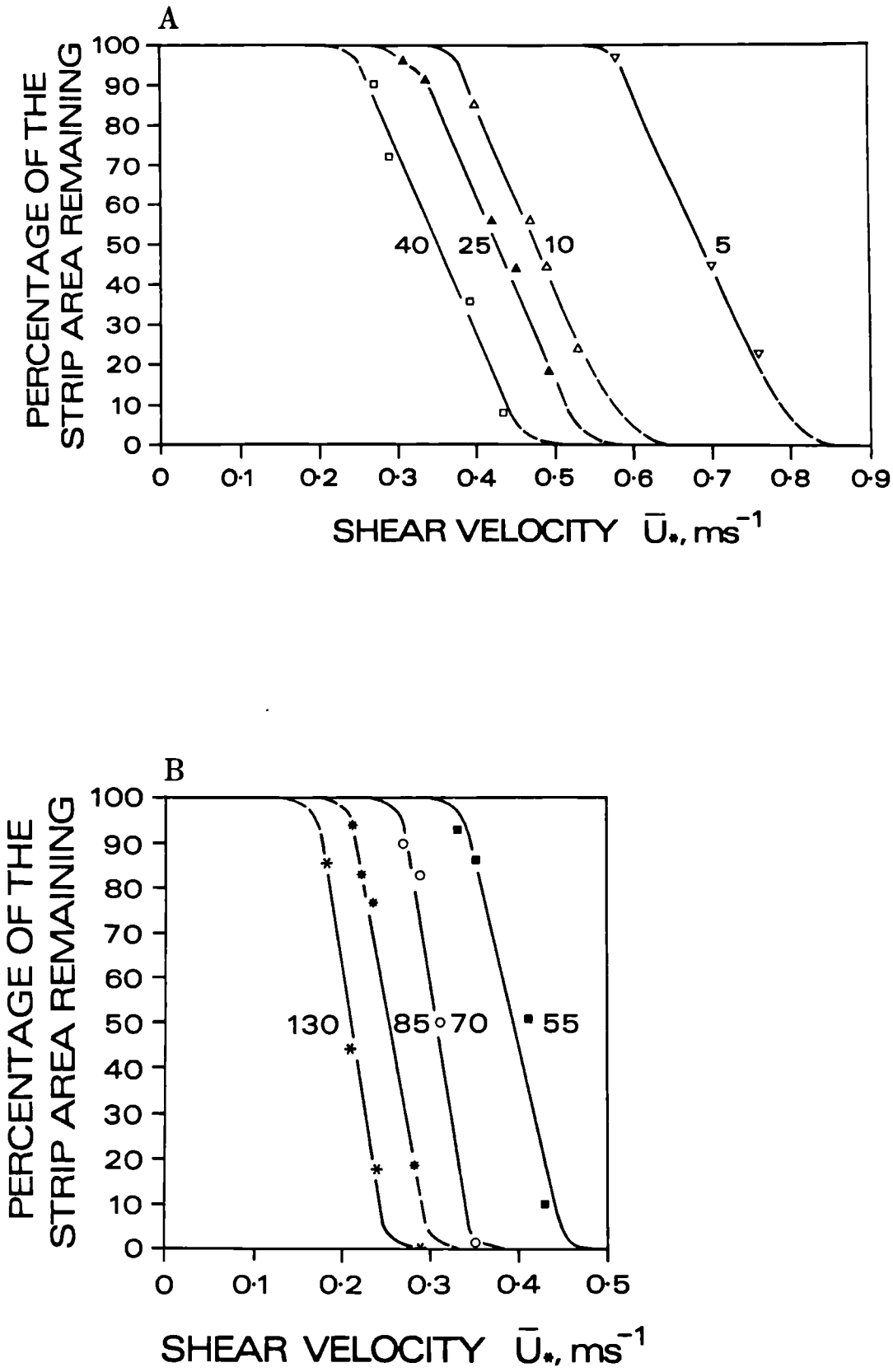

Figure 4.7 Erosion of 180-150μm aeolian sand strips.

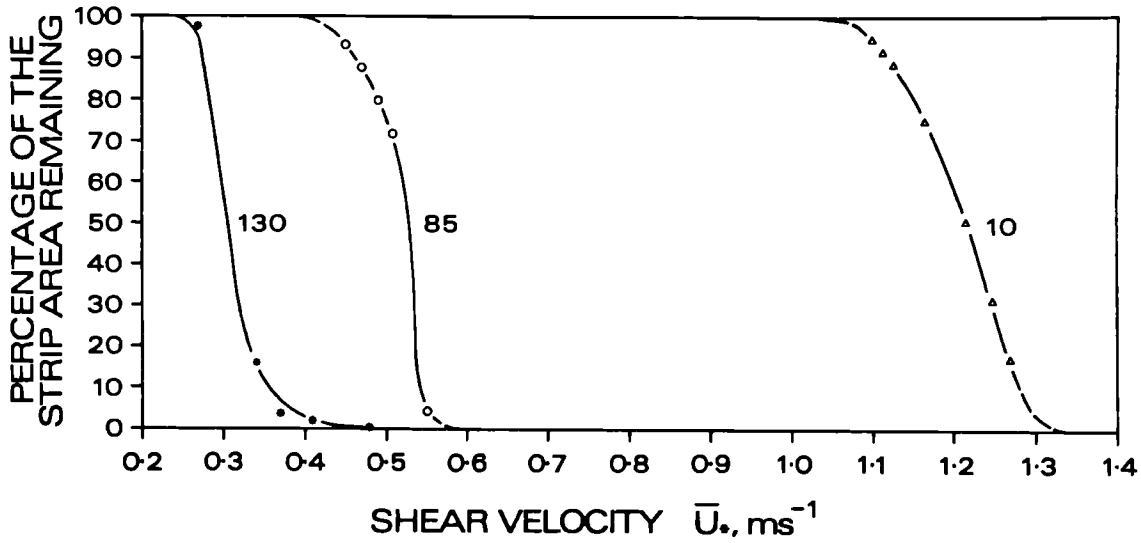

Figure 4.8 Erosion of 710-600μm sugar crystal strips.

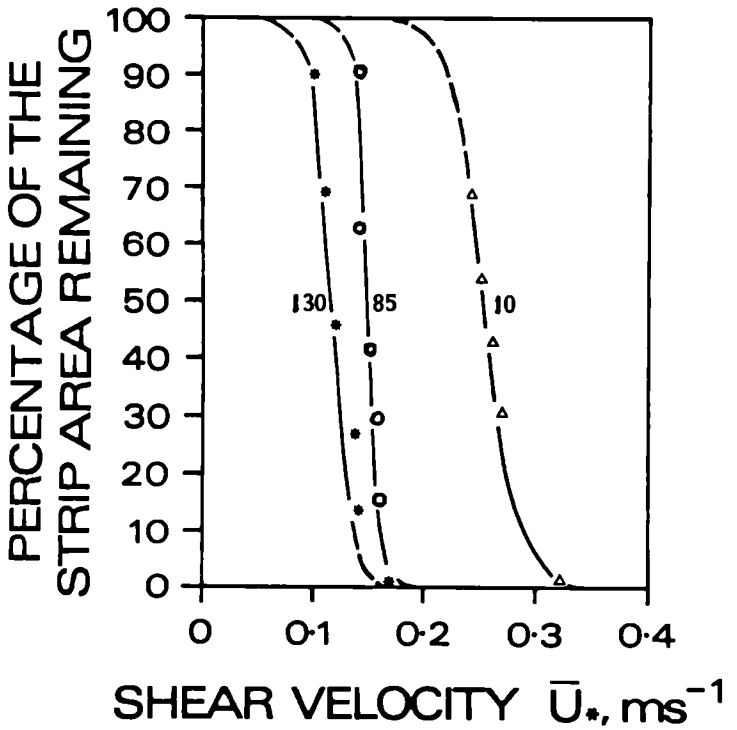

Figure 4.9 Erosion of 180-150μm salt crystal strips.

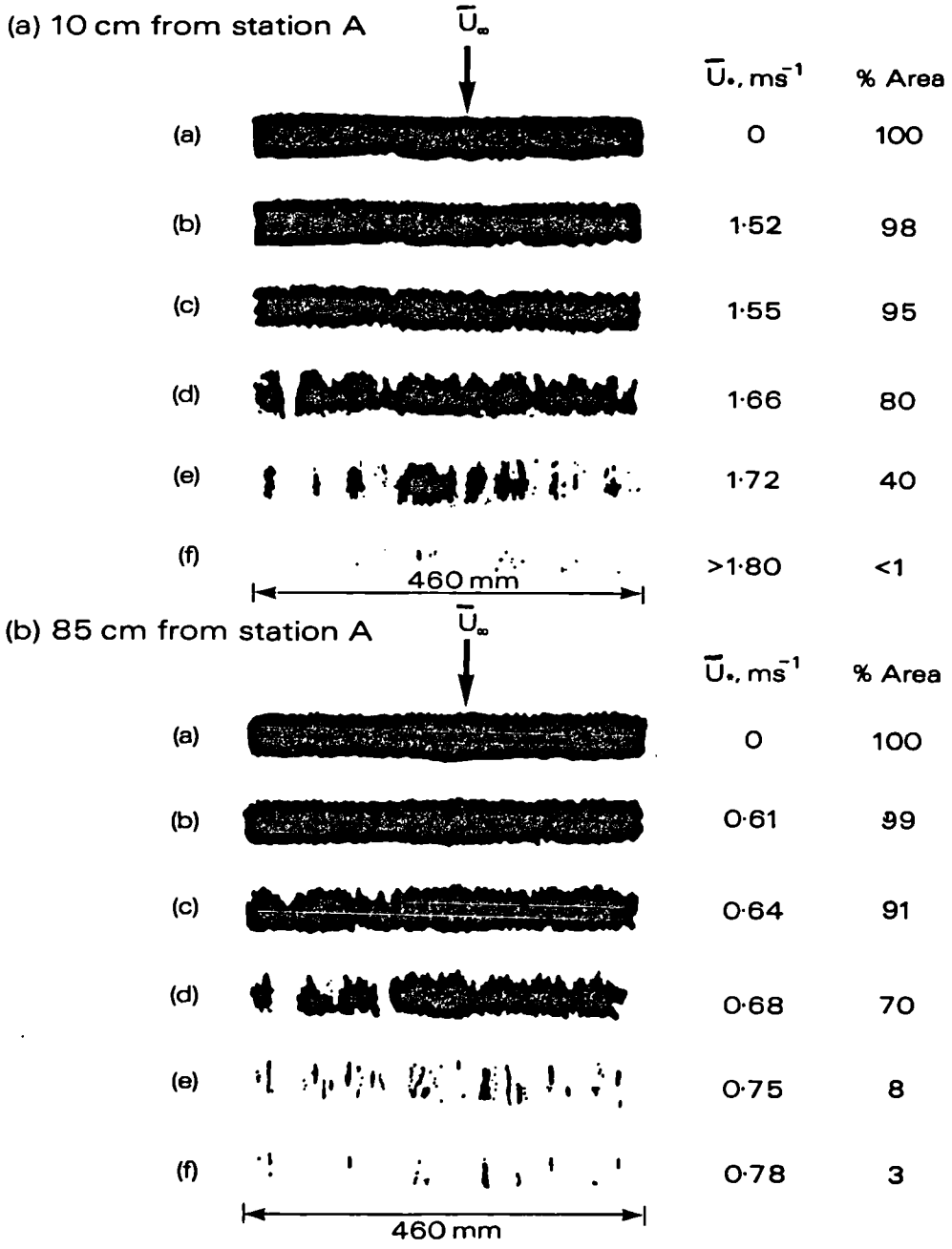

Figure 4.10 Strip erosion sequences for 1.7-1.4mm ballotini.

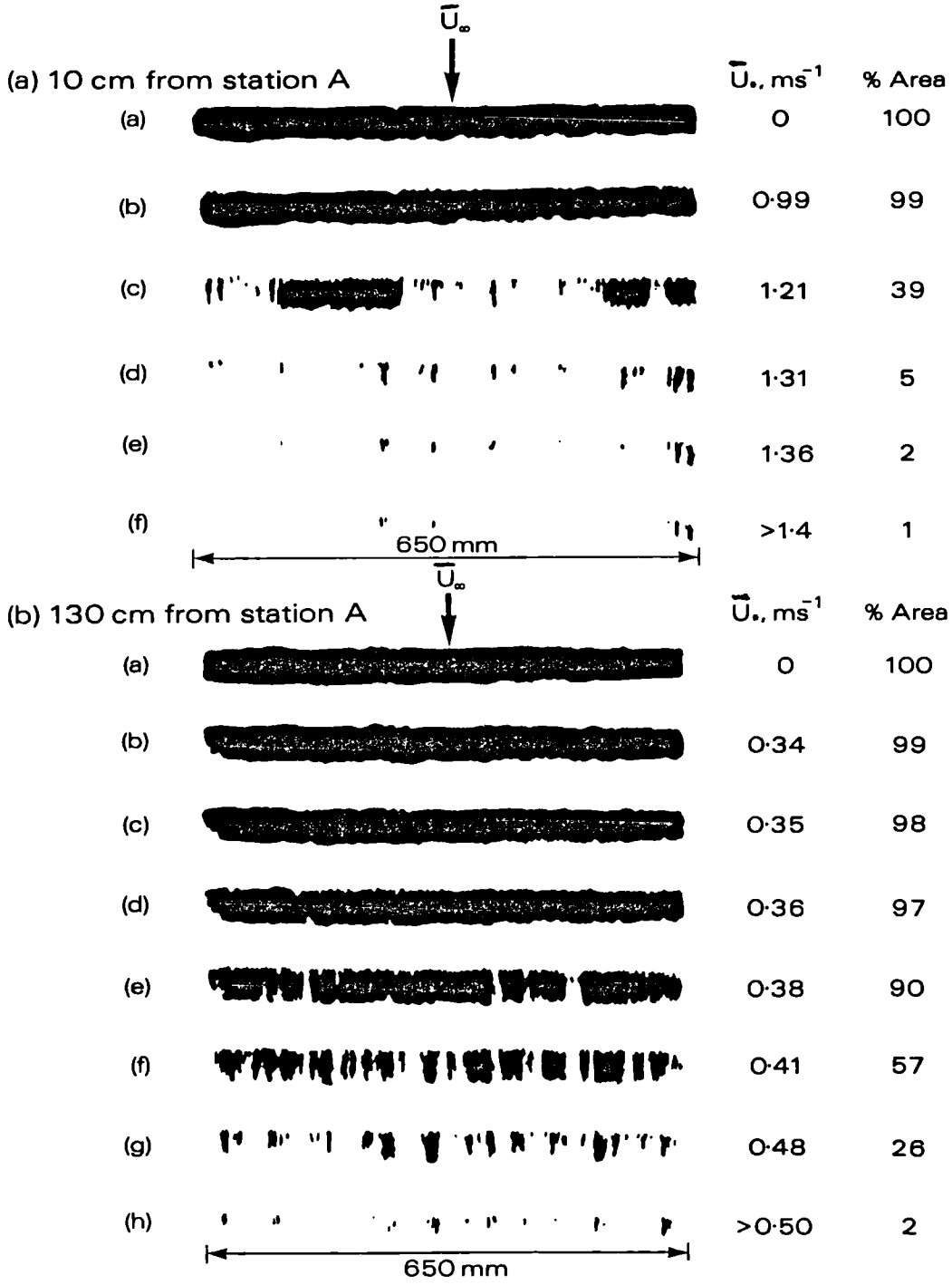

Figure 4.11 Strip erosion sequences for 710-600μm ballotini.

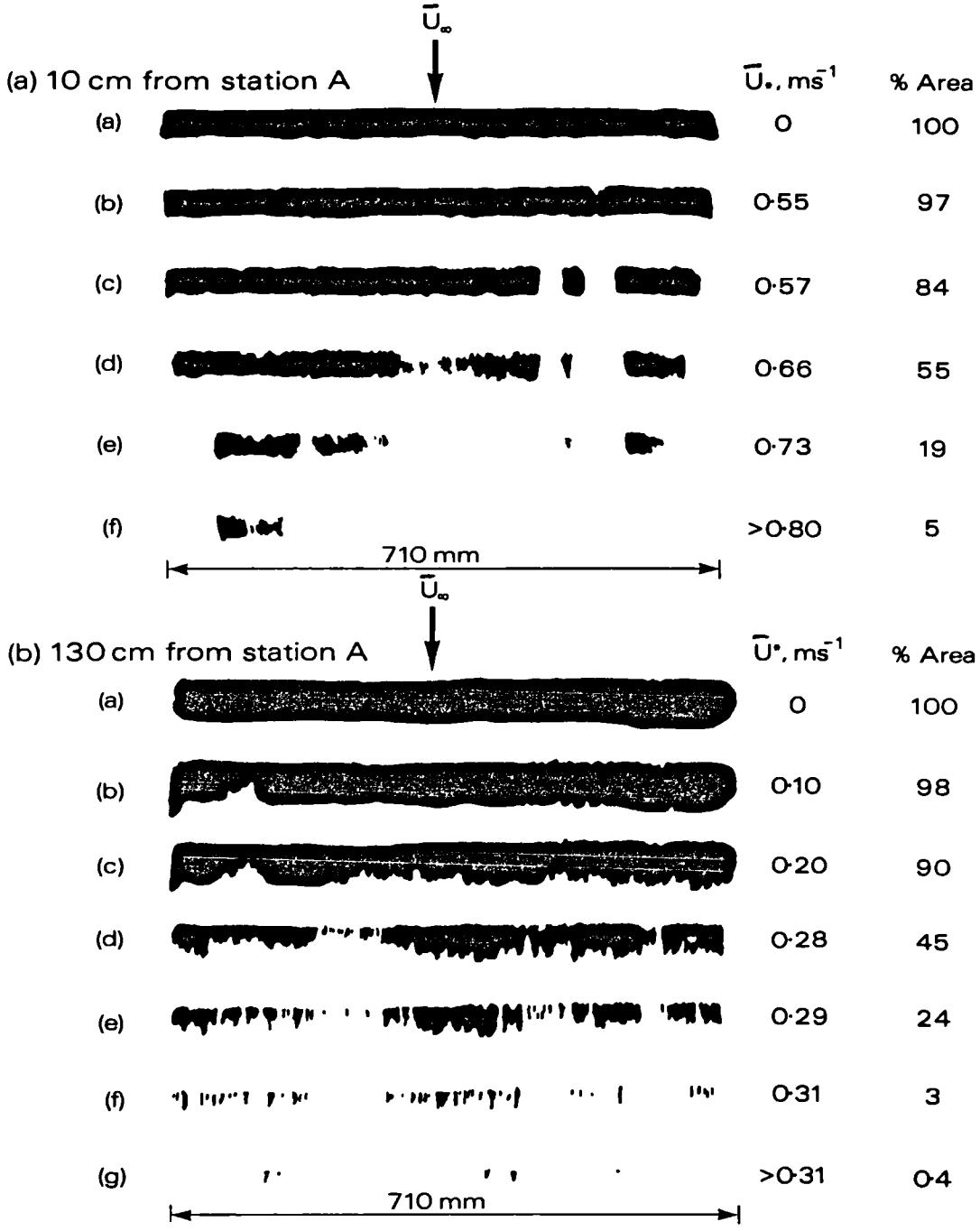

Figure 4.12 Strip erosion sequences for 355-300μm ballotini.

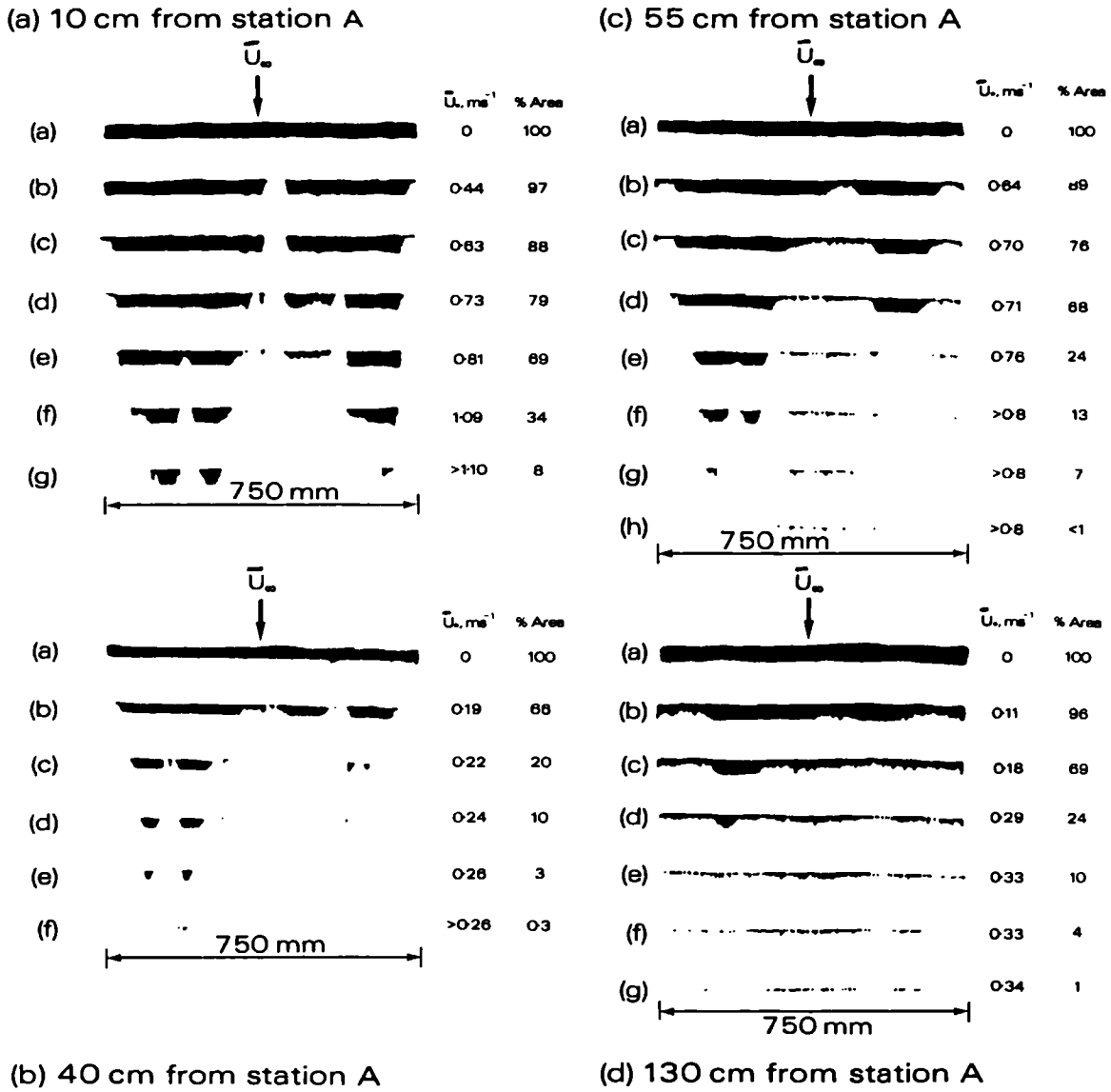

Figure 4.13 Strip erosion sequences for 180-150μm ballotini.

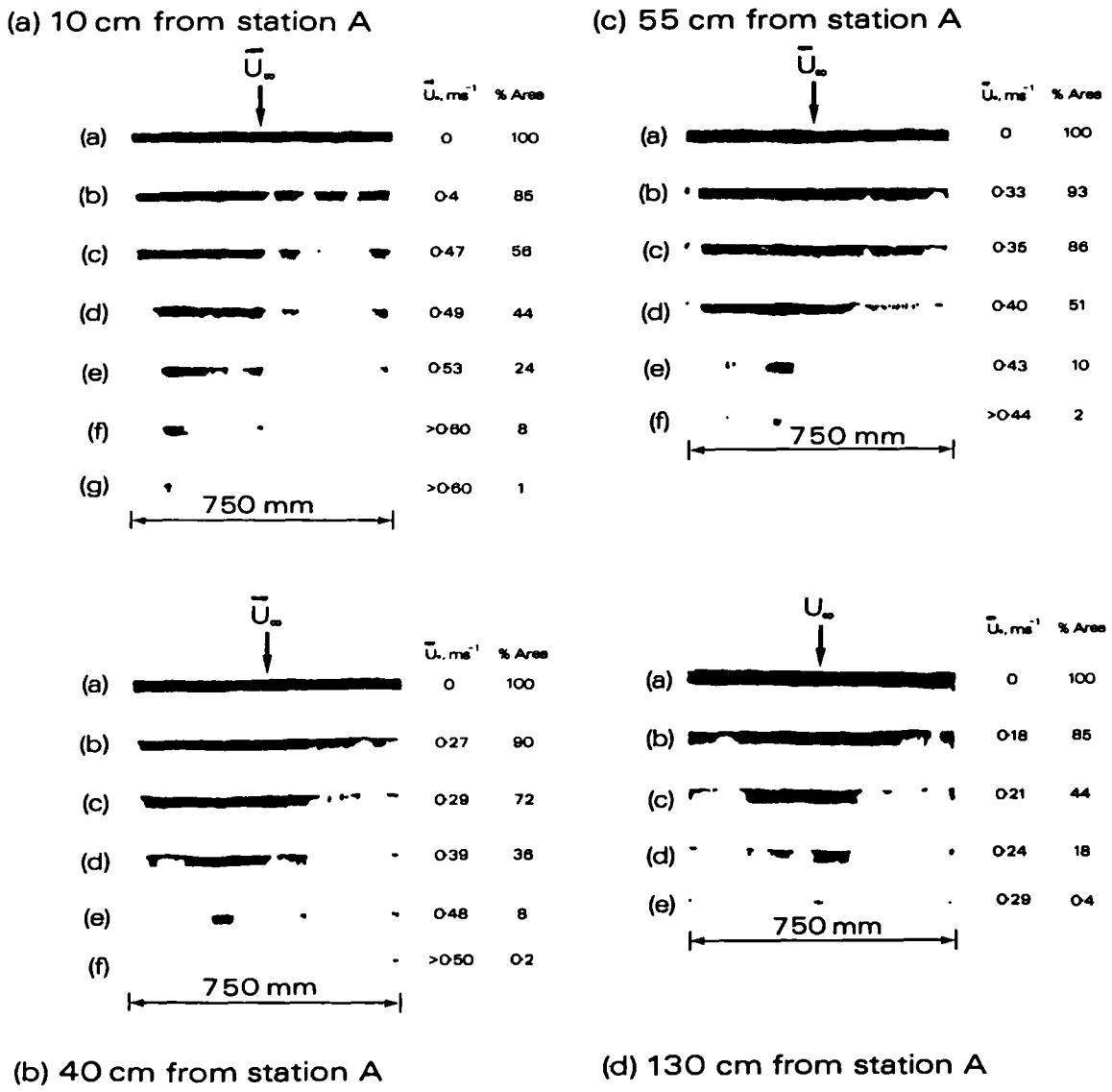

Figure 4.14 Strip erosion sequences for 180-150μm aeolian sand.

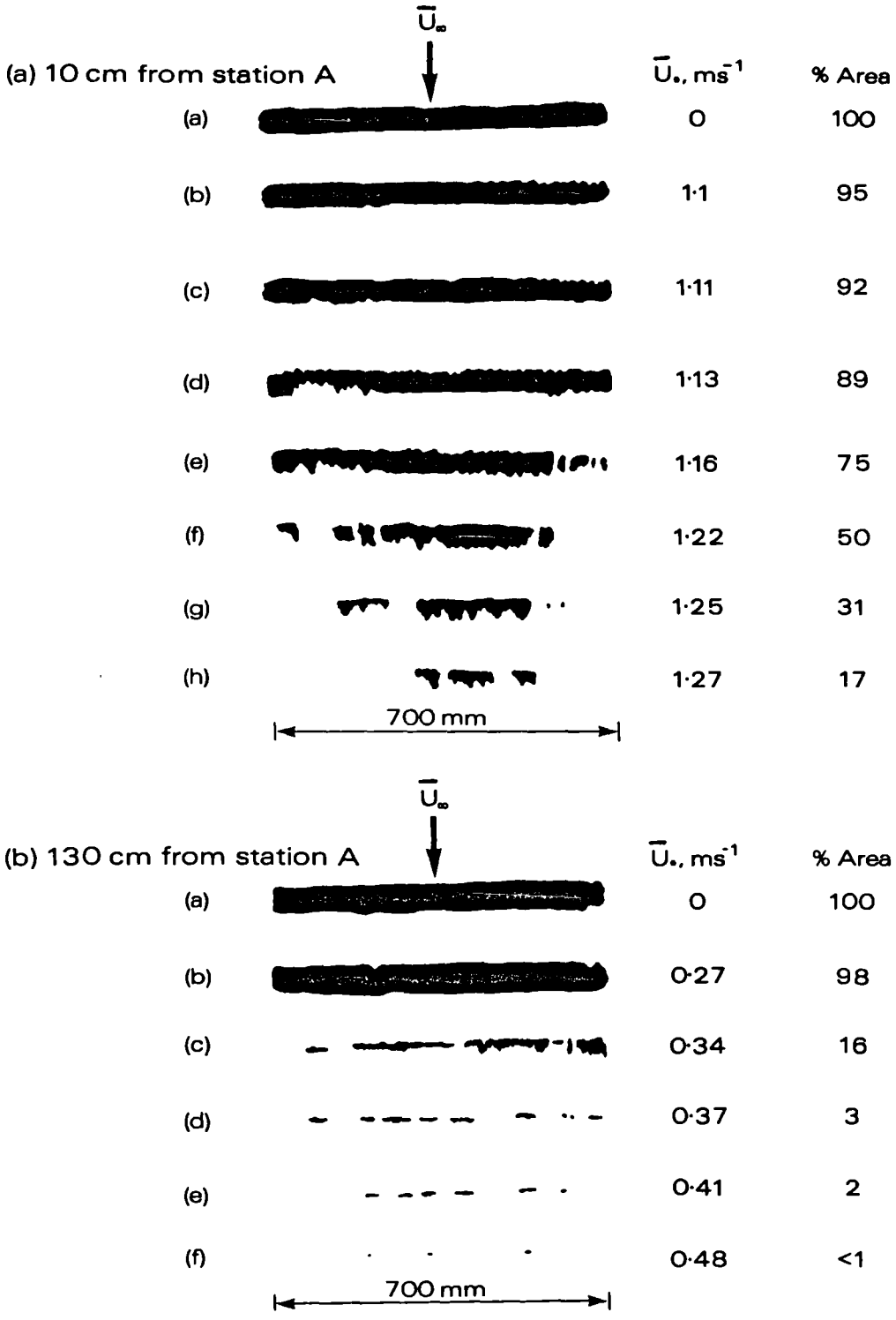

Figure 4.15 Strip erosion sequences for 710-600μm sugar crystals.

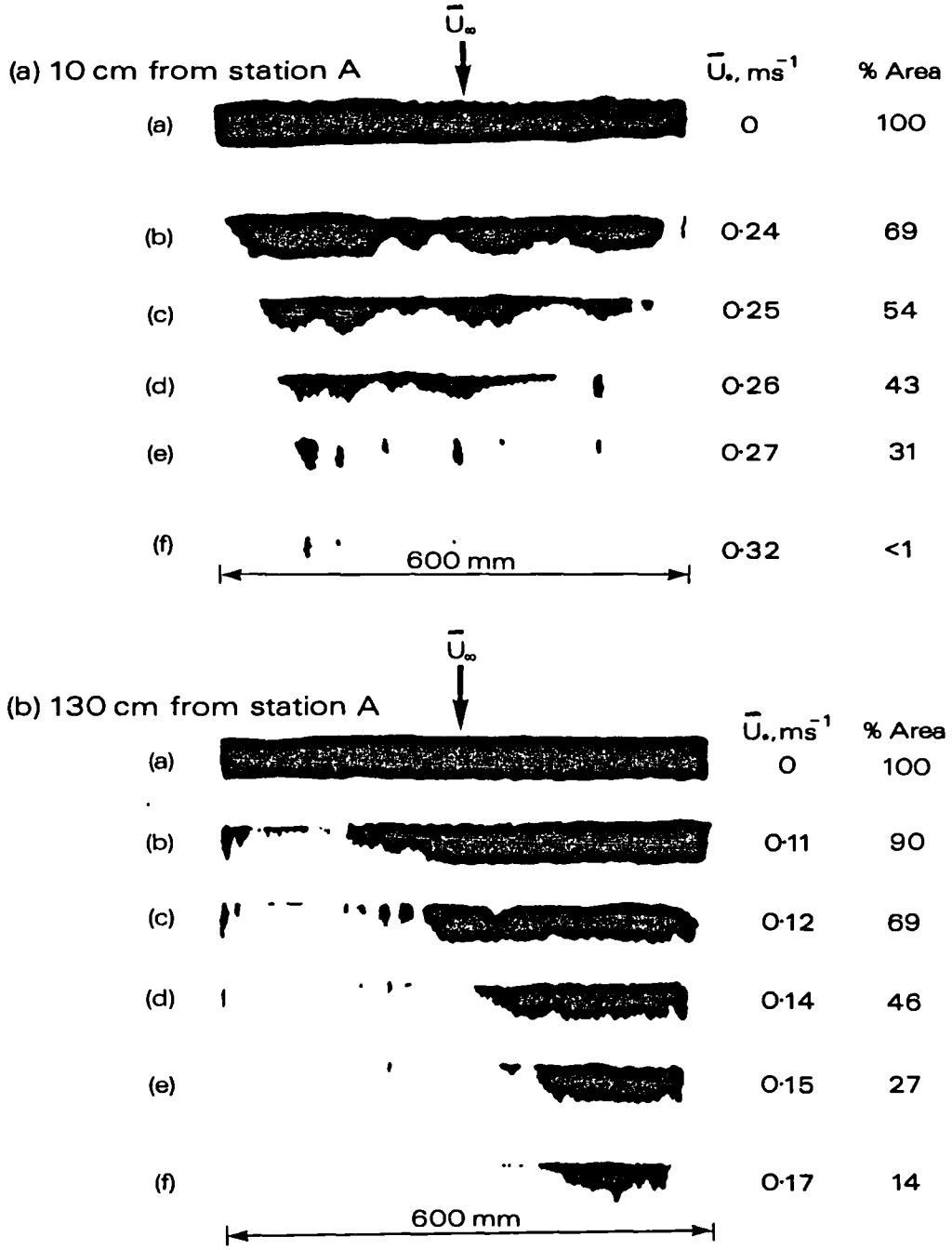

Figure 4.16 Strip erosion sequences for 180-150μm salt crystals.

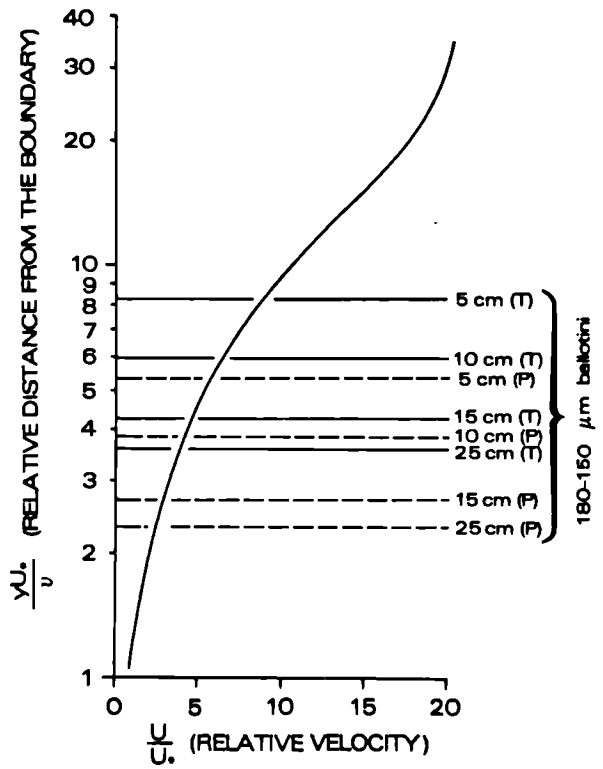

Figure 4.17 Theoretical grain exposure in a laminar boundary layer. (T) and (P) refer to triangular and pentagonal support geometry respectively (data in Table 4.16).

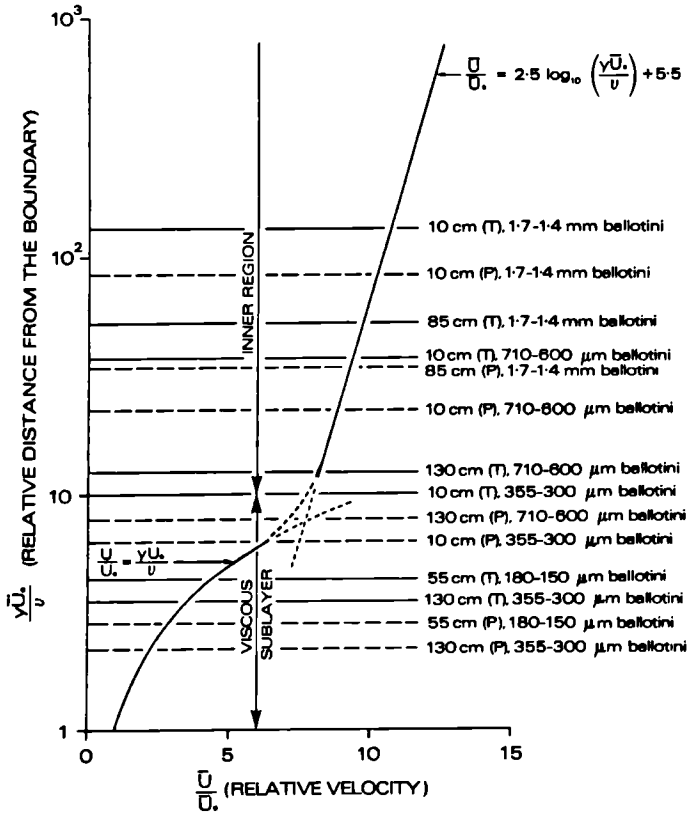

Figure 4.18 Theoretical grain exposure in a turbulent boundary layer. (T) and (P) refer to triangular and pentagonal support geometry respectively (data in Table 4.17).

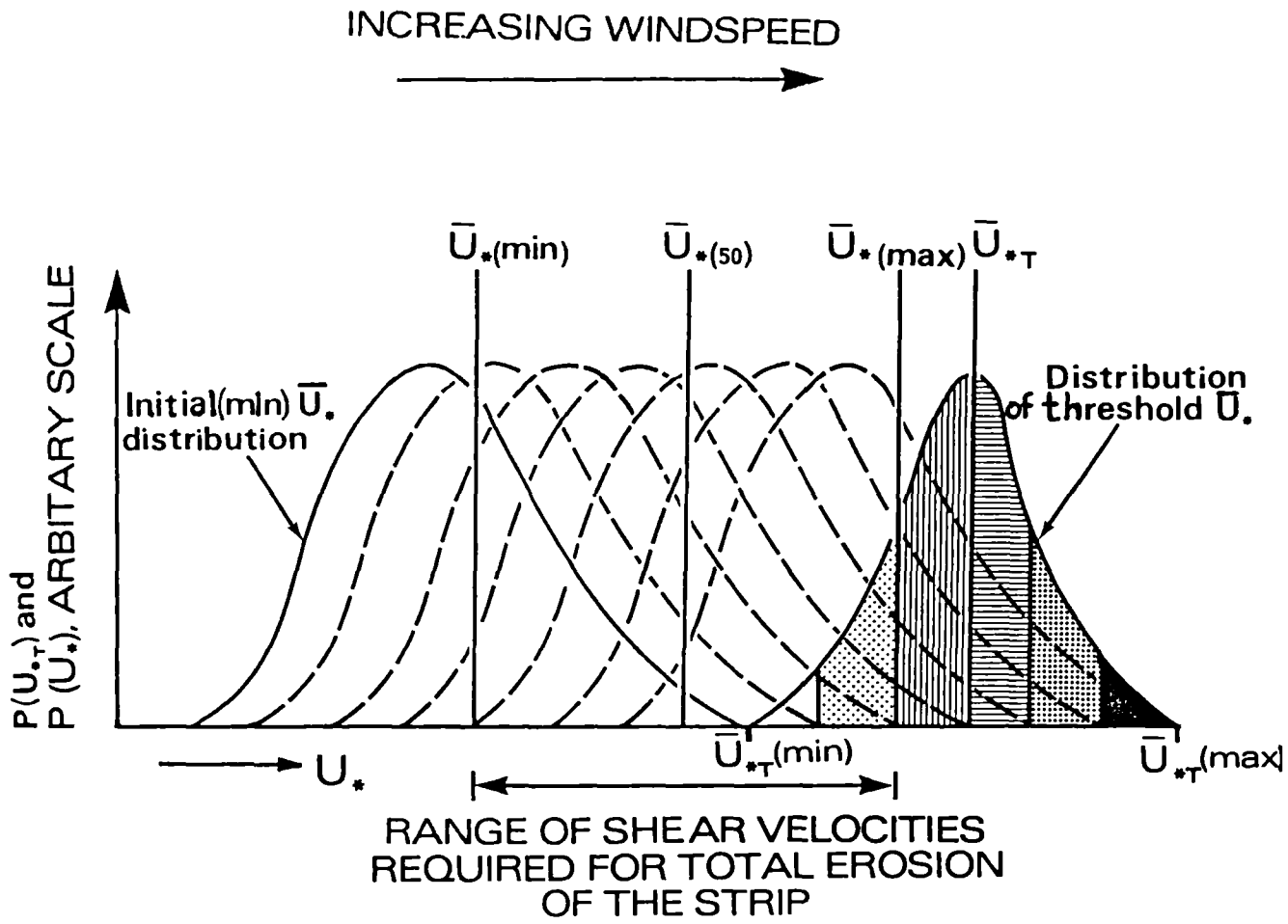

$\bar{U}_{*(min)}$ = MEAN SHEAR VELOCITY AT THRESHOLD

$\bar{U}_{*(50)}$ = MEAN SHEAR VELOCITY WHEN 50 % OF THE STRIP REMAINS UNERODED

$\bar{U}_{*(max)}$ = MEAN SHEAR VELOCITY REQUIRED TO ERODE ALL THE MATERIAL IN A TEST STRIP

$\bar{U}_{*T}$ = MEAN VALUE OF $P(U_{*T})$ DISTRIBUTION ASSOCIATED WITH THE TEST MATERIAL

Figure 4.20 Sequential erosion of a test strip represented by progressive overlap of the probability distributions $P(U_*)$ and $P(U_{*T})$, (schematic).

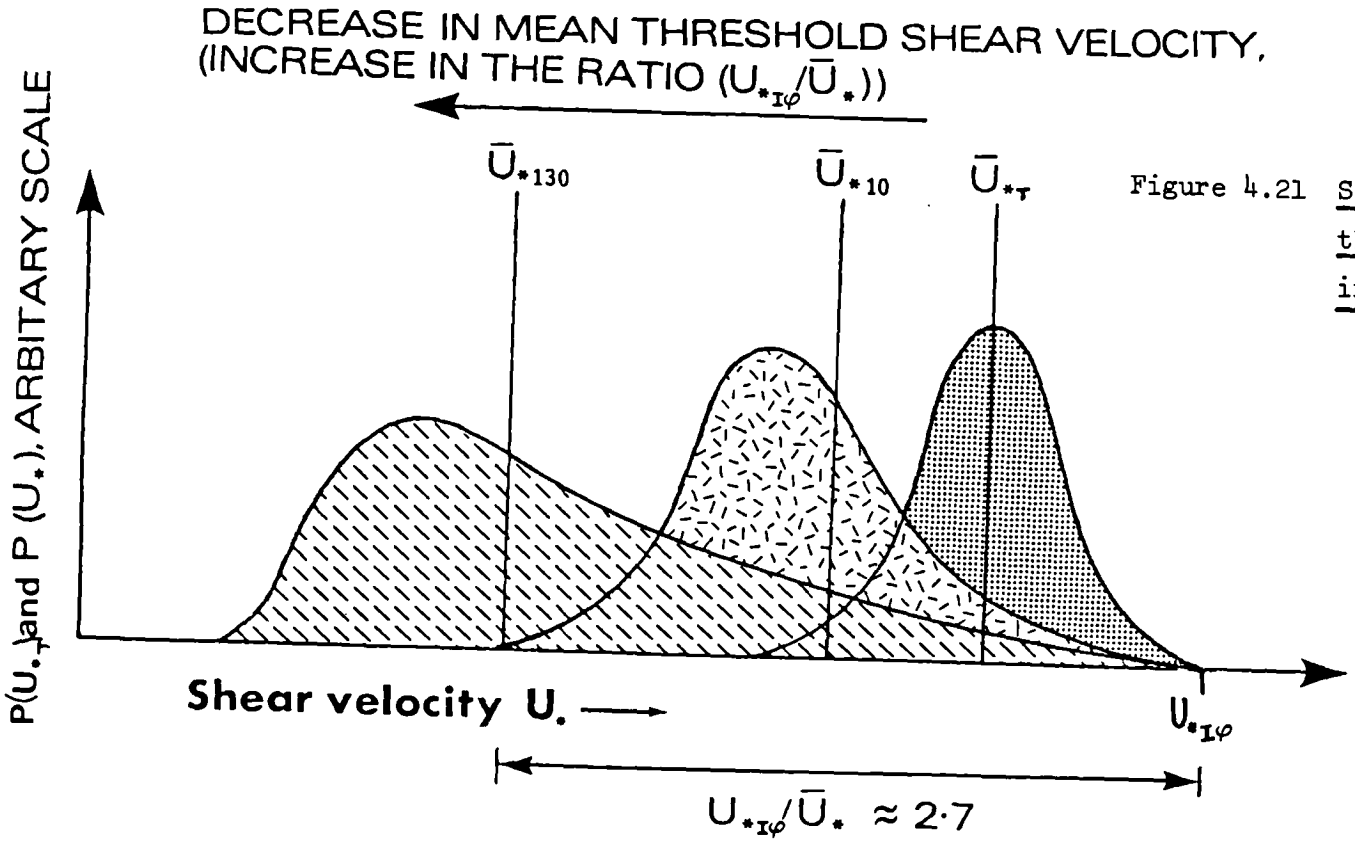

Figure 4.21 Schematic representation of the downwind reduction in $\bar{U}_{*T}$.

$\bar{U}_{*T}$ = MEAN VALUE OF THE P (U_{*T}) DISTRIBUTION (threshold) ASSOCIATED WITH THE TEST MATERIAL

$\bar{U}_{*10}$ = MEAN SHEAR VELOCITY AT 10 cm DOWNWIND FROM STATION A (at threshold)

$\bar{U}_{*130}$ = MEAN SHEAR VELOCITY AT 130 cm DOWNWIND FROM STATION A (at threshold)

$U_{*I\varphi}$ = INSTANTANEOUS PEAK SHEAR VELOCITY

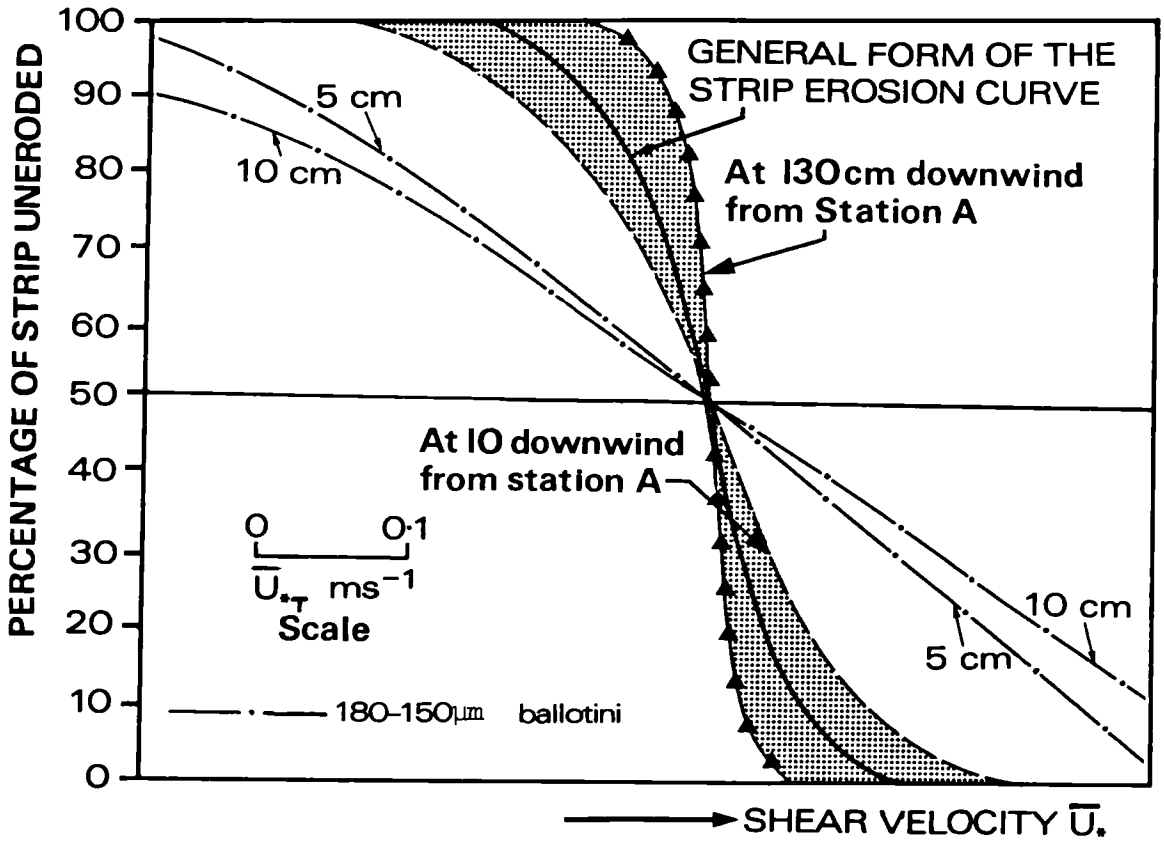

Figure 4.19 Characteristic erosion curves derived from amalgamation of all tests (from Figures 4.3 to 4.9).

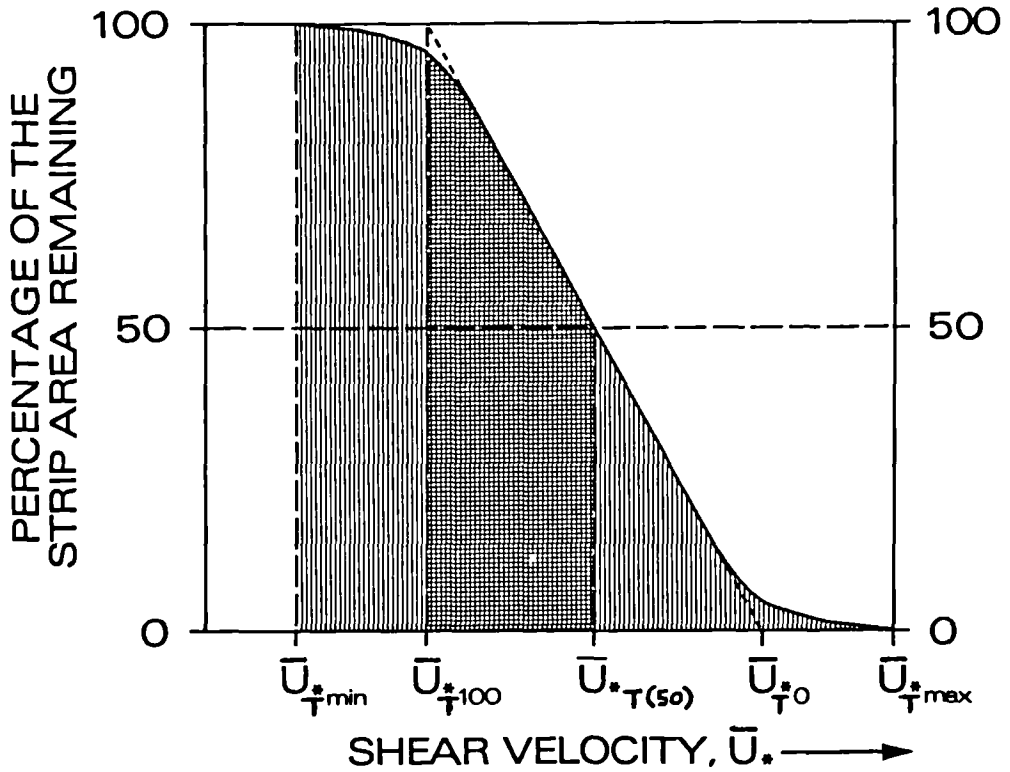

$\bar{U}_{*_{T\min}}$ = Shear velocity required to set the first grain in motion (observed)

$\bar{U}_{*_{T100}}$ = Minimum incipient threshold shear velocity (defined by the graph)

$\bar{U}_{*_{T(50)}}$ = Shear velocity required to entrain 50% of the total strip area

$\bar{U}_{*_{T0}}$ = Maximum incipient threshold shear velocity (defined by the graph)

$\bar{U}_{*_{T\max}}$ = Shear velocity required to set the last grain in motion (observed) (Termed ultimate threshold by Bagnold, 1941)

Figure 4.22 Objective definitions of aeolian threshold conditions

CHAPTER FIVE

Comparison between published and experimental aeolian threshold data

5.1 Introduction

This chapter compares a representative selection of aeolian threshold values published in the literature with the experimentally determined threshold values derived in this study and discussed in Chapter 4 (hereafter referred to as 'experimental data values' or 'experimental threshold data'). The experimental data reflect aeolian threshold conditions for a range of particle sizes and test materials in different boundary layer flow regimes on the surface of the plate. Using these data it should be possible to reconcile some of the differences between published aeolian threshold values and to assess the relative significance of the principal factors controlling aeolian threshold values identified in Chapter 1.

To make comparison possible, it was necessary to reduce the considerable quantity of published and experimental data to a manageable size and to then incorporate these values into dimensionless grain entrainment expressions. These expressions include: (a) Shields (1936) criterion (θ_T), Yalin's (1972) parameter (Ξ) and Bagnold's (1941) coefficient (A) which describe the ratio between the average fluid force acting on the bed and the submerged particle weight at the threshold; and (b) the roughness or grain Reynolds number (Re* or B) which describes flow conditions at the scale of single grains on the bed. In general, these dimensionless expressions combine the physical characteristics of the particles and the fluid (i.e. air) in such a way as to permit direct comparison between published and experimental aeolian threshold data.

The fundamental relationships between the dimensionless entrainment expressions give rise to a number of characteristic curves

commonly employed to predict threshold conditions. These curves are collectively referred to as 'Universal empirical curves', and include the following: Shields (1936) curve ($\log\theta_T$ versus $\log Re^*$); Yalin's (1972) curve ($\log\theta_T$ versus $\log(\Xi)^{1/2}$); and the universal A-B curve (Iversen et al., 1973) (logA versus logB). In addition, less widely applicable empirical curves of the type developed by Hjulstrøm (1935) (e.g. mean threshold shear velocity versus particle diameter) are also used in the comparative studies presented in this chapter. These curves are generally referred to as 'restricted empirical curves'.

5.2 Review of threshold curves

Before using the restricted and universal empirical threshold curves to compare the published and experimental threshold data it is necessary to review briefly their merits and limitations, and to describe their physical meaning.

5.2.1 Restricted empirical threshold curves

At the threshold of particle motion, the relationship between a flow parameter (e.g. mean shear velocity) and a particle characteristic (e.g. grain diameter) can be determined experimentally using a pre-defined entrainment criterion (e.g. Table 1.4). This relationship can then be used to predict the threshold shear velocity for any chosen grain size provided that the fluid and grain density values, temperature and viscosity are approximately the same as those pertaining in the original experiment. However, the usefulness of these relationships is rather limited as they are unable to predict threshold conditions associated with granular materials having different sizes, densities and

shapes from those used to develop the relationship, even assuming similar fluid flow properties. Furthermore, the relationships are rendered invalid should the physical characteristics of the fluid flow change. Despite these drawbacks, such empirical relationships are widely used to predict thresholds of sediment motion and are often incorporated into empirical expressions to calculate the rate of aeolian transport (1.7).

In studies of sediment entrainment by Hjulstrøm (1935), Inman (1949), Lane (1955), Sundbørg (1956), Bagnold (1941, 1963), Benedict et al. (1966) and Gessler (1971), the conditions at the threshold in turbulent boundary layer flow were simply expressed in terms of the mean bed shear velocity $\overline{U}_{*T}$ and the mean grain diameter $\overline{d}$ of a given test sample (e.g. Bagnold, 1941, Figure 1.2). The resulting data points were found to lie on a curve over a limited range of grain Reynolds number values. These curves are reviewed in detail by Graf (1971), Gessler (1971) and Miller et al. (1977). Two curves of this type for air are examined and assessed in 5.3.1 and 5.4.1 using the experimental data from this study together with a selection of published data derived from aeolian threshold studies.

5.2.2 Universal empirical threshold curves

To overcome the limitations of the restricted relationships described above, it is desirable to use general relationships that are capable of predicting threshold conditions for sediments with a wide range of physical characteristics irrespective of the working fluid. Three such relationships are illustrated in Figure 5.1. These are: (a) Shields (1936) curve; (b) Yalin's (1972) curve; and (c) the A-B curve (Iversen et al., 1976).

(a) Shields (1936) curve

Figure 5.1(a) illustrates the functional relationship between Shields parameter (θ) and the grain Reynolds number (Re*). This relationship is usually expressed in the form

$$\theta = \frac{\bar{\tau}_T}{(\sigma-\rho)g\bar{d}} = f\left(Re^* = \frac{\bar{U}_{*T}\bar{d}}{\nu}\right) \qquad 5.1$$

where $\bar{d}$ = mean particle diameter m

Shields originally solved this functional relationship experimentally by determining the threshold conditions for a range of granular materials with different physical characteristics. (Although Shields relationship usually refers to threshold conditions in water, it is equally applicable to air, Miller et al., 1977). At the threshold, θ is said to have a critical value termed 'Shields criterion' (θ_T). Values of θ above θ_T represent conditions in which sediment transport is possible, whilst θ values below θ_T imply no bed motion. Shields argued that the inclusion of all the physical and dynamic parameters of the fluid and sediment in θ and Re* gave the relationship between θ and Re* universal properties and it can be used, therefore, to predict threshold conditions for any granular material in any fluid, provided that flow characteristics are the same.

However, despite its apparent elegance, Shields curve is rather limited as it is only really applicable to flat beds of contiguous particles and it relies on a certain degree of bed motion to define threshold conditions, (Grass, 1970; Karahan, 1975; Yalin and Karahan,

1979). Further, mean shear stress, mean shear velocity and particle diameter are inappropriately used in equation 5.1 because as dependent and independent variables, they are interchangable. Mean threshold shear velocity for a given material must be found, therefore, using an iterative procedure (Yang, 1973). In addition, Shields relationship takes no account of variations in grain exposure and lift forces, and only considers applied mean tangential forces, (Fenton and Abbot, 1977).

Both Vanoni (1964) and Yalin (1972) have suggested methods to overcome some of these difficulties whilst retaining the general applicability of Shields relationship. Vanoni (1964) combined fluid and grain parameters in the dimensionless form given by equation 5.2, ('Vanoni's parameter').

$$\frac{d}{\nu}\left(0.1\ \frac{(\sigma-\rho)gd}{\rho}\right)^{1/2} \qquad 5.2$$

Using an additional scale on Shields plot, values of Vanoni's parameter are found to plot diagonally from the right to left along the face of the Shields curve. Using appropriate d, ν, σ and ρ values, Vanoni's parameter can be calculated, and by following one of the constant lines until it intersects with Shields curve, θ_T and Re* can be determined directly. Using these values it is then possible to determine directly the threshold shear velocity for any chosen sediment.

(b) Yalin's (1972) curve

Shields curve was further simplified by Yalin (1972) who

proposed a new parameter which eliminated U_{*T} from the abscissa of Shields plot (i.e. Re*). The dimensionless '<u>Yalin parameter</u>' (Ξ) is given by equation 5.3.

$$\Xi = \frac{Re_*}{\theta_T} = \frac{(\sigma-\rho)gd^3}{\rho\nu^2} \qquad 5.3$$

Generally, θ_T is plotted against $\Xi^{1/2}$ using a logarithmic scale (Figure 5.1(b)) and, using known fluid and grain parameters, Ξ can be calculated to give θ_T directly. θ_T values can then be used to determine threshold shear velocity values for a given sediment and fluid using

$$U_{*T} = \left(\theta_T \frac{(\sigma-\rho)gd}{\rho}\right)^{1/2} \qquad 5.4$$

The Yalin plot is usually applied in studies of sediment entrainment thresholds in water, but the universal nature of its dimensionless terms render them equally applicable to studies of aeolian threshold conditions.

(c) <u>A-B curve</u>

A new impetus to work on devising universal threshold parameters has been provided by space research (see 1.1). Work has been undertaken by numerous authors including Ryan (1964), Sagan and Pollack (1969), Arvidson (1972), Iversen et al. (1973, 1976), Greeley et al. (1974, 1976, 1977, 1980a,b), Sagan and Bagnold (1975) and Iversen and White (1982). One aspect of this work has been attempts to establish a universal

function relationship able to predict aeolian threshold conditions in unusual environments (e.g. Mars, Venus and Titan) as well as on Earth. Iversen et al. (1973) described an apparently universal functional relationship between Bagnold's (1941) coefficient A (equation 1.19) and grain Reynolds number (conventionally symbolised as B in this case). This relationship takes the form

$$A = \frac{\bar{U}_{*T}}{(\sigma g \bar{d}/\rho)^{1/2}} = f\left[B = \frac{\bar{U}_{*T}\bar{d}}{\nu}\right] \qquad 5.5$$

and is shown in Figure 5.1(c). Using reported and experimental threshold data from a wide range of sources, Greeley et al. (1974) examined the functional relationship described by equation 5.5 and found that, despite a certain degree of scatter, the data lay on a characteristic curve over a limited range of B values.

5.2.3 Physical meaning of universal empirical threshold curves

The universal empirical relationships described above are all concerned with representing the threshold conditions for granular material using basic physical and dynamic properties of sediments and fluids. In physical terms, decreasing values on the abscissae of the graphs in Figure 5.1 (e.g. Re*) reflect a decrease in either the size or density of the granular materials, and the curves themselves represent the threshold condition determined in 'fully turbulent' boundary layer flow. Ordinate values (e.g. A) above the curve represent varying degrees of particle motion on the bed. Values close to the curve indicate the entrainment of a few grains whilst general bed motion, and hence active aeolian transport, is indicated by larger ordinate values. Conversely,

values below the threshold curve indicate that no entrainment occurs.

Before it is possible to compare and discuss the published and experimental data using these universal relationships, it is necessary to interpret their physical meaning in detail. As all the relationships illustrated in Figure 5.1 are related, it is unnecessary to discuss each one individually. The A-B curve (Figure 5.1c) is used here, therefore, to illustrate the basic concepts of the universal empirical relationship for two reasons. Firstly, the coefficient A is defined as the square root of Shields criterion θ_T, thus the physical explanation of the A-B relationship is equally applicable to either Shields or Yalin's curve. Secondly, the A-B curve was principally developed to describe incipient motion in air and is particularly relevant, therefore, to the present study of aeolian thresholds.

Bagnold (1941) found that the threshold shear velocity associated with grains larger that 80μm in air was proportional to the square root of the submerged particle weight and the grain diameter (equation 1.18). The constant of proportionality is termed Bagnold's coefficient (A) which for particles larger than 80μm assumes a constant value of approximately 0.1. However, Bagnold found that the value of A increased for particle sizes smaller than 80μm so that the square root law was no longer valid (1.2). Bagnold suggested that changes in the value of A are related to changes in the flow conditions close to grains on the bed and the large scale flow characteristics associated with the boundary layer. Flow conditions at the scale of single grains are appropriately described by the grain Reynolds number (B) (equation 2.7) and the functional relationship between A and B forms the basis of the universal dimensionless A-B curve, Figure 5.1(c).

The drag force acting on particles at the threshold is largely governed by the grain Reynolds number and important changes in the local flow condition close to a bed of grains occur at Re* values around 3.5. These changes alter the tangential aerodynamic drag forces acting on particles and thus directly affect the mean threshold shear velocity value associated with a given material. These changes, in turn, modify the value of Bagnold's coefficient A. At Re* values less than 3.5, air is able to slip past grains in an undisturbed state. In these conditions grains are completely enclosed in viscous flow and the drag (skin friction) is consequently carried equally by every grain on the bed. In these conditions, grains have no effect on the general fluid motion and are typically referred to as being 'aerodynamically smooth' flows. However, as Re* values rise above 3.5, fluid inertial forces assume progressively greater dominance and as a result, the grain boundary layer separates and gives rise to an eddying wake downwind of the particle. In addition to the viscous drag, the resulting reduction in fluid pressure in the wake region now gives rise to a net pressure drag on the grains. At Re* values greater than 70, vortex shedding by individual roughness elements is so vigorous that it significantly affects the general flow characteristics. Such flow conditions are typically referred to as being 'aerodynamically rough'. The drag exerted on particles in these flow regimes is relatively insensitive to changes in Re* between 70 and 10^3, (Schlichting, 1979).

At Re* values smaller than 3.5, Bagnold (1941) argued that because the drag was carried equally by every bed particle, the threshold shear velocity must be higher than that associated with Re* values greater than 3.5 where projecting grains on the bed are subjected to significantly higher drag forces by virtue of their exposure. It is

likely, therefore, that the value of Bagnold's coefficient is independent of Re*, providing Re* is greater than 70. However, Figure 5.1(c) shows that A is approximately independent of Re* for Re* values greater than 3.5. In view of the preceding discussion, this is an unexpected result as one would expect A to be dependent on Re* for Re* values less than 70, owing to the changes in dominance between the viscous drag and the pressure drag acting on a grain in this Re* range. In these transitional flow regimes (i.e. $3.5 < Re^* < 70$) it is suggested that negative lift forces may oppose the action of the viscous and pressure drag components of total drag by pressing grains against the bed. It was shown in 1.4.2 that such negative lift forces have been recorded in flows characterised by Re* values smaller than 100 (e.g. Askoy, 1973) and these may act in such a way as to offset the changes in Bagnold's coefficient induced by changing aerodynamic drag forces as Re* increases between 3.5 and 70. No simultaneous experimental measurements of lift and drag forces in this range of grain Reynolds number are available and thus the suggestion that grain motion is suppressed by negative lift forces must remain only speculative.

The slow increase in A over the range $1 < Re^* < 3.5$ probably reflects the increasing shelter given to grains in the viscous flow close to the bed which makes their extraction more difficult. At Re* values smaller than 1, however, the increase in A is extremely rapid (Figure 5.1(c)) and, intuitively, this appears to be inconsistent with the preceding arguments based on the changes in fluid dynamic forces acting on particles. The mass of a grain decreases at a rate proportional to the cube of its diameter whilst the projected area decreases at a rate proportional to the square of its diameter. Therefore, providing particles are totally enclosed by viscous flow, a

relatively larger force acts on smaller particles than larger ones and consequently a mean threshold shear velocity lower than experimentally determined values should be required to entrain grains. It is likely, therefore, that some other agency is intervening at Re* values smaller than 1. Past experimental evidence indicates that inter-particle cohesive forces are largely responsible for the rapid increase in A values at Re* smaller than 1.

Sagan and Bagnold (1975) investigated the relationship between U_{*T} and d on purely aerodynamic grounds. Their investigations were specifically concerned with threshold conditions at low Re* values (i.e. Re* smaller than 3.5). Sagan and Bagnold (1975) derived expressions for U_{*T} and d from equation 5.5 to give

$$U_{*T} = [A^2 g\ (\sigma-\rho)\ Re^*/\rho]^{1/3} \qquad 5.6$$

$$d = [\rho\nu^2\ (Re^*)^2/A^2 g\ (\sigma-\rho)]^{1/3} \qquad 5.7$$

When U_{*T} is plotted against d, the characteristic increase in threshold shear velocity for particle sizes below about 80μm (see Figure 1.2) is not apparent and threshold shear velocities continue to fall as particles decrease in size. Sagan and Bagnold conclude that the turn-up in the A-B curve at Re* values smaller than 1 is not chiefly a fluid dynamical effect but is largely due to cohesive forces between bed particles, (see 1.4.3).

Iversen et al. (1976) also questioned whether the A-B curve is universal over the range of Re* values given in Figure 5.1(c) (i.e. 10^{-1} to 10^{0}), and examined the relationship between A and B for small

particles. By combining the expressions in equation 5.5 they obtained a dimensionless mean threshold shear velocity expression.

$$[U_{*T}(\rho/\sigma g\nu)^{1/3}] = [(A^2B)^{1/3}] \qquad 5.8$$

Iversen et al. (1976) argued that if the A-B curve were universal (i.e. A = A(B)), then $(A^2B)^{1/3}$ would be a function of B only. When $(A^2B)^{1/3}$ is plotted against B, data were found to plot on a curve and to show little scatter for B values greater than 5. This, therefore, confirms the idea of a minimum threshold shear velocity. However, for B smaller than 5, the data began to spread out and a large degree of scatter was associated with B values smaller than 1. Iversen et al. (1976) also included the low air density data from Weinberger and Adlon (1971) and this suggested that the scatter at B smaller than 5 is partially controlled by the fluid/particle density ratio, ρ/σ. Some of the small, dense particles used by Iversen et al. (1973, 1976) and Greeley et al. (1973) in the investigation of threshold conditions at low Re* values were metallic and consequently the forces due to electrical interactions between particles were larger than those for non-metallic particles, (e.g. Kuhn, 1961, p.48).

To assess the significance of the density ratio ρ/σ further, Iversen et al. (1976) combined grain and fluid parameters to give

$$U_{*T}(\rho/\sigma)^{1/2} = A(gd)^{1/2} \qquad 5.9$$

When $U_{*T}(\rho/\sigma)^{1/2}$ was plotted against $d^{1/2}$, two curves could be drawn through the scatter of points, and for a given particle size it was found that light particles had higher $U_{*T}(\rho/\sigma)^{1/2}$ values

than heavy particles. Therefore, it appears that the data scatter associated with B values smaller than 5 is due to both changes in aerodynamic and inter-particle forces. In addition, the materials themselves also have unique attractive forces which are related to the density ratio, ρ/σ and this may partly explain why data points do not coincide on the A-B plot for values smaller than 5.

The A-B plot illustrated in Figure 5.1(c) was obtained by measuring the mean threshold shear velocities associated with a wide range of particles in turbulent boundary layer flow. The characteristic Reynolds number associated with the large scale boundary layer flow is seldom given by investigators and, in general, it is assumed that the long working sections of wind tunnels conventionally used by researchers in this field (1.1) ensure that the boundary layer flow is fully turbulent by the time it reaches the test bed. However, in boundary layer flow regimes characterised by different intensities of flow turbulence, Bagnold (1941) and Greeley et al. (1977) found that the mean shear velocity required to entrain grains decreased as the intensity of turbulence increased. (The same result was recorded in this investigation for test material on the surface of the plate). The increase in $\overline{U}_{*T}$ values in less turbulent flow gives rise to higher A values than those associated with fully turbulent flows, even though the general relationship between A and B remains the same. Thus, the A-B curve illustrated in Figure 5.1(c) is only one of a family of curves which are governed by the large scale boundary layer flow characteristics. Further discussion of the relationship between A and large scale flow characteristics is given below.

5.3 Comparisons between published and experimental threshold data

During this study a range of mean threshold shear stress values was recorded for any single strip of test material at a given position on the plate (Chapter 4). The minimum threshold shear velocity values ($\overline{U}_{*T(min)}$) recorded were associated with the motion of the first few grains, whilst the maximum values ($\overline{U}_{*T(max)}$) were recorded when little or none of the test strip remained on the surface of the plate. In order to standardize the experimental threshold data of this study it was necessary, therefore, to define a representative measurement of the mean threshold shear velocity associated with the complete erosion of test strips. In the circumstances, the average shear velocity required to erode completely a given test strip (i.e. $\overline{\overline{U}}_{*T}$) was considered to be the most appropriate measurement. Values of $\overline{\overline{U}}_{*T}$ for all the test materials and strip positions on the plate were obtained accordingly from Tables 4.7 to 4.13. As the shear velocity associated with test strip erosion was measured using the momentum integral method (2.6.3(c) and 4.3.3), the $\overline{\overline{U}}_{*T}$ values not only define the average shear velocity to erode completely a test strip, but also reflect the average value of the fluctuating instantaneous shear velocity component associated with the local boundary layer flow regime at that strip position. In general, most authors have defined the threshold shear velocity in a similar fashion and thus the experimental results in this form are consistent with the majority of the published data examined in this chapter.

In this chapter, published threshold data and experimental data from this study are compared using the parameter given in Table 5.1 to plot various restricted and universal empirical threshold curves. In addition to the values for $\overline{\overline{U}}_{*T}$ (Tables 4.7 to 4.13), calculation of

these dimensionless parameters also required values for mean surface shear stress ($\bar{\bar{\tau}}_T$), particle and fluid density (σ and ρ), kinematic viscosity (ν), particle diameter (d) and the acceleration due to gravity (g, taken as $9.81 ms^{-1}$). Values for $\bar{\bar{\tau}}_T$ were found from the experimental $\bar{\bar{U}}_{*T}$ values in Tables 4.7 to 4.13 using the relationship $\bar{\bar{\tau}}_T = \bar{\bar{U}}^2_{*T}\rho$. In the case of published work, the values for these variables were taken from the original source. In some cases, however, this was not possible and reference was made to the excellent review paper by Miller et al. (1977). The required physical properties of the test materials (ballotini, aeolian sand, sugar crystals and salt crystals) were known (Table 3.4). The appropriate densities and kinematic viscosities for air were taken from standard tables making allowance for differences in air temperature and pressure recorded during the strip erosion experiments.

As the test samples used in the experiments on the plate were obtained by sieving, each sample was characterised by a range of particle sizes (e.g. 710-600μm). To standardize this range of sizes, mean particle diameter ($\bar{d}$) of the 1/4ϕ sieve fractions was generally used in the calculation of the dimensionless entrainment parameters (Table 5.1). In some instances, however, it was possible to incorporate the maximum (d_{max}) and minimum (d_{min}) particle sizes associated with a given sieve fraction.

Table 5.2(a) presents the mean threshold shear stress ($\bar{\bar{\tau}}_T$) and mean threshold shear velocity ($\bar{\bar{U}}_{*T}$) values associated with the range of test materials and strip positions on the surface of the flat plate. In addition, the corresponding values for Shields criterion (θ_T), grain Reynolds number (Re*) and Bagnold's coefficient (A) are also presented.

Values of Yalin's parameter are presented in Table 5.2(b). In this case the maximum and minimum particle diameters associated with a given sample (e.g. 710μm and 600μm) were used to calculate maximum and minimum values of Yalin's parameter. Published data were generally extracted from the original source and then plotted with the experimental data in Figures 5.2 to 5.6. Figures 5.2 and 5.3 show two restricted empirical curves and Figures 5.4 to 5.6 illustrate the three universal empirical curves introduced above (see Figure 5.1).

5.3.1 Using restricted empirical threshold curves

Figure 5.2 shows the relationship between mean threshold shear velocity ($\bar{U}_{*T}$) and grain diameter (d). In Figure 5.2(a), data from Bagnold (1941), Zingg (1953) and Lyles and Woodruff (1971) are shown. This figure also includes the experimental data for ballotini which are shown using shaded bars. These bars show the range of $\bar{\bar{U}}_{*T}$ values recorded for strips of test material at different positions on the plate (vertical scale) and the range of particle sizes within a given test sample (horizontal scale).

Figure 5.3 also shows the relationship between mean threshold shear velocity ($\bar{U}_{*T}$) and particle diameter (d). In this case, however, $\bar{U}_{*T}$ is plotted on a linear axis and d is plotted on a square root scale (after Bagnold, 1941). This figure includes data from Bagnold (1941), Zingg (1953), Chepil (1959) and Lyles and Krauss (1971). The experimental data for ballotini are shown as shaded bars in the manner described above.

5.3.2 Using universal empirical threshold curves

In Figure 5.4(a), (Shields curve), the published data for air is taken from Bagnold (1941), Zingg (1953), Chepil (1959), Greeley et al. (1973) and Miller et al. (1977) and encompasses a particle size range between 60μm and 1.34mm and a particle density range of 1.59gcm^{-3} (sugar crystals) to 7.80gcm^{-3} (bronze). Published data for water is taken from Shields (1936), White (1940), Grass (1970) and Vanoni (1974). Particle size and density in this case range between 40μm to 1.85mm and 1.30gcm^{-3} (material unknown) to 11.35gcm^{-3} (lead shot), respectively. Curves through the data points for water are given by Grass (1970), Vanoni (1974) and Miller et al. (1977) and are based on additional threshold data from Gilbert and Murphy (1914), Casey (1935), Tison (1953), Bogardi (1965), Sutherland (1966) and White (1970) (data not shown in Figure 5.4(a)). The curve through the data points for air is taken from Miller et al. (1977). As Bagnold (1941) does not provide mean threshold data in tabular form, it was necessary to transpose values from his threshold curve (Bagnold, 1941, p. 88). Bagnold's data is illustrated by the curve labelled Bagnold (1941) which runs roughly parallel to the curve labelled Millet et al. (1977).

The experimental data for ballotini, aeolian sand, sugar crystals and salt crystals are illustrated in Figures 5.4(a) and 5.4(b) respectively. In both these figures, the experimental data sets are shown as shaded rectangles, the heights and widths of which reflect the range of $\overline{\overline{U}}_{*T}$ values measured at the various test sites on the plate (Table 5.2). Mean grain diameter ($\overline{d}$) has been used to calculate both θ and Re* so the range of particle sizes in the test sample is not shown in these figures.

In Figure 5.5(a), (Yalin curves), published data for threshold conditions in air are taken from Bagnold (1941), Zingg (1953), Chepil (1945b, 1959), Kadib (1963), Lyles and Woodruff (1971), Greeley et al. (1974) and Iversen et al. (1976). The published data for air included a particle size range from 8μm (lead shot) to 1.29mm (clover seed) and a density range between $0.21gcm^{-3}$ (instant tea) and $11.35gcm^{-3}$ (lead shot). The curve placed through this data is taken from Miller et al. (1977). In the case of threshold conditions in water, data were taken from Miller et al. (1977) who used the same data as that described above for the Shields curve. Also included in Figure 5.5(a) are the experimental data for ballotini. In Figure 5.5(b), experimental data for aeolian sand, sugar crystals and salt crystals are illustrated. In both these figures, shaded bars are used to depict the range of experimental threshold data. In common with Figure 5.4, the vertical extent of the bars reflects the range of measured mean threshold shear velocity values ($\overline{U}_{*T}$) on the plate. In this case, however, the horizontal extent does reflect the range of particle sizes as d_{max} and d_{min} were used to calculate the range of Yalin parameter values.

Figure 5.6(a) shows A-B curves derived from published data from Bagnold (1941), Chepil (1945b, 1959), Zingg (1953) and Iversen et al. (1976). The A-B curve in Figure 5.6(a) labelled Iversen et al. (1976) was based on data from empirical threshold studies in air by Greeley et al. (1974) and Iversen et al. (1976) using particles ranging in size and density from 8.0μm (lead shot) to 1.29mm (clover seed) and from $0.89gcm^{-3}$ (silica gel) to $11.35gcm^{-3}$ (lead shot), respectively. To avoid unnecessary clutter, only a small selection of these data are shown in Figure 5.6(a). Also included in Figure 5.6(a) are two curves derived from equations 5.15 and 5.16 below (Iversen and White, 1982) and the

experimental data for ballotini. In Figure 5.6(b), the experimental data for aeolian sand, sugar crystals and salt crystals are shown.

5.4 Discussion

5.4.1 Restricted empirical threshold curves

In Figure 5.2(a) it can be seen that the mean threshold shear velocity required to entrain grains is a function of grain diameter. $\bar{U}_{*T}$ reaches a minimum value at a critical particle diameter of approximately 80μm (Bagnold, 1941).

It is clear from inspection of Figure 5.2(a) that there is a large discrepancy between the published mean threshold values despite the similarities between the physical characteristics of the test materials. For example, a difference in $\bar{U}_{*T}$ values of $4cms^{-1}$ exists between the data of Bagnold (1941) and Zingg (1953) for 250μm grains, and a difference of $22cms^{-1}$ between the data of Bagnold (1941) and that of Lyles and Woodruff (1971) for the same grain size. Further, variation in published mean threshold shear velocity values occurs across a large range of particle sizes (100 to 1000μm).

The experimental data presented in Table 5.2 are illustrated in Figure 5.2 and in this form, suggest several likely reasons for the differences between the published data sets. The vertical extent of the shaded bars represents the range of mean threshold shear velocity values ($\bar{\bar{U}}_{*T}$) measured for strips of test material at various locations on the surface of the plate. Maximum $\bar{\bar{U}}_{*T}$ values were measured close to the

leading edge of the plate (Station A). The $\bar{\bar{U}}_{*T}$ values were found to decrease progressively with increasing distance downwind of Station A to reach minimum values at the rear of the plate (Chapter 4). In other words, $\bar{\bar{U}}_{*T}$ values reduced as the boundary layer flow regime became increasingly turbulent (Chapter 4). These experimental $\bar{\bar{U}}_{*T}$ values more than cover the range of published threshold values and the minima of the experimental values tend towards the values given by Bagnold (1941). This result suggests, therefore, that the range of published mean threshold shear velocity values for similar test materials may result from differences in the flow characteristics associated with the experimental wind tunnels used by these authors in their studies.

It is equally likely, however, that the criteria adopted to define incipient bed motion gave rise to the differences between published threshold values. For example, Bagnold (1941, p.85) describes the entrainment threshold as a condition in which "a few grains here and there begin to be dislodged", whilst Zingg (1953) and Lyles and Woodruff (1971) consider it to be conditions "just large enough to maintain sustained grain motion". Use of these different criteria in experimental determinations of mean threshold shear velocity would obviously lead to the derivation of different $\bar{\bar{U}}_{*T}$ values and would thus give rise to discrepancies in published $\bar{\bar{U}}_{*T}$ values irrespective of the test material studied or wind tunnel conditions during the study.

A further cause for differences between published $\bar{\bar{U}}_{*T}$ values concerns the experimental technique used to measure mean surface shear stress or mean shear velocity. Zingg (1953) used a floating shear tray to measure the mean shear stress directly. More generally, a form of the logarithmic wind profile equation is used to obtain $\bar{\bar{U}}_{*T}$ values using

averaged wind velocity measurements in the boundary layer (2.6). In recognition of the restrictions this method imposes, Lyles and Woodruff (1971) state that such mean velocity measurements are only valid if taken within the lower 20% of a fully turbulent boundary layer (i.e. the inner region (Chapter 2)). Thus the discrepancy between published $\bar{U}_{*T}$ values may have arisen from inappropriate use of the log wind profile equation. Given this range of possible experimental errors, therefore, it is difficult to reconcile the differences between published data objectively, as it appears that the different incipient motion criteria combine with different experimental procedures and apparatus to create sets of empirical relationships which are unique to each individual author and his methods.

Despite this, however, the experimental data indicate that the largest variation in $\bar{U}_{*T}$ values for any given sediment results from variations in the local boundary layer flow regime (in this study a function of the distance of a given test strip downwind from Station A). The experimental data also indicate that the choice of an incipient motion criterion may also be significant even though the range of particle sizes within a given sample is relatively small. Figures 4.3 to 4.9 show the range of measured shear velocities required to erode all the material in a given strip. This range covers a whole series of threshold criteria from motion of the first few grains ($\bar{U}_{*T(min)}$) to general bed motion ($\bar{U}_{*T(max)}$). In general, this range was approximately $20cms^{-1}$ irrespective of the test material or strip position on the plate. Thus, it seems likely that the lack of standardized entrainment criterion may account for at least some of the variation in published aeolian threshold values.

Figure 5.2(b) illustrates the $\bar{\bar{U}}_{*T}$ data for sugar crystals, aeolian sand and salt crystals. The most striking feature is the similarity in $\bar{\bar{U}}_{*T}$ values between 710-600μm ballotini and sugar crystals, and between 180-150μm ballotini and aeolian sand. The 180-150 μm salt crystals on the other hand display much lower $\bar{\bar{U}}_{*T}$ values than equivalently-sized ballotini or aeolian sand. It is surprising to find that $\bar{\bar{U}}_{*T}$ values for ballotini and sugar crystals are so similar. As the density of ballotini is 1.6 times greater than sugar (Table 3.4), the force required to induce movement of sugar crystals ought to be less than that required for ballotini. However, it seems likely that the high $\bar{\bar{U}}_{*T}$ values for sugar crystals are a direct consequence of moisture absorption which apparently increases both the specific gravity and cohesion of the sugar particles and thus raises the mean threshold shear velocity. The specific gravity of aeolian sand is comparable with ballotini, therefore it would be expected that the $\bar{\bar{U}}_{*T}$ values measured at various distances along the plate would also be similar. The data shown in Figure 5.2(b) indeed bears this out. However, the greater angularity of the sand particles appears to modify the boundary layer structure in comparison with the regime measured over 180-150μm ballotini (see 4.4(a)), and in general the $\bar{\bar{U}}_{*T}$ values associated with aeolian sand are lower than for ballotini. The $\bar{\bar{U}}_{*T}$ values determined for sand at sites more than 10cm downwind from Station A are similar to values measured using 180-150μm ballotini and agree well with values reported by Bagnold (1941) and Zingg (1953), Figure 5.2(a). The problems of moisture absorption associated with salt crystals were overcome to some extent by including a small amount of desiccant particles in the test samples (i.e. magnesium carbonate and sodium hexacyanoferrate II). The $\bar{\bar{U}}_{*T}$ values are lower than those recorded for 180-150μm ballotini and aeolian sand and probably reflect the lower specific gravity of salt crystals. The

effect of crystal shape cannot be quantitatively assessed but it may act to lower the entrainment threshold by increasing the level of turbulence generated by individual roughness elements (Chapter 4). Further, the cubic crystal form of salt has a larger aerodynamic drag coefficient than a sphere and, therefore, its susceptibility to entrainment in any given flow is likely to be raised by virtue of its shape. (At a Reynolds number value of 10^4, the coefficient of drag, C_D, for a sphere is 0.4 whereas for a cube C_D is 1.1).

Figure 5.3 shows an enlarged portion of Figure 5.2(a). Data from Bagnold (1941), Zingg (1953), Chepil (1959) and Lyles and Krauss (1971) are included and show the mean threshold shear velocities for a range of particle sizes. Also included are experimentally determined $\overline{\overline{U}}_{*T}$ values for all the ballotini sizes. In Figure 5.3 the published mean threshold data from Bagnold and Zingg for sand (σ = 2.65gcm^{-3}) were determined experimentally by these workers. In contrast, data labelled 'Chepil (1959) computed' are $\overline{U}_{*T}$ values derived from an empirical equation for mean threshold shear stress (equation 1.20, Chepil, 1959). This equation expresses average threshold conditions for a given sample of loose particles in wind regimes characterised by a specified level of turbulence intensity.

Also illustrated in Figure 5.3 are $\overline{U}_{*T}$ values published by Lyles and Krauss (1971) for sand (σ= 2.59gcm^{-3}). Lyles and Krauss used two different criteria to define threshold conditions in their study. These were: (a) the motion of the first grain; and (b) general bed movement. The range of $\overline{U}_{*T}$ values encompassed by these threshold criteria are shown in Figure 5.3 by the shaded area between the lines labelled 'general motion' and 'motion of the first grain'. The range of

$\overline{U}_{*T}$ values between these two lines clearly illustrates the importance of using an objective definition of incipient motion when determining $\overline{U}_{*T}$ values in air. Experimental threshold data from Bagnold (1941) and Zingg (1953), and computed threshold values from Chepil (1959), all fall below the critical $\overline{U}_{*T}$ values determined by Lyles and Krauss (1971) for motion of the first grain, despite there being close similarities between the test materials and the reported entrainment criteria. The different techniques used to measure $\overline{U}_{*T}$ are unlikely to account for such a large variation in threshold values. Thus it is likely that differences in the boundary layer flow regime over the test materials accounts for these differences. Unfortunately, very little information on the local flow conditions over the test beds is reported by authors and therefore the significance of variations in flow cannot be assessed.

5.4.2 Universal empirical threshold curves

(a) Shields (1936) curve

Shields entrainment function (θ) is plotted against the grain Reynolds number (Re*) in Figure 5.4(a). The form of Shields curves for both air and water are shown. The reasons for differences in the form of Shields curve for air and water are puzzling as the variations in fluid properties should be accounted for in Shields parameter. A brief discussion of some possible reasons is given below. The experimental data are illustrated using shaded rectangles in both Figure 5.4(a), (ballotini), and 5.4(b), (aeolian sand, sugar crystals and salt crystals). These rectangles result from incorporating the range of ($\overline{U}_{*T}$) values measured at various positions on the plate for any given test material in the dimensionless parameters and Re*, (Figure 5.4).

The published threshold data for air and water show a significant degree of scatter about the mean threshold curves illustrated in Figure 5.4(a). In view of the preceding discussion, this scatter may be attributed to: (a) the criterion of initial bed motion used by a particular author; (b) the local boundary layer flow regime; and (c) the characteristics of the test particles used in threshold experiments.

The effect of adopting different criteria for initial bed motion was investigated by Grass (1970) using experimental data derived in low grain Reynolds number flow conditions (i.e. Re* smaller than 2). It was shown in 2.5.2 that the degree of overlap between the probability distribution of the instantaneous bed shear stress $P(\tau_I)$ and the probability distribution of threshold bed shear stress ascribed to particles $P(\tau_T)$ in a given test sample defined static, threshold and active entrainment conditions on a sediment bed, (see Figure 2.12). Grass (1970) argued that the distribution $P(\tau_I)$ can be defined in terms of $P(\tau_T)$ in the form

$$\bar{\tau}_I + n'\sigma_{\tau I} = \bar{\tau}_T - n'\sigma_{\tau T} \qquad 5.10$$

where

$\bar{\tau}_I$ = average value of the instantaneous bed shear stress (i.e.) Nm^{-2}

$\bar{\tau}_T$ = average value of the threshold bed shear stress values associated with a given test sample Nm^{-2}

$\sigma_{\tau I}$ = standard deviation defined as: $(\Sigma(\tau_I - \bar{\tau})^2/n_o)^{1/2}$ Nm^{-2}

$\sigma_{\tau T}$ = standard deviation defined as: $(\Sigma(\tau_T - \bar{\tau}_T)^2/n_o)^{1/2}$ Nm^{-2}

τ_I = instantaneous bed shear stress Nm^{-2}

τ_T = threshold shear stress for a given grain Nm^{-2}

n_o = the number of τ_I or $\bar{\tau}_T$ values dimensionless

n' = multiplication factor defining the intersect point between the $P(\tau_I)$ and $P(\tau_T)$ distributions dimensionless

By experiment, Grass (1970) found that

$$\frac{\sigma_{\tau T}}{\bar{\tau}_T} \approx 0.4 \qquad 5.11(a)$$

and

$$\frac{\sigma_{\tau I}}{\bar{\tau}_I} \approx 0.3 \qquad 5.11(b)$$

By substituting equations 5.11(a) and 5.11(b) into equation 5.10, Grass obtained the expression

$$\bar{\tau}_I = \frac{\bar{\tau}_T(1 - 0.3n')}{(1 + 0.4n')} \qquad 5.12$$

Using different values of n' to simulate different degrees of overlap between the $P(\tau_I)$ and $P(\tau_T)$ distributions, (i.e. n' = 0, 1 and 2), Grass calculated τ_I values using experimentally determined $\bar{\tau}_T$ values. This permitted the calculation of Shields parameter (θ) for a given test material using

$$\theta = \frac{\bar{\tau}_I}{(\sigma-\rho)gd} \qquad 5.13$$

The resulting data were found to plot as straight lines running roughly parallel with Shields curve. These data for n' = 0, 1 and 2 are illustrated in Figure 5.7.

Grass (1970) found that the expression describing these straight line segments was in the form

$$\overline{\tau}_I = 63.3\nu^{0.49}d^{0.27}\left[\frac{1 - 0.3n'}{1 - 0.4n'}\right] \qquad 5.14$$

Figure 5.7 shows that threshold conditions are defined by n' = 0.625 and Grass found that equation 5.14 was applicable for particles smaller than 250μm in diameter in water over a temperature range of $0^{o}C$ to $30^{o}C$. Using this criterion, Grass (1970) proposed the extention to the Shields curve illustrated in Figure 5.4(a).

On the basis of these measurements, and the associated statistical analysis, Grass (1970) suggested that the scatter of data on the Shields curve reflected different degrees of overlap (reflected by the term $n(\sigma_{\tau I}+\sigma_{\tau T})$) between the distribution of instantaneous bed shear stress and the distribution of threshold shear stresses associated with a given sediment. In other words, the value of θ for a given sediment depends on the criterion of initial movement used by an investigator. The objective definition of threshold conditions proposed by Grass (1970) would, therefore, appear to be an appropriate solution to resolve data scatter providing the shear stress distributions associated with both the boundary layer flow and the sediment are known.

The effect of adopting different criteria of bed motion was discussed in Chapter 4 and using Figures 4.3 to 4.9 it was shown that the range of mean threshold shear velocities required to erode a given strip was quite large, (approximately $20cms^{-1}$ in most cases), despite the relatively small range of particle sizes associated with a given sample.

The results were shown to be similar in many respects to those obtained by Grass (1970) in water and thus it seems likely that at least some of the data scatter associated with $\overline{U}_{*T}$ values in air over the range of grain Reynolds numbers shown in Figure 5.4(a) results from the use of different entrainment criteria by various authors. However, this effect cannot be quantified as nothing is known about the $P(\tau_I)$ and $P(\tau_T)$ distributions associated with the published experimental data.

The scatter in the reported threshold values may also be attributed in part to differences in the general characteristics of boundary layer flow regimes used by investigators. More specifically, it is likely that some of the data scatter resulted directly from differences in the ratio of instantaneous to mean local shear stress above a given bed of particles. It was argued in Chapter 4 that sediment entrainment is most likely to be instigated by peak shear stress events (i.e. fluid sweeps), and that the spatial and temporal frequency of such events governed the entrainment characteristics of granular material. Any differences in the magnitude and the spatial and temporal frequency of peak shear stress events associated with flow over loose granular material are, therefore, likely to have a considerable influence on measured mean shear velocity values.

In an interesting investigation of incipient sand motion in glycerol and water, Yalin and Karahan (1977) were able to obtain threshold data for both laminar and turbulent boundary layer flow. Their results are illustrated in Figure 5.8 and show clearly that a considerable data scatter could result if threshold conditions are inadvertently measured in a range of boundary layer flow regimes

characterised by different levels of flow turbulence. Similar conclusions were also drawn by Komar and Miller (1973) and Greeley et al. (1977).

Thus, if the entrainment of sediment is to be related to mean shear velocity, it is critical to ensure that the intensity and the spatial and temporal frequency of peak shear velocity events occurring on a bed of particles is exactly the same, irrespective of the test material. Failure by authors to standardize flow conditions over test beds in this way may have inadvertently led to some of the data scatter in published $\bar{U}_{*_T}$ values for both air and water.

It is also likely that some of the data scatter may have resulted from the differences in the shape of test particles. However, the published data does not provide any information on the shape of particles used in threshold experiments and thus this effect is impossible to assess. However, it is probable that test samples (e.g. sand) used by the different investigators originated from widely different sources and are, therefore, likely to have had different shape characteristics, despite other similarities in particle size and density. Such differences in particle shape would result in different drag coefficients between samples and thus would inadvertently give rise to different entrainment thresholds regardless of similarities between all the other experimental variables.

Some of the scatter associated with the published data may also be attributable to differences in the geometric configurations of particle test beds used by the various investigators. White (1970), Grass (1970) and Williams and Kemp (1971) noted that loose sediment beds

were subject to ripple formation in threshold flow conditions which led to modifications to the local flow conditions. These changes in the bed configuration would obviously alter both the $P(\tau_T)$ and $P(\tau_I)$ distributions (Grass, 1970) and hence affect entrainment thresholds directly. Carson (1971) found that typical θ_T values for rippled surfaces in water ranged between 0.1 and 0.25 and suggested that similar modifications of threshold conditions could arise in air if the bed geometry was sufficiently disturbed. As no standard technique to prepare sediment beds for threshold measurements has been universally adopted, it is likely that some of the data scatter associated with the published results is attributable to differences in the test bed configurations used by researchers.

Sagan and Bagnold (1975) suggest several physical explanations of why Shields curves for water and air should be so different. Threshold conditions in water are generally characterised by slight grain motion as the most susceptible grains move to more secure sites. Often such movement is difficult to detect and may go unrecorded during experimental runs. Initial motion in air, however, is characteristically violent, with entrained particles inducing motion of other grains through collision. Further, these collisions often cause other grains to become lodged insecurely on the bed and these, in turn, may then be entrained. Therefore, an observable degree of bed entrainment is apparent at relatively lower shear velocities in air than in water. This different response of granular materials to threshold flow conditions in air and water has inadvertently led researchers to apply different threshold criteria in studies of incipient motion in air and water and thus may have given rise to an overestimation of $\bar{U}_{*T}$ values in water. In addition, the wide differences in the ratios of fluid to particle

densities for air and water is also thought to be implicated in the different response characteristics of granular materials at the threshold in air and water (i.e. σ/ρ for quartz grains = 2000:1 in air and 1.65:1 in water), (Bagnold, 1941; Sagan and Bagnold, 1975; Leeder, 1985). The precise effects of this fundamental difference, however, have not been quantitatively assessed.

Variations in the relative magnitude of the instantaneous bed shear velocities in turbulent flows in air and water provide a further possible reason for the differences in θ values for these fluids. The experimental evidence presented in Chapter 4 suggests that peak shear velocity at the threshold in turbulent flow exceeds 2.7 times the mean. In water, Shen and Wang (1970) found peak shear velocity to be smaller than or equal to 2.3 times the mean in threshold flow conditions. On the basis of this evidence, therefore, it seems likely that the value of θ will be lower for air as θ is calculated using mean threshold shear stress.

(b) Yalin's (1972) curve

Yalin curves showing the functional relationship between $\Xi^{1/2}$ and θ at the threshold of particle motion are shown in Figure 5.5(a) for both air and water and are based on a range of published data (see 5.2.2(b)). The form of these Yalin curves is similar to Shields curves (Figure 5.4) and shows that θ values for air are nearly constant for Ξ values greater than 10^1. For Ξ values less than 10^1, θ values for air are shown to increase markedly and reflecting both the change to aerodynamically smooth flow and the increase in the relative significance of inter-particle forces.

The published data illustrated in Figure 5.5(a) shows a significant degree of scatter about the Yalin curve for air (Miller et al., 1977). Aeolian thresholds for sand given by Lyles and Woodruff (1971) and Kadib (1965) are seen to differ markedly from the other published results and are more typical of θ values for water (Miller et al., 1977). The θ values calculated using the mean threshold shear velocity ($\bar{\bar{U}}_{*T}$) measurements from the rear of the plate agree well with the published data. However, $\bar{\bar{U}}_{*T}$ values measured at positions much closer to Station A give rise to much larger θ values and reflect differences in the boundary layer flow regime. The largest range of θ values is associated with 180-150μm ballotini. The Yalin plot is similar in many respects to Shields diagram (Figure 5.4) and therefore all the comments made regarding the underlying reasons for the scatter in the published data on that diagram are equally applicable in this case. Miller et al. (1977) consider the Yalin plot to be "the most useful general plot available for sediment threshold" Miller et al. (1977, p. 515) owing to the ease with which threshold conditions for loose granular material can be determined using simple fluid and grain properties.

(c) A-B curve, (Iversen et al. 1973)

A number of A-B curves are shown in Figure 5.6(a) and are based on published data from a variety of sources (see 5.2.2(c)). Iversen and White (1982) developed two empirical equations to describe the A-B relationship over a certain range of B values, primarily for the study of entrainment when unusual combinations of particle and gas densities are considered. These are

$$A = 0.129[(1+0.006/\sigma gd^{2.5})^{0.5} / (1.928B^{0.092}-1)^{0.5}] \qquad 5.15$$

$$A = 0.120(1+0.006/\sigma gd^{2.5})^{0.5}.(1-0.0858e^{[-0.0617(B-10)]}) \qquad 5.16$$

Equations 5.15 and 5.16 apply over B values of $0.03 < B < 10$ and $B > 10$, respectively. A and B values predicted by these equations are plotted in Figure 5.6(a) for particle densities of $1.1 gcm^{-3}$ (nut shell) and $11.35 gcm^{-3}$ (lead shot). The resulting curves show clearly the effect of the stronger inter-particle forces associated with metallic particles when B is smaller than or equal to 10. At B values greater than 10 this effect becomes much less significant and aerodynamic forces become dominant (see Figure 5.6(a)).

The experimental data for ballotini are plotted in Figure 5.6(a) and data for aeolian sand, salt crystals and sugar crystals are plotted in Figure 5.6(b). The spread of experimental data largely results from the range of measured threshold shear velocity values ($\overline{\overline{U}}_{*T}$) for test materials at different positions on the plate. The comments made regarding the scatter of published data and the experimental data from the plate in 5.3.4(a) are equally applicable in this case as the graphs are essentially the same (i.e. $A = (\theta)^{1/2}/$). Like Shields curve (Figure 5.4), the A-B plot includes $\bar{U}_{*T}$ in the expressions A and B and therefore it is necessary to apply an iterative procedure to find $\bar{U}_{*T}$ for an unknown test material. However, using the arguments given by Yalin (1972) it was possible to devise a new dimensionless expression Ψ which effectively eliminates $\bar{U}_{*T}$ from the abscissa. Ψ is derived from

$$\Psi = \frac{Re^{*2}}{A} = \frac{Re^{*2}}{(\theta)^{1/2}} = \frac{(\bar{U}_{*T}d/\ )^2}{\bar{U}_{*T}/(\sigma gd/\rho)^{1/2}} = \sigma gd^3/\rho\nu^2 \qquad 5.17$$

When A is plotted against Ψ (not illustrated), the form of the resulting curve is similar to the A-B plot in Figure 5.6(a) and (b).

5.5 Conclusion

In this chapter, comparisons have been made between published threshold data from a wide range of sources and the experimental data presented in Chapter 4. Both restricted and universal empirical curves which express threshold conditions in terms of fundamental fluid and grain characteristics have been used. Using the aeolian threshold conditions measured in the developing boundary layer on the surface of the flat plate, it has been possible to assess the significance of the three factors identified in Chapter 1 as being fundamental controls of aeolian entrainment thresholds, namely: (a) the criterion of initial bed motion; (b) the local boundary layer flow regime; and (c) the characteristics of the test grains.

The experimental evidence from the erosion of test strips (Chapter 4) showed that the choice of entrainment criterion significantly affected the interpretation of aeolian thresholds regardless of the test material or the boundary layer flow regime. It is likely, therefore, that at least some of the scatter associated with published threshold data results from researchers considering a wide range of grain motion states as being indicative of the threshold condition. The statistical analysis by Grass (1970) provides an objective definition of threshold conditions provided that the $P(\tau_I)$ and $P(\tau_T)$ distributions are known.

Measurements of $\overline{\overline{U}}_{*T}$ at various positions on the plate indicated that peak shear velocity was the main variable controlling

initial particle motion. As the magnitude and the spatial and temporal frequency of peak shear velocities increases with the boundary layer Reynolds number it is essential to ensure that threshold experiments are conducted in flows characterised by the same Reynolds number, irrespective of the test material. Given the large variation in the dimensions of wind tunnels used by various investigators it is likely that this condition is not always met and the resulting differences in the peak shear stress characteristics associated with a given flow regime probably contributes to the scatter in published threshold values. Given these problems it is desirable, therefore, to standardize the characteristics of the boundary layer flow over test samples in studies to determine $\overline{U}_{*T}$. The flat plate is one of several ways in which such flow control may be achieved.

A number of other factors have also been identified as contributors to the scatter of published threshold values. These include the arrangement of test material (i.e. the flatness of the bed), differences in inter-particle cohesion and the use of insufficiently uniform test materials. Further, tests using unconventional materials such as instant tea and lead shot (Iversen et al. (1976)) in aeolian threshold studies indicate that the density ratio ρ/σ may be a significant factor giving rise to data scatter, particularly for Re* values less than 5.

Parameter	Definition	Units
$\bar{\tau}_T$	Mean threshold shear stress	Kgm^{-2}
$\bar{U}_{*T}$	Mean threshold friction velocity $(\bar{\tau}_T/\rho)^{1/2}$	ms^{-1}
θ_T	Shields criterion $\bar{\tau}_T/(\sigma-\rho)g\bar{d}$	dimensionless
Re*	Roughness or grain Reynolds number $\bar{U}_{*T}\bar{d}/\nu$	dimensionless
A	Bagnolds coefficient $\bar{U}_{*T}/(\sigma g\bar{d}/\rho)^{1/2}$	dimensionless
Ξ	Yalin parameter Re^{*2}/θ_T	dimensionless

Table 5.1 Parameters used in the comparison of published and experimental threshold data.

x, cm	5		10							15	25					40					55				
Material code (see legend)	4	5	1	2	3	4	5	6	7	4	1	2	3	4	5	1	2	3	4	5	1	2	3	4	5
$\bar{\tau}_T$, kgm^{-3}	1.8	0.57	3.19	1.83	0.49	0.67	0.27	1.71	0.08	0.3	1.89	1.18	0.37	0.14	0.19	1.43	0.91	0.27	0.06	0.16	1.23	0.6	0.2	0.52	0.18
$\bar{U}_{*T}$, ms^{-1}	1.21	0.68	1.61	1.22	0.63	0.74	0.47	1.18	0.26	0.49	1.24	0.98	0.55	0.34	0.40	1.08	0.86	0.47	0.22	0.36	1.00	0.7	0.4	0.65	0.38
θ_Tx 10^{-2}	42.7	13.6	8.1	10.9	5.8	15.9	6.4	16.8	2.2	7.1	4.8	7.1	4.4	3.3	4.5	3.6	5.4	3.2	1.4	3.8	3.1	3.6	2.3	12.4	4.2
Re*, (B)	13	7.6	169	54	14	8	5.24	52	2.9	5	130	43	12	4	5	113	38	10	3	4	105	31	8.9	7	4
A	0.65	0.37	0.28	0.33	0.24	0.4	0.25	0.41	0.15	0.27	0.22	0.27	0.21	0.18	0.21	0.19	0.23	0.18	0.11	0.19	0.18	0.19	0.15	0.35	0.2

x, cm	70			85							130					
Material code (see legend)	1	4	5	1	2	3	4	5	6	7	2	3	4	5	6	7
$\bar{\tau}_T$, kgm^{-3}	0.84	0.36	0.12	0.59	0.32	0.13	0.30	0.07	0.29	0.03	0.19	0.08	0.08	0.06	0.17	0.02
$\bar{U}_{*T}$, ms^{-1}	0.83	0.54	0.31	0.69	0.51	0.32	0.49	0.24	0.49	0.15	0.39	0.25	0.25	0.23	0.37	0.12
θ_Tx 10^{-2}	2.1	8.6	2.8	1.5	1.9	1.6	7.1	1.6	2.8	0.86	1.1	0.96	1.9	1.4	1.6	0.57
Re*, (B)	87	6	3	72	23	7	5	2.7	22	1.7	17	5.5	2.8	2.6	16	1.3
A	0.15	0.29	0.17	0.12	0.14	0.12	0.27	0.13	0.17	0.1	0.11	0.1	0.14	0.12	0.12	0.07

Material code	YALIN PARAMETER, $(\Xi)^{1/2}$
1	510 to 681
2	143 to 184
3	51 to 65
4	18 to 23
5	18 to 23
6	143 to 184
7	18 to 23

LEGEND	
Material code	Material
1	1.7-1.4mm ballotini
2	710-600μm ballotini
3	355-300μm ballotini
4	180-150μm ballotini
5	180-150μm aeolian sand
6	710-600μm sugar crystals
7	180-150μm salt crystals

Table 5.2 Summary of experimental aeolian threshold data.

(a) SHIELDS CURVE

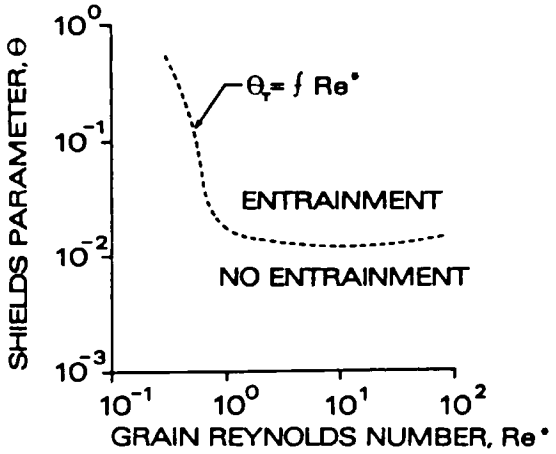

(b) YALIN'S CURVE

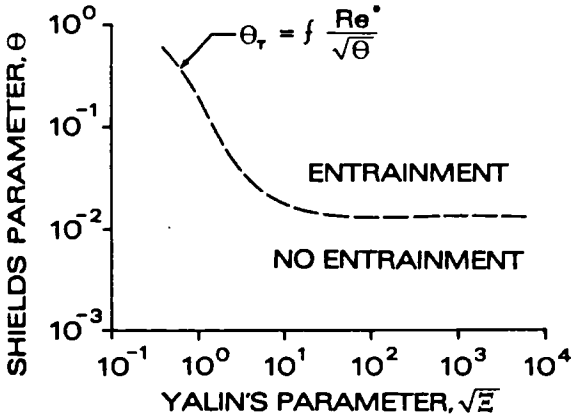

(c) UNIVERSAL A-B CURVE

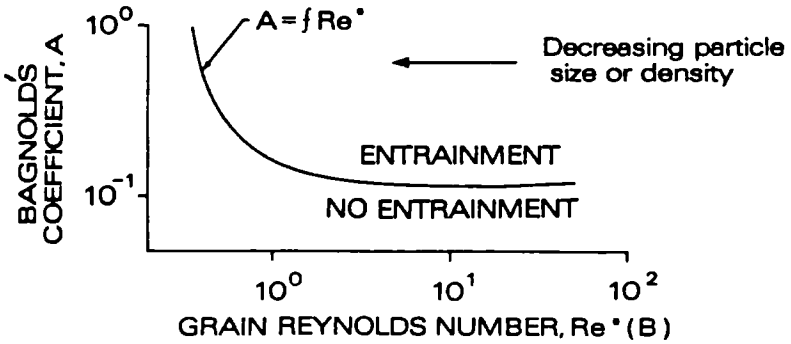

Figure 5.1 Universal empirical threshold curves.

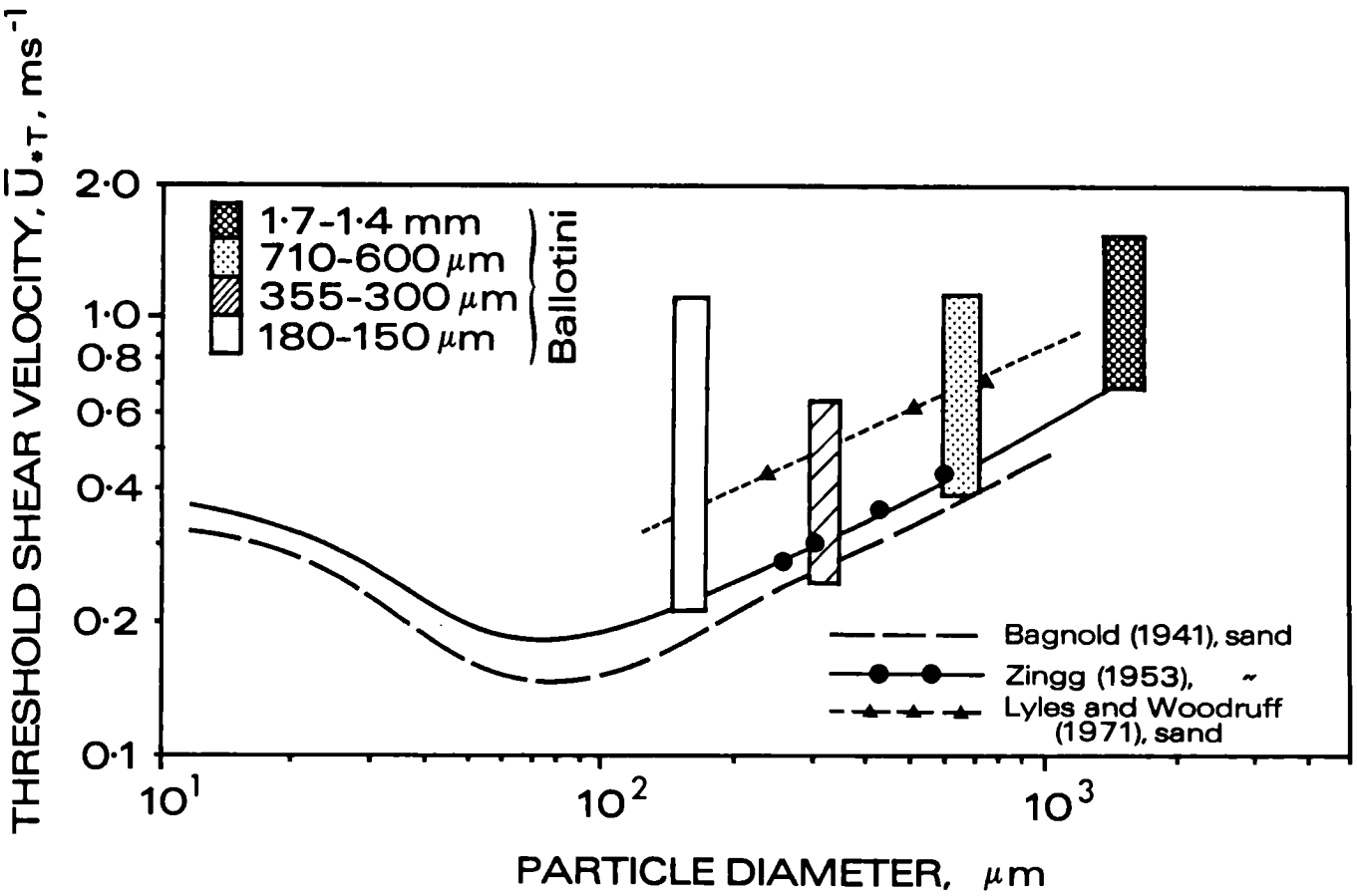

Figure 5.2(a) Relationship between mean threshold shear velocity and particle diameter showing published and experimental data.

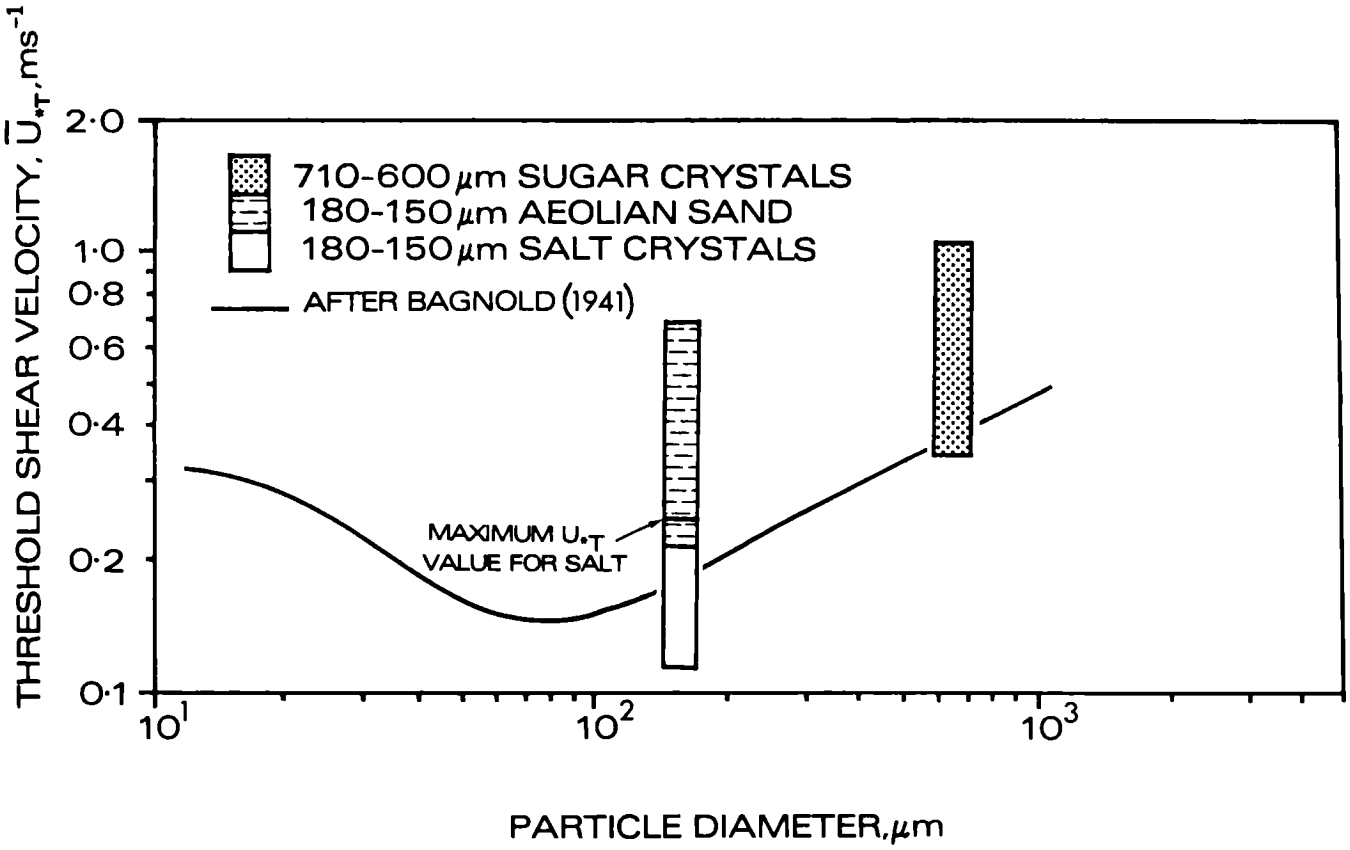

Figure 5.2(b) Relationship between mean threshold shear velocity and particle diameter showing published and experimental data.

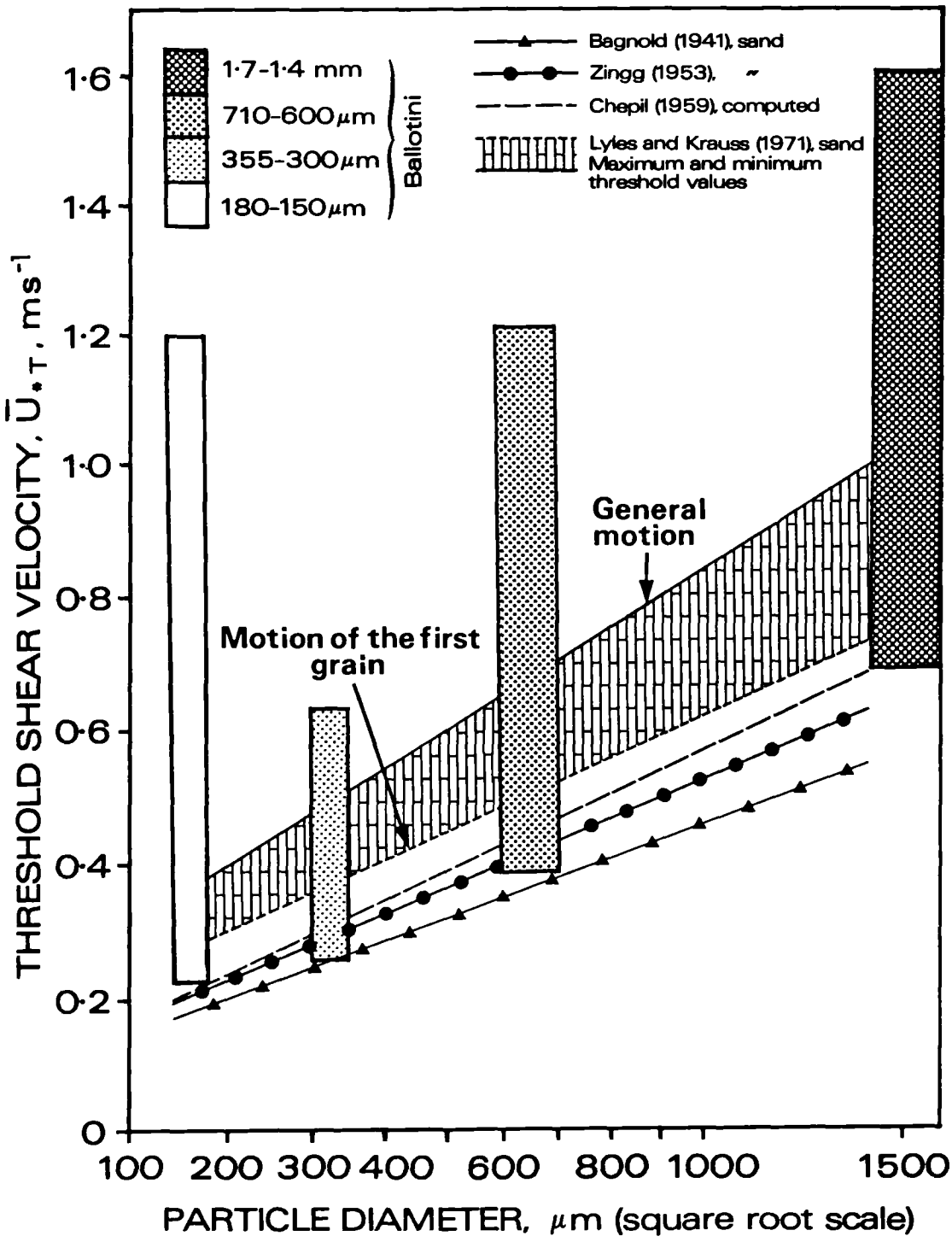

Figure 5.3 Relationship between mean threshold shear velocity and particle size (square root scale) showing published and experimental data.

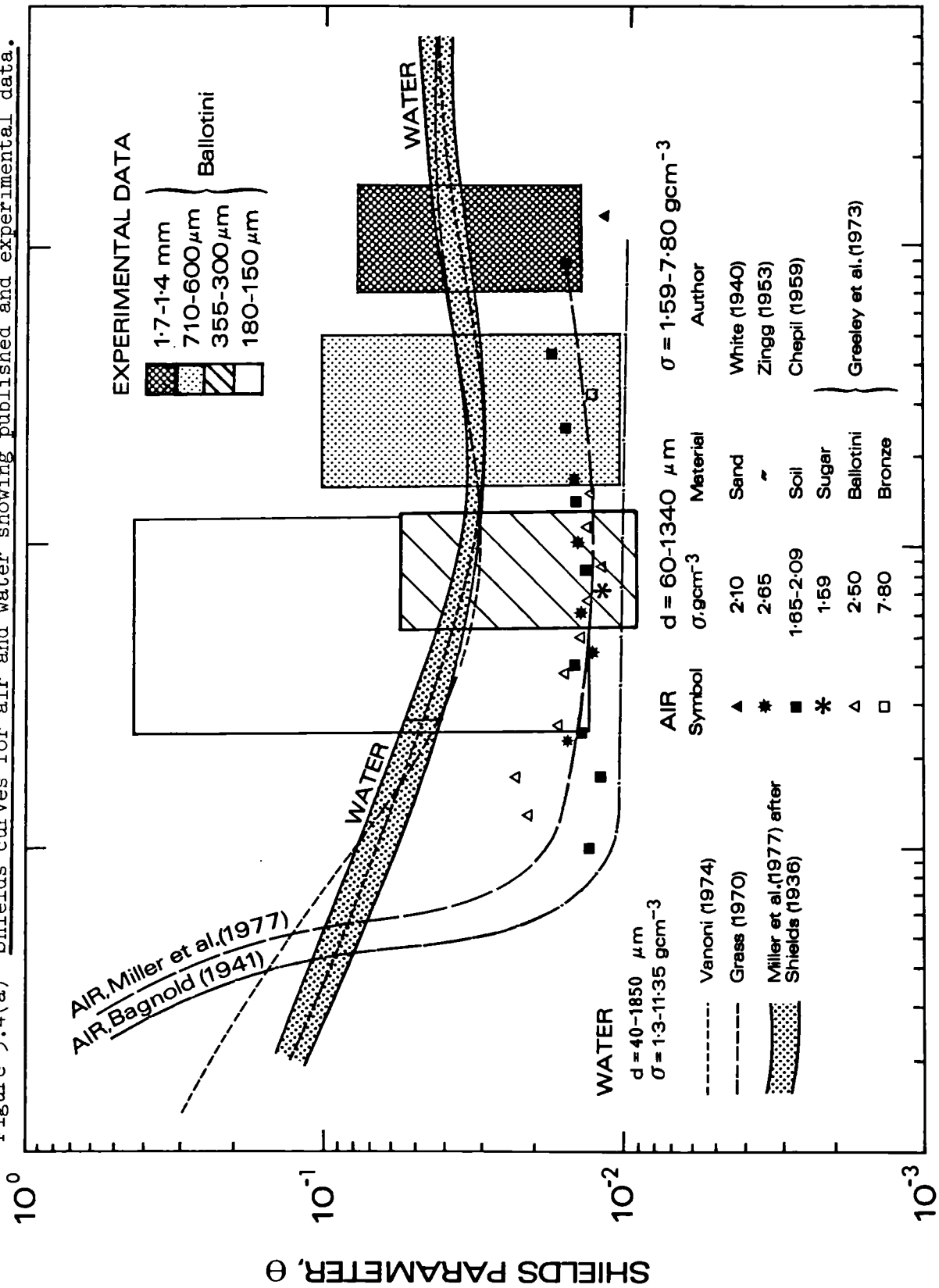

Figure 5.4(a) Shields curves for air and water showing published and experimental data.

Figure 5.4(b) Shields curve for air showing experimental data.

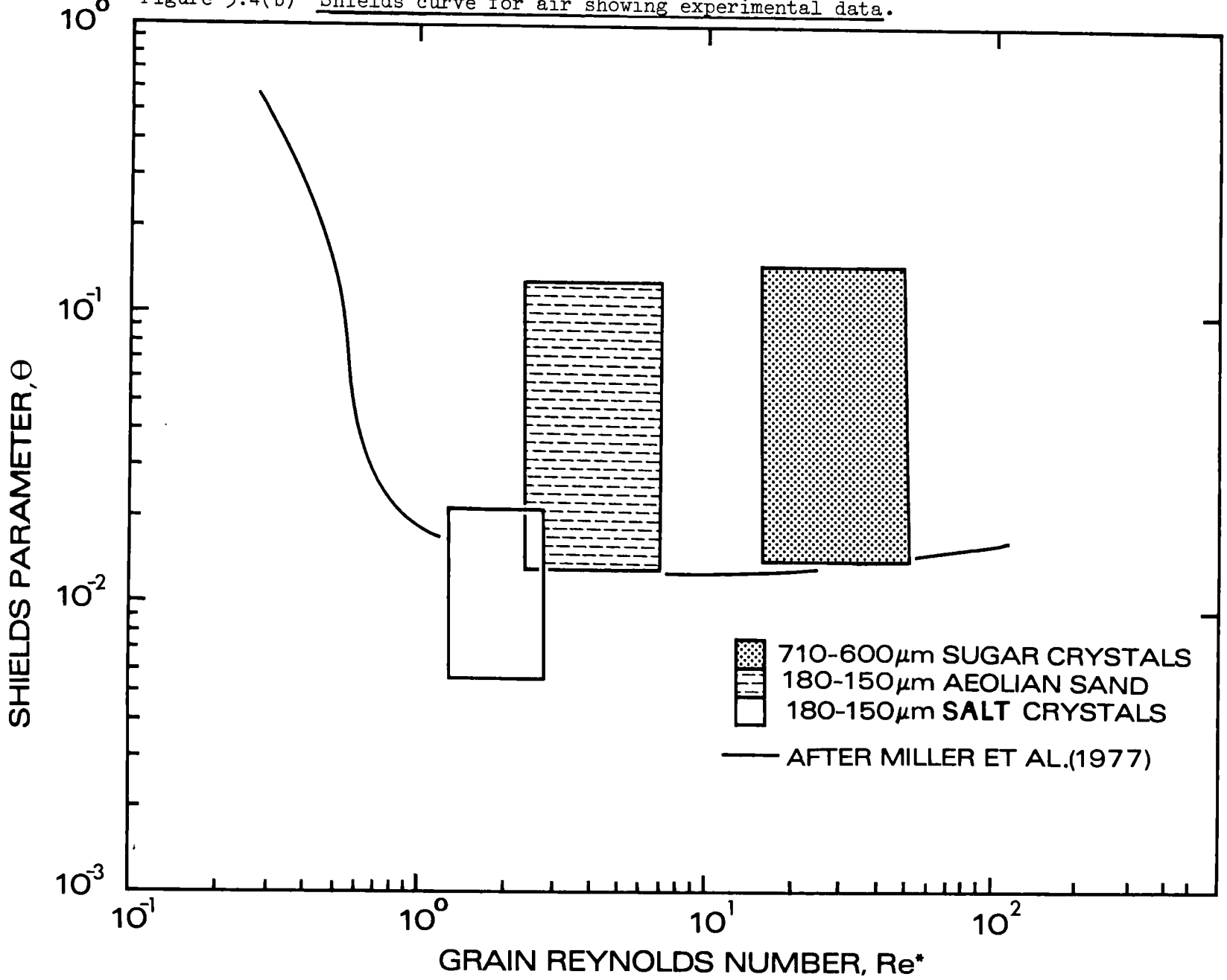

Figure 5.5(a) Yalin curves for air and water showing published and experimental data.

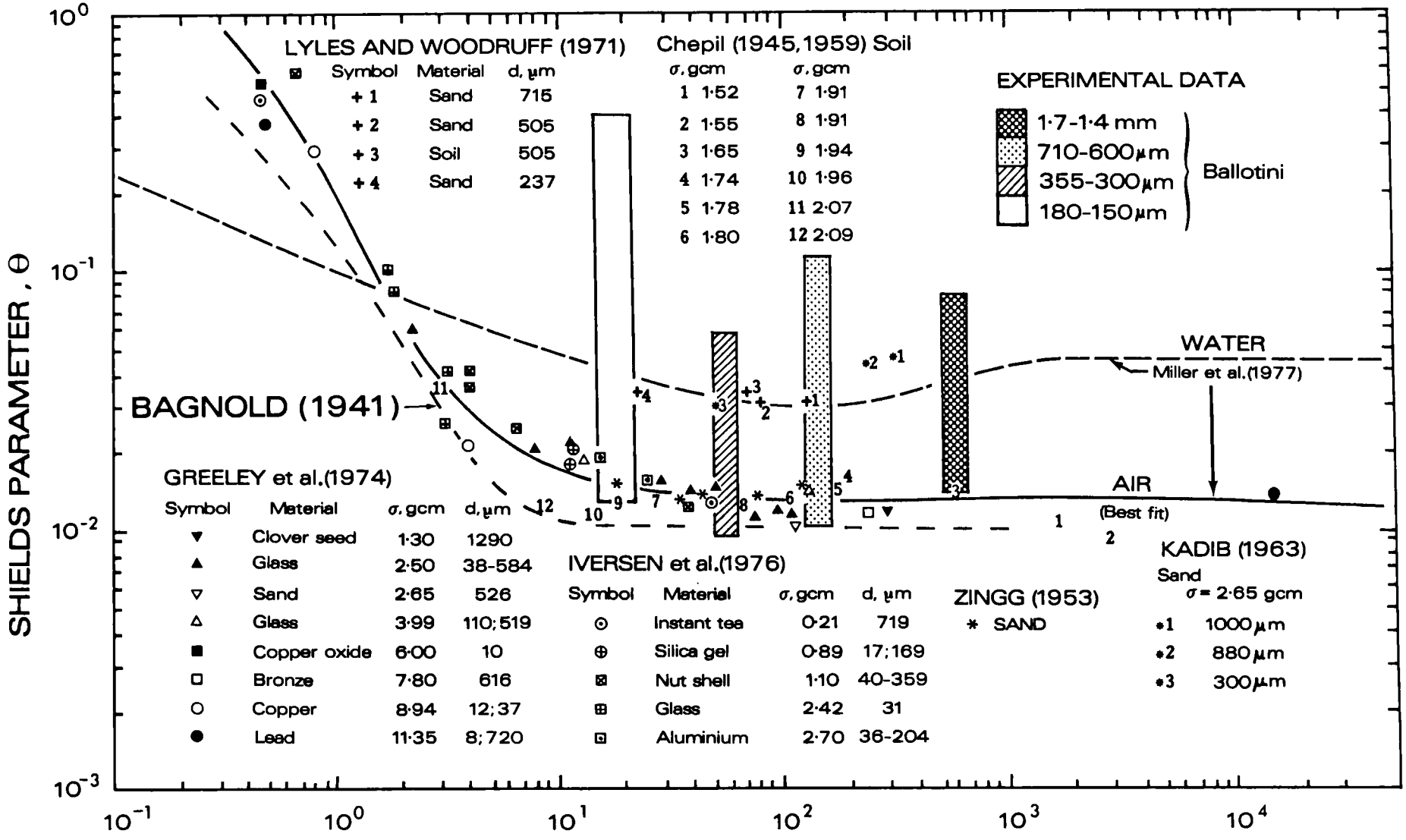

Figure 5.5(b) Yalin curve for air showing experimental data.

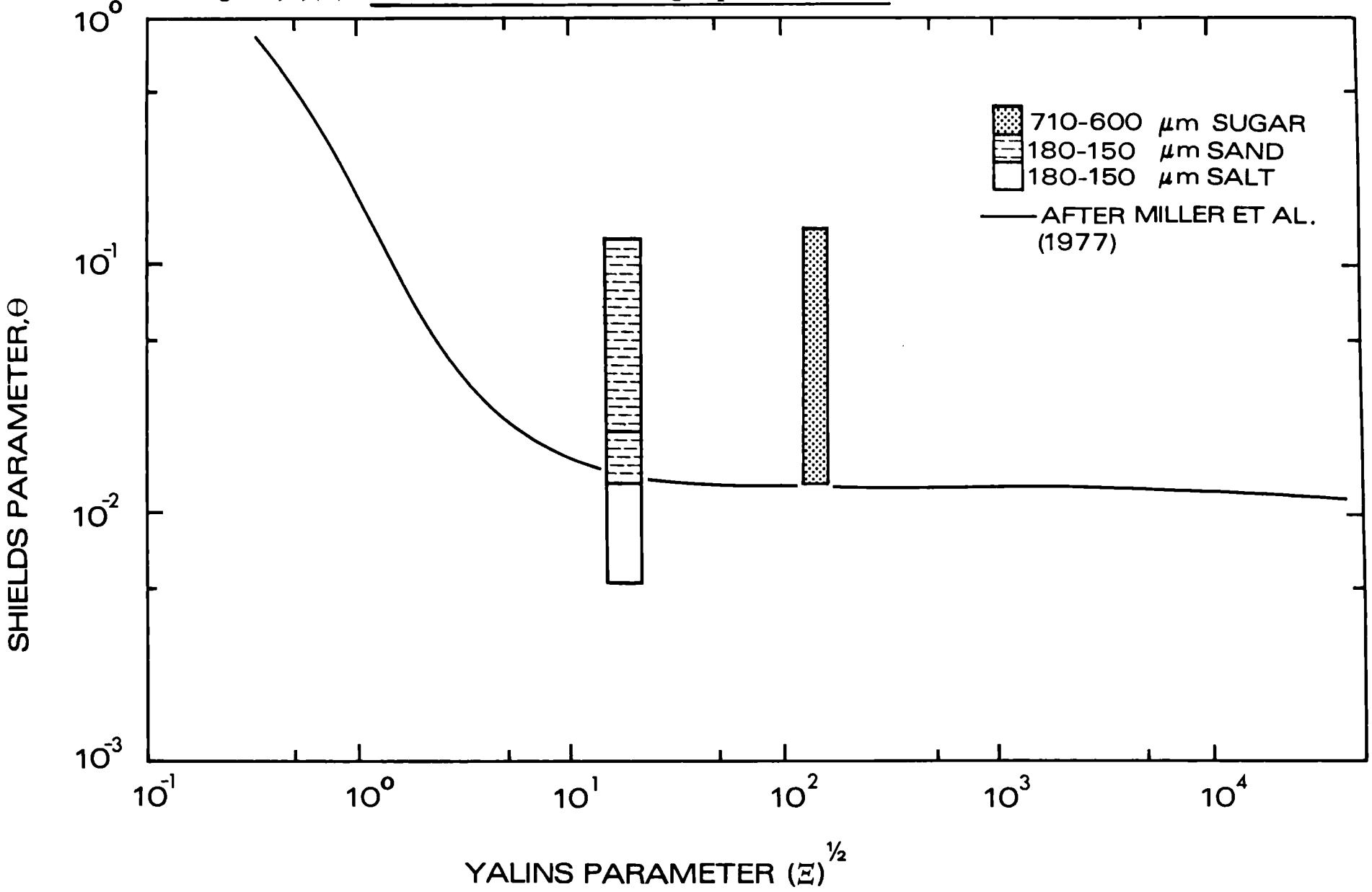

Figure 5.6(a) A-B curves for air showing published and experimental data.

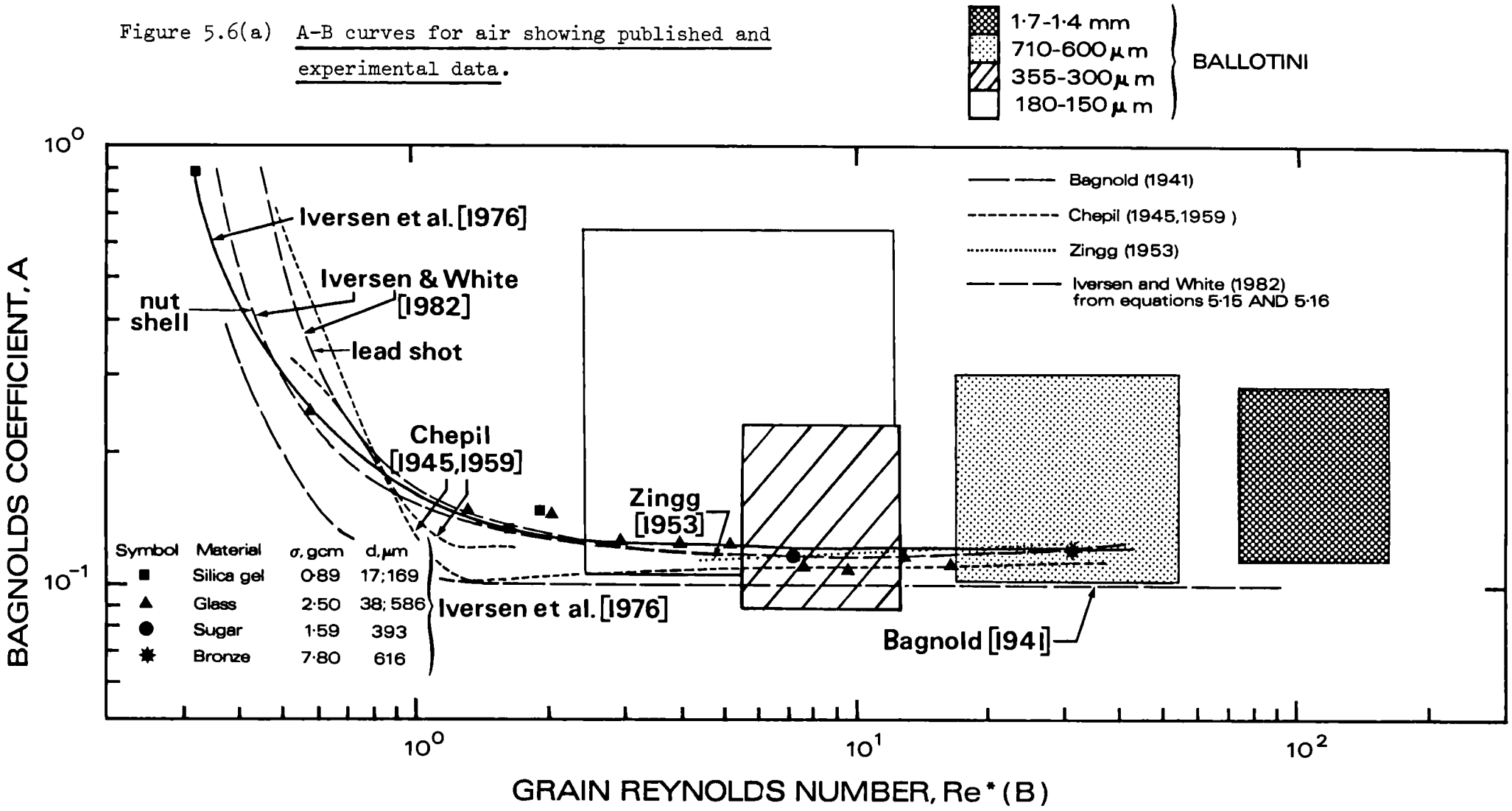

Figure 5.6(b) A-B curve for air showing experimental data.

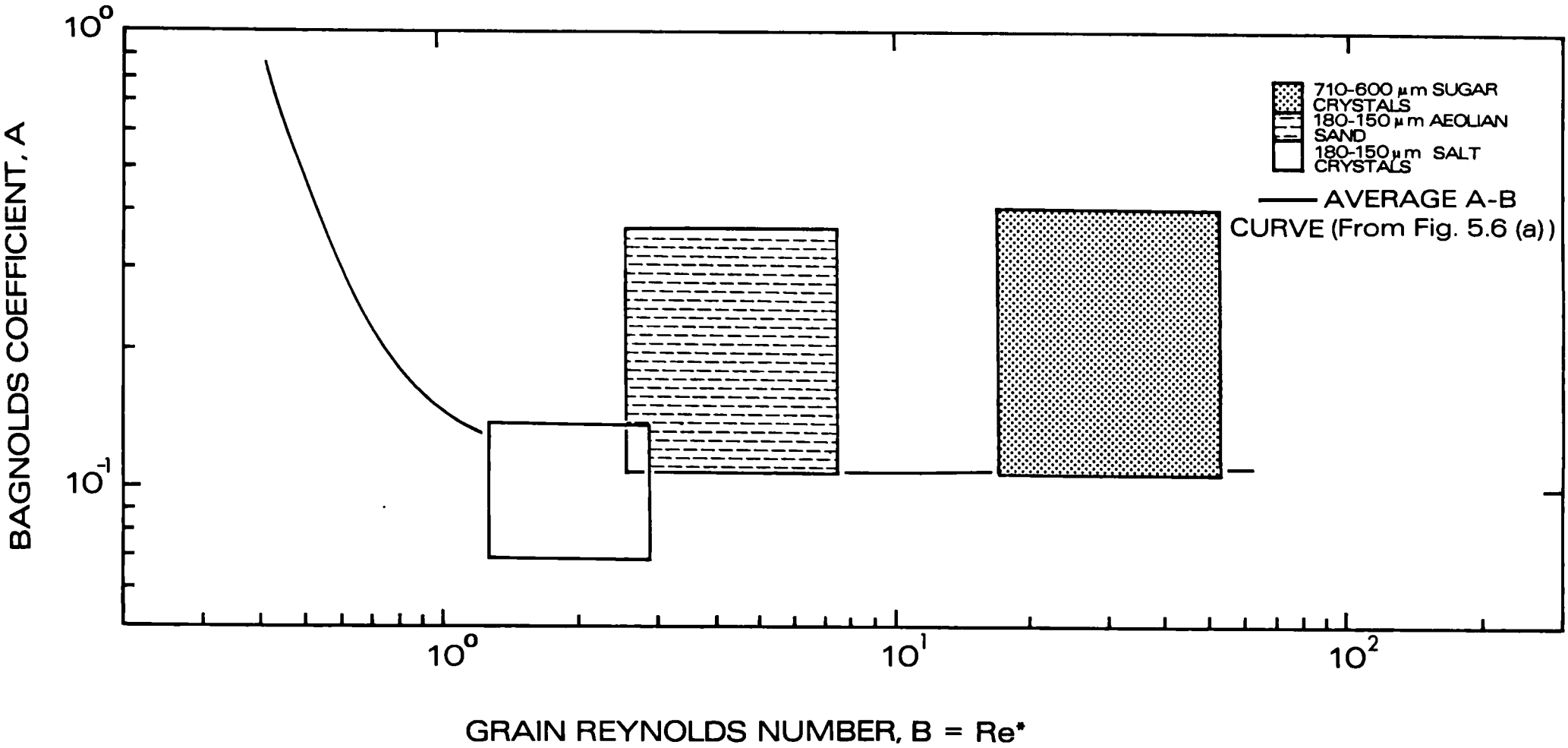

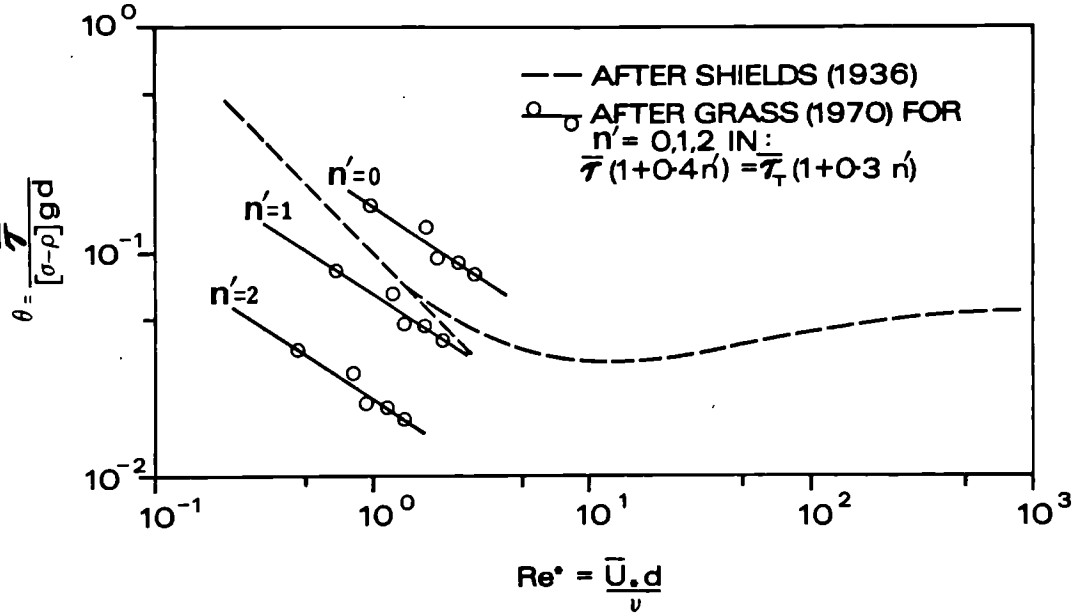

Figure 5.7 Comparison between Shields curve and data obtained by Grass (1970).

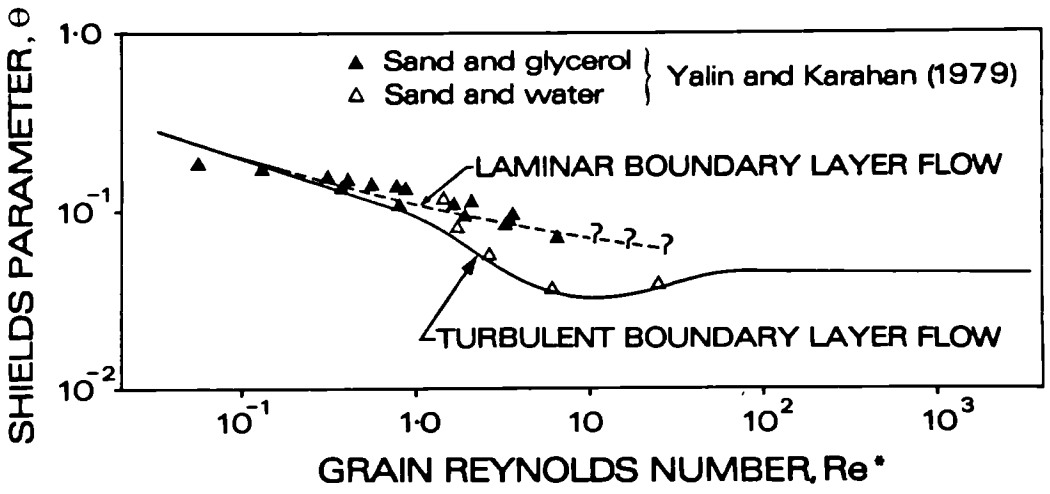

Figure 5.8 Form of Shields curve in laminar and turbulent boundary layer flow.

CHAPTER SIX

Rate of aeolian entrainment from test strips and beds

6.1 Introduction

The experiments reported in Chapter 4 established the range of free stream wind speeds through which aeolian transport developed from movement of the most susceptible grains to complete removal of all loose material from a strip. Using this information, it was decided to examine the rate of entrainment which resulted when a free stream wind speed equal to the higher threshold was applied to strips of loose particles at selected study sites on the surface of the plate. It was also decided to examine the erosion of a continuous bed of loose particles. Since the threshold velocities tended to decrease along the plate, it seemed that the loose particles would clear from the downwind edge of the bed as the free stream wind speed was gradually raised. The upwind progress of the resulting clearance line with time or with rising tunnel speed might, therefore, yield further useful insights into the aeolian threshold condition.

6.2 Experimental apparatus and procedures

6.2.1 Aeolian entrainment from strips at threshold wind velocities

(a) Experimental apparatus

The experimental apparatus used to record the rate of aeolian entrainment from strips of test material on the plate is illustrated in Figure 6.1. The plate was initially covered with the appropriate test material using the technique described in 3.6 and then installed in the working section of the large blow-down wind tunnel (Figure 3.4). A loose strip of the same test material was then laid across the plate at a

predetermined distance downwind from Station A using the method described in 3.8. Table 6.1 lists the range of test materials and strip positions examined in this investigation.

An Olympus OM1-N camera with 50mm f1.4 Zuiko lens was positioned above a perspex window in the roof of the wind tunnel working section using a sturdy tripod so as to give an unrestricted view of the loose strip on the plate surface. The camera was equipped with a motor-drive unit capable of advancing the film at a maximum rate of four frames per second. The motor drive was controlled using an Olympus timing unit. This allowed rapid camera operation and left the operator free to observe visually the erosion of the strip. A strip floodlight was positioned outside the working section and light was directed at approximately 60^{o} on to the strip (Figure 6.1). Using this lighting arrangement and Ilford HP5 black and white film rated at ASA/ISO 500, it was possible to set an exposure time of 1/1000 second at f1.4. Use of this fast shutter speed was necessary for sharp images because of the unavoidable vibration caused by the motor-drive unit on the camera, particularly when operating at the maximum wind-on speed of four frames per second.

(b) Experimental procedures

As this study was concerned with the rate of aeolian entrainment from strips at threshold wind speeds, it was necessary to use a wind velocity just sufficient to erode completely, a given test strip ($\bar{U}_{\infty max}$). As $\bar{U}_{\infty max}$ values were originally determined in the investigations of strip erosion reported in Chapter 4, the appropriate values were known. The wind speed was measured using a Betz manometer which recorded the static pressure increase between the intake and

exhaust of the contraction section of the wind tunnel. In addition, the free stream wind speed was measured at a height of 16cm using a pitot-static probe positioned directly above the test strip.

The initial configuration of the strip was photographed using the single frame advance setting on the motor drive and the wind velocity was then increased to a stand-by value just below the minimum threshold velocity ($\bar{U}_{\infty min}$). The motor-drive control unit was then set to run at four frames per second. In some instances, a number of particles were entrained from the strip at the stand-by velocity but these losses never accounted for more than a few percent of the total strip area. Such losses were allowed for in subsequent analysis by excluding them from the adjusted initial strip area.

The experimental run was started by quickly increasing the tunnel wind speed to the velocity just capable of entraining all the material in the strip ($\bar{U}_{\infty max}$). Whilst increasing the wind velocity, the strip was observed using a mirror mounted on the tripod and when strip erosion started, the motor-drive was set running to record the loss of material from the strip at 1/4 second intervals. When little or none of the strip remained the motor drive was switched off and the film was recovered for processing. In some cases, complete erosion of the strip took longer than nine seconds and the 36 exposure film was finished. Although some data was lost, the erosion of at least 90% of the initial strip area was photographed in all cases except the largest ballotini (i.e. 1.7-1.4mm).

6.2.2 Aeolian entrainment from flat beds in a developing boundary layer

(a) Experimental apparatus

The experimental apparatus used to record aeolian entrainment from flat beds of test material on the plate is illustrated in Figure 6.2. The surface of the plate was covered with the appropriate test material and installed in the working section of the blow-down wind tunnel (Figure 3.4). For this second series of tests, the base layer of fixed particles was prepared as before, then a sufficient quantity of the same test material as that covering the plate was carefully sprinkled on to the whole plate surface to give a uniform cover approximately one grain diameter in thickness. The test bed was then repeatedly rolled using a soft rubber print roller. This had the effect of spreading the loose grains out evenly on the plate surface by forcing the projecting particles between those in direct contact with the fixed grains. After each rolling operation the plate was gently tapped from below using a wooden mallet. The combined effect of repeated rolling and tapping gave a flat, homogenous bed of test material approximately one grain diameter in thickness. Material outside the required test region was then carefully brushed aside using a steel rule as a guide. This technique left a rectangular bed of loose grains on the surface of the plate. The range of test materials studied and the dimensions of the respective test beds are summarized in Table 6.2.

The Olympus OM1-N camera with 28mm f3.5 Zuiko lens was then mounted above the wind tunnel so as to give an unrestricted view of the test bed, (Figure 6.2). The 28mm lens and enlargement to the working section window gave the extended field of view necessary to photograph

the whole test bed. Two strip floodlights were used. These were clamped into position using retort stands and were stationed in front of and behind the tripod, (Figure 6.2). By experiment it was found that the most even illumination of the bed was achieved when each light was directed downwards at approximately 45^{o} from the horizontal position. In this way, the light unit downstream of the camera illuminated the up-wind portion of the test bed and vice versa.

The overall illumination of the test bed was measured using a series of spot meter readings taken at various distances along the bed. These readings were then averaged to give a mean exposure value. As the light was spread over a much larger area than in the case of the strips (6.2.1), it was necessary to use uprated Ilford HP5 black and white film. Typically, ASA/ISO values between 800 and 1600 were set in order to accommodate the shutter speed and lens aperture requirements. These included a shutter speed of at least 1/250 second to minimise the risk of camera shake and a maximum lens aperture of f8. Although the aperture setting of the lens was considered to be relatively unimportant in previous studies using the 50mm lens, it was necessary to choose a small aperture when using the wide angle 28mm lens owing to slight image distortion at large apertures (especially at f3.5 and f5.6). The uprated HP5 film generally allowed camera settings of at least 1/250 second at f8. Great care was taken to ensure that the film plane and the test bed were aligned in parallel as slight displacement would result in reduced planimetric accuracy and hence errors in subsequent determinations of bed areas from the photographs.

(b) Experimental procedure

The initial configuration of the test bed was photographed and the wind velocity was gradually raised to a value determined by experiment (Chapter 4) to be just below the threshold for grains at the downwind edge. The velocity was then increased to a pre-determined value and the ensuing erosion of the bed was recorded photographically at intervals appropriate to the rate of erosion.

However, as some test materials were eroded very rapidly, it was not possible with existing equipment to photograph some bed erosion in sufficient detail using the method described above. For instance, the 1.7-1.4mm ballotini bed took just six seconds to be completely eroded, whilst other beds were completely eroded in even shorter times when the wind velocity was set immediately to the value required for total bed erosion. In such cases it was found necessary to erode the bed in several stages by using a range of experimentally determined velocity settings. Using this technique, wind velocity was generally increased to a pre-determined value and the resulting partial erosion of the bed was photographically recorded at known time intervals. In most cases it was found that the entrainment of material from the bed had effectively ceased after a 10 minute erosion period. Subsequent increases in the wind velocity caused further particle entrainment from the bed. In most cases, the total removal of all loose material of the bed was recorded in a sequence of 30 pictures. The last few percent of the smallest particles (180-150μm) proved to be particularly resistant to erosion near the leading edge of the plate and could not be removed at even the highest velocities safely attainable in the working section. In all cases, the free stream wind velocity was measured at a height of 16cm

above the eroding portion of the bed surface using a pitot-static probe.

6.3 Data extraction and reduction

The majority of data obtained was in photographic form. A detailed account of film processing techniques is given in Appendix A3. The resulting negatives were catalogued and image quality was assessed by contact printing them on to Ilford multi-grade paper. If the contrast between the loose material of the strip or flat bed on the base layer was poor, the experiments were repeated and re-photographed using modified lighting conditions. In most cases this repeat procedure was found to be unnecessary. The negatives were then enlarged and printed on Ilford multi-grade paper using a Phillips PCS 2000 enlarger to give sets of prints depicting the erosion sequences for strips and beds of test material on the plate. Ilfospeed chemistry was used throughout all the paper processing stages.

The outlines of the strips or beds of test material were then traced directly on to polyester drawing film using a 0.2mm ink pen. The area enclosed by the traced outline was then determined by laying the tracing over metric graph paper and manually counting the number of enclosed millimetre squares. The resulting area values were then recorded in terms of the percentage of the initial strip or bed area remaining at each erosion stage.

Pitot-static probe pressure measurements were used to calculate the free stream air velocity using the computer program given in Appendix A1.

These analyses gave information on the nature and rate of erosion of strips and beds of test material at threshold wind speeds. Data resulting from erosion of the strips included the percentage of strip remaining after erosion by a wind of measured free stream velocity. It was also possible to calculate variations in the rate of strip erosion, as the time interval between each photograph of the erosion sequence was set by the speed of the motor-drive (generally 1/4 second). Resultant data on erosion of the test beds included the percentage area of the bed remaining after erosion by a wind of known free stream velocity and estimated friction velocity. In addition, visual observations of entrainment were also made during the various experimental runs as an aid to later interpretation of the experimental results.

6.4 Results

6.4.1 Aeolian entrainment from strips at threshold wind velocities

Data on the loss of material from a strip of 1.7-1.4mm ballotini at 25cm from Station A are tabulated in Table 6.3. This shows losses and gains of material at the upwind and downwind edges of the strip, the net loss of material from the strip and the cumulative elapsed time of erosion for each erosion stage. During the erosion sequence 41% of the initial strip area was removed by a wind velocity of $20.5ms^{-1}$. This preliminary run gave enough information to enable the experimental investigations to proceed.

The data presented in Table 6.3 are illustrated graphically in Figures 6.3 and 6.4. In Figure 6.3, the area of sediment remaining

(percent) is plotted as a function of elapsed time (minutes) on linear axes. Figure 6.4 shows temporal variation in the components of the net loss of material from the strip, again using linear scales. These include the loss from the upwind edge of the strip (mm^2), the loss from the downwind edge of the strip (mm^2) and the gain at the downwind edge of the strip (mm^2). Figure 6.4(d) shows the net loss from the strip (mm^2) as a function of time (min). In this case net loss is calculated from the summation of losses from the upwind and downwind edges of the strip minus any gains of material recorded at the downwind edge of the strip.

Raw data on losses from strips of the other test materials used (Table 6.1) are summarized in Table 6.4. Table 6.5 summarizes the measured free stream wind velocity values for each test material and strip position on the experimental plate. Table 6.6 shows the time taken for given strips to erode. These times (in seconds) refer to the duration of erosion measured from when 80% of the strip area remained until only 10% remained. These values were obtained graphically using the data presented in Table 6.4.

6.4.2 Aeolian entrainment from flat beds in a developing boundary layer

It was found by experimentation that virtually all the test material in a bed of 1.7-1.4mm ballotini could be removed at a free stream velocity of $22.6ms^{-1}$. Consequently, the erosion sequence at this velocity was recorded at a rate of four frames per second. Raw data from this experiment are presented in Table 6.7 where the percentage of the bed area remaining uneroded after quarter second sequential intervals is given. (For convenience, raw data from erosion of other test beds is

also given in Table 6.7). To illustrate this erosion sequence more clearly, selected erosion stages are shown in Figure 6.5(a). This illustration shows outline traces of the test bed taken directly from the appropriate photographs and subsequently reduced. Figure 6.5(a) is annotated to show the percentage of the bed remaining and the total elapsed time for each erosion stage. Data from Table 6.7 are plotted on linear graph axes in Figure 6.6 where the percentage of the bed area remaining uneroded is plotted as a function of time. These same data are plotted in Figure 6.7 in the form $\log_e$ % bed area uneroded against time.

Preliminary studies using a bed of 710-600μm ballotini showed that erosion occurred very rapidly if the wind velocity was increased to the value known to give complete erosion of the bed (6.2.2(b)). In such cases, even a photographic recording speed of four frames per second gave inadequate resolution of the bed erosion sequence. Thus it was found necessary to erode the bed of 710-600μm ballotini in a series of stages using stepwise increases in wind velocity. Initially, the wind velocity was set to a value slightly greater than the known $\bar{U}_{\infty(min)}$ for the downwind end of the bed and erosion was allowed to proceed until entrainment had effectively ceased. Photographs were taken of the bed at time intervals appropriate to the rate of erosion. When erosion was seen to have ceased, the velocity was increased a little, thereby initiating the next phase of erosion. This procedure was repeated until none of the bed material remained on the surface of the plate.

The raw data for the erosion of the 710-600μm ballotini bed are presented in Table 6.7 where the percentage of the bed remaining at a given time and wind velocity are shown. The erosion of the test bed is illustrated in Figure 6.5(b) which shows outline traces of seven selected

bed erosion stages. The figure is annotated to show the bed area (expressed as a percentage of the initial area), the free stream wind speed and the total elapsed time of erosion. Data from Table 6.7 are illustrated in Figures 6.8 and 6.9 where $\log_e$ values of percentage of the bed remaining uneroded are plotted against time and free stream wind velocity, respectively.

Subsequent investigations of entrainment from test beds of 355-300μm ballotini, 180-150μm ballotini, 710-600μm sugar crystals and 180-150μm salt crystals were also undertaken using the experimental procedure described above and similar graphical analyses. Raw data derived from the erosion of these test beds are also presented in Table 6.7. In addition, selected stages in the bed erosion sequences for 355-300μm and 180-150μm ballotini, 180-150μm aeolian sand, 710-600μm sugar crystals and 180-150μm salt crystals are illustrated in Figures 6.5(c) to (g) respectively. These figures are annotated in the same manner as Figure 6.5(b). Graphical relations for bed materials other than 710-600μm ballotini are not provided here, however.

6.5 Discussion of results

6.5.1 Aeolian entrainment from strips at threshold wind velocities

The analysis of the erosion sequence recorded for a strip of 1.7-1.4mm ballotini at 25cm from Station A was more detailed than subsequent analyses for other materials as it was hoped that a detailed inspection of the photographic erosion record for this large material would yield more precise information on the process of entrainment from test strips at the threshold wind speed than that derived from other

materials. During the erosion sequence, the wind velocity over the plate surface was maintained at a constant value of $20.5ms^{-1}$ and this gave rise to the removal of 41% of the total strip area over a 12.4 minute erosion period. The shape of the curve depicting the rate of overall loss of strip area by erosion (Figure 6.3) suggests some form of exponential or power function of time and shows that the initial entrainment of material was extremely rapid. As erosion proceeded, the rate of entrainment declined and eventually reached a stage where little or no material was removed despite the fact that 59% of the original strip area remained. Further analysis of the relationship between the percentage of strip area remaining and time is given below.

In addition to considerations of net material losses from the 1.7-1.4mm ballotini strip, net losses and gains of material from its upwind and downwind edges (Figure 6.4) were also analysed. Careful inspection of these results showed that the majority of particles were entrained from the upwind edge of the strip during the first minute of erosion (Figure 6.4(a)). Most of these entrained grains were removed completely but some were re-deposited near the downwind edge of the strip (Figure 6.4(b)). A small proportion of the total strip area was also lost from the downwind edge of the strip (Figure 6.4(c)). Visual observation of these initial erosion stages indicated that re-distribution of the test grains was occurring and that in the initial stages of strip erosion, the grains most susceptible to entrainment were located in the upwind portion of the strip.

Figure 6.4 shows that after the first minute of erosion, losses of material from the downwind portion of the strip were equal to and sometimes greater than the losses recorded from the upwind portion.

After approximately seven minutes, the losses from the upwind edge were found to be greater than those from the downwind edge. All gains of material at the downwind edge of the strip became negligible after approximately 3.5 minutes. The balance between the various components of net loss is shown in Figure 6.4(d) which shows the net loss of material from the ballotini strip through time. Removal of the material from the strip is seen to occur sporadically and to reduce gradually in magnitude over time. This suggests that in the initial erosion phase, a large number of particles were susceptible to entrainment by the local flow regime at this location on the plate. As particles were removed from the strip, the population of susceptible grains declined and the rate of entrainment tended towards zero (Figure 6.3). It was found that erosion again proceeded rapidly when the free stream wind velocity was increased from $20.5ms^{-1}$ (the initial velocity setting, Table 6.3) to $22.0ms^{-1}$. In this case the majority of the remaining strip area (59%) was removed to leave only a few grains on the plate surface. This observation supports the experimental evidence presented in Chapter 4 which suggested that even for closely graded particles with similar physical characteristics, a range of threshold wind speeds is required to erode a strip completely, (see Figure 4.19).

The graph in Figure 6.3, showing the percentage of strip area remaining uneroded as a function of erosion time for the 1.7-1.4mm ballotini strip at 25cm from Station A, suggests that the decrease in strip area at threshold wind speeds obeys an exponential decay law. Similar curves were also obtained when using data derived from the erosion of other test strips (Table 6.4). Assuming that erosion of the strips proceeds as an exponential function of time, it is then possible to derive a theoretical expression for the rate of strip erosion.

At a certain wind velocity, a certain proportion of the grains in a strip are susceptible to entrainment and will move when the local instantaneous shear velocity exceeds the forces resisting particle motion. If the initial number of susceptible grains is represented by an area A_B, and the rate at which grains leave the strip is proportional to the area A_{BS} of susceptible grains remaining, then

$$\frac{dA_B}{dt} \propto A_{BS} \qquad 6.1$$

where t is the time of erosion. As dA_B/dt represents a loss of material from the strip, equation 6.1 may be expressed as

$$\frac{dA_B}{dt} = -kA_{BS} \qquad 6.2$$

where k is a constant. Thus

$$\frac{dA_B}{A_{BS}} = -kdt \qquad 6.3$$

At a certain time t, the loss of material may therefore be expressed as:

$$\int_{A_B}^{A_{BS}} \frac{dA_B}{A_{BS}} = -k \int_o^t dt \qquad 6.4$$

$$\left[\text{Ln } A_B\right]_{A_B}^{A_{BS}} = -kt \qquad 6.4(a)$$

$$\text{Ln } A_{BS} - \text{Ln } A_B = -kt \qquad 6.4(b)$$

$$\text{Ln}\frac{A_{BS}}{A_B} = -kt \qquad 6.4(c)$$

Hence,

$$\frac{A_{BS}}{A_B} = e^{-kt} \qquad 6.5$$

The coefficient k in equation 6.5 represents the initial rate of decrease in the area of the strip.

Data presented in Tables 6.3 and 6.4 were initially analysed using a least squares curve-fitting computer program. This program permitted objective assessment of the goodness-of-fit of the experimental data to standard mathematical expressions. These included: $Y=a+kx$; $Y=ae^{kx}$; $Y=ax^{k}$; $Y=a+(k/x)$; $Y=1/akx$; and $Y=x/(a+kx)$. In all cases except the strip of 1.7-1.4mm ballotini at 25cm from Station A it was found that the relationship between the percentage of strip area remaining uneroded (Y) and time (x) was best described by the inverse exponential function $Y=ae^{-kx}$. Thus analysis of empirical data from the wind tunnel studies supports the simple theoretical model of strip erosion rate presented as equation 6.5.

Using a computer program for least squares correlation and regression, best-fit relationships between percentage strip area remaining uneroded (Ys) and erosion time (t) were derived for all experimental data presented in Table 6.3 and 6.4 using the regression equation:

$$Ys = ae^{-kt}$$

Table 6.8 presents correlation coefficients (r) and k exponents for exponential relationships of this form for all test materials and strip positions used on the plate. Also given are Student 't' statistics and associated degrees of freedom.

The Student t values permit a statistical assessment of the goodness-of-fit of the experimental data to the exponential expression. Accordingly, when t values were assessed at the 0.01 significance level, in all cases except 710-600μm sugar crystals at 25cm from Station A, it was found that the calculated t values were larger than critical t-values. Thus with this one exception, the analysis showed that there is a highly significant fit of the experimental data to an inverse exponential curve indicating that decrease in strip area over time at threshold wind speed follows an exponential decay function with time. This result clearly validates the theoretical model proposed above.

Although data derived from the erosion of the 1.7-1.4mm ballotini strip was found to fit an inverse exponential function with high statistical significance, initial analysis using the least squares curve-fitting program indicated that the reduction in strip area over time could be expressed more appropriately as a power function. The erosion data (Table 6.3) was therefore analysed using a program for two variable geometric correlation. In this case, the correlation coefficient was found to be -0.9915 with a Student t value of 43.76. These statistics indicate that erosion of this particular strip can be best described by a power function ($Y=at^{-k}$) and suggest that the mechanisms of entrainment at the threshold may have been fundamentally different in this case.

In general, strips of particles smaller than or equal to 710μm were observed to erode from their downwind edges whereas the majority of entrainment associated with erosion of the 1.7-1.4mm ballotini occurred from the upwind edge of the strip. Material ejected from this strip was observed to collide violently with stationary grains located a short distance downwind. The ensuing ejection of particles resulted in rapid erosion along the entire downwind edge of the strip.

These observations therefore imply that the amount of aeolian entrainment at threhsold is:

(a) an exponential function of time when only the boundary layer flow is responsible for entrainment; and

(b) a power function of time when avalanching occurs.

The low correlation coefficient and statistically insignificant t value calculated using erosion data for the 710-600μm sugar crystal strip at 25cm from Station A (Table 6.4) suggested that entrainment at the threshold was modified in some way. On the basis of previous experimental work reported in Chapter 4, it appears that moisture played a crucial role in increasing interparticle cohesion which gave rise to modified entrainment rates and characteristics. However, the role of moisture is not clearly understood as erosion of a similar test strip at 130cm from Station A proceeded in the usual manner (i.e. loss of material was found to be an inverse exponential function of time). Further discussion of this result is given below.

Inspection of k values in Table 6.8 suggests that for a given position on the plate surface, the rate of aeolian entrainment is independent of particle size at the threshold. However, the k values show that there is a downwind increase in the rate of strip erosion

irrespective of the test material. As the wind is fully turbulent at the rear of the plate over all the test surfaces these k values are further evidence of the greater entrainment efficiency of turbulent boundary layer flow.

Corroborative evidence of the greater entrainment efficiency of turbulent flow is obtained when considering the time taken for a given strip area to decrease from 80% to 10% of its initial area. These values were determined graphically using data from Table 6.4 (% strip area remaining as a function of time) and are presented in Table 6.6. (Data for the 1.7-1.4mm ballotini strip are not included as only 41% of the total strip area was eroded during the experimental run). Table 6.6 shows that the duration of erosion at threshold wind speed was greater at the front of the plate than at the rear, irrespective of the test material. This observation is, therefore, consistent with the trend of erosion rate exponents (k values) given in Table 6.8. As the wind velocity at each strip position was just sufficient to erode between 90-100% of the total strip area, the results in Tables 6.6 and 6.8 suggest that there are differences in the effectiveness of the local boundary layer flow regime with regards aeolian entrainment.

It is thought that the differences in the duration of strip erosion recorded on the surface of the plate resulted from differences in both the characteristic local $P(U_*)$ distribution of the flow and in the interactions between the $P(U_*)$ and the $P(U_{*T})$ distribution associated with a strip of test particles. In Chapter 4 it was shown that the $P(U_*)$ distribution becomes increasingly positively skewed as the intensity of flow turbulence increases. This change is considered to bring about the downwind reduction in $\bar{U}_{*T}$ values associated with strips

of test material on the surface of the plate (Figure 4.21). This figure also shows that the probability of a given threshold shear velocity event occurring decreases with distance downwind and thus implies a corresponding downwind decrease in the duration of strip erosion for flow conditions just in excess of the threshold. However, the strip erosion times presented in Table 6.6 show clearly that erosion proceeded more rapidly at downwind sites that at sites close to Station A and this suggests, therefore, that in conditions of active grain entrainment the interaction between the $P(U_*)$ and $P(U_{*T})$ distributions may differ significantly from that depicted in Figure 4.21.

A schematic diagram of the way in which variation in the rates of aeolian entrainment may be brought about by differences in the degree of overlap between the $P(U_*)$ and $P(U_{*T})$ distributions is shown in Figure 6.10. In this configuration, mean threshold shear velocity decreases downwind and the frequency of threshold shear velocity events associated with the $P(U_*)$ distribution at 130cm downwind from Station A is higher than that associated with the $P(U_*)$ distribution at 10cm downwind from Station A. The downwind increase in the frequency of threshold shear velocity events that result from such an interaction would result in an increase in the rate of erosion at downwind study sites. Thus the model shown in Figure 6.10 is considered to be a plausible explanation of the downwind increase in strip erosion rates recorded in this study.

The time taken to erode the strip of 180-150μm ballotini at 25cm from Station A is nearly three and a half times as long as that for a strip of the same material at 130cm from Station A despite the wind speed being just in excess of the threshold in both cases (Table 6.6). This

suggests that the differences in the characteristic $P(U_*)$ distribution associated with flow regimes over this surface are greater than over other test materials. The results given in 4.5.1 indicate that the boundary layer flow was laminar for approximately 40cm downwind of Station A over the 180-150μm ballotini surface. It thus seems likely that the much longer time required to erode strips of this material at 25cm from Station A resulted from this fundamental difference in the local flow regime.

It was suggested in 4.5.1 that at 25cm from Station A, the flow regime over 180-150μm aeolian sand and salt crystals was transitional in character and was probably characterized by cycles of turbulent spot growth. Therefore, it is likely that the frequency of threshold shear velocity events was greater at 25cm from Station A over the sand and salt surfaces than over the same size range of ballotini. Consequently, the times taken to erode strips of 180-150μm aeolian sand and salt crystals at 25cm from Station A are less than the time taken to erode the 180-150 μm ballotini strip at the same plate position. Similarly, differences between k exponents for 180-150μm aeolian sand and salt crystal strips at 25 and 130cm from Station A are less than for the 180-150μm ballotini strips at the same position (Table 6.8).

The erosion time for a strip of 710-600μm sugar crystals at 130cm from Station A was significantly lower than for a strip of 710-600 μm ballotini at the same position (Table 6.6). As the windspeed was set to the threshold value for each test strip, it is unlikely that the differences in particle density gave rise to these different erosion times. As the prismatic crystal shape of sugar has a higher drag coefficient ($C_D \approx 0.9$ at Re greater than 10^4) than spherical ballotini

(C_D = 0.4 at Re=10^4), this probably contributed to its more rapid entrainment. Similarly, strips of 180-150μm salt crystals at 25cm and 130cm from Station A were also eroded more quickly than equivalently sized ballotini strips at the same positions on the plate (Table 6.6). Although the difference in density between salt crystals ($2.164x10^3 kgm^{-3}$) and ballotini is not as great as that between sugar crystals and ballotini, the drag coefficient for the cubic crystal shape of salt (C_D=1.1 at Re greater than 10^4) is significantly higher than for ballotini and this probably contributed to the more rapid entrainment of the salt crystal strips.

The effect of atmospheric moisture on entrainment threshold values was most noticable when comparing erosion of the 710-600μm ballotini strip at 25cm from Station A with that of 710-600μm sugar at the same position. Given the lower particle density and higher particle drag coefficient of sugar crystals, one would expect the threshold wind velocity for the sugar crystal strip to be lower than that for ballotini, particularly when this was found to be the case for strips at 130cm from Station A. As the experimental runs using sugar crystals were conducted on days with similar relative humidities (86% and 89% respectively) the most likely explanation concerns the differences in the time between laying the strip on the plate and actually eroding it. The sugar crystal strip at 25cm from Station A was left on the surface of the plate for half an hour prior to the run. (This delay was unavoidable owing to temporary failure of the camera motor drive). At the time of the run, therefore, the moisture content of the strip was probably higher than that for the strip at 130cm from Station A and probably gave rise to this anomalous result.

6.5.2 Aeolian entrainment from flat beds in a developing boundary layer

(a) 1.7-1.4mm ballotini

The bed of 1.7-1.4mm ballotini (60x55cm) was completely eroded in less than six seconds by a free stream wind velocity of $22.6ms^{-1}$. The gradual reduction in bed area recorded during the erosion sequence is illustrated in Figure 6.5(a). This figure shows that erosion proceeded from the downwind edge of the bed in an upwind direction, finally leaving small, isolated islands of particles very close to Station A. These islands of material were not entrained at the stated velocity even though the wind was allowed to blow for a further 10 minutes after the time of the last photograph. A small proportion of the bed material was also eroded from the upwind edge of the bed during the first few seconds of the run. Small crenations appeared along the upwind edge of the bed and tended to enlarge and extend downwind as additional material was slowly winnowed out by the modified local air flow in the resulting gaps. Downwind migration of these gaps and removal of material from the downwind edge of the bed gave rise to rapid erosion of the test bed.

The loss of material from this bed is illustrated graphically in Figure 6.6 where the percentage of the bed area remaining is plotted as a function of time on linear axes. The shape of this graph suggests an asymptotic relationship between these two variables. As the wind speed increases to a maximum value of $22.6ms^{-1}$, the first 10-20% of the bed area is removed at an increasing rate until a maximum entrainment is reached. After a short time, the rate of erosion then progressively decreases until only a few grains remain on the plate close to Station A (Figure 6.5a). As stated earlier, at the beginning of the experimental

run, the wind velocity was set to a stand-by value just below the threshold for material located at the downwind edge of the bed and to ensure complete bed erosion, it was then necessary to increase the windspeed to a higher pre-determined value. During the few seconds it took for the wind tunnel to adjust to this new velocity setting, a portion of material was eroded from the rear of the bed. During this adjustment period, the rate of erosion increased in the manner illustrated by the upper portion of the asymptotic curve in Figure 6.6 until the higher, steady flow velocity had been reached whereupon further erosion of the bed occurred until only a few percent of the original bed area remained. Once this stable wind speed ($22.6ms^{-1}$) had been attained, the decrease in bed area appears to be an inverse exponential function of elapsed time as illustrated by the lower portion of the asymptotic curve in Figure 6.6 which describes the removal of the last 50-60% of the bed. The apparently constant rate of erosion for erosion between 70-30% uneroded area (Figure 6.6) may, in fact, represent a transition from a period of progressively increasing erosion, due to wind velocity increase, to a period of progressively decreasing (exponential) erosion once steady wind velocity is attained, the latter being the usual rate of erosion recorded for strips under constant threshold wind.

In many respects, the erosion of this 1.7-1.4mm test bed proceeded in a manner analogous to that recorded for a narrow strip of the same material at 25cm from Station A (i.e. bed area decreased as an inverse exponential function of time). However, unlike the erosion of narrow strips, the majority of particles were lost from the downwind regions of the bed and the downwind limit of the test bed moved slowly upwind as erosion proceeded, finally leaving a few particles adjacent to Station A (the upwind limit of the bed). The majority of particles in

the downwind portion of the bed were directly entrained by the wind. However, a significant number of grains were also lost from the upwind edge of the bed. In some instances these were observed to cause entrainment further downwind due to impact with other bed particles which were subsequently ejected into the wind in a manner similar to that observed for strips of this test material. This undoubtedly caused more rapid erosion than that which could be attributable to the direct shear force of the wind alone.

The erosion sequence illustrated in Figure 6.5(a) reflects the changing downwind characteristics of the boundary layer over the test bed and suggests that the wind is more effective in entraining particles as the downwind distance from Station A increases, despite the fact that freestream wind velocity above the boundary layer remains constant. In 4.5.1 it was suggested that the ratio of instantaneous to mean shear stress and the frequency of peak shear stress events at the surface of the plate increased downwind of Station A. Thus, bed particles at the downwind limit of the bed area were subjected to a turbulent flow regime in which threshold shear stress events occurred with much greater frequency and magnitude than at positions further upwind. Therefore, the likelihood of a significant shear stress event occurring in the vicinity of susceptible particles increased downwind of Station A. As a consequence the test bed of loose material eroded in an upwind direction.

(b) Other test beds

As stated earlier, an initial experiment using a bed of 710-600 μm ballotini showed that it was not possible to record the erosion sequence in detail using a single free stream wind velocity setting

because erosion of the downwind portion of the bed proceeded too rapidly to be recorded using available equipment. It was necessary, therefore, to erode the bed in stages and to record the reduction in area resulting from several stepwise increases in free stream wind velocity settings. Consequently, a bed of 710-600μm ballotini (70cm by 50cm) was eroded using nine wind velocities during an 8.8 minute erosion period (Table 6.7). Seven selected stages in the erosion sequence are illustrated in Figure 6.5(b). This figure shows that entrainment occurred initially from the downwind portion of the bed and that the downwind limit of the bed progressively moved upwind in response to (a) increases in the free stream wind velocity, and (b) a steady free stream wind velocity over a period of time (Figure 6.5(b), (c) and (e)). Data from Table 6.7 are plotted in Figures 6.8 and 6.9. These figures show percentage of bed area remaining ($\log_e$ scale) as a function of time and free stream wind velocity, respectively. The straight line relationship between the variables again indicates that the area of the bed remaining is an inverse exponential function of time and free stream velocity.

Owing to the problems associated with rapid entrainment of bed material by a wind velocity able to erode the entire bed, the experimental procedure adopted for the study of the 710-600μm ballotini bed was also used to investigate the erosion of subsequent test beds of 710-600μm sugar crystals, 355-300μm ballotini, and 180-150μm ballotini, aeolian sand and salt crystals. Raw experimental data from these investigations are presented in Table 6.7. Initial plots of these data in the form % bed area remaining ($\log_e$ scale) as a function of time (e.g. Figure 6.8) and free stream velocity (e.g. Figure 6.9) indicated strong linear relationships between the variables and thus suggested that, for these test beds, area uneroded could be described appropriately

by an inverse exponential function.

In order to test this hypothesis, a computer program for two variable exponential correlation and regression was used to analyse all the data presented in Table 6.7. The results of this analysis are presented in Tables 6.9 and 6.10. These tables present correlation coefficients (r) and Student t values for the relationships of % bed area remaining ($\log_e$ values) to time and free stream velocity, respectively. Also included in these tables are k exponents from the regression equations expressing the rate of decrease in bed area as functions of time and free stream velocity (see below). All t values were tested at the 0.01 significance level and were found to exceed the critical value in all cases.

This analysis therefore confirmed that uneroded bed area under threshold wind speeds is an inverse exponential function of both erosion time and free stream velocity. Thus the theoretical model developed to describe the erosion of test strips at the threshold (6.5.1) is equally applicable in this case. Thus the erosion of all or part of a test bed in a developing boundary layer can be expressed as:

$$Y_A = ae^{-kt} \qquad 6.10$$

or

$$Y_A = ae^{-kU_\infty} \qquad 6.11$$

where

Y_A = the percentage of bed area uneroded at time t or threshold free stream velocity $\bar{U}_\infty$ %

a = regression coefficient

k	=	rate of bed erosion per unit time or per unit velocity	% per unit time or velocity

In common with results obtained using strips of test material, values of the k exponent in Tables 6.9 and 6.10 indicate that the rate of bed erosion is independent of particle characteristics at the threshold.

The bed erosion sequences illustrated in Figure 6.5(a) to (g) suggest a simple method to quantify the threshold of particle motion in a given boundary layer flow regime. Particles which define the downwind edge of the test bed must be in equilibrium with the local flow conditions in the boundary layer once entrainment ceases. Measurements of the local shear stress at this position should, therefore, indicate maximal threshold shear stress values for a given test material in a specified boundary layer regime.

Irregularities in the spanwise flow on the plate are suggested by the unevenness of the downwind eroding edge of the bed. However, measurements of boundary layer velocity profiles from spanwise stations at three positions downwind of Station A (see Chapter 3) did not indicate any significant flow anomalies. Thus the uneven erosion patterns illustrated in Figure 6.5(a) to (g) suggest that at or near the threshold of motion, particles are extremely sensitive to variations in the local flow conditions. Further, these figures suggest that the test materials became increasingly sensitive to such conditions as their size decreased.

The erosion sequences recorded for 180-150μm ballotini, aeolian sand and salt crystal beds, illustrated in Figure 6.5(d), 6.5(e) and 6.5(g) respectively, reveal several interesting features which indicate

differences in the erosion regimes in the developing boundary layer on the plate. These figures show that as wind velocity increased, entrainment occurred from the downwind edge of the beds in a manner similar to that recorded for other test materials. Further velocity increases caused the downwind edge of the bed to migrate upwind as additional material was eroded. At a certain point, however, the spatial distribution of bed erosion changed and small islands of particles were left on the surface of the plate as the downwind edge of the bed receded upwind. In addition small, irregular patches of the underlying surface of the plate became visible in regions where the bed material was less completely eroded. This region of patchy erosion became indistinct as wind velocity was increased still further and bed erosion then proceeded in the usual way. In the final stages of erosion, a nearly continuous and irregular narrow strip of test material was left adjacent to Station A. This proved to be extremely resistant to erosion, even at the maximum safe wind tunnel speed.

Figure 6.5(d,b) shows that the downwind edge of the 180-150μm ballotini bed eroded to leave small islands of test material in a region extending approximately 40 to 55cm downwind from Station A. Similarly, Figures 6.5(e) and (f) show the same patchy erosion pattern in this region in 180-150μm aeolian sand and salt crystal beds. These experimental results suggest that particles located at this plate position are less susceptible to entrainment than those located further upwind or downwind. In Chapter 4, it is shown that mean surface shear velocity values ($\overline{U}_{*T}$) for strips of 180-150μm ballotini and aeolian sand were higher in this region than at neighbouring sites and therefore indicated that the local boundary layer flow conditions were in some way much less effective in entraining the loose grains. It is considered

that these apparently anomalous results are related to viscous sublayer shelter effects which acted to reduce local shear stresses on the strips and thereby raise the aeolian entrainment threshold.

The lag deposits shown in Figures 6.5(d), (e) and (g) are, then, most likely a reflection of these same viscous sublayer shelter effects and are therefore associated with the same transitional boundary layer flow. In the case of bed erosion it was possible to erode these deposits completely by increasing the wind velocity by a relatively small amount, (smaller than $2ms^{-1}$). This suggests the presence of some other entrainment mechanism which tended to increase the entrainment efficiency of the wind in the case of the lag deposits from these test beds. The most likely mechanisms are turbulent spot growth (see below) and impact between the grains entrained from sites further upwind (i.e. the downwind edge of the receding bed) and the lag deposits. Such collisions were observed to eject particles directly into the air flow and thereby gave rise to rapid erosion. The test strips in this position, on the other hand, were not subjected to impacts from entrained grains and thus proved to be more resistant to increases in windspeed.

The uneven nature of the lag deposits illustrated in Figures 6.5(d), (e) and (g) also suggests that the local flow regime on the plate was significantly different in this region. It is unlikely that the unevenness of erosion resulted entirely from collisions between entrained grains and the lag deposits as material was entrained from along the whole downwind edge of the receding bed. Therefore, impacts with the lag deposits must have occurred fairly evenly over the whole plate width. It was shown in Chapter 4 that the boundary layer flow in this region was essentially transitional and therefore characterised by the sporadic

development of turbulent spots (2.4). Turbulent spots give rise to locally high bed shear stresses and, if these are sufficiently energetic, they could give rise to local erosion on the test bed (Browand et al., 1983). The uneven erosion recorded in this region suggests, therefore, that there are certain local areas on the bed in which the conditions for turbulent spot development are more favourable than others. These conditions may be related to upwind flow disturbances, such as single grains projecting above the mean bed level. At Reynolds number values typical of threshold conditions, such projecting particles would shed a broad wake of turbulent air likely to be of sufficient intensity to trigger turbulent spot development. In addition, it is also likely that spontaneous transition occurred near the bed region characterised by patchy erosion owing to the general instability of the laminar boundary layer and the action of vortex shedding from upwind grains at the mean bed level.

With the exception of the 1.7-1.4mm ballotini, the bed configuration characterising the final erosion stages consisted of a nearly continuous narrow strip of test material close to Station A. These remaining particles were found to be extremely resistant to entrainment despite their apparent vulnerability to erosion and their likely protrusion through an extremely thin boundary layer. This suggests that flow turbulence close to the leading edge of the experimental plate was either completely absent or only partially developed (2.2). These observations further confirm that turbulent boundary layer flow is much more effective in entraining granular material than laminar or transitional flow.

The experimental investigations of beds of 710-600μm sugar

crystals and 180-150μm aeolian sand and salt crystals suggest that particle shape is a significant factor in determining the threshold of particle motion. In all cases, the experimental results were compared with threshold values for the equivalent size range of ballotini. However, the effect of shape could only be assessed relatively because differences in particle density and the variable effects of atmospheric moisture absorption, especially in the case of sugar crystals, tended to obscure any direct effect of shape on threshold values.

During the investigations of test bed erosion, particle entrainment and other related phenomena were observed visually. In all cases particles just upwind of the eroding bed edge were seen to vibrate sporadically. Particles further upwind were also observed to vibrate, but such events were rare. Particle vibration, therefore, appears to be a precursor of entrainment and is thought to indicate that the local flow conditions are almost competent to move material. In general, vibration characteristics appeared to be the same irrespective of the particle size or position on the surface of the plate. Lyles and Krauss (1971) suggested a possible link between particle vibration and the turbulence structure in the boundary layer. In their studies, particle vibration frequency was found to be approximately 1.8Hz and the average peak frequency of longitudinal turbulence was determined to be 2.3Hz. They suggest this supports the hypothesis that the frequency of particle vibration at or close to the threshold of motion is related to the frequency band containing the maximum energy of the turbulent air flow. However, in this study observations of particle vibration in 180-150μm ballotini, aeolian sand and salt crystals when very close to Station A do not support this hypothesis as the boundary layer flow in this region was essentially laminar in character.

Flow in the wake of an object such as a single grain on the bed is characterised by the formation and shedding of vortices alternately from one side of the particle and then the other. The frequency of vortex shedding is given in terms of the Strouhal number, S, (Strouhal, 1878) which in turn is a function of the Reynolds number. Here, the Strouhal number is defined as

$$S = \frac{n_f d}{\bar{U}_\infty} \qquad 6.10$$

where n_f = frequency of vortex shedding from one side of the grain

Vortex shedding from one side of a particle would tend to impart a net displacement force by virtue of the changes in the local pressure distribution and relative drag on the particle. If the supporting grain geometry beneath the particle is such as to permit slight movement in response to this force, it can be seen that alternate vortex shedding from one side of the particle and then the other would be manifest as oscillatory particle motion. The restoring force necessary for such motion is likely to arise from gravity and relative drag changes as vortex shedding switches to the opposite side of the grain. In turbulent flow, these conditions may only occur for short periods as a region of relatively high velocity fluid passes over and around a particle. However, in laminar flow, a particle could oscillate for much longer periods owing to the steady nature of the flow. Observations of particles on the plate in both turbulent and laminar boundary layer flow indicated that the time of particle oscillation decreased with distance from Station A, i.e. as the boundary layer flow became increasingly turbulent. However, salt crystals near Station A were not observed to oscillate violently before they were entrained. In this case, the mean

threshold free stream wind velocity was much less than that for equivalent size aeolian sand and ballotini because of the combined effects of their lower particle density and higher particle drag coefficient.

As the threshold wind speed was lower for salt crystals than ballotini or aeolian sand it is likely that the Strouhl number was less than the critical value necessary to induce natural particle oscillation at the threshold of motion. Further downwind of Station A, however, salt crystals were observed to oscillate periodically despite there being a reduction in threshold free stream wind velocity and thus a reduction in the value of the Strouhl number. In this case it seems likely that particle oscillation was linked in some way with turbulent air motion and most probably resulted from interactions with particle wake flows.

6.6 Summary of experimental results

The investigation of strip erosion reported in this chapter has examined the rate and characteristics of aeolian entrainment at threshold wind velocities using a range of test materials at selected positions on the surface of the plate. Analysis of the resulting data produced a number of significant results.

1) The mean threshold wind speed required for complete strip erosion decreased with increasing distance from the leading edge of the plate irrespective of the test material.

2) Although a wind of given velocity was able to entrain all the material in the strip, motion did not occur en masse despite the close uniformity of test particle sizes and shapes. The proportion of test strip left uneroded was found to be an inverse exponential function of time in the majority of cases. The nature of erosion of the 1.7-1.4mm ballotini strip placed near the leading edge of the plate suggests that the rate of aeolian entrainment is different when stationary particles are ejected into the airflow by collisions with grains entrained further upwind. In such circumstances, the data analysis suggests that the uneroded area is more appropriately described as an inverse power function of time.

3) The rate of erosion of strips was found to increase with distance downwind of Station A. It was considered that the downwind increase in erosion rates reflected differences in the degree of overlap between the characteristic $P(U_*)$ distribution associated with the local flow regime and the $P(U_{*T})$ distribution associated with the test strips. No relationships were found between erosion rates and particle size in flow conditions just exceeding the threshold.

4) A detailed analysis of the 1.7-1.4mm ballotini strip erosion sequence revealed that most material was lost from the upwind edge of the strip. Removal of these grains thereby exposed less susceptible material which was subsequently entrained. Evidence of material redistribution was found during the early stages of erosion and was manifest as areas of redeposited material behind the downwind edge of the strip. Active erosion sites were distributed rather unevenly along both the upwind and downwind strip edges in the latter erosion stages and entrainment was observed to occur in a sporadic fashion.

The results obtained from erosion of test beds reflected the changing nature of the developing boundary layer on the plate. Analysis of the experimental data gave additional information on aeolian entrainment rates and characteristics at the threshold.

1) Irrespective of the bed material, mean threshold wind velocity was found to decrease as downwind distance from leading edge of the plate increased. It is suggested that this downwind reduction in mean threshold velocity resulted from a downwind increase in the ratio of instantaneous to mean shear stress in the developing boundary layer.

2) Despite bed erosion proceeding in discrete stages in the majority of investigations, (each stage related to an increase in wind velocity), the bed area remaining uneroded was found to decrease exponentially as both (a) time and (b) wind velocity increased. Further, each of the bed erosion stages was characterised by an inverse exponential decrease in bed area over time.

3) The patchy bed erosion recorded in 180-150μm ballotini, aeolian sand and salt crystals at approximately 40cm from Station A was found to differ markedly from the generally observed erosion patterns. Using evidence presented in Chapter 4, it is speculated that the local flow regime in this region was transitional. It is suggested that this patchy erosion pattern resulted from the joint action of sporadic turbulent spot development and collisions between entrained grains from the upwind edge of the receding bed and the lag deposits further downwind. These observations are shown to be consistent with the significantly higher mean surface shear velocities recorded

in this region for strips of the same material (Chapter 4). Despite the marked difference in boundary layer flow properties, erosion in this region apparently proceeded as an inverse exponential function of time.

4) It is argued that particles at the downwind edge of the eroding bed must be in an equilibrium state with the prevailing flow conditions when entrainment ceased. Such particles are therefore at the threshold of movement and careful measurements of the flow properties at the scale of individual grains would thus provide an accurate assessment of threshold wind conditions.

5) The length of time individual grains were observed to oscillate at the threshold decreased with increasing distance from Station A. In the case of 180-150μm salt crystals, particle oscillation at threshold was not observed at positions less than 25cm from Station A. It is suggested that such oscillation results from vortex shedding and favourable support geometry and that, generally, oscillation is a precursor of entrainment.

6) Entrainment of particles by winds of threshold velocities occurred sporadically leading to fluctuations in erosion rates over the time of erosion. However, despite this pulsatory erosion pattern, the rate of erosion generally decreased over time.

6.7 Conclusion

In conclusion, it is necessary to examine the experimental results reported in this chapter in a broader context and to assess their

contributions to the understanding of aeolian entrainment thresholds. The experiments have validated the major results reported in Chapter 4 concerning the reduction in mean threshold wind velocity in response to increasing boundary layer flow turbulence intensity along the plate. In addition it has been found that at the threshold, aeolian erosion proceeds sporadically but leaves an uneroded bed area which decreases exponentially with time irrespective of the boundary layer flow regime or particle characteristics. This result implies that aeolian entrainment at the threshold is governed primarily by the availability of susceptible grains and that the rate of entrainment is governed by the local flow characteristics. The greater rates of sporadic erosion recorded at downwind sites on the plate suggest that turbulent boundary layer flow is much more effective in entraining material than either laminar or transitional flow. Aeolian entrainment would, therefore, appear to be governed by the spatial and temporal distribution of peak shear stress events in the boundary layer as previously suggested by Grass (1970).

When bed erosion ceases, particles at the downwind edge of the remaining test bed must be in equilibrium with the prevailing flow conditions. Such grains must be at the threshold of motion. This observation suggests a new, objective means of defining aeolian threshold conditions in any given boundary layer flow regime. By considering the conditions at the downwind edge of the bed as threshold conditions, it is no longer necessary to use aeolian entrainment criteria to define the threshold and it disposes of the need to detect a defined degree of bed motion. This technique therefore simplifies the problems associated with accurate determinations of aeolian thresholds in the laboratory.

Observations of particle oscillation in both strips and beds of test material indicated that such motion is a precursor of entrainment in the majority of boundary layer flow regimes on the plate. Particle oscillation was observed in essentially laminar flow and thus such particle motion is unlikely to be directly connected with the interactions between particles and flow turbulence as suggested in the literature. In view of this evidence it is hypothesised that oscillation results from the displacement forces on particles due to vortex shedding by alternate grain faces. If the supporting geometry beneath the grain is such as to permit side to side motion, the rapid succession of displacing forces associated with vortex shedding would be manifest as an oscillatory motion.

Erosion of 180-150μm ballotini, aeolian sand and salt crystal beds revealed differences in aeolian erosion and entrainment characteristics in transitional boundary layer flow regimes. These observations are shown to validate results presented in Chapter 4 where mean threshold shear velocity values for strips of the same materials are shown to be significantly higher in such regions than at neighbouring sites. Materials in the transition region are thought to be less susceptible to erosion owing to viscous sublayer shelter effects given to particles. The greater susceptibility of particles at sites either side of this region indicates that shelter effects were either absent completely or only partially effective.

Table 6.1 Test materials and strip positions used to study rates of aeolian entrainment.

Test material	Strip position on the plate (distance downwind from Station A, cm)
1.7 - 1.4mm ballotini	25
710 - 600μm ballotini	130
355 - 300μm ballotini	25, 130
180 - 150μm ballotini	25, 130
180 - 150μm, aeolian sand	25, 130
710 - 600μm, sugar crystals	25, 130
180 - 150μm, salt crystals	25, 85, 130

Table 6.2 Test materials and bed dimensions used to study rates of aeolian entrainment.

Test material	Dimensions of sediment bed	
	Length, (cm)	Width, (cm)
1.7 - 1.4mm ballotini	55	60
710 - 600μm ballotini	70	50
355 - 300μm ballotini	85	45
180 - 150μm ballotini	65	45
180 - 150μm, aeolian sand	65	45
710 - 600μm, sugar crystals	70	30
180 - 150μm, salt crystals	80	30

Time (sec)	Loss of material from up-wind edge of strip (mm^2)	Loss of material from down-wind edge of strip (mm^2)	Gain of material at down-wind edge of strip (mm^2)	Net loss of material from strip (mm^2)	Area of the strip (calculated from photo-graphs (mm^2)	% of strip area uneroded
0	0	0	0	0	3179	100
15	382	0	105	277	2902	91
25	144	19	18	145	2757	87
35	74	24	49	49	2708	85
45	58	10	50	18	2690	84
55	13	41	3	51	2639	83
65	19	32	15	36	2603	82
75	14	27	31	10	2593	81
85	7	77	0	84	2509	79
95	12	14	13	13	2496	78
105	12	26	6	32	2464	77
115	31	29	1	59	2405	76
125	10	13	1	22	2383	75
145	18	8	0	26	2357	74
165	31	33	0	64	2293	72
185	18	27	11	34	2259	71
205	15	9	0	24	2235	70
225	20	24	1	43	2192	69
245	15	21	2	34	2158	68
265	2	7	0	9	2149	67
285	31	17	0	48	2101	66
305	1	3	1	3	2098	66
325	5	10	0	15	2083	65
345	12	1	0	13	2070	65
365	10	1	0	11	2059	64
385	6	0	0	6	2053	64
405	6	4	2	8	2045	64
425	8	6	1	13	2032	63
465	25	7	0	32	2000	63
505	5	3	3	5	1995	62
545	8	7	0	15	1980	62
585	17	7	0	24	1956	61
625	17	7	0	24	1932	60
665	12	15	0	27	1905	60
705	8	5	0	13	1892	59
745	7	9	0	16	1876	59

Table 6.3 Raw erosion data for erosion of 1.7-1.4mm ballotini strip at 25cm downwind from Station A ($\bar{U}_\infty$ = 20.5ms-1).

| Test material | Distance downwind from Station A | Time, sec | | |

Table 6.5 Free stream wind velocity values ($\bar{U}_{\infty_T}$) used in strip erosion for all test materials and strip positions, (ms^{-1}).

Test material	Strip position on the plate (distance downwind from Station A, cm)		
	25 $\bar{U}_{\infty_T}$	85 $\bar{U}_{\infty_T}$	130 $\bar{U}_{\infty_T}$
1.7 - 1.4mm ballotini	20.5		
710 - 600 m ballotini			8.6
355 - 300μm ballotini	9.0		6.3
180 - 150μm ballotini	13.3		4.9
180 - 150μm, aeolian sand	12.8		4.8
710 - 600μm, sugar crystals	13.6		8.1
180 - 150μm, salt crystals	5.4	1.9	1.7

Table 6.6 Strip erosion times (sec). The times refer to the period of erosion measured from when 80% of the strip area remained until 10% remained. Data obtained graphically from data in Table 6.4.

Test material	Strip position on the plate (distance downwind from Station A, cm)		
	25	85	130
710 - 600μm ballotini			4.40
355 - 300μm ballotini	1.09		0.75
180 - 150μm ballotini	3.99		1.20
180 - 150μm, aeolian sand	1.92		1.05
710 - 600μm, sugar crystals	1.75		0.85
180 - 150μm, salt crystals	1.73	1.90	1.05

| | | |

Table 6.8 Exponential correlation and regression analysis of strip erosion, i.e. % strip area remaining uneroded as an inverse exponential function of time. (Data in Tables 6.3 and 6.4).

	Distance of strip downwind from Station A, cm											
	25				85				130			
Test material	r	df	t	k	r	df	t	k	r	df	t	k
1.7-1.4mm *ballotini*	-.93	33	14.5*	$-6x10^{-4}$								
710-600µm *ballotini*									-.98	33	26.8*	-0.5
355-300µm *ballotini*	-.91	5	4.9	-2.7					-.90	6	5.1	-3.6
180-150µm *ballotini*	-.98	13	19.1*	-0.7					-.98	7	13.0*	-2.9
180-150µm aeolian sand	-.95	4	6.4*	-1.0					-.97	8	10.8*	-1.4
710-600µm sugar crystals	-.70	4	2.0*	-0.8					-.94	5	6.4*	-2.4
180-150µm salt crystals	-.99	5	16.7*	-1.7	-.84	10	-4.9	-2.1	-.98	8	13.3*	-2.2

Legend r = Correlation coefficient t = Student t value * Significant at 0.01 level.

df = Degrees of freedom k = regression exponent from $Y=Ae^{-kt}$

Table 6.9 Exponential correlation and regression analysis of bed erosion, i.e. % bed area remaining uneroded as an inverse exponential function of time. (Data in Table 6.7).

Test material		r	df	t	k
1.7-1.4mm	ballotini	-.91	22	9.9	-.71
710-600μm		-.96	22	16.2*	-.02
355-300μm		-.95	31	17.7*	-.05
180-150μm		-.99	28	34.7*	-0.6
180-150μm aeolian sand		-.99	16	24.8*	-.11
710-600μm sugar crystals		-.99	7	26.1*	-.05
180-150μm salt crystals		-.99	10	34.7*	-.04

* Significant at 0.01 level.

Legend r = Correlation coefficient t = Student t value

df = Degrees of freedom k = regression exponent from $Y=Ae^{-kt}$

Table 6.10 Exponential correlation and regression analysis of bed erosion as a function of free stream wind velocity, i.e. % bed area remaining uneroded as an inverse exponential function of free stream wind velocity (Data in Table 6.8).

Test material	r	df	t	k
1.7-1.4mm ballotini				
710-600µm ballotini	-.96	22	14.5*	-1.1
355-300µm ballotini	-.97	31	20.9*	-1.2
180-150µm ballotini	-.99	28	45.7*	-0.3
180-150µm aeolian sand	-.99	16	19.1*	-0.6
710-600µm sugar crystals	-.99	7	22.5*	-0.2
180-150µm salt crystals	-.99	10	67.5*	-0.5

* Significant at 0.01 level.

Legend

r = Correlation coefficient

t = Student t value

df = Degrees of freedom

k = regression exponent from $Y=Ae^{-kt}$

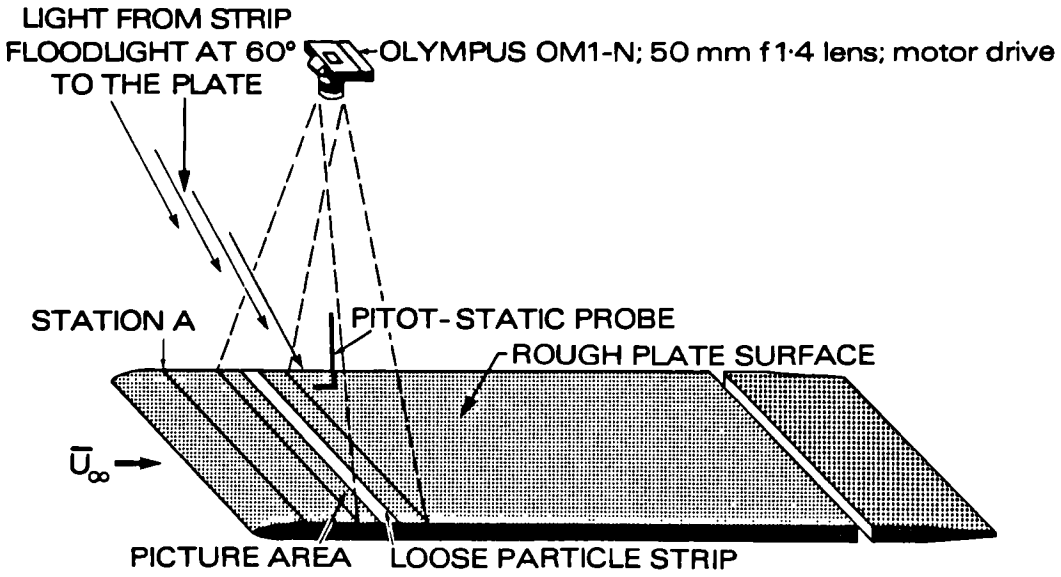

Figure 6.1 Experimental apparatus to study the rate of aeolian entrainment from test strips.

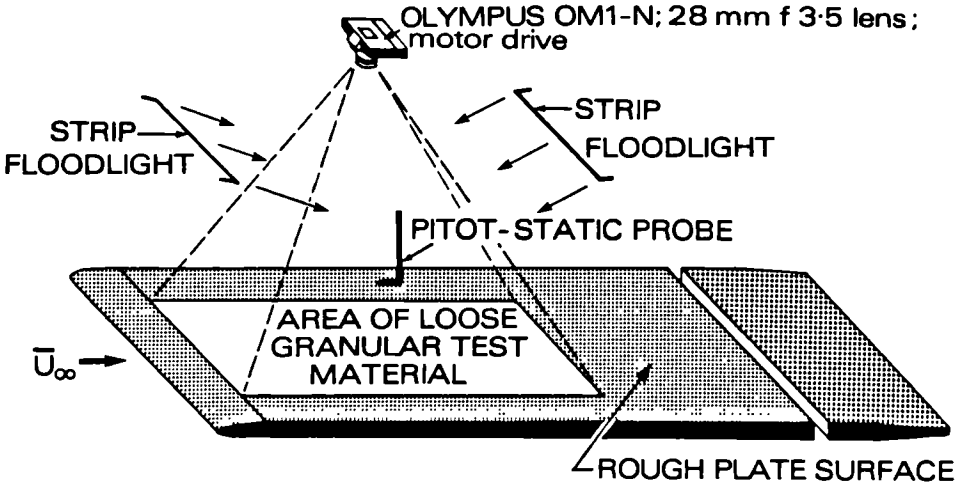

Figure 6.2 Experimental apparatus to study the rate of aeolian entrainment from test beds.

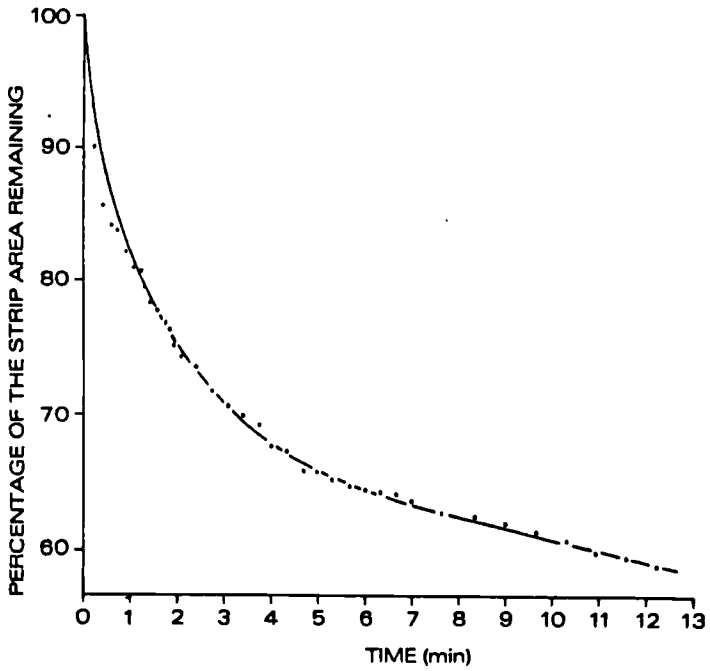

Figure 6.3 Temporal variation in percentage strip area uneroded; 1.7-1.4mm ballotini, 25cm downwind from Station A.

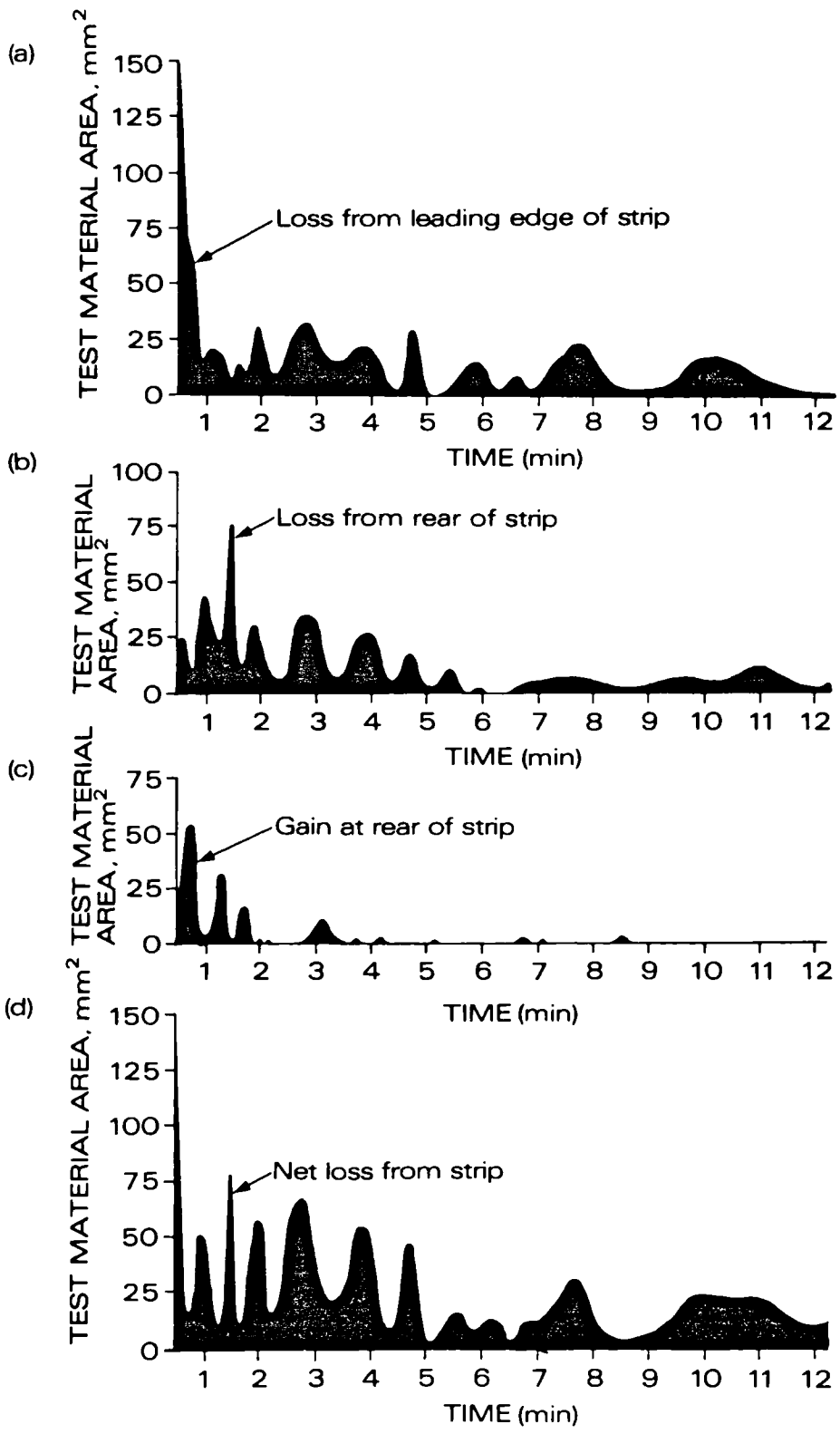

Figure 6.4 Losses and gains of material from a test strip; 1.7-1.4mm ballotini, 25cm downwind from Station A.

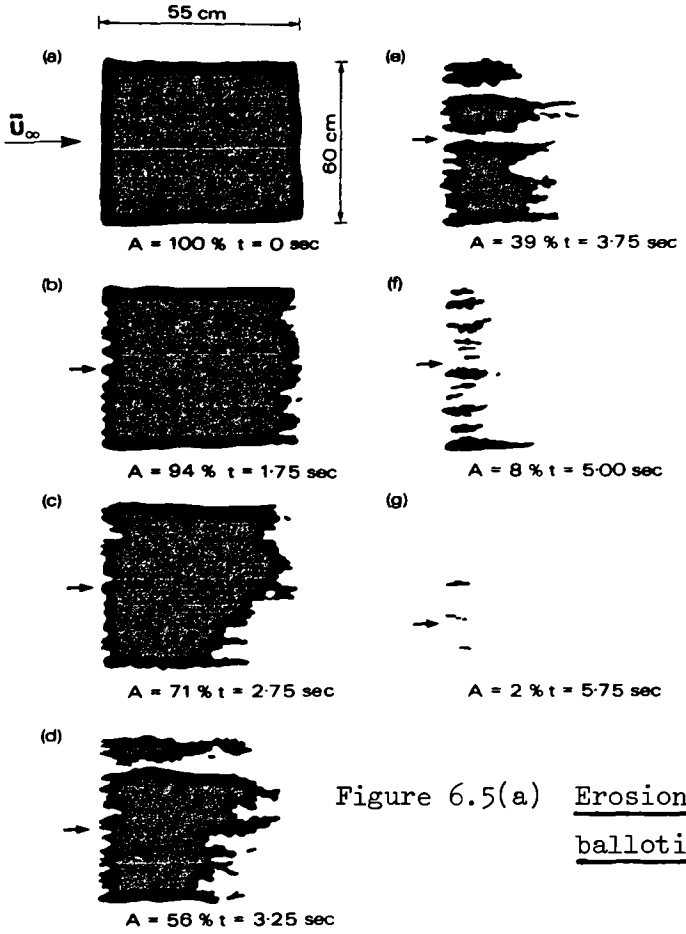

Figure 6.5(a) Erosion of 1.7-1.4mm ballotini bed.

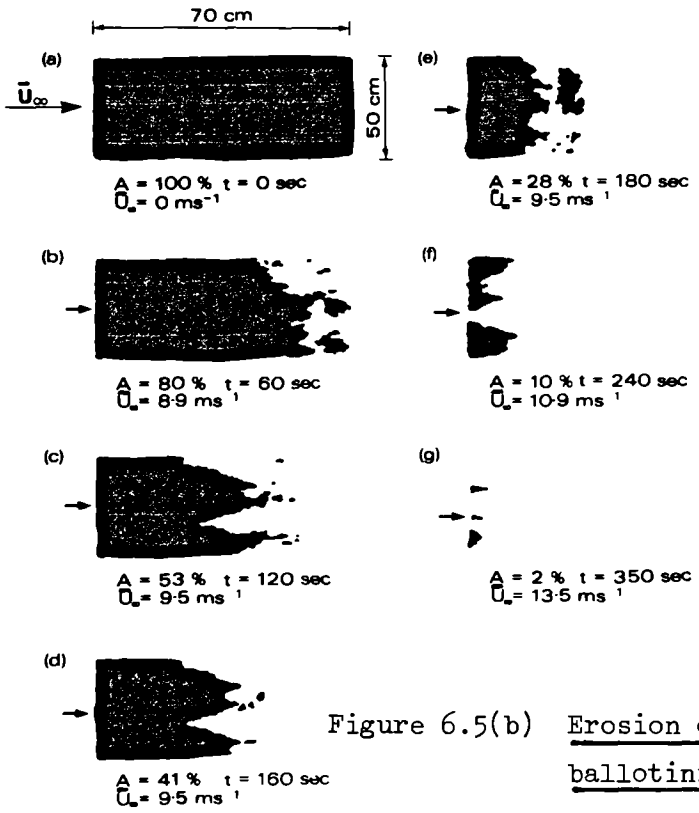

Figure 6.5(b) Erosion of 710-600μm ballotini bed.

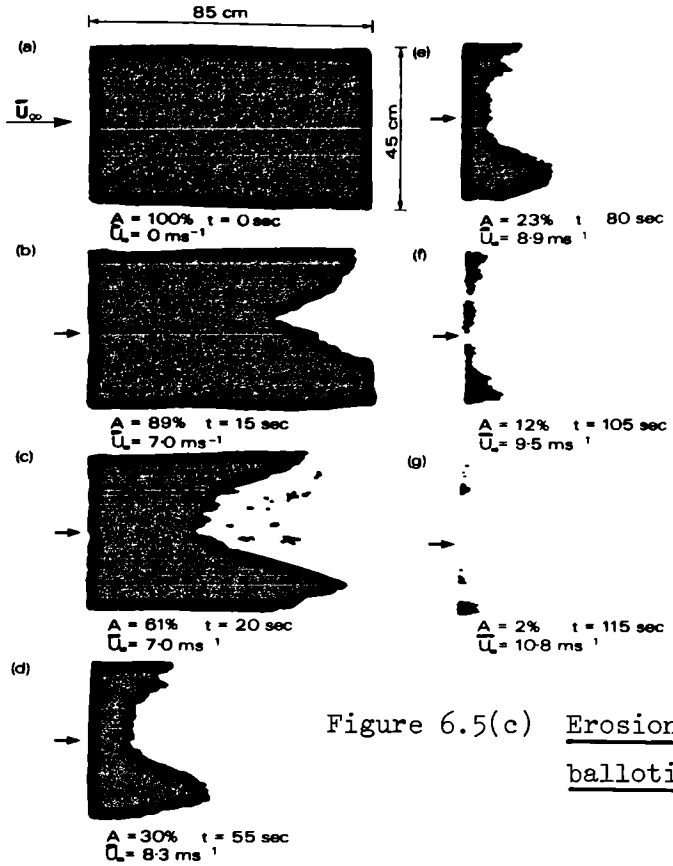

Figure 6.5(c) Erosion of 355-300μm ballotini bed.

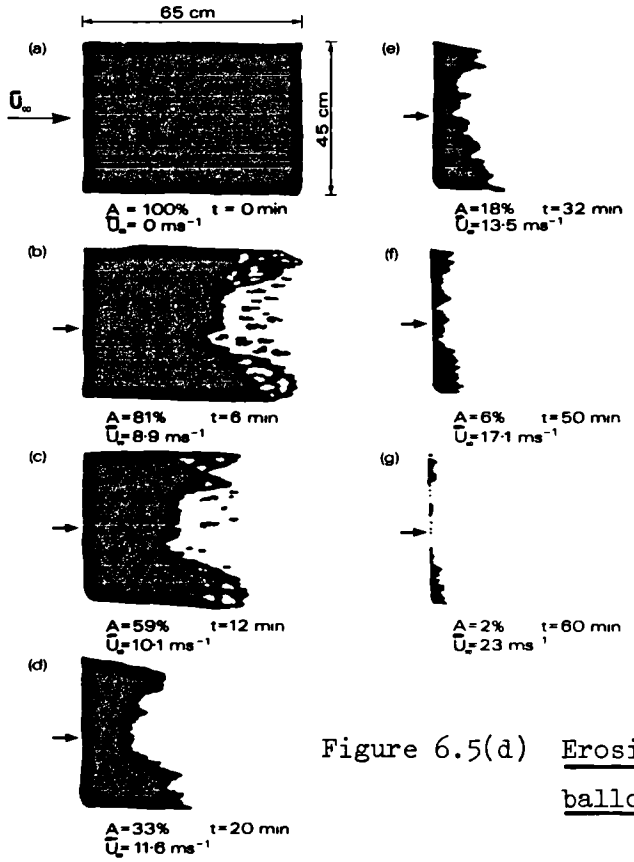

Figure 6.5(d) Erosion of 180-150μm ballotini bed.

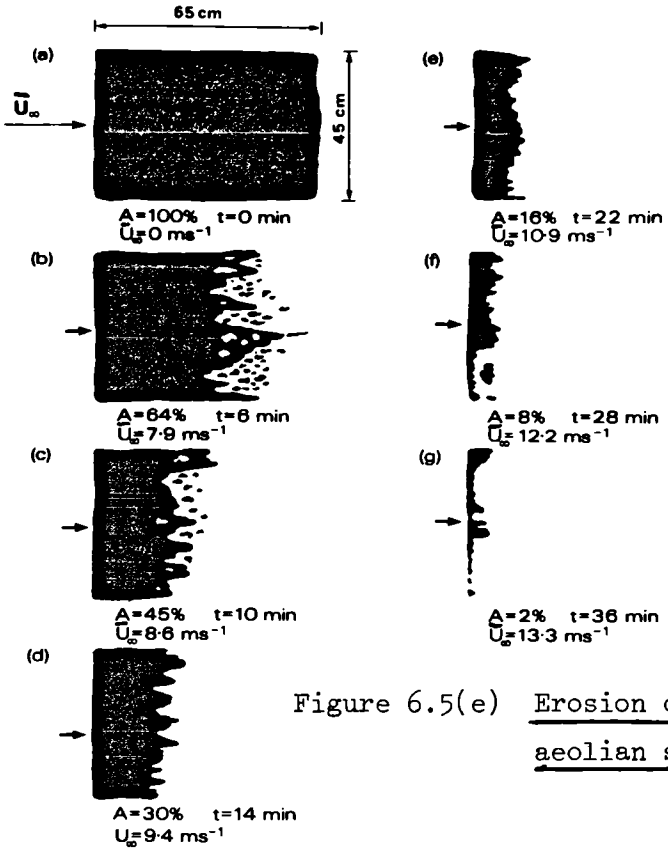

Figure 6.5(e) Erosion of 180-150μm aeolian sand bed.

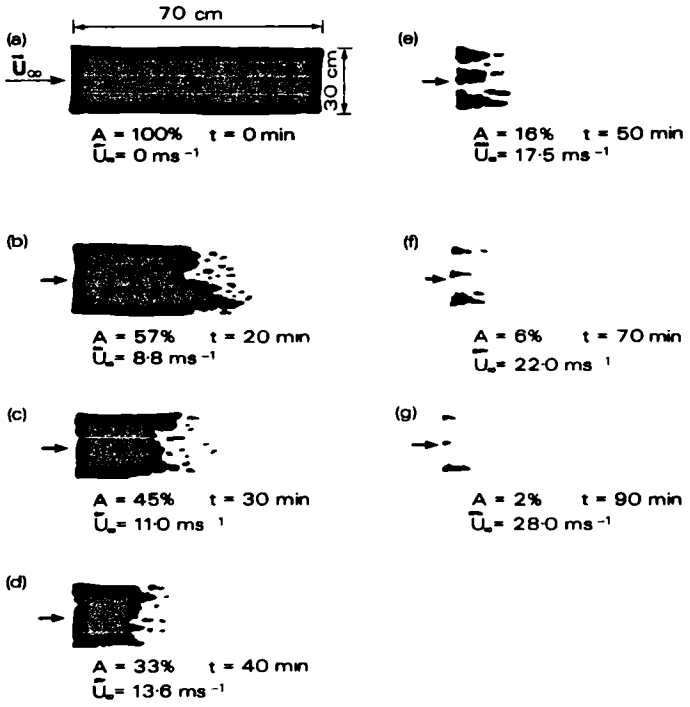

Figure 6.5(f) Erosion of 710-600μm sugar crystal bed.

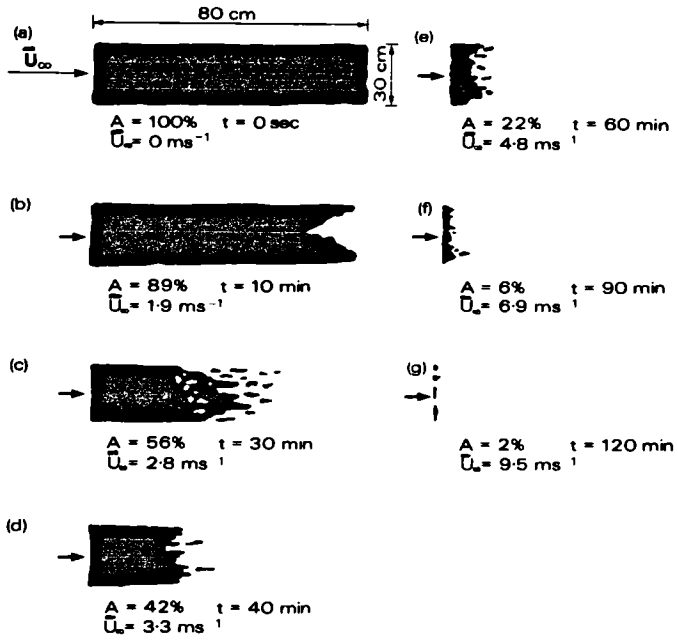

Figure 6.5(g) Erosion of 180-150μm salt crystal bed.

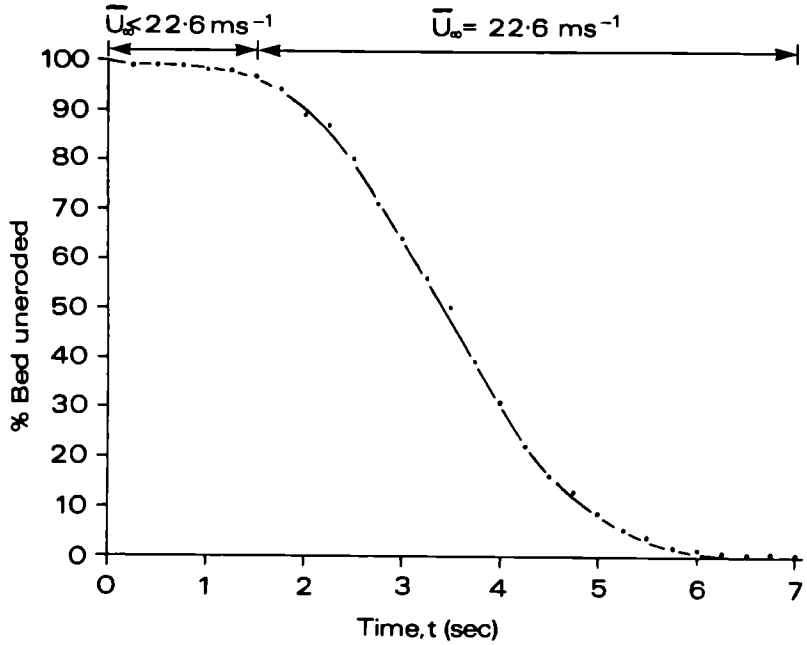

Figure 6.6 Temporal variation in percentage bed area uneroded; 1.7-1.4mm ballotini.

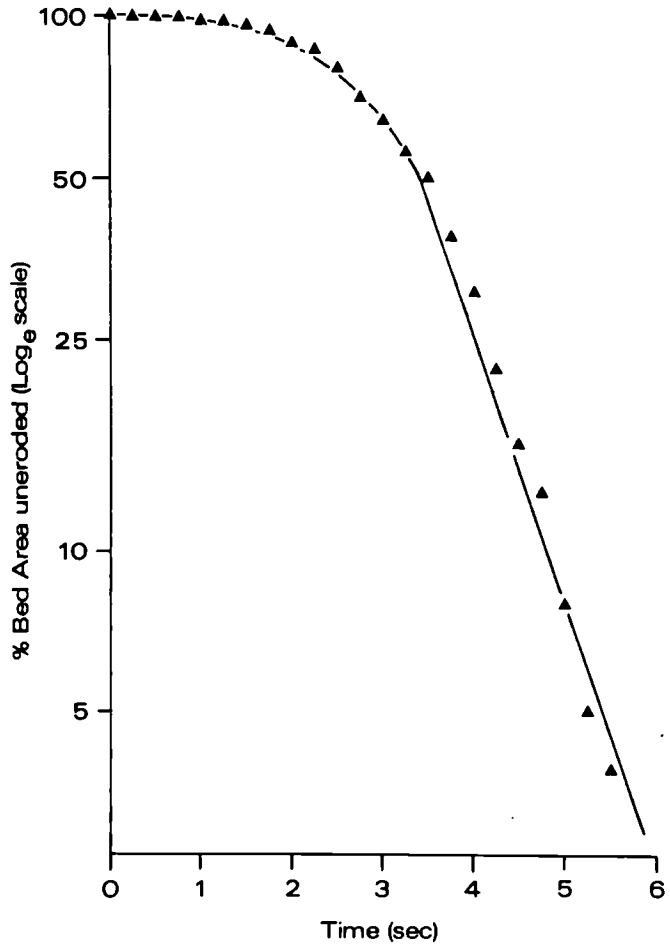

Figure 6.7 Temporal variation in percentage bed area uneroded (log_e scale); 1.7-1.4mm ballotini.

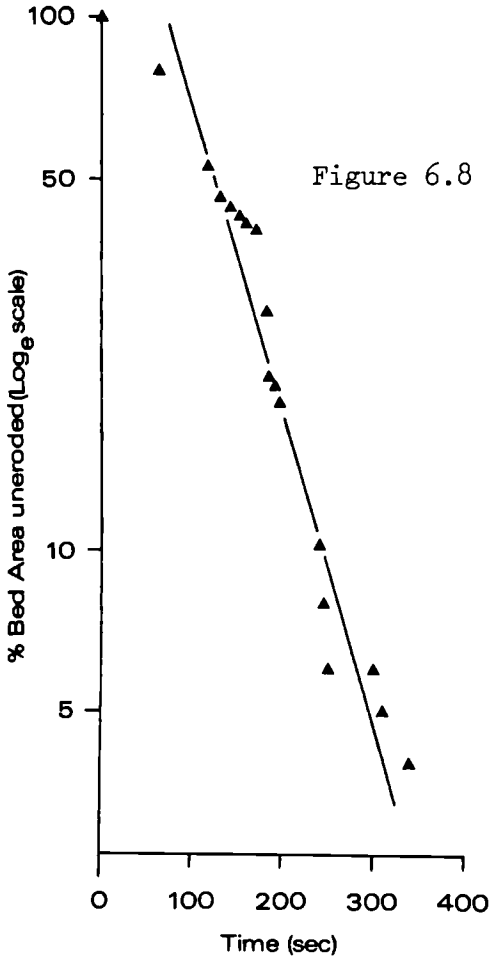

Figure 6.8 Temporal variation in percentage bed area uneroded ($\log_e$ scale); 710-600µm ballotini.

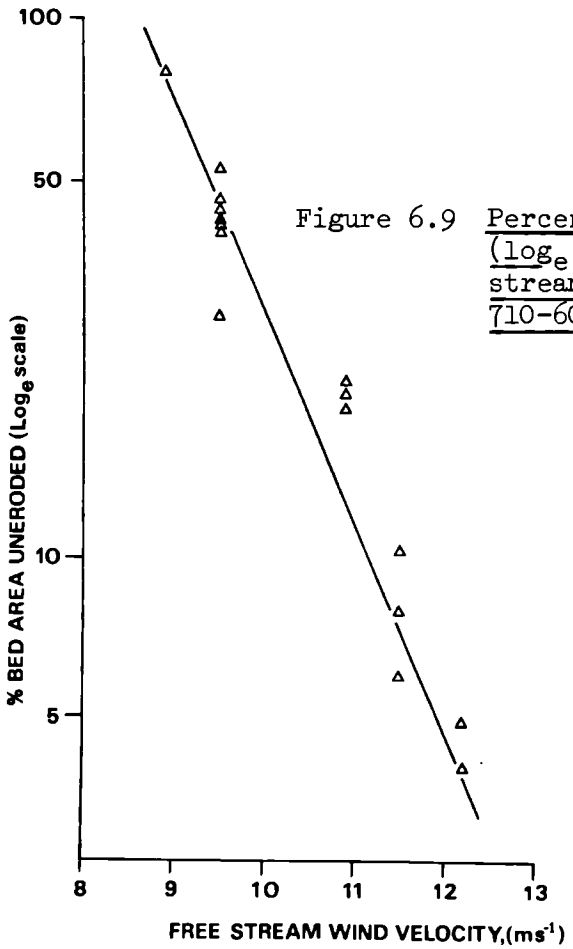

Figure 6.9 Percentage bed area uneroded ($\log_e$ scale) versus free stream wind velocity; 710-600µm ballotini.

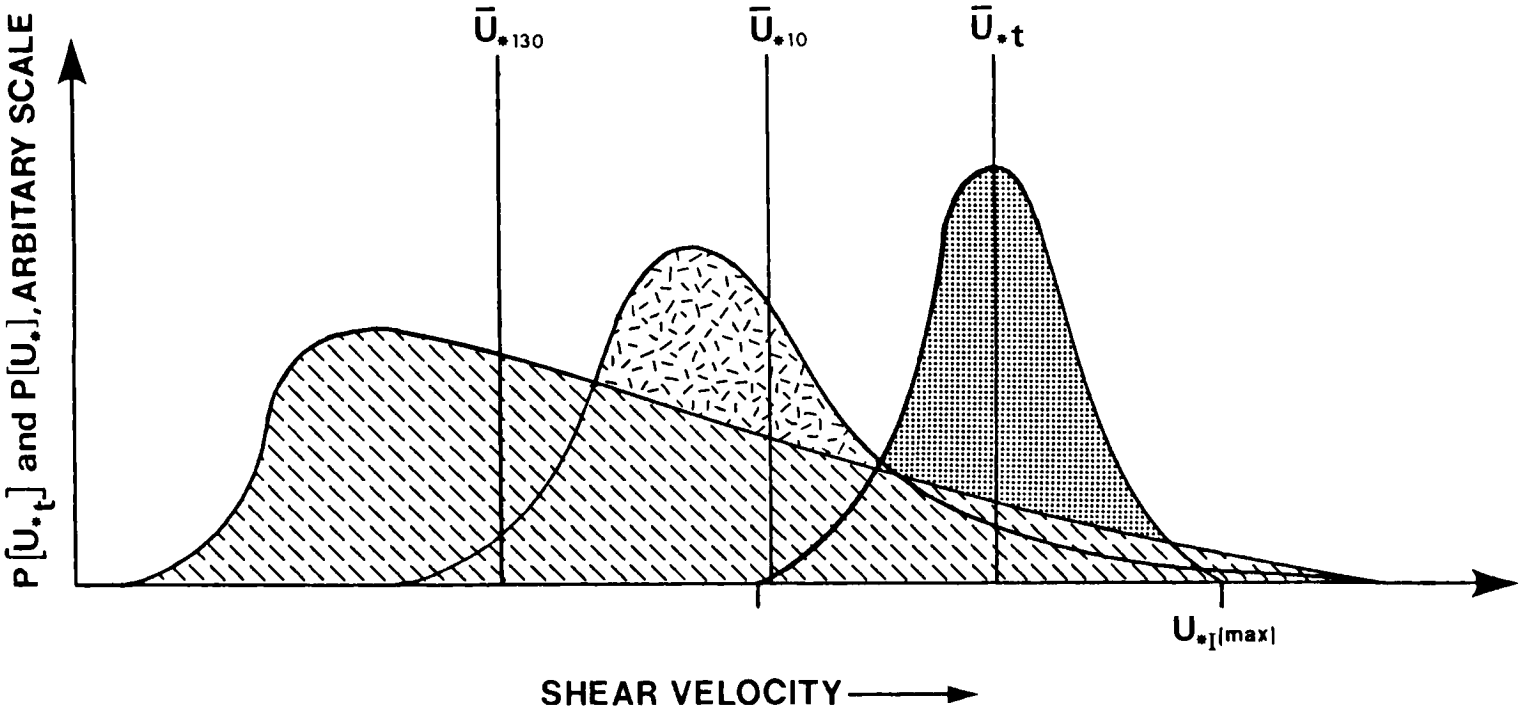

$\bar{U}_{*T}$ = MEAN VALUE OF THE P (U_{*T}) DISTRIBUTION (threshold) ASSOCIATED WITH THE TEST MATERIAL

$\bar{U}_{*10}$ = MEAN SHEAR VELOCITY AT 10 cm DOWNWIND FROM STATION A (at threshold)

$\bar{U}_{*130}$ = MEAN SHEAR VELOCITY AT 130 cm DOWNWIND FROM STATION A (at threshold)

Figure 6.10 Schematic representation of variation in erosion rates at 10cm and 130cm downwind from Station A.

CHAPTER SEVEN

Aeolian thresholds on impervious and permeable test beds

7.1 Introduction

It has been suggested in the literature (Bisal and Nielsen, 1962) that sediment permeability may influence entrainment thresholds and processes but no study has been undertaken to evaluate its significance directly. Most sediment transport dynamics have been concerned with flow over permeable surfaces (e.g. wind blowing over aeolian sands, soil, vegetation or snow) but surprisingly few workers have examined the influence of a permeable boundary on local flow conditions or entrainment. Studies by Beavers and Daniel (1967), Chu and Gelhar (1972), Zagni and Smith (1976), Nakagawa and Nezu (1980) and Zippe and Graf (1983) suggest that the boundary resistance over a rough permeable surface is higher than that over a rough impervious surface in identical flow conditions. It is likely, therefore, that the local flow modifications over a permeable sand surface may have a significant effect on aeolian entrainment thresholds. This chapter reports an investigation of aeolian thresholds and the subsequent erosion of test materials using permeable and impervious surfaces in a laboratory wind tunnel.

A possible link between thresholds of movement and bed permeability is suggested by Bisal and Nielsen (1962) in their study of particle motion in an artificially generated pressure gradient. The apparatus used by Bisal and Nielsen consisted of a short glass tube held in the centre of a square cardboard support and then placed in a wind tunnel (see Figure 7.1 for details of a replication). The tube was placed onto a bed of pebbles (3-8mm diameter) and the cardboard support was subsequently covered with a single layer of pebbles. The lower end of the glass tube was set to project a few millimetres below the general bed surface. Upwind and downwind, beyond the limits of the pebble bed,

the tunnel working section was filled with soil to the level of the uppermost pebbles. A few loose soil grains (0.1-0.5mm diameter) were then placed inside the tube and observed whilst the wind velocity in the tunnel was gradually raised. At a critical wind velocity, the loose grains vibrated inside the tube. For a small velocity increase in excess of some critical value individual particles left the surface momentarily, and at yet higher velocities some particles acquired sufficient momentum to rise momentarily greater distances up the tube before falling back again. This behaviour was observed using tubes of various lengths and diameters. Further, it was noted that such motion could be reduced or stopped altogether by decreasing the surface permeability. The object of the glass tube was to protect any grains which were lifted off the surface from the horizontal component of wind velocity, so that any such grains were not immediately swept away downwind and lost to view. The experiment, however, overlooked the other aerodynamic effects which would be produced.

Nevertheless it was considered that insight into the processes operating might be gained simply by performing a preliminary study in which the experiment of Bisal and Nielsen was repeated. The grain motion observed by Bisal and Nielsen was successfully reproduced but it soon became clear that the explanation for this behaviour was to be found in the special aerodynamics of the arrangement. Flow over the mouth of the tube produced a marked reduction in static pressure in its interior. This indicates a flow of air through the permeable bed and up into the tube where, in passage between the larger, non-erosive pebbles, its velocity is sufficient to entrain the fine erosive grains and convey them upwards. The flow rates produced were not sufficient to maintain the particle's upward motion once it is clear of the jets emerging from the

bed and the grain returns to the bed under gravity. In other words, the reduced pressure within the glass tube itself creats a miniature fluidised bed. There would seem to be no reason why any such flow should exist in absence of the tube.

However, it is perhaps possible that the pressure fluctuations associated with turbulent boundary layer flow (2.5) may be sufficient to generate secondary flows within a permeable sediment bed and may, therefore, affect aeolian thresholds in a significant way. Lyles and Krauss (1971), Lyles and Woodruff (1971) and Bisal (1973) called such pressure fluctuations '<u>impulsive forces</u>', and attach a good deal of significance to them with respect to aeolian entrainment processes. Total pressure in a boundary layer can be represented by the Bernoulli equation;

$$P_T = P_o + P_S \qquad 7.1$$

$$\text{Thus} \quad P_T = 1/2\rho U^2 + P_S \qquad 7.2$$

$$\text{where} \quad P_T = \text{total pressure} \qquad Nm^{-2}$$

The rapid fluctuations in velocity associated with turbulent boundary layers are manifest as pressure fluctuations in the steep velocity gradient near the surface. Such fluctuations in pressure, however, do not necessarily imply a net movement of fluid. They represent a dissipation of turbulent energy at the fluid boundary and this suggests that the nature of the surface may be significant in determining the effectiveness of this process. The motion of air at the scale of single grains is such that viscous effects are significant

making the Bernoulli equation not strictly valid. However, over a short time interval, a similar relationship between pressure and velocity will hold.

In a discussion of aeolian entrainment, Warren (1979, p. 325) suggests the possible importance of bed permeability: "Although not demonstrated experimentally, differences in velocity around the grains at rest on a bed could happen in two ways: by acceleration of flow over the obstacle itself, or by the difference in pressure between very slowly moving air in the voids beneath the particle, and in the steeply rising velocity gradient on its projected parts". In other words, a permeable sedimentary bed may increase the susceptibility of an individual particle to entrainment by virtue of the air flow beneath it. In a flume study by Grass (1971), various aspects of sediment transport were investigated and it was suggested that bed permeability may have had a significant effect on particle entrainment thresholds. Whilst studying bursting sequences over rough permeable surfaces, Grass both observed and measured that: "entrainment (of fluid in a burst) was extremely violent ... with ejected fluid rising almost vertically from between interstices of the roughness elements", Grass (1971, p. 252). The entrainment of low momentum air from the passive reservoir beneath a permeable sediment also suggests, therefore, that entrainment processes and aeolian threshold values may be modified by bed permeability.

The investigation reported here attempted to establish, by direct and indirect comparison, whether such flow properties have any effect on threshold values over permeable and impervious surfaces. In addition, it was hoped that any modification of boundary layer structure induced by the permeable bed would be detectable and might contribute to

the explanation of any changes in fluid threshold values which might be found. The investigation involved four stages: 1) An existing wind tunnel was re-designed and re-constructed to incorporate a false floor and a glass working section to allow easy access and viewing. 2) A technique was developed to produce non-erodible permeable beds to any required depth. This allowed comparison of boundary layer velocity profile measurements over impervious and a variety of permeable beds. 3) By placing a central permeable bed flanked on either side by parallel, impervious beds in the working section of the wind tunnel, it was possible to compare directly the erosion of a loose ballotini strip on impervious and permeable surfaces and, therefore, to determine if permeability had any effect of entrainment thresholds. 4) By inducing additional turbulence into the boundary layer using a fence, the magnitude of the 'impulsive force' could be increased so that comparisons of threshold velocities over the permeable beds could be made in order to determine the significance of permeability for the threshold velocity in conditions of high turbulence intensity.

Two terms are used throughout this chapter to describe certain properties of the test samples and beds. Before proceeding, it is necessary to define these to prevent any misunderstanding.
(a) Permeability. This term describes the ability of a test bed to permit the passage of air through the inter-particle voids. An assessment of test bed permeability was made during preliminary experimental work. (b) Porosity. In this investigation, 'porosity' is defined as the total percentage of inter-particle void space by volume and does not necessarily imply permeability. However, test beds used in this study were both porous and permeable.

7.2 Materials and methods

7.2.1 The wind tunnel

The wind tunnel used in this investigation of porosity effects (see Figure 7.2) is an open return 'suction' type designed to incorporate a number of features which permit the study of loose particle motion. It consists of four units: (a) the contraction section; (b) the run-up and working section; (c) the diffuser section; and (d) the settling chamber and fan unit.

(a) Contraction Section

The contraction section is shown in Figure 7.2(a) and 7.2(c). It had an area reduction ratio of 15 and incorporated honeycomb and gauze screens to smooth the flow at entry. Static pressure tappings were installed immediately downwind of the entry gauze and at the exit of the contraction section and were connected to the limbs of an inclined alcohol manometer. The static pressure drop caused by flow acceleration through the contraction section was indicated by the manometer, giving an accurate indication of tunnel speed.

(b) Working Section

A number of design considerations are important for any working section. Generally, the length should not exceed three equivalent tunnel diameters and ideally should taper outwards slightly downwind to offset growth of the boundary layer on the walls, floor and roof. However, as it was desirable to study particle movement in a well developed,

turbulent boundary layer, the working area was sited around 20 tunnel diameters downwind of the contraction. A further aerodynamic consideration is the inducement of secondary flows near the working section corners. However, such flows were found to be so small and localised they could be disregarded (see 7.4.1). A photograph of the working section in its final operational form is given as Figure 7.2(b).

The main consideration in the design of the working section was to ensure ease of access into the test area. This was accomplished by employing a false floor which could be easily sealed into the working section (see Figure 7.2(a) and 7.2(b)). It consisted of a stout piece of blockboard fixed to a laboratory jack and overlain by a glass plate just large enough to fit snugly into the hole cut through the working section floor (0.5m long and 0.16m wide). Test beds were prepared on the glass plate and were raised into the working section on the false floor using the laboratory jack. The walls and roof of the working section were constructed entirely from glass to allow both clear viewing and photography of the test area from most angles. Manually operated pitot-tube traversing gear was positioned above the test area and is illustrated in Figure 7.2(a) and 7.2(b). To ensure that the boundary layer was well-developed over the test area, the entire floor of the working section was covered with the same ballotini as those used in the test area. 'Contact' clear film, glued to the tunnel floor sticky side up using 'spraymount' aerosol adhesive, proved a suitable method of adhesion (see 3.6).

(c) Diffuser Section

A diffuser section was added downwind of the working section to

reduce the velocity and hence the kinematic energy of the flow before it passed into the settling chamber, thus reducing somewhat the power required of the driving fan. The finalised design of the experimental tunnel diffuser incorporated a 5^{o} expansion angle and was about one metre long. It is shown in Figure 7.2(a) and 7.2(b).

(d) Settling Chamber and Fan Unit

The settling chamber is shown in Figure 7.2(a) and 7.2(b). It consisted of a box, as large as the constraints of the available space would allow, in which the flow velocity falls to a level which allowed entrained particles from the working section to settle out of the flow. A butter muslin screen in the settling chamber acted as an additional barrier. All particulate material deposited on the floor of the settling chamber could be easily recovered via an access hatch (Figure 7.2(a)). The existing centrifugal fan unit, driven by a single speed A.C. electric motor, was mounted onto the settling chamber so that air was drawn through the wind tunnel. Speed control was achieved by a variable aperature on the chamber wall opposite the fan entry. This aperature allows external air to enter the fan without passing through the tunnel, (Figure 7.2(a)).

During preliminary investigations of the flow regime in the working section, it was found necessary to install a diffuser section on the fan exhaust in order to improve fan efficiency and to direct flow away from the tunnel intake. The diffuser incorporated 90^{o} turning vanes at its outlet and prevented highly turbulent air from the fan outlet from being drawn directly into the contraction. Additional design features included the use of foam rubber under the rigid fan unit and

tunnel supports to isolate the working section from motor and fan vibration. Airtight seals were formed between the sections of the tunnel units using foam draught excluding strips.

7.2.2 Preparation of test beds

Three test samples were investigated, two closely graded, chosen to represent the approximate extremes of the aeolian size range; (i.e. 710-600μm and 180-150μm ballotini), and a mixture of 1.7-1.4mm and 710-600μm ballotini. The test beds had a length of 0.5m and a width of 0.16m, and three different types were prepared: (a) permeable beds of 4, 12 and 24mm depth using 710-600μm ballotini; (b) bed consisting of a streamwise permeable strip flanked by impermeable strips, using all three samples of ballotini; and (c) an impervious bed of 710-600μm ballotini. In all three types, the grains were fixed in position as described below.

(a) Non-erosive permeable beds

The non-erosive, permeable 710-600μm ballotini beds were prepared by the following method. The glass plate section of the false floor was sprayed with RS Aerosol Lacquer (stock number 556-222) and loose ballotini were then poured on to the surface. After an experimentally determined drying time of half an hour, the glass plate was tipped and grains not stuck to the surface rolled away to reveal a loosely bonded layer of grains approximately one grain diameter in thickness. This layer was then sprayed with lacquer and more loose grains were tipped on to the surface. After the lacquer had dried, the glass plate was again tipped to expose a second layer of bonded ballotini. The bond between each grain was found to consist of a small

lacquer deposit left behind as the aerosol solvents evaporated at the point of contact between each particle. The natural porosity and permeability of the ballotini was found to be virtually unaffected by this adhesion technique (see 7.2.3). The process was repeated a number of times in order to prepare a fixed test bed of the required depth. A smooth top surface was produced by drawing a soft rubber roller across the bed several times whilst the lacquer was still tacky. This final surface was similar in many respects to that obtained by sticking ballotini on to the adhesive side of 'Contact' film (3.6).

(b) Non-erosive impervious/permeable beds

The second type of test bed prepared allowed direct comparison between entrainment thresholds on impervious and permeable surfaces under identical flow conditions. This bed consisted of a streamwise permeable bed flanked on either side by impervious beds. It is illustrated in Figure 7.3, which also shows a loose sediment strip running across the permeable and impervious surfaces (see below). It was prepared on the glass base plate by the following method. Two strips of hardboard, 60mm apart and 10mm in thickness, were secured to the glass plate using double sided adhesive tape. This created two raised surfaces either side of a shallow trough. Clear contact adhesive film was then glued to the hardboard, sticky side up, and coated with the chosen ballotini (see 3.6). These two strips acted as the impervious sediment beds. The glass plate was then raised into the working section of the wind tunnel on the false floor, care being taken to ensure that the impervious surfaces were flush with the rest of the floor. Precise adjustment of this level was controlled using the laboratory jack, and when correctly adjusted, the small gaps between the false floor and the working section were sealed

using plasticine and adhesive tape. Loose ballotini were then dropped into the trough and the false floor was repeatedly knocked to ensure secure grain packing. The surface was then levelled and great care was taken to ensure that the surfaces of the test and the adjacent areas were flush. Several light sprays of lacquer were then applied on the entire bed area which was then allowed to dry overnight. By experiment, three to four sprays were found to be sufficient to create a firm, but representative permeable bed between the two impervious beds.

A close-up photograph of a test bed which has been prepared using a mixture of 1.7-1.4mm and 710-600μm ballotini is given in Figure 7.3(b). In Figure 7.4, a more general view of the working area is shown. The permeable and impervious surfaces are clearly visible. This photograph, taken during a preliminary feasibility study, shows a strip of loose particles laid across the impervious and permeable beds. In subsequent experiments strips were positioned at a distance 45cm downwind from the junction between the run-up section and the test bed.

7.2.3 Determination of porosity and permeability

It was not known whether the use of aerosol lacquer affected the porosity and permeability of the fixed, permeable beds. Therefore, before conducting the erosion experiments, it was necessary to compare the porosity of loose ballotini and the permeable ballotini beds.

The term porosity as used in this study refers only to intergranular void space as the particles themselves are not considered to be porous. This distinction is made by Jones and Mills (1961) in their study of fluid flow through porous media. Simply porosity, Pn, may

be defined as;

$$Pn = \frac{\text{total voids volume}}{\text{total sediment volume}}$$

and it is generally expressed as a percentage.

Porosity of natural sands has been studied in detail by Kolbuszewski (1948, 1953) and Kolbuszewski et al. (1950). In general, porosity values for any granular material are found to lie between two values determined by the maximum and minimum packing values. Smith et al. (1929) examined lead spheres in close-hexagonal and simple-cubical arrays and found porosity values of 26% and 48% respectively. Perfect geometric spheres have porosity values ranging between 25.95% and 47.64% for rhombohedral and cubic packing respectively, Granton and Fraser, (1935) and Scott (1960). Typically, when spheres are piled irregularly, the arrangement may be statistically regarded as hexagonal and cubical arrays assembled in proportions yielding the observed porosity. MaCrae and Gray (1961) make the point that particle packing can only be described adequately using two inseparable values; (i) porosity and (ii) the co-ordination number (or the number of contacts per sphere). Theoretically, particle size does not affect porosity yet Fraser (1935), Bernal and Mason (1960) and Beard and Wey (1973), cite friction, adhesion and bridging as factors increasing porosity in fine material. Porosity measurements of sands and loam by Ellis and Lee (1919), (Table 7.1), illustrate this increase in voids percentage with decreasing grain size. Fraser (1935) also found particle shape to be significant in determining porosity (Table 7.2). In the context of this study it is interesting to note from Table 7.2 that sub-rounded beach and dune sands have similar porosities to lead shot (spherical), and thus the permeable ballotini

beds used in this study are considered to have similar properties to natural aeolian sand beds.

Table 7.2 indicates that random arrangements of particles will naturally exhibit a range of porosity values which gives rise to difficulties when assessing the significance of the aerosol lacquer treatment, as the natural range of porosity due to grain packing may be greater than differences in porosities between loose ballotini and the porous, permeable ballotini test beds. A criterion was therefore established that, should measured porosity fall below the lower theoretical limit for random sphere packing (i.e. 26%), then the spray was considered to have a significant effect and this method of porous permeable bed preparation should be rejected.

Scheidegger (1957) and Collins (1961) list a number of methods employed for the experimental determination of porosity for both consolidated and unconsolidated material. They include:

(a) Direct methods. The material is compressed so as to destroy all the voids.

(b) Optical methods. These methods rely on the assumption that the plane porosity of a random section is identical to the sample porosity. Calculation of the void area is generally automated.

(c) Density methods. The bulk density ρ_B and material density σ are related to porosity P by the equation;

$$P_n = 1 - \rho_B/\sigma \qquad 7.3$$

Thus knowing σ and ρ_B, porosity may be determined.

(d) Gas expansion. This direct method measures the gas volume to fill the voids after evacuation of a test sample. (Details of this technique are given by Beeson, 1950).

(e) Infiltration or imbibition methods. A dry sample is immersed in a fluid under vacuum and the quantity of fluid held is then determined. Despite the time required to ensure total infiltration Collins (1961) states, "this is perhaps one of the best methods of porosity measurement in current use", Collins (1961, p.38).

The method used to determine the porosity of the untreated and treated ballotini in this study was that of total infiltration of a known sample volume under vacuum. Full details of this method are given in Appendix A4. In addition a visual assessment of bed permeability was made by simply immersing a test bed in water coloured with green food dye. The results of the porosity and permeability tests are given below in 7.5.2.

7.2.4 Residual adhesion of beds

An additional simple test was to assess whether a sprayed surface remained slightly 'sticky', despite a long drying period. In this test one half of a glass plate was sprayed with lacquer. After a suitable drying period a thin layer of loose ballotini was spread out across both the lacquered and the unlacquered surfaces and the plate was inclined gradually. Had there been a greater tendency for adhesion to the surface treated with lacquer, it would have been observable using this test. No such tendency was detected and it was therefore considered that lacquer treated surfaces possessed no residual stickiness which

might have invalidated subsequent experimental studies of aeolian thresholds on the test beds.

7.3 Experimental procedure

7.3.1 Flow in the working section

Prior to all investigations in the wind tunnel, it was necessary to assess the flow characteristics in the working section adjacent to the test beds. Had there been any flow anomalies present, they would have led to serious misinterpretations of the subsequent experiments. Two aspects of flow in the working section were analysed. Firstly, the overall flow was mapped using 134 individual measurements of wind velocity taken with a standard pitot-static probe ($\bar{U}_\infty$=24ms^{-1}). Secondly, detailed wind velocity profiles on the test bed (710-600μm ballotini) were taken using pitot-tube array 2 (4.2.2) at 11 spanwise sites. These sites were located at 15mm intervals to the left and right of a station in the middle of the test bed.

7.3.2 Boundary layer velocity profiles on impervious and permeable test beds

Using an impervious bed of 710-600μm ballotini (7.2.2(a)), detailed boundary layer profiles were taken on the downwind limit of the test bed at four wind velocities. These measurements acted as a standard with which profiles taken over a variety of permeable surfaces could be compared. Three thicknesses of permeable test bed were examined. These were: 4mm; 12mm; and 24mm. In all cases wind velocity values were the same as those set for profiles previously taken on the impervious surface.

7.3.3 Aeolian entrainment on impervious and permeable test beds: indirect comparison

Whilst taking boundary layer velocity profile measurements on the impervious and permeable 710-600μm ballotini beds (7.3.2), the opportunity was taken to measure aeolian threshold conditions on each of the test beds studied. A narrow, loose strip of 710-600μm ballotini (30mm wide) was placed 45cm downwind of the junction between the run-up section and the test bed on each of the 710-600μm ballotini test beds (an impervious bed and permeable beds of depths 4, 12 and 24mm). These loose ballotini were coloured using a permanent marker pen and were thus clearly visible on the non-erosive test beds. (By tilting samples in a preliminary test it was shown that the inter-particle cohesion of coloured ballotini was the same as that associated with normal test samples).

A photograph of the initial strip configuration was taken and the wind velocity was gradually raised until a few particles in the strip were seen to oscillate sporadically. A further small increase in velocity resulted in the entrainment of a number of loose grains from the strip. After five minutes, erosion ceased and a second photograph of the loose strip was taken. The wind velocity was then increased to a slightly higher value than the previous one and after five minutes of erosion, a third photograph of the strip was taken. This procedure was repeated until the strip was completely eroded using stepwise increases in wind velocity. Generally, this involved ten erosion stages per strip.

Mean free stream wind velocity was measured using the pitot-static probe positioned in the centre of the working section directly above an eroding test strip. In this way it was hoped to relate any differences in the mean threshold free stream wind velocity of particles in the test strips to differences in bed permeability.

7.3.4 Aeolian entrainment on impervious/permeable test beds: direct comparison

Whilst conducting these initial experiments it became apparent that if permeability was a factor in the entrainment process, its effects were difficult to detect and so a different approach was tried.

To examine aeolian entrainment on impervious and permeable beds in greater detail, a strip of coloured ballotini was laid across a given impervious/permeable test bed (7.2.2(b)), at a site 45cm downwind from the junction between the run-up section and the test bed. The strip was then eroded using the procedure described in 7.3.3. This procedure was undertaken for the ballotini sizes:

Impervious/permeable bed	'Erosive' sediment strip
710-600μm	710-600μm
180-150μm	180-150μm
1.7-1.4mm and 710-600μm	710-600μm

Figure 7.4 shows the experimental arrangement prior to the erosion of a test strip used in a preliminary study. Subsequent investigation always examined the erosion of strips at 45cm downwind from the junction between the run-up section and the test bed.

7.3.5 Aeolian entrainment on impervious/permeable test beds in highly turbulent flow

In a further series of experiments, a small bevelled wooden strip was placed upwind of an impervious/permeable test bed which had been prepared using a mixture of 1.7-1.4mm and 710-600μm ballotini. This obstruction to the flow acted as a fence and thereby increased downwind turbulence on the test bed. It was considered that generation of increased turbulence in this way would also increase the magnitude of the 'impulsive force' (Bisal, 1973, see 7.1) and thereby exaggerate any effects bed permeability may have on aeolian thresholds and entrainment processes.

A loose strip of 710-600μm ballotini was placed on the impervious/permeable test bed at the selected distance downwind from the fence (5, 45, 75, 150 or 250mm). Stepwise increases in the wind velocity caused a given strip to be eroded in a number of discrete stages and these were recorded photographically for later analysis. Again, erosion was allowed to proceed at each increased windspeed until entrainment from the strip had ceased. The mean free stream wind velocity corresponding to each erosion stage was recorded using a pitot-static probe positioned in the centre of the working section directly above the strip.

7.4 Data extraction and experimental results

7.4.1 Flow in the working section of the wind tunnel

A diagrammatic summary of the flow regime measured in the working section of the wind tunnel adjacent to the 710-600μm ballotini

test bed is given in Figure 7.6. Mean flow velocity values, which were calculated from pitot-static pressure measurements using the computer program given in Appendix A1, were plotted in Figure 7.6(a) using 134 point wind velocity measurements contoured by isovels at $2ms^{-1}$ intervals, ($\bar{U}_\infty=24ms^{-1}$). Spanwise variations in the boundary layer velocity profiles measured using pitot-tube array 2 on the impervious 710-600μm ballotini bed are illustrated by the shaded curve in Figure 7.6(b). This figure shows dimensionless wind velocity ($\bar{U}/\bar{U}_\infty$) against height above the boundary (Y) determined from 11 spanwise wind velocity profile measurements, ($\bar{U}_\infty=10ms^{-1}$).

7.4.2 Ballotini porosity, test bed porosity and permeability

Results of the determination of bed porosity for loose ballotini and ballotini test beds are presented in Table 7.3. This table includes mean porosity values (expressed as the percentage of inter-granular void spaces in a sample (7.2.3)) of (i) ballotini test beds prepared using the techniques described in 7.2.2, and (ii) loose ballotini samples, for all the ballotini size ranges used in this study. Mean porosity values were determined from five independent test samples. The standard deviation of mean porosity values is also included in Table 7.3. Results from the visual assessment of test bed permeability are discussed in 7.5.2.

7.4.3 Boundary layer profiles over impervious and permeable test beds

In order to compare the velocity profiles over each test surface, the velocity data were reduced to the dimensionless form $\bar{U}/\bar{U}_\infty$. In all cases $\bar{U}_\infty$ was measured by a pitot-static probe positioned in the centre of the working section directly above the test bed. The reduced

data are presented in Table 7.4 which shows $\bar{U}/\bar{U}_\infty$ values measured at seven heights and four free stream wind velocity values on 710-600μm ballotini test beds of thicknesses 0mm (impervious) and 4, 12 and 24mm (permeable). The standard deviation of the data on all the test beds at a given height above the surface is also included.

7.4.4 Aeolian thresholds on impervious and permeable test beds: indirect comparison

The erosion stages of each strip were recorded photographically on Ilford FP4 (ASA/ISO 160) films which were processed using the techniques described in Appendix A3. The changing strip outlines were then analysed using the same methods as before (see 4.3.2). Using calculated values of percentage of initial strip area remaining uneroded, it was then possible to relate a known degree of strip erosion on a given ballotini bed to a measured free stream wind velocity. Results of this analysis are presented in Table 7.5 which shows the percentage of strip area uneroded on the stated ballotini bed, and the corresponding free stream wind velocity measurement using the pitot-static probe.

7.4.5 Aeolian thresholds on impervious/permeable test beds: direct comparison

In this case the areas remaining on impervious and permeable sections of the impervious/permeable test bed were determined making it possible to relate directly free stream wind velocity to the amount of strip erosion occurring on both impervious and permeable parts of the test bed.

The results of this analysis are presented in Tables 7.6, 7.7 and 7.8 which show the percentage of the strip area uneroded on both the impervious and permeable test bed sections of 710-600μm, 180-150μm and 1.7-1.4mm/710-600μm ballotini for various free stream wind velocities. In addition, typical strip erosion stages on these test beds (selected from the 15 recorded stages) are illustrated in Figures 7.7 to 7.9. The shaded areas depicting the configuration of a given strip on the impervious/permeable test bed were traced directly from the photographs and give a visual impression of each strip erosion sequence recorded during this study. These figures are annotated to show the impervious and permeable sections of the test bed, the dimensions of the strip, the wind direction, the elapsed erosion time and the free stream wind velocity.

7.4.6 Aeolian thresholds on impervious/permeable test beds in highly turbulent flow

Data describing the sequential erosion of 710-600μm ballotini test strips at distances of 5, 45, 75, 150 and 250mm downwind of the fence on the 1.7-1.4mm and 710-600μm ballotini impervious/permeable test bed were derived from analysis of the photographic records using the method described in 4.3.2. These data are presented in Table 7.7 which shows the percentage of the strip area uneroded on both the impervious and permeable test bed sections at the stated mean free stream wind velocity for each strip erosion stage and position downwind of the fence. In addition, strip erosion stages at each of these test sites are illustrated in Figure 7.10. These strip outlines were also traced directly from the photographs, and are annotated to show the strip position on the impervious/permeable test bed (expressed as distance

downwind of the fence), the elapsed erosion time, the mean free stream wind velocity and the wind direction relative to a given strip.

7.5 Discussion of results

7.5.1 Flow in the working section of the wind tunnel

Figure 7.6(a) shows clearly that the flow regime in the working section was free from any large flow anomalies likely to affect aeolian grain entrainment from the test beds. It also shows that the boundary layer adjacent to the floor of the working section was significantly thicker than boundary layers developed on the other inner surfaces of the working section. This arises from the higher aerodynamic drag of the run-up section floor which was lined with 710-600μm ballotini.

The shaded curve in Figure 7.6(b) was obtained by amalgamating 11 spanwise dimensionless boundary layer velocity profiles. It shows that the maximum recorded spanwise variation in $\overline{U}/\overline{U}_{\infty}$ values was only 0.05, confirming that spanwise boundary layer flow characteristics were uniform on the test area. These data show that strips of test material placed upon the impervious and permeable test beds in subsequent experiments were subjected to virtually the same boundary layer flow regime across their entire width and were, therefore, unaffected by spanwise flow anomalies likely to affect aeolian threshold values and hence the interpretation of the experimental results.

7.5.2 Ballotini porosity and test bed porosity and permeability

Experimentally determined values of porosity for loose ballotini

and ballotini test beds are presented in Table 7.3. They show that the aerosol lacquer used to prepare the permeable test beds had little effect upon their porosity. Differences between the porosity of loose ballotini and permeable ballotini test beds are small and it is considered that this variation in porosity probably resulted from differences in the grain packing associated with test samples rather than from any variations caused by the preparation technique. On the basis of this evidence, it is considered that the natural porosity of ballotini was preserved when test beds were prepared using the two fixing techniques described in 7.2.2.

During the measurement of porosity, a qualitative assessment of permeability was made on the basis of water infiltration rates through a number of samples (Appendix A4). It was generally observed that infiltration was rapid and homogeneous throughout the entire sample regardless of the particle size or lacquer treatment applied. The only exception to this was the porous bed made by successive lacquer sprayings, (i.e. 710-600μm ballotini (7.2.2(b)). Reduced inter-void connection was manifest as small but infrequent pockets of air trapped beneath the surface. However, this reduction in permeability was found to be very localised and was considered to be insignificant in the context of an entire permeable test bed.

7.5.3 Boundary layer velocity profiles on impervious and permeable test beds

To permit comparison between profiles, velocity profiles measured at four free stream wind settings on the downwind limit of

710-600μm ballotini test beds of depths 710-600μm (impervious) and 4, 12 and 24mm (permeable) are presented in the dimensionless form $\bar{U}/\bar{U}_\infty$ in Table 7.4. The standard deviation of velocity at a specified height above the bed is also presented in Table 7.4 and incorporates the velocity data associated with each of the four free stream wind velocity values. These values thus reflect differences in the dimensionless velocity ($\bar{U}/\bar{U}_\infty$) values on the impervious and the permeable test beds examined in this study. Inspection of the $\bar{U}/\bar{U}_\infty$ values and the associated standard deviations (Table 7.4), reveals that the boundary layer velocity profile characteristics were very similar irrespective of the test bed considered. On the basis of this evidence, therefore, it appears that permeable beds of the dimensions used have no detectable influence on the mean boundary layer velocity profile. The overall shape of the mean velocity profile, however, is a comparatively insensitive indication of the precise state of the boundary layer.

Work by Zippe and Graf (1983) indicates that the boundary resistance on a permeable test bed is marginally higher than that on an impervious test bed. Zippe and Graf (1983) detected this difference by measuring boundary layer velocity profiles on long impervious and permeable test beds using a sensitive constant-temperature hotfilm-anemometer sited within the inner region of the turbulent boundary layer (2.5.1). The differences they detected were attributed to flow actually entering and leaving the permeable bed so that the no-slip condition normally found at the surface of an impervious bed is located at some distance within the permeable bed. It seems, therefore, that a permeable bed does modify the characteristics of the boundary layer flow close to the surface and this may exert some influence on aeolian threshold conditions on permeable beds.

There are three possible reasons why differences in boundary layer velocity profiles over impervious and permeable beds detected by Zippe and Graf (1983), were not found in this study. (a) The pitot-tube arrays used here were insufficiently sensitive to detect the small differences in the boundary layer velocity profile close to the surface of the impervious and permeable test beds which were found by Zippe and Graf. (b) The length of the permeable test beds used in this study (0.5m) was insufficient to allow detectable differences to develop (permeable beds studied by Zippe and Graf were 8m long). (c) The particle size used to prepare the test beds (710-600μm) was much smaller than the particles used by Zippe and Graf (1983), (2.883mm). It is concluded, then, that if the effect is present, it is very small. The data of Zippe and Graf (1983) indicates that the modifications to boundary layer characteristics are relatively slight and are, therefore, considered unlikely to increase or decrease aeolian threshold values greatly.

7.5.4 Aeolian thresholds on impervious and permeable test beds: indirect comparison

Results from the analysis of erosion of a strip of 710-600μm ballotini placed on the four different depths of like material are presented in Table 7.5. This shows the approximate percentage of strip area uneroded at the stated free stream wind velocity for each test bed studied. It is clear from inspection of these results that the value of percentage strip area uneroded associated with a given free stream wind velocity is virtually the same irrespective of the test bed permeability. However, it may be questioned whether mean free stream wind velocity is a suitably representative measure of threshold flow

condition on the test bed. In view of the results obtained by Zippe and Graf (1983), it is considered that mean free stream wind velocity is a relatively insensitive indicator of differences in threshold flow conditions on the impervious and permeable beds as the most significant changes to the boundary layer on permeable beds are manifest in the flow close to the surface. Therefore, the results presented in Table 7.5 must be interpreted with caution. Table 7.5 does indicate, however, that if permeability of a bed is a significant factor in raising or lowering aeolian thresholds then its effects cannot be detected using this technique.

The recorded patterns of strip erosion (not illustrated) were similar in many respects to those reported in Chapter 4 for strips on the flat plate. Most entrainment occurred from the downwind edge of the strip and visual observation of entrainment on these test beds indicated that initial grain motion characteristics were the same irrespective of the underlying bed permeability.

7.5.5 Aeolian thresholds on impervious/permeable test beds: direct comparison

The problems associated with detecting differences in aeolian threshold values on impervious and permeable beds described above were overcome by examining the erosion of test strips which spanned both impervious and permeable sections of special test beds (i.e. the impervious/permeable bed described in 7.2.2(b)). Results of this study examining the erosion of loose strips on impervious/permeable ballotini test beds are presented in Tables 7.6, 7.7 and 7.8 for 710-600μm, 180-150 μm and 1.7-1.4mm/710-600μm ballotini, respectively. In addition, Figures

7.7 to 7.9 illustrate selected strip erosion stages on the impervious/ permeable beds above. Tables 7.6 to 7.8 show the uneroded strip area associated with a given mean free stream wind velocity on both the impervious and permeable sections of the impervious/permeable test beds. As these values were derived from the same strip on the test bed, these data may be compared directly. Tables 7.6 to 7.8 show that on no occasion were the mean threshold free stream wind velocity ($\bar{U}_{\infty_T}$) values associated with a given amount of strip erosion on the impervious and permeable surface found to differ by more than $0.2ms^{-1}$. In fact, $\bar{U}_{\infty_T}$ values in most cases differed by only $0.1ms^{-1}$ or were the same. On the basis of this evidence, therefore, it is considered that permeable beds of the dimensions used in this study have no significant effect upon the $\bar{U}_{\infty_T}$ values associated with the ballotini.

Visual evidence to support this deduction is provided by the selected strip erosion stages illustrated in Figures 7.7 to 7.9. Figure 7.7 shows the erosion history of a 710-600μm ballotini strip exposed to threshold free stream velocity values increasing between $14ms^{-1}$ and $20ms^{-1}$. The loss of material from the strip is seen to occur fairly uniformly from sites along the entire width of the strip. Similarly, Figures 7.8 and 7.9 (180-150μm and 1.7-1.4mm/710-600μm ballotini respectively) show that strip erosion patterns recorded on both the impervious and permeable test bed sections are essentially the same and thereby reinforce the conclusion that a permeable bed of the dimensions used in this study has little influence on aeolian threshold conditions. Strip erosion patterns are again seen to be similar to those reported in Chapter 4.

Visual observations of grain entrainment from these test strips

on both the impervious and permeable test beds also indicated that the entrainment processes involved were similar regardless of the underlying bed characteristics. At the threshold condition, just prior to entrainment, particles were observed to oscillate and a subsequent small increase in the wind velocity caused grains to be rolled over their neighbours. These entrained grains then collided with stationary grains further downwind and were thereby ejected away from the bed acquiring progressively greater bounce heights in subsequent downwind collisions. Whether beds were permeable or impermeable made no observable difference to this process.

7.5.6 Aeolian thresholds on impervious/permeable test beds in highly turbulent flow

The sequential erosion of 710-600μm ballotini strips located at 5, 45, 75, 150 and 250mm downwind of the fence on the 1.7-1.4mm and 710-600μm impervious/permeable ballotini bed is summarized in Table 7.9 and illustrated in Figure 7.10. Table 7.9 shows the percentage of a given strip uneroded at a stated mean threshold free stream wind velocity for the portions of the strip lying on both the impervious and permeable sections of the test bed. Table 7.9 shows that slightly more strip material was uneroded at a given $\bar{U}_{\infty T}$ value on the permeable section of the test bed for strip positions 5 and 45mm downwind of the fence. However, at strip positions 75, 150 and 250mm downwind from the fence the percentage of uneroded strip material on the permeable surface was generally less than that associated with the impervious surface, at a given $\bar{U}_{\infty T}$ value. As the fence gave rise to highly turbulent downwind flow conditions which could not be measured using the pitot-tube array, it was not possible to relate the erosion history of strips at the

various study sites to the local flow conditions directly. However, as this study was essentially concerned with differences in aeolian thresholds on impervious and permeable beds in highly turbulent flow, this was considered to be unimportant and the experiment was considered to serve its intended purpose. As the percentages of uneroded strip on the impervious and permeable sections of the bed did not differ by more than 8% at any $\bar{U}_{\infty T}$ value regardless of the strip location (Table 7.9), it is considered that bed permeability had no significant effect in either raising or lowering the aeolian threshold value associated with this test material in these highly turbulent flow conditions.

Outlines of each strip erosion sequence are given in Figure 7.10 and are annotated to show the elapsed erosion time and the mean threshold free stream wind velocity. The shaded portions on each strip outline show the portion of strip lying on the permeable section of the test bed. The erosion sequences are similar to those illustrated in Figures 7.7 to 7.9 and show that the patterns of erosion recorded on both the impervious and permeable test bed sections are indistinguishable from each other.

On these beds also, visual observations of aeolian entrainment indicated that initial grain motion characteristics were the same irrespective of the permeability of the underlying surface. It was observed, however, that a significant portion of the test material in the strip located at 5mm downwind from the fence moved upwind in threshold flow conditions. A number of these grains were deposited in the lee of the fence but most were subsequently blown downwind. These upwind motions are considered to have resulted from grain interactions with the re-circulation region just upwind of the boundary layer re-attachment zone

(Figure 7.5).

7.6 Conclusion

The experiments reported in this chapter have permitted a critical examination of the influence of bed permeability upon initial movement of loose granular materials by wind. No differences were detected between the boundary layer velocity profiles over an impervious bed and those over a range of permeable beds. It may be concluded that the large-scale characteristics of the boundary layer are the same on beds of the dimensions used in this investigation irrespective of bed permeability. However, in view of data published by Zippe and Graf (1983), it is highly likely that the characteristics of the boundary layer close to the bed are modified by a long permeable bed in such a way that the boundary resistance is effectively increased. Whether or not these changes also occur on permeable beds composed of aeolian sized particles (i.e. 710-600μm) at flow Reynolds numbers (Re*) characteristically associated with aeolian threshold conditions cannot be deduced from data presented in this present study or from data published in the literature. Of greater importance to the present investigation was to establish whether or not bed permeability had any detectable effects on grain entrainment characteristics and hence aeolian threshold conditions.

No differences between aeolian threshold conditions on impervious and permeable test beds are indicated by data derived from indirect comparisons of strip erosion, nor were any differences detected during visual observations of the entrainmen processes on these test beds. Similarly, direct comparisons of aeolian thresholds on impervious/

permeable test beds, both with and without fence-induced increases in intensity of flow turbulence, also failed to detect any significant differences. On the basis of this evidence it may be concluded that, in comparison with other parameters such as grain size, shape and density and the large scale boundary layer flow characteristics, bed permeability is a factor of little importance in controlling aeolian threshold conditions.

It is still possible that at wind velocities well in excess of the threshold, the flow in and out of the bed may be sufficiently energetic to alter the manner in which particles behave as they are initially dislodged. However, at such velocities most particles will actively saltate and accordingly will modify the wind velocity profile to such an extent that shear velocities are unlikely to exceed the threshold value at the bed surface (1.3.1(b)). It is highly likely, therefore, that the natural permeability of aeolian sediment surfaces has little or no effect on aeolian threshold values.

Table 7.1 Typical sand porosity (% voids by volume), (after Ellis and Lee, 1919)

MATERIAL	POROSITY %
Coarse sand	39 - 41
Meduim sand	41 - 48
Fine sand	44 - 49
Fine sandy loam	50 - 54

Table 7.2 Porosity of selected loose and compacted materials (after Fraser, 1935)

Material	Shape	Specific gravity	Porosity %	
			Type of Packing (dry)	
			Loose	Compacted
Lead shot	Spherical	11.21	40.1	37.2
Beach Sand	Sub-rounded	2.66	41.2	36.6
Dune Sand	Sub-rounded	2.68	41.2	37.6
Halite	Cubic	2.18	52.1	43.5
Mica	Flat plates	2.84	93.5	86.6

Table 7.3 Experimentally determined porosity of loose ballotini and ballotini test beds

BALLOTINI SIZE RANGES	PREPARATION	MEAN POROSITY %	STANDARD DEVIATION %
1.7-1.4mm and 710-600μm	Loose grains	32.4	0.08
1.7-1.4mm and 710-600μm	Bed prepared using a surface lacquer spray	31.2	0.016
710-600μm	Loose grains	36.4	0.009
710-600μm	Bed prepared using a surface lacquer spray	35.1	0.014
710-600μm	Bed prepared using a	33.6	0.013
180-150μm	Loose grains	33.0	0.01
180-150μm	Bed prepared using a surface lacquer spray	33.9	0.022

		Mean free stream wind velocity, $\bar{U}_\infty$, ms^{-1}																Standard Deviation
		9.0				11.0				12.9				15.1				
TYPE OF TEST BED		IMPER-MEABLE	PERMEABLE			IMPER-MEABLE	PERMEABLE			IMPER-MEABLE	PERMEABLE			IMPER-MEABLE	PERMEABLE			
TEST BED THICKNESS		710-600μm	4mm	12mm	24mm	710-600μm	4mm	12mm	24mm	710-600μm	4mm	12mm	24mm	710-600μm	4mm	12mm	24mm	
Height above the test bed, y (mm) (PITOT TUBE ARRAY 2	4.7	0.53	0.54	0.54	0.57	0.55	0.55	0.55	0.57	0.55	0.54	0.55	0.54	0.55	0.53	0.54	0.55	0.011
	9.7	0.66	0.65	0.66	0.65	0.66	0.66	0.66	0.67	0.65	0.66	0.65	0.66	0.66	0.65	0.65	0.66	0.006
	19.2	0.74	0.75	0.75	0.74	0.76	0.75	0.74	0.76	0.73	0.74	0.74	0.74	0.74	0.74	0.73	0.74	0.009
	39.0	0.84	0.83	0.83	0.82	0.84	0.84	0.82	0.83	0.82	0.82	0.82	0.83	0.83	0.81	0.81	0.82	0.010
	69.1	0.95	0.93	0.93	0.94	0.93	0.94	0.93	0.95	0.93	0.94	0.92	0.93	0.93	0.93	0.93	0.93	0.008
	98.5	1	1	1	1	1	1	1	1	1	1	1	1	1	1	1	1	0

Table 7.4 Summary of boundary layer velocity profile data for the impervious and permeable (four) test beds of various depths of 710-600μm ballotini. [Data reduced to the dimensionless form $\bar{U}/\bar{U}_\infty$]

	Percentage of the strip area uneroded.	IMPERVIOUS 710-600μm	Sediment bed depth PERMEABLE		
			4mm	12mm	24mm
1.	More than 90%	14.1	14.2	14.2	14.0
2.	Between 50% and 60%	18.2	18.2	18.1	18.2
3.	Less than 10%	21.3	21.3	21.2	21.3

Table 7.5 Percentage of strip area uneroded at stated threshold free stream wind velocities (ms^{-1}) on the impervious and three permeable test beds of different depths, (710-600μm ballotini).

	Percentage of the strip area uneroded	Test bed	
		IMPERVIOUS	PERMEABLE
1.	More than 90%	14.0	14.0
2.	Between 50% and 60%	18.2	18.3
3.	Less than 10%	21.2	21.0

Table 7.6 Direct comparison of mean threshold free stream wind velocities (ms^{-1}) on impervious/permeable 710-600μm ballotini beds.

	Percentage of the strip area uneroded	Test bed	
		IMPERVIOUS	PERMEABLE
1.	More than 90%	8.0	8.1
2.	Between 50% and 60%	10.4	10.4
3.	Less than 10%	15.1	15.0

Table 7.7 Direct comparison of mean threshold free stream wind velocities (ms^{-1}) on impervious/permeable 180-150μm ballotini beds.

	Percentage of the strip area uneroded	Test bed	
		IMPERVIOUS	PERMEABLE
1.	More than 90%	17.3	17.3
2.	Between 50% and 60%	19.9	19.9
3.	Less than 10%	23.1	23.1

Table 7.8 Direct comparison of mean threshold free stream wind velocities (ms^{-1}) on impervious/permeable 1.7-1.4/710-600μm ballotini beds.

	DISTANCE DOWNWIND OF THE FENCE (mm)														
	5			45			75			150			250		
	% strip area uneroded			% strip area uneroded			% strip area uneroded			% strip area uneroded			% strip area uneroded		
EROSION STAGE	IMPER-VIOUS	PERM-EABLE	$\bar{U}_\infty$	IMPER-VIOUS	PERM-EABLE	$\bar{U}_\infty$	IMPER-VIOUS	PERM-EABLE	$\bar{U}_\infty$	IMPER-VIOUS	PERM-EABLE	$\bar{U}_\infty$	IMPER-VIOUS	PERM-EABLE	$\bar{U}_\infty$
i	100	100	0	100	100	0	100	100	0	100	100	0	100	100	0
ii	89	92	14.0	95	96	15.6	81	79	14.3	88	86	13.7	88	90	14.0
iii	64	68	16.8	59	61	17.8	13	11	15.9	18	12	15.5	19	16	15.2
iv	23	35	19.6	6	5	20.1	1	1	18.6	3	2	17.6	2	0	19.7
v	-	-	-	-	-	-	-	-	-	1	1	19.7	-	-	-

Table 7.9 Erosion of test strips (710-600μm ballotini) on the 710-600μm impervious/permeable test bed at five sites downwind of the fence

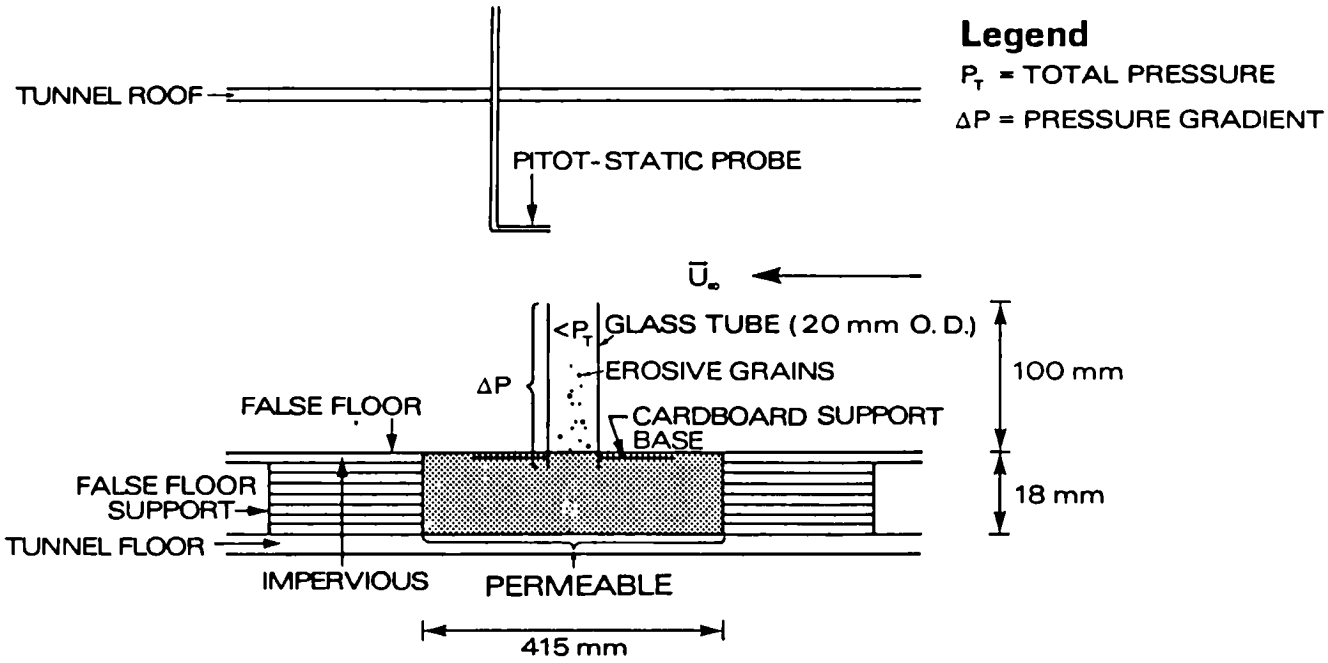

Figure 7.1 Apparatus used to replicate the investigation by Bisal and Nielsen (1962).

Figure 7.2 Wind tunnel used to study the effect of bed permeability on aeolian threshold conditions.

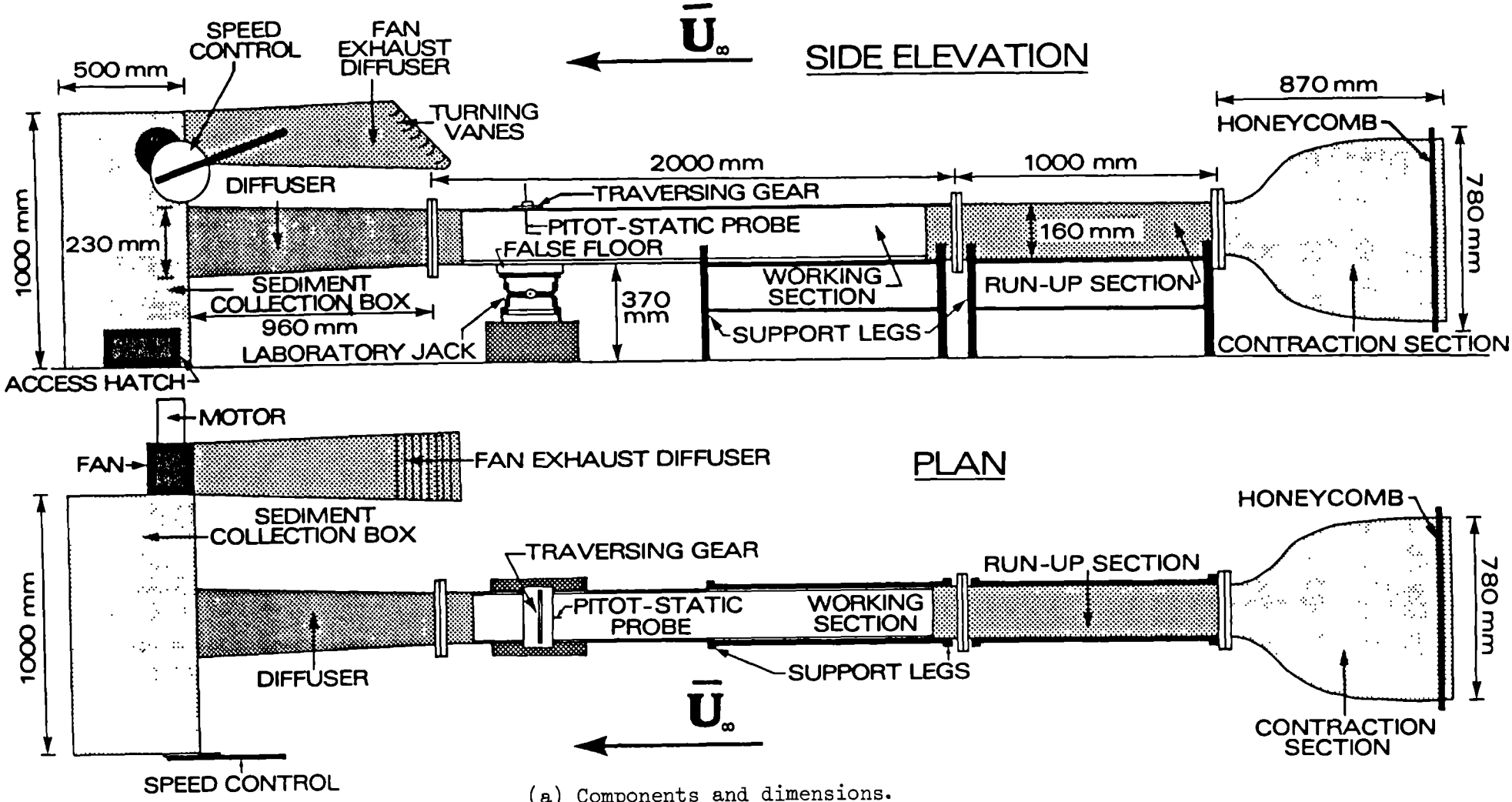

(a) Components and dimensions.

Figure 7.2 (C n't)

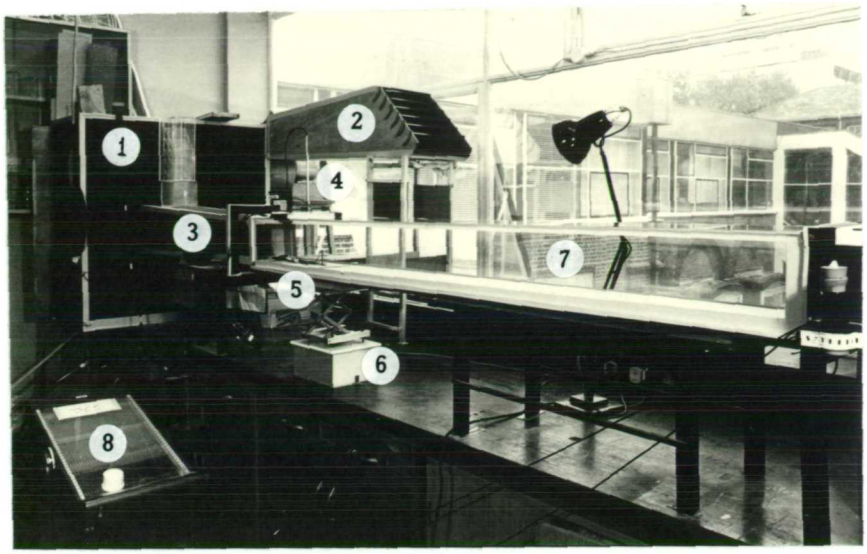

(b) General view of working section (flow from right to left).

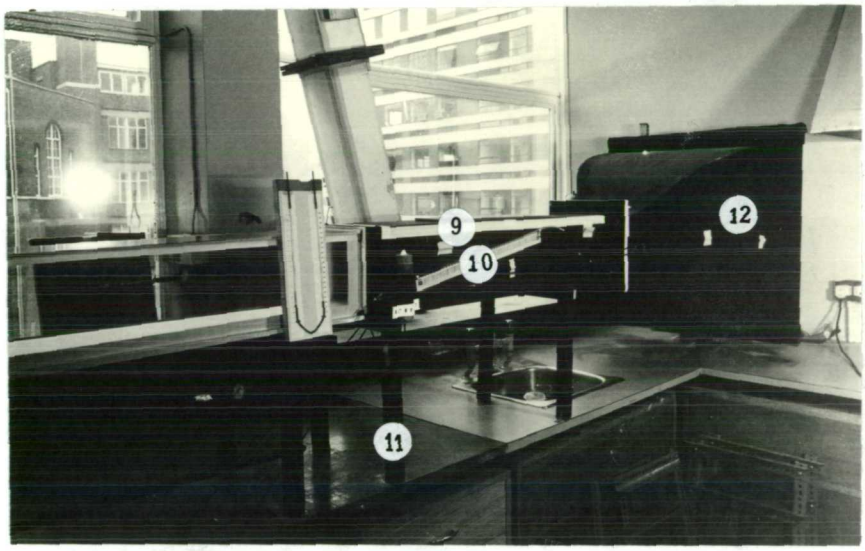

(c) General view of the contraction and run-up sections (flow from right to left).

Legend

1 Sediment collection box.
2 Fan exhaust diffuser.
3 Diffuser.
4 Motor and fan unit.
5 False floor.
6 Laboratory jack.
7 Working section.
8 Multi-tube manometer.
9 Run-up section.
10 Manometer (to monitor contraction reference pressures).
11 Support leg.
12 Contraction section.

Figure 7.3 Apparatus f r direct comparison of aeolian threshold conditions on an impervious/ permeable test bed.

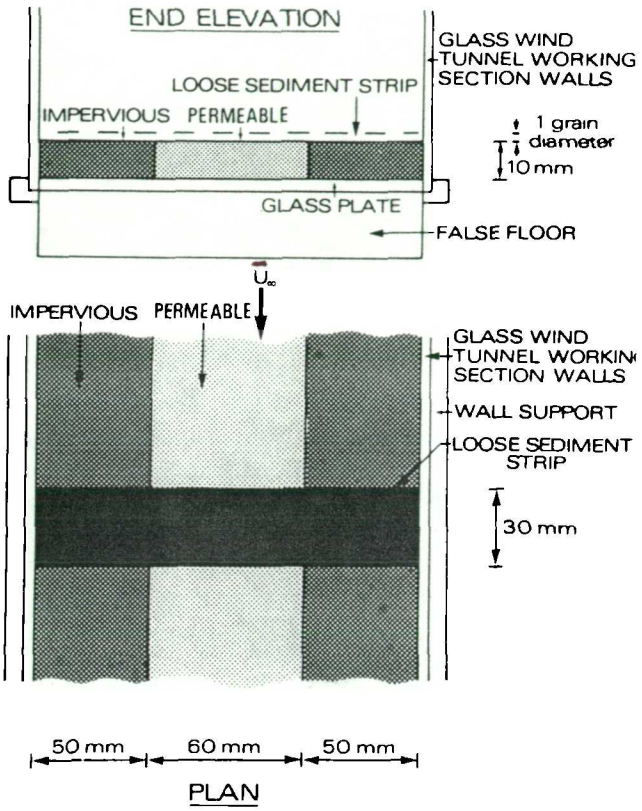

(a) Dimensions.

(b) Close-up of the test bed and the run-up section floor (1.7-1.4mm and 710-600μm ballotini).

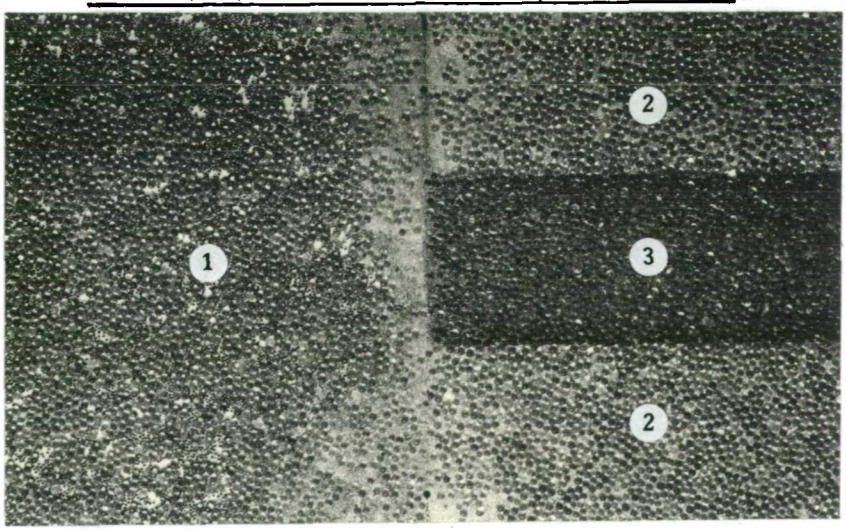

Legend

1 Run-up section floor.
2 Impervious.
3 Permeable.

Figure 7.4 Preliminary experimental configuration used to study aeolian thresholds on an impervious/ permeable test bed.

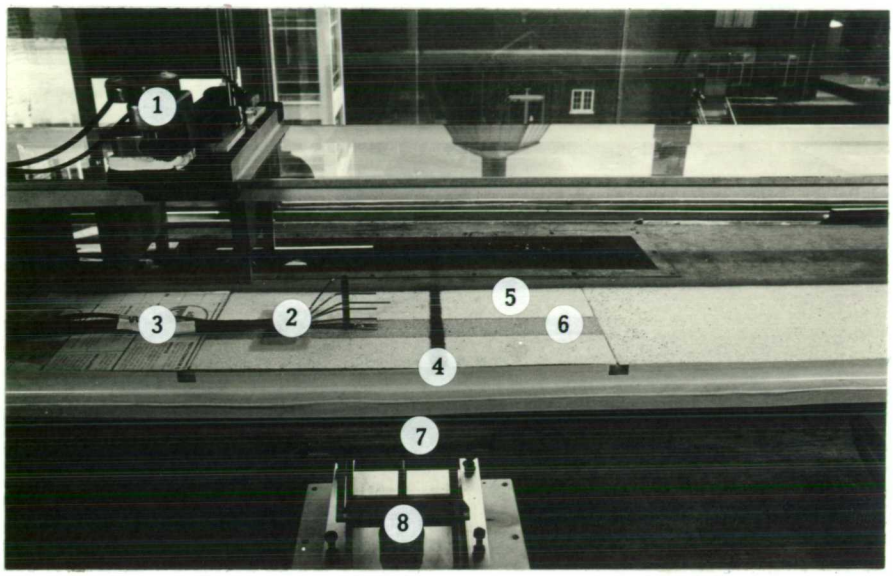

Legend

1 Pitot-tube traversing gear.
2 Pitot-tube array 2.
3 Leads to multi-tube manometer.
4 Test strip.
5 Impervious.
6 Permeable.
7 False floor.
8 Laboratory jack.

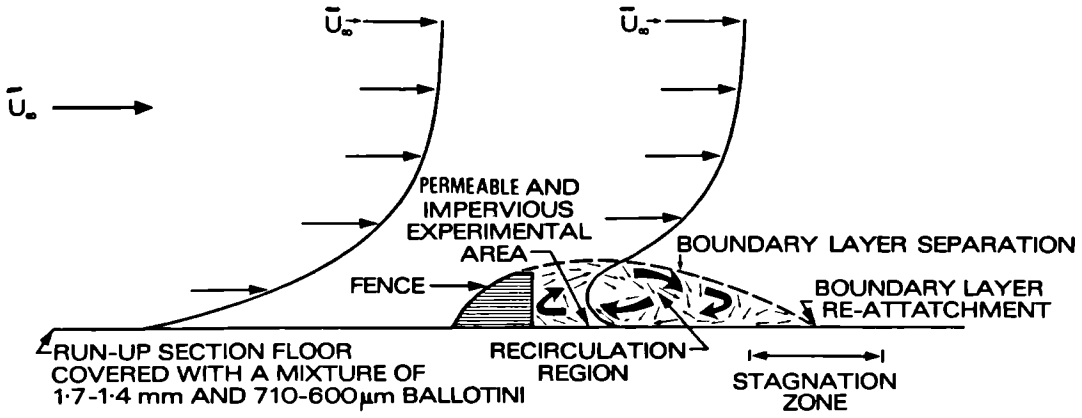

Figure 7.5 Schematic representation of air flow in the wake of a fence.

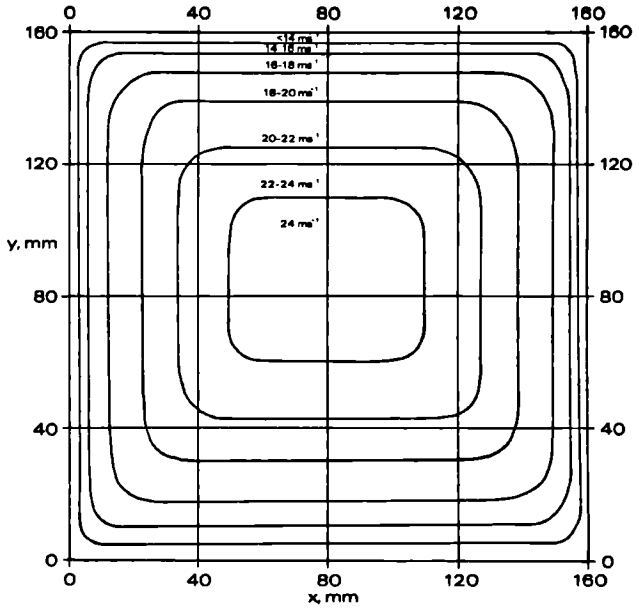

(a) Approximate mean isovels.

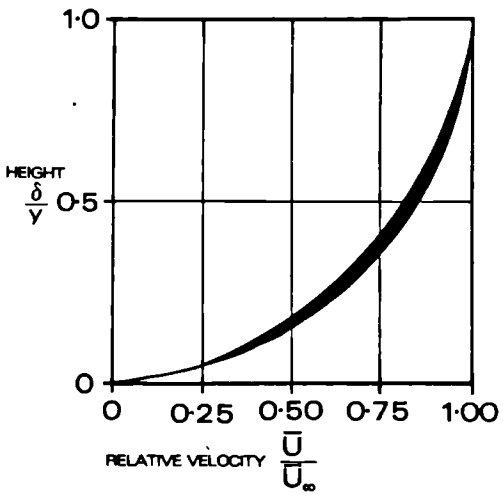

(b) Spanwise boundary layer velocity profile variation on the impervious/ permeable test bed.

Figure 7.6 Summary of flow regime in the working section of the wind tunnel.

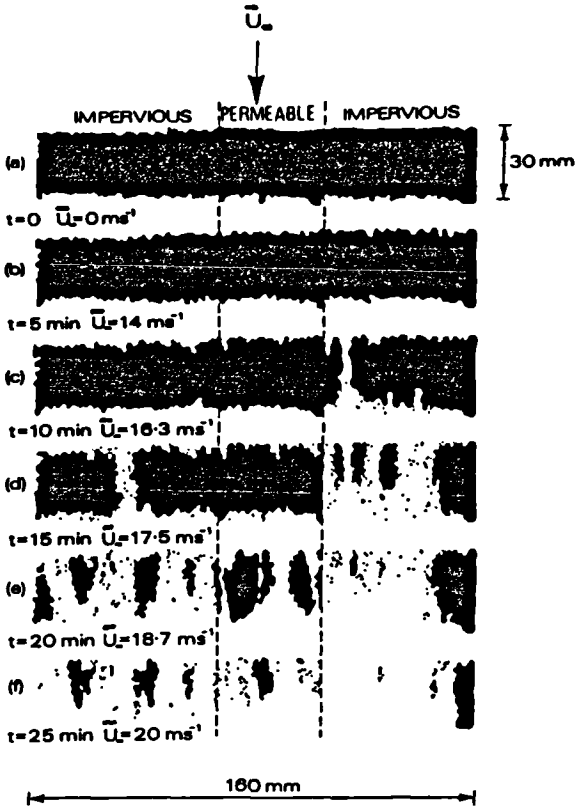

Figure 7.7 Erosion of test strip on impervious/permeable test bed; 710-600μm ballotini.

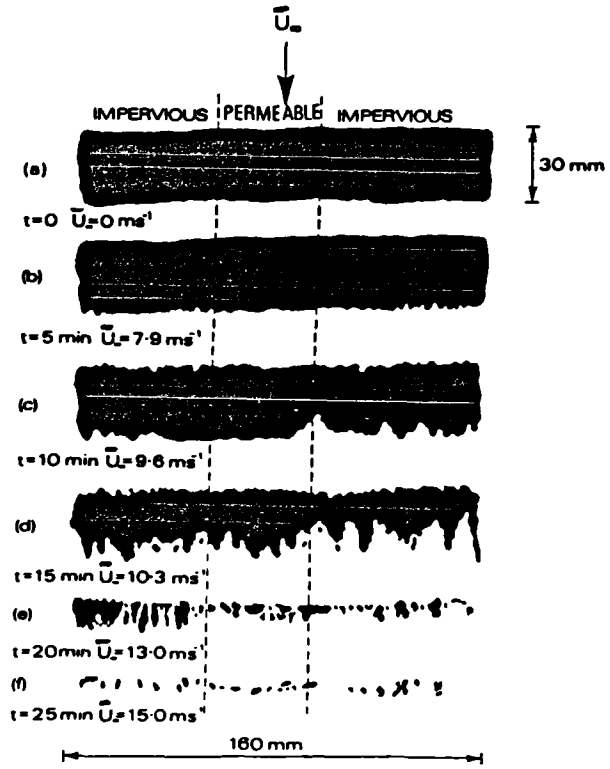

Figure 7.8 Erosion of test strip on impervious/permeable test bed; 180-150μm ballotini.

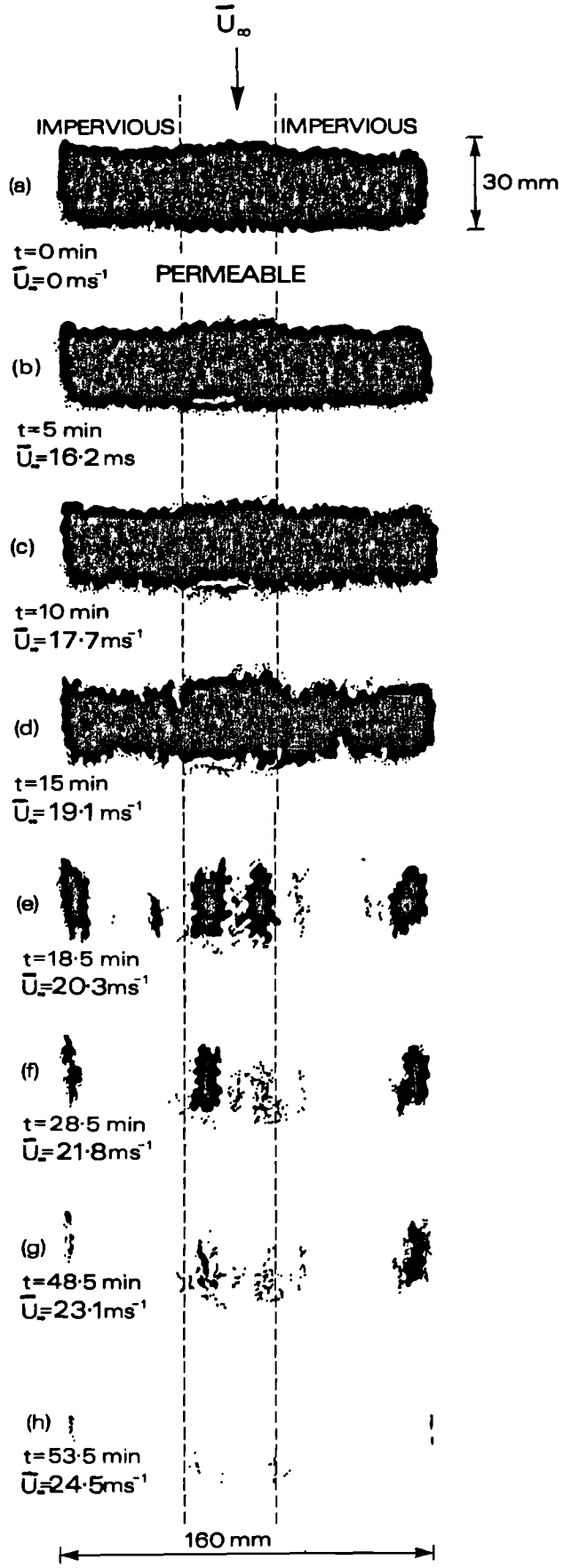

Figure 7.9 Erosion of test strips on the impervious/permeable test bed; 1.7-1.4mm and 710-600μm ballotini mixture.

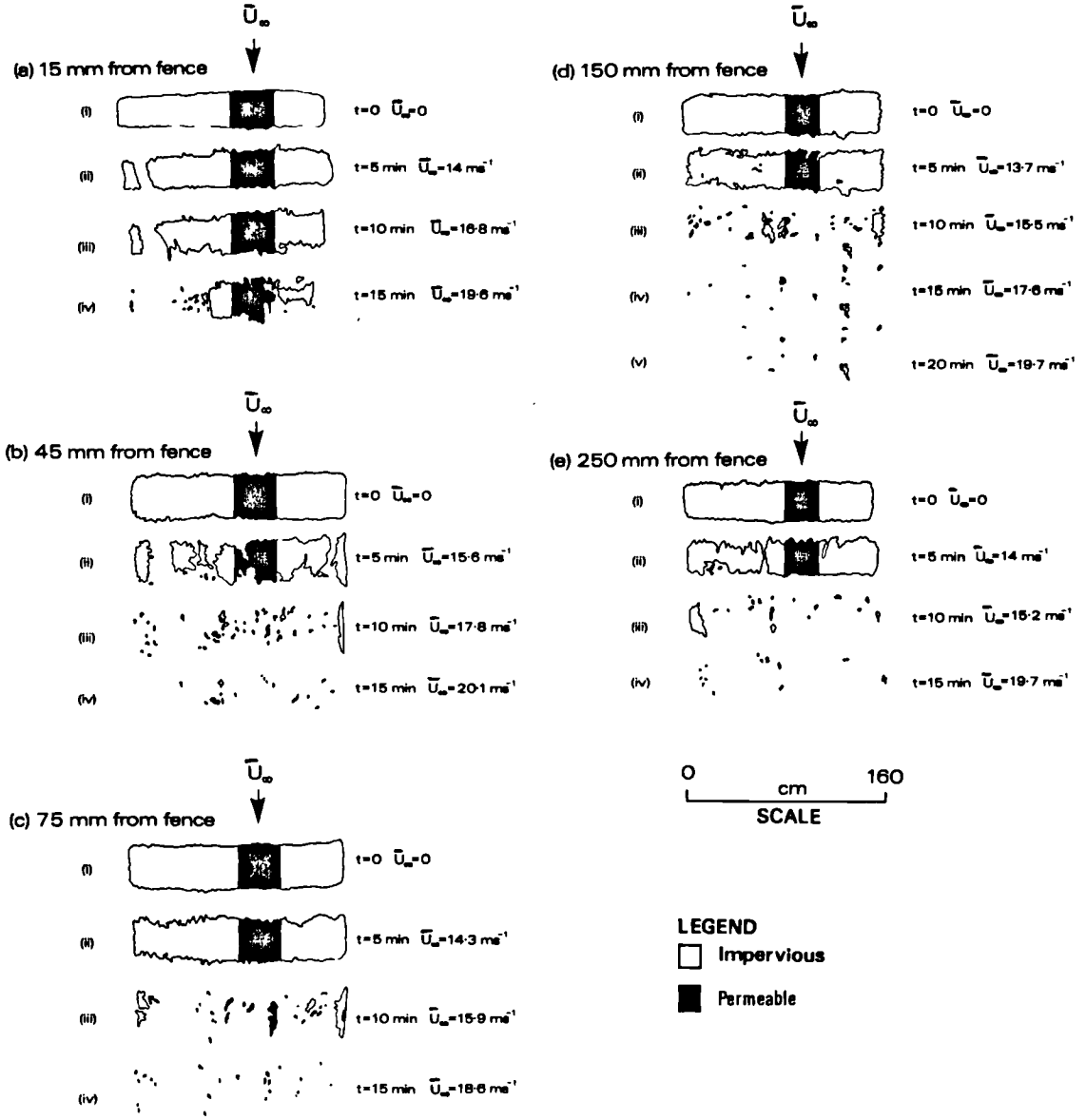

Figure 7.10 Erosion of test strips at stated distances downwind of the fence on the impervious/permeable test bed; 710-600μm ballotini.

CHAPTER EIGHT

Conclusion

8.1 Introduction

In the introduction to his classic book, Bagnold (1941) states that one of the major problems facing the geomorphologist concerned with the interactions between fluids and sediments, has been to "co-ordinate the vast amount of piecemeal work by students of different outlooks in many unrelated fields", (Bagnold, 1941, p. XV). Owing to the dispersion of relevant publications in an extremely broad literature, this problem is one that still confronts researchers and has, if anything, increased with recent developments in the understanding of flow turbulence. More specifically, advances in understanding of the structure of turbulent boundary layers over the past 20 years has increased the perceived complexity of sediment transport phenomena in the minds of geomorphologists and sedimentologists alike, and only recently have the potential applications of this amassed knowledge been fully appreciated. Where the challenge of relating fluid flow phenomena to sediment motion has been undertaken, progress has generally been made in the development of physically realistic models of natural sediment transport processes.

By way of the experimental investigations reported in this thesis it has been possible to examine the interaction between boundary layer flow structure and loose granular material. Although it was not possible to measure air flow characteristics in great detail, the experimental data collected, together with assimilated knowledge from many other detailed investigations of boundary layer flow structure, has provided a means by which to analyse the aeolian threshold condition and to deduce the processes giving rise to aeolian grain entrainment.

The aeolian threshold condition is shown in Chapter 1 to mark a

fundamental boundary between a static sediment bed and an active, energetic mass transport system. Little or no erosion is accomplished by wind unless it is charged with saltating and suspended grains, and no net erosion will occur unless the energy supplied to the surface by the wind exceeds the threshold value associated with a given sediment. The aeolian threshold condition thus defines the critical state between largely static and largely mechanical aeolian processes operating in the natural environment. A number of endogenous and exogenous parameters are identified in Chapter 1 as being the principal controls of the aeolian threshold conditions for a loose, granular material. These include the characteristics of the local flow regime, the size of the grains, and the aerodynamic shape of grains exposed to the flow. In addition, sediment moisture, atmospheric humidity, inter-granular salt bonding, slope, surface roughness and bed permeability are also identified as being factors which may become significant in particular environmental conditions.

The majority of the experimental work reported here is concerned with determination of the relationships between the boundary layer flow structure and grain size at the aeolian threshold condition. In addition, experiments were also conducted to examine the effect of particle shape and bed permeability on threshold conditions, and to examine other aspects of aeolian entrainment processes in the range of flow regimes associated with the developing boundary layer on the surface of a flat plate. In view of the experimental results derived from these investigations, and the insight they have provided into particle-boundary layer interactions at the threshold of motion, it is now possible to discuss the broader implications of this research for entrainment processes in natural environments. In addition, it is also appropriate

to consider how these studies may have helped to resolve some of the problems facing geomorphologists and sedimentologists interested in natural aeolian processes.

During the experimental work it became apparent that certain aspects of the experimental design could be usefully applied in studies of other related aeolian processes. In particular, the flat plate apparatus is considered to be an extremely useful device for producing a continuum of controlled and reproducible boundary layer flow regimes. In view of this, a number of suggestions for further research into aeolian processes using similar experimental apparatus and procedures are made in 8.10.

8.2 Definition of aeolian threshold conditions

The problems associated with defining the aeolian threshold condition are discussed in 1.2 where it is suggested that the subjective criteria used by researchers to specify and identify initial grain motion probably give rise to different interpretations of the aeolian threshold condition for a given sediment. The investigations of initial grain motion from strips and beds of test particles reported in this thesis, however, suggest two means by which the threshold of motion in granular materials may be objectively defined.

By eroding strips of test material it was possible to deduce the relationship between the percentage of the strip area uneroded and the mean shear velocity, $\bar{U}_*$. When these data were plotted in graphical form they produced characteristic asymptotic erosion curves which clearly illustrate the range of $\bar{U}_*$ values required to erode a given strip of

test material on the surface of the plate (e.g. Figure 4.19). Using these graphs it is shown that the $\bar{U}_*$ value associated with the erosion of a given percentage of strip area could be used to define a specified amount of erosion. As these graphs are derived from the photographic record of erosion and not from visual observation, they provided a range of objective definitions of the aeolian threshold condition for a given test material. These definitions range from 'motion of the first few grains' (more than 99% of the strip is uneroded) to the ultimate threshold condition (no strip material remains on the surface of the plate). Using this technique, it is no longer necessary to rely on conventional, visual entrainment criteria and the accuracy with which the aeolian threshold condition can be expressed is considerably improved.

In the case of beds of particles, it was shown that entrainment generally occurred progressively from the downwind edge and that after a certain period of erosion at a constant wind speed, entrainment ceased, leaving a portion of the test bed uneroded (see Figure 6.5). It is argued in Chapter 6, that under these conditions grains defining the downwind limit of the test bed are in equilibrium with the prevailing flow conditions, and as such, may be considered to be at the threshold of motion. The observed rapid erosion from the downwind edge of the bed following a small increase in wind velocity confirms that this assumption is correct. Like the definition above, this technique permits a precise and objective definition of aeolian threshold conditions, provided that the local flow conditions which characterize initial grain motion can be measured.

Both these experimental techniques provide standardized methods by which to determine objectively the aeolian threshold condition,

regardless of sediment characteristics. In addition, they allow threshold conditions to be related directly to specific, local flow structure and can thus be used to define initial motion in granular material in air or water.

Grass (1970) defined the threshold condition associated with fine sand in water in terms of a critical degree of overlap between the probability distribution of instantaneous bed shear stress associated with the local flow regime $P(\tau)$, (or $P(U_*)$), and the probability distribution of threshold bed shear stress ascribed to each individual particle in a given test sample $P(\tau_T)$, (or $P(U_{*T})$), (see 2.5.3). This definition accounts for the apparently random interactions between peak shear stress events close to a sediment bed and the range of grain susceptibilities to erosion brought about by differences in particle characteristics and exposure. In practice, use of this definition requires knowledge of both the $P(U_*)$ and $P(U_{*T})$ distributions. The characteristic asymptotic curves of strip erosion on the plate are shown to reflect the $P(U_{*T})$ distribution associated with a given granular material, (4.5.4(a)). In this investigation, however, it was not possible to determine the characteristic $P(U_*)$ distribution associated with the local flow regime from pitot-tube velocity data. It was, therefore, not possible to examine directly the ways in which the $P(U_*)$ and experimentally determined $P(U_{*T})$ distributions inter-relate at the aeolian threshold condition. However, the experimental results of this study suggest a number of ways in which the $P(U_*)$ and $P(U_{*T})$ distributions are likely to interact and thus they provide the basis for a useful model of aeolian threshold conditions and initial grain motion.

The entrainment model proposed by Grass (1970) does not in

itself provide a direct solution to the practical problems of determining the critical shear velocity required for entrainment and subsequent transport of a sediment by wind as, by definition, no grain motion occurs at the threshold. For aeolian transport to ensue, there must be a critical degree of overlap between the $P(U_*)$ and $P(U_{*T})$ distributions. In water, the amount of sediment transport associated with a given flow velocity will be a function of the degree of overlap between the $P(U_*)$ and $P(U_{*T})$ distributions as entrainment results principally from fluid shear, ballistic impact effects being relatively much less significant. In air, however, the degree of overlap between $P(U_*)$ and $P(U_{*T})$ is considered to be critical as it will determine whether or not aeolian transport will be sustained by the wind once the first few grains are set into motion by the peak fluctuations of the $P(U_*)$ distribution. Aeolian transport will only be sustained if the entrained grains are sufficiently energetic and numerous to cause downwind avalanching, and if the frequency of U_* fluctuations in excess of the impact threshold is sufficiently high to provide the energy necessary to exceed the solid shear resistance of the saltating grain population. The self-regulation of the aeolian transport system suggested by Owen (1964), (see Figure 1.4), would appear to be a mechanism by which this condition may be achieved.

Although this study has not provided any information on the $P(U_*)$ distribution associated with boundary layer flow on a rough surface, or on impact threshold conditions, it has revealed a simple and effective means by which to determine the $P(U_{*T})$ distribution associated with a granular material of specified size range. The experimental technique used to determine this distribution is applicable in any boundary layer flow regime and may be applied in the study of the

initial motion characteristics of any loose, granular material regardless of its physical properties. Further progress in the understanding of the interactions between granular material and the wind at the threshold of grain motion requires, therefore, an improvement in the knowledge of air flow and turbulence characteristics over rough, granular surfaces, both in the laboratory and in the field.

8.3 The role of turbulence in aeolian entrainment

Measurements of the mean threshold shear velocity associated with entrainment from strips of test material on the surface of the plate revealed that, in general, $\bar{U}_{*T}$ values decreased with increasing distance downwind from the leading edge of the plate. It is argued that because the force required to entrain a given particle must be the same irrespective of its location, the peak fluctuations in bed shear velocity responsible for entrainment must also be the same at any position on the surface of the plate. Thus, the downwind reduction in $\bar{U}_{*T}$ values measured in this study must reflect changes in the $P(U_*)$ distribution of the local boundary layer flow regime. Such changes are shown to be associated with the downwind increase in flow Reynolds number and are manifest by a downwind increase in the positive skewness of the $P(U_*)$ distribution. It was not possible to investigate whether $\bar{U}_{*T}$ values reduced still further at distances over 130cm from the leading edge of the plate owing to the problems of the static pressure gradient in the boundary layer induced by the tail section (see 3.4.3). Although $\bar{U}_{*T}$ values were found to decrease at each successive downwind study site, the rate of decrease tended to decline as the downwind distance increased. Had the plate been longer it is suggested that $\bar{U}_{*T}$ would have been found to approach some minimum value asymptotically. In the context of

the entrainment model proposed by Grass (1970), this also implies that the positive skewness of the $P(U_*)$ distribution may also attain a maximum value in this region. Flow at this location may, therefore, be described as being 'fully turbulent'.

It is likely that the positive skewness of the $P(U_*)$ distribution associated with the natural wind blowing over a sediment will also attain a maximum value, providing the fetch is long enough. It is conceivable, therefore, that in certain circumstances, $\bar{U}_{*T}$ values may be modified by differences in the characteristic $P(U_*)$ distribution associated with the atmospheric boundary layer. Even more likely, however, are spatial differences in the $P(U_*)$ distribution associated with the internal boundary layer close to the grains. Spatial differences in the $P(U_*)$ distribution may also arise when the wind blows over surfaces with different roughness characteristics (e.g. a ripple sand surface and a flat bed), and thus may give rise to spatial differences in entrainment thresholds.

The above discussion casts serious doubts on the suitability of $\bar{U}_{*T}$ as a parameter with which to express forces acting on grains at the threshold unless the $P(U_*)$ distribution attains the maximum degree of positive skewness possible in given conditions (i.e. the flow is 'fully turbulent'). In view of this, it is suggested that use of $\bar{U}_{*T}$ as a threshold parameter greatly oversimplifies an extremely complex situation and that aeolian threshold conditions are much more appropriately expressed in terms of a critical degree of overlap between the local characteristic $P(U_*)$ and $P(U_{*T})$ distributions.

8.4 Grain exposure and aeolian threshold conditions

Careful preparation of erosive test strips and beds ensured that no single grain projected more than one grain diameter above the mean, non-erosive surface of the plate. This experimental arrangement is significantly different from those used by other workers in studies of aeolian threshold conditions where conventionally initial grain motion from a loose, flat bed of sediment has usually been considered. In this case, the exposure of individual grains is significantly less than that associated with the test strips and beds used in the experiments reported here and $\overline{U}_{*T}$ values, in consequence, may be larger. However, at the scale of individual grains, a natural aeolian sediment bed typically consists of a haphazard arrangement of particles so that particles at the surface exhibit a range of exposures to the flow by virtue of their variable underlying support geometry. Further, spatial variations in the degree of grain exposure may also occur at the scale of aeolian bedforms (e.g. ripples and dunes, Table 1.1). In this case, grains located at the crest of such bedforms may have a greater susceptibility to erosion than grains located in more sheltered sites in the bedform troughs and the lee slopes. In view of the significance of grain exposure in the determination of $\overline{U}_{*T}$ values for a given sediment, it is likely that threshold shear velocities of natural sediments are over-estimated when determined using flat, erosive beds in the laboratory. Strips of test material, however, because of their high degree of exposure, provide a means of determining the minimum $\overline{U}_{*T}$ values likely to be associated with a haphazard arrangement of grains. This experimental arrangement is analogous, therefore, to the aeolian threshold conditions likely to arise on the crest of aeolian bedforms or on a natural, flat sediment surface characterised by differing degrees of grain exposure.

It is considered above that $\bar{U}_{*T}$ values associated with strips of a given test material would continue to decrease with increasing distance downwind beyond the furthest measurement station and would slowly approach a constant value. It is shown in Chapter 5 that $\bar{U}_{*T}$ values for strips of test material at the most downwind measurement station were approximately the same as those determined by previous workers using flat test beds. This suggests, therefore, that had $\bar{U}_{*T}$ values been determined at sites further downwind, they would have been lower than $\bar{U}_{*T}$ values reported in the literature and, more significantly, would be less that the $\bar{U}_{*T}$ values predicted by the empirical equations discussed in 1.5. In view of these results it may be that the aeolian threshold and entrainment conditions associated with natural sediment beds are lower than those predicted by the empirical equations quoted. It is also conceivable that $\bar{U}_{*T}$ values may be lowered still further by the increase in U_{*I} values associated with increased flow turbulence over a rippled sediment bed. As a result, it seems unlikely that $\bar{U}_{*T}$ values determined in laboratory wind tunnel studies can be related directly to those pertaining to natural sediment beds and surface winds.

A further aspect of grain exposure relevant in this context is the relationship between grains and the viscous flow very close to the surface. In the same flow conditions, a large grain will project further from the bed than a small grain and will, in consequence, be subjected to larger forces by virtue of its exposure. At the threshold, therefore, these larger forces may compensate for the increased weight of larger grains and suppress the expected increase in threshold shear velocity. This mechanism is clearly evident from the studies of strip erosion on the plate where it was found that the $\bar{U}_{*T}$ value required to entrain

strips of 180-150μm ballotini was higher than that for 355-300μm ballotini at the same location and only slightly lower than that for 710-600μm ballotini (Table 4.8 to 4.10). It is believed that the varying degrees of viscous sublayer protection afforded to these various test strips was substantially different at this location on the surface of the plate and gave rise to the marked increase in $\overline{U}_{*T}$ values for 180-150μm ballotini. This results provides important evidence of the role played by grain exposure in determining aeolian threshold conditions.

Further evidence of the significance of grain exposure in determining aeolian threshold conditions is provided by the theoretical consideration of grain projection heights in both laminar and turbulent boundary layer flows on a smooth surface in threshold conditions (4.5.3). Although the results of this analysis cannot be related directly to flow on rough surfaces, they do illustrate clearly that the forces acting on grains at the threshold are governed to a large extent by their exposure.

8.5 Published and experimental aeolian threshold data

The scatter associated with published aeolian threshold data is examined in Chapter 5 using a number of both 'restricted' and 'universal' empirical relationships. Critical examination of these relationships, and experimental evidence derived from the present study revealed that a number of factors, acting quite independently of one another, give rise to the differences in reported aeolian threshold values.

Flow in the test sections of most wind tunnels used in previous studies of aeolian threshold conditions has normally been assumed to be

fully turbulent (i.e. the maximum level of flow turbulence possible within the confines of the wind tunnel). In these conditions, U_{*I} values are likely to be at a maximum and thus will give rise to the minimum $\overline{U}_{*T}$ value for a sediment (see 8.3). However, it is likely that these conditions are not replicated by every wind tunnel owing to the range of tunnel designs used by different workers (Table 1.3), and thus the intensity and the spatial and temporal frequency of U_{*I} events is likely to differ from one working section to another. In view of the experimental results presented in Chapter 4 it is concluded that these differences contribute, in part, to the differences in $\overline{U}_{*T}$ values reported by various authors.

Other factors identified as contributing to variations in reported $\overline{U}_{*T}$ values are: differences in grain exposure; differences in the shapes of test particles and hence in their characteristic aerodynamic drag coefficient; and differences in inter-particle cohesion caused both by external factors, such as moisture and humidity, and by the physical characteristics of the particles themselves. In addition, failure on the part of most researchers to define objectively and identify consistently a pre-determined degree of bed motion has led to inadvertent misinterpretations of the aeolian threshold condition. Owing to the limited experimental data provided by authors, it is not possible to assess the relative contributions of these factors to the scatter clearly evident in published data about both the 'restricted' and the 'universal' empirical threshold curves (Figures 5.2 to 5.6). However, in view of the experimentally-derived $\overline{U}_{*T}$ values for strips of ballotini on the surface of the plate, it is thought that differences in flow characteristics and incipient motion criteria provide the most significant sources of variation in published aeolian threshold data. It

may be concluded, therefore, that the controlled and reproducible flow conditions associated with the developing boundary layer on the plate, and the objective threshold definitions (8.2), provide a means by which to reduce the number and complexity of interacting variables which must be considered and thereby a means of simplifying the laboratory determination of aeolian threshold conditions.

8.6 Aeolian entrainment processes

Visual observation and medium/high-speed movie film of grain oscillation and entrainment in flow conditions approximating to the threshold provided valuable insight into several controversial aspects of initial grain motion by wind. The oscillation of grains marks a critical boundary between stable and unstable bed conditions and is considered to be indicative of aeolian threshold conditions both in the laboratory wind tunnel and in the field (see 1.2). A number of equivocal hypotheses have been proposed in the literature to explain grain oscillation and are reviewed by Jones (1981). These include: self excitation arising from vortex shedding; wake interaction and vorticity amplification; and self excitation arising from the interactions between individual grains and intense flow turbulence generated in the bursting cycle identified as a feature of turbulent boundary layer flows. It is evident from the present study that the geometric arrangement of supporting grains plays a crucial role in grain oscillation phenomena and was observed to determine whether or not rapid particle oscillation occurred in a spanwise or streamwise direction in response to rapidly fluctuating displacement forces.

Grain oscillation was recorded in both laminar and turbulent

boundary layer flow regimes on the surface of the plate but the duration of oscillation was found to be significantly longer in essentially laminar flow. The fact that grain oscillation occurs at all in laminar flow immediately discounts the possibility that the motion is induced by flow turbulence. It seems likely that grain oscillation results primarily from vortex shedding phenomena in critical flow conditions as defined by the Strouhl number. In laminar flow, it is considered likely that these critical conditions persist for a longer time than in turbulent flow and, as a result, the duration of oscillation is also likely to be longer. It is also possible, however, that oscillation may be reinforced by interactions between grains and the wakes shed by upwind particles. Further, in turbulent flow, the temporary adverse pressure gradients imposed on the bed by relatively high speed fluid sweeps may also contribute in part to the momentary displacement forces necessary for grain oscillation at the threshold.

The detailed mechanics of aeolian entrainment were not examined in this study, but visual observations, cine film and indirect experimental evidence reported in the previous chapters indicate some of the processes involved. The initial rise of grains near vertically from test beds during entrainment as widely reported in the literature, (e.g. Chepil, 1945(b); Bisal and Nielsen, 1962; Greeley and Iversen, 1985), was not observed during these studies. On the basis of the experimental evidence it is considered that in flow conditions just in excess of the threshold, particles are simply pushed along the bed by aerodynamic forces and are thereby made to roll up and over other downwind grains. Subsequently, increasingly violent downwind collisions cause particles to rebound away from the bed and acquire progressively greater bounce heights at each successive collision. In this way, grains eventually

attain typical saltation trajectories.

However, the experimental evidence discussed above indicates that the flow conditions on the surface of the plate were not as turbulent as those associated with flow in the test sections of wind tunnels used by previous workers. It is still possible, therefore, that in highly turbulent flow, grains may leave the bed in near vertical trajectories in special circumstances. Such circumstances may arise as a result of a sudden drop in static pressure close to the grains caused by energetic turbulent bursting so that susceptible grains are simply 'plucked' from the bed. However, no evidence of this process was observed during the present investigations using test strips and beds on both permeable and impervious surfaces. Indeed, initial grain motion in the form of rolling and bouncing observed during these investigations is consistent with the observations of Bagnold (1941) who states "a foot or so downwind of the point at which rolling began, the grains could be seen to have gathered sufficient speed to start bouncing off the ground; and over the remainder of the floor the 'sand cloud' effect of true saltation was maintained", Bagnold (1941, p.33).

Recent advances in the understanding of the apparently chaotic fluid motions associated with a shear flow such as the turbulent boundary layer have revealed organised, hierarchical fluid motions ('coherent structures') that may be characterised by approximate length scales and persistence times. The majority of surface shear stress in a turbulent boundary layer is generated in the bursting cycle. This subsequently diffuses away from the bed in a complex hierarchy of interacting vortex loops which act as a powerful mechanism for momentum transfer throughout the boundary layer (see 2.5.2). The ejection of low momentum fluid from

regions close to the bed and its replacement by high momentum fluid from regions away from the bed in the bursting cycle generate high bed shear stresses which are found to correlate with peak U_{*I} values close to the surface. Experimental evidence reported by Grass (1970) shows that particle motion in water can be initiated by these fluid inrush events (or sweeps) which were observed to transport the loose bed material downstream violently.

The susceptibility to erosion of grains in a strip did not differ significantly along the span of a strip, and thus the fairly regular spacing of eroded gaps in a strip (e.g. Figure 4.11(b) and (f)) indicates that the spatial distribution of threshold shear stresses on the surface of the plate was organised in some way. In 2.5.2 it is shown that flow close to the bed in a turbulent boundary layer consists of alternate 'streaks' of relatively high and relatively low momentum fluid, and that the downwind passage of fluid sweeps in the bursting cycle (responsible for peak bed shear stress generation) is largely governed by the spatial distribution of the low-speed streaks. As such events are considered to be the most likely mechanism responsible for grain entrainment, the experimental evidence indicates that the recorded pattern of strip erosion reflects the spatial distribution of fluid sweep events on the surface of the plate.

It is considered that the small crenations frequently eroded in the upwind edge of a strip in turbulent flow indicate areas where the local shear velocity values exceed the threshold. It was observed that these crenations enlarged as wind speed was increased so that gaps were eroded through the strip, often leaving small islands of loose grains on the surface of the plate. It was also observed that the number and

frequency of gaps eroded through the strips increased in response to an increase in wind speed. This observation is consistent with the hypothesis above as it is well known that the spacing of low-speed streaks decreases as the Reynolds number increases, thereby giving rise to a corresponding decrease in the spacing between sites of downwind sweep passage.

However, in studies associated with the calibration of the Preston tube (e.g. Patel, 1965) on a flat plate, more or less regularly spaced spanwise variations in mean surface shear stress have been noted in turbulent boundary layers. These variations are considered to originate from flow disturbances caused by minute surface imperfections on the leading edge. It is unclear whether these variations occur in most real situations or whether they are confined to flows downwind of an identifiable leading edge. It is possible, therefore, that the recorded patterns of strip erosion in turbulent boundary layer flows reflect spatial variations in shear stress induced by exposed grains on the leading edge of the plate. However, regardless of whether these variations are caused by this mechanism or by organised sweep passage, the fact that semi-organised spatial variations in threshold shear stresses are associated with turbulent flow on granular surfaces is an important finding in the context of understanding aeolian threshold conditions.

Erosion patterns associated with strips of particle less than 180μm in diameter at positions close to the leading edge of the plate, however, were found to be quite different from those described above (e.g. Figure 4.13(a)). In view of this, it is considered that the interactions between the boundary layer flow and the loose strip material

were also different. As the boundary layer flow in the region extending 40cm downwind from Station A over 180-150μm ballotini and aeolian sand was shown to be essentially laminar in character, it is suggested that threshold shear stresses were probably distributed fairly evenly along the entire strip width. In this case grain motion should have occurred approximately en masse. Figures 4.13(a) and 4.14(a) show that erosion occurred over relatively large areas of the test strips and suggest, therefore, that in laminar flow, entrainment is accomplished by threshold shear stresses distributed fairly evenly on the surface of the plate.

Figures 4.10(b) and 4.13(d), depicting erosion sequences at the furthest downwind study sites, show that the frequency of eroded gaps in the strips increases as particle size decreases. It thus seems likely that on rough surfaces, the spatial distribution of threshold shear stresses is also partially controlled by the dimensions of roughness elements themselves.

In the case of the atmospheric boundary layer, variation in the spatial distribution of shear stresses on a bed of sediment are also likely to occur and may give rise to spatial differences in aeolian threshold conditions and rates of entrainment. These differences may be even more distinct on rippled beds or other bedforms. Visual evidence that spatial variation in aeolian entrainment may occur on a natural, loose sediment bed is given by the familiar 'sand streamers' clearly evident on unconsolidated sediments in windy conditions. However, it is unclear whether these phenomena are related to sweeping events directly or to the powerful secondary flow vortices in the atmospheric boundary layer close to the surface. They could conceivably result from the joint action of both.

8.7 Rate of aeolian entrainment

In the majority of studies reported in Chapter 6, the rate of aeolian entrainment at threshold wind speeds was found to be an inverse exponential function of both time and free stream wind velocity, irrespective of the test material or position on the surface of the plate. However, in the case of test strips, the rate of erosion was found to be significantly different at different positions on the plate despite the wind speed being sufficient to erode completely a given strip in each case. These differences are thought to arise from differences in the intensity and spatial and temporal frequency of peak shear stress events associated with the developing boundary layer on the plate. These results, therefore, provide additional evidence that the intensity of flow turbulence is the principal factor governing aeolian entrainment, and in the natural environment, differences in the turbulence structure of natural winds may lead to spatial variation in the rate of aeolian entrainment.

The results also confirm that interactions between wind and loose granular material at the threshold is essentially probablistic in nature. Increasing the wind speed to a value determined by experiment to be just sufficient to entrain all material in a test strip did not result in instantaneous erosion of the strip. As implied by the inverse exponential relationship between the percentage of strip area uneroded and time, erosion proceeds very rapidly at first and decreases as less and less material is available for erosion.

Differences in the rate of test strip erosion at different locations on the surface of the plate could be interpreted as reflecting

different degrees of overlap between $P(U_*)$ distributions associated with the local flow regime and the $P(U_{*T})$ distribution associated with a given test material (Figure 6.10). Strips located at the downwind end of the plate eroded significantly faster than strips sited near the leading edge. Further, the threshold free stream wind velocity required to erode all the material in the test strips was found to decrease downwind. It is considered that, although the value of peak shear velocity capable of completely eroding a given test strip at any location on the plate must be the same, the spatial and temporal frequency of peak shear stress events increases with distance downwind. This gives rise to greater rates of aeolian entrainment at downwind localities on the plate, despite the decrease in the threshold free stream wind speed in this direction.

In view of the experimental results, this explanation is considered to be the most plausible in the circumstances. The relationship shown in Figure 6.10 also implies that the more frequent, lower intensity threshold shear velocity events are responsible for the majority of aeolian entrainment in flow conditions just in excess of the threshold, irrespective of the test material. At the global scale, Warren (1979) also considers that for time-averaged conditions the majority of aeolian transport is accomplished by the "moderately fast and moderately common winds", Warren (1979, p.334).

The erosion of test beds on the surface of the plate is also found to be an inverse exponential function of both time and free stream wind velocity. During active erosion, the majority of entrainment occurred from the downwind edge of the bed. After a certain time erosion ceased, leaving a portion of the test bed uneroded on the surface of the

plate. In these conditions the bed responded quickly to an increase in wind speed, with a portion of material from the downwind edge of the bed being eroded rapidly. However, the length of time taken for an equilibrium configuration to evolve was found to depend on the distance downwind from the leading edge. The equilibrium configuration was attained much more quickly at downwind sites than at sites closer to the leading edge. This result would also seem to reflect a downwind increase in the intensity of air turbulence in the boundary layer (Figure 6.10).

These results provide, therefore, additional evidence that spatial differences in the rate of aeolian entrainment could arise on natural sediment surfaces by virtue of spatial differences in the intensity of air turbulence, irrespective of the physical characteristics of the sediment. The results of strip erosion experiments also imply that the majority of aeolian entrainment is accomplished by the more frequent, lower intensity threshold shear velocity events associated with a characteristic $P(U_*)$ distribution of the flow. Together, these results indicate that in flow conditions just in excess of the threshold, entrainment is best expressed in probability terms.

8.8 Aeolian threshold conditions on permeable and impervious beds

No differences could be detected in boundary layer profiles over impervious and permeable test beds of the dimensions and depths used. Similarly, no detectable differences in aeolian threshold conditions were observed on these surfaces (see Chapter 7). No significant differences in aeolian entrainment processes were recorded and, in general, initial grain motion was the same from impervious and pérmeable beds as those observed for test strips and beds on the impervious surface of the flat

plate. In view of these experimental results it seems likely that bed permeability is not a significant factor in determining the aeolian threshold condition.

However, the evidence from Zippe and Graf (1983) of a slight increase in boundary resistance on a permeable surface means that it is possible that small differences in $\overline{U}_{*T}$ values may result if sediment beds of long lengths are composed of uniform size-sorted sediments characterized by variable geometric grain packing and hence by variable permeabilities. The resultant spatial variation of permeability may render some areas of a sediment bed more susceptible to erosion than others. Such variation of bed permeability was not detectable on the short-length test beds used in this study, however. Further, the ejection of fluid from between grain interstices during the bursting cycle, as observed by Grass (1971) in water, may also occur in air and may give rise to additional net lift forces on susceptible grains at the threshold condition. However, in view of the evidence presented in Chapter 7, it seems this phenomenon had no detectable effect of aeolian threshold in these experiments.

8.9 Suggestions for further research

In the experimental investigations of aeolian threshold conditions reported in Chapter 4, it was only possible to study particles from four size ranges. It is suggested, therefore, that useful additional data pertaining to aeolian thresold conditions could be obtained by repeating those experiments using other particle sizes in order to extend the range of grain sizes considered and to confirm the findings of this research. Further, as very little is known about the

range of particle sizes within a given test sample, it is also thought that the use of more closely graded materials in future studies would enable more precise determination of relationships between particle size and threshold flow conditions to be established. In particular, this would allow comparisons to be made between the distribution of $P(U_{*T})$ and grain size/texture. Similarly, it is suggested that future studies should examine the aeolian threshold conditions associated with other characteristic particle shapes using other crystalline materials. However, owing to the problems of moisture adsorption encountered during the present investigations into the effect of particle shape using sugar and salt crystals, it is essential that a range of materials is chosen that exhibits characteristic size-shape properties but is unaffected by atmospheric humidity. It may then be possible to assess objectively the effect of particle shape in determining the aeolian threshold condition.

It is suggested that the aeolian threshold condition may be defined most appropriately by a critical degree of overlap between the characteristic $P(U_*)$ and $P(U_{*T})$ probability distributions associated with the boundary layer flow regime and the test material, respectively. To achieve this objective, it would be necessary to develop a stochastic model capable of predicting both (a) the spatial and temporal occurrence of threshold sweeping events on a given sediment surface and (b) the response of that sediment to the relatively high momentary shear stresses associated with these events at the threshold condition. It is shown that the $P(U_{*T})$ distribution for a given test material can be obtained relatively simply from the asymptotic erosion curve derived from the erosion of a test strip on the surface of the plate. It would seem that this technique could be applied also to natural aeolian sediments characterized by a range of particle sizes, and thus could provide a

means of defining objectively the appropriate aeolian threshold condition for such sediments. If the factors controlling the spatial and temporal distribution of threshold shear stress events could be determined, it would then be possible to develop a probablistic model of aeolian grain entrainment.

In 8.4 it is suggested that the flat plate used in the present study was of insufficient length to ensure the development of the maximum flow turbulence intensity possible for a given free stream Reynolds number and surface roughness value. In consequence, the $\bar{U}_{*T}$ values determined for test materials on the surface of the plate are believed to be higher than $\bar{U}_{*T}$ values associated with fully developed turbulent flow. It is suggested, therefore, that studies should be undertaken to assess the factors which govern the development of maximum turbulence intensity on a given surface so that in future studies of aeolian threshold conditions it would be possible to conduct experimental work in identical flow regimes regardless of test particle characteristics. In this way it may be possible to reduce considerably the variation in $\bar{U}_{*T}$ values caused by differences in the local boundary layer flow regime.

Two means of defining objectively the aeolian threshold condition have been developed during these present investigations. Neither definition relies on subjective visual assessment of a degree of initial grain motion in critical flow conditions, and both are specific to a given test material and the boundary layer flow regime. It is suggested, therefore, that detailed measurements of the fluctuating local shear stresses associated with strips and beds of test material on the surface of the plate would serve to improve the precision of these definitions.

In this context the largest gaps in present knowledge of aeolian threshold conditions are (a) lack of field evaluation of $\overline{U}_{*T}$ values under natural conditions and (b) quantitative measurements of atmospheric boundary layer structure close to natural sediment surfaces. Previous field evaluations of aeolian threshold conditions have involved the use of portable wind tunnels (see Table 1.3). However, no study has been undertaken in the field to relate the surface shear stress events associated with the natural wind and aeolian threshold conditions. It is considered, therefore, that well-framed quantitative field studies are required to provide a link between empirical laboratory studies in wind tunnels and threshold conditions associated with particles on natural sediment surfaces.

It is shown here that individual grain exposure to the flow is a fundamental variable controlling erosion susceptibility, and a number of ways in which spatial differences in grain exposure may result in modifications to aeolian threshold conditions have been discussed. Clearly, further evaluation of this important factor is necessary for the development of physically realistic models of entrainment. It is suggested, therefore, that detailed studies of the micro-morphology of natural sediment surfaces are required. In addition, it is also necessary to consider the ways in which certain surface configurations may arise by natural processes.

The flat plate technique may also provide a means to study the relationship between flow structure and relative degrees of exposure of grains at the threshold on rippled sediment beds. Such surfaces could be prepared on the surface of the plate in two ways. Firstly, solid ripples, made using a suitable modelling material, could be covered with

a single layer of non-erosive test grains using the technique described in 3.6. Loose grains could then be placed at a chosen study site and relationships between grain exposure, ripple geometry and aeolian threshold conditions deduced. Secondly, a rippled sediment bed could be produced by airflow across a deep loose sediment bed on the surface of the plate. As the characteristics of the boundary layer change downwind, it is likely that downwind changes in ripple geometry will also occur and will result in a suit of fluid drag and ballistic ripple morphometries on the surface of the plate. These ripples could be rendered non-erosive in subsequent investigations by the application of the aerosol lacquer described in Chapter 7. Using this technique, it may then be possible to assess directly relationships between aeolian threshold conditions, entrainment and ripple geometry.

Finally, it is considered that the experimental techniques developed in the present study to examine threshold conditions in air are equally applicable to studies of sediment dynamics in water. Using these techniques it should be possible to define objectively the threshold condition for any given test material or boundary layer flow regime. The flat plate apparatus may also be used in the study of other aeolian processes such as saltation and creep where controlled and reproducible flow conditions are required.

8.10 Summary

This study examined the aeolian threshold condition using: (a) the controlled and reproducible flow conditions associated with the developing boundary layer on the impervious surface of a flat plate; and (b) permeable test beds. Analysis of the data has established the

significance of factors identified in Chapter 1 as being fundamental controls of threshold conditions for sediment in air and has elucidated certain aspects of initial grain motion. To summarize, a list of the most important results is now given.

1) Two new objective techniques to define the aeolian threshold condition are described.

2) Aeolian threshold conditions are considered to be most appropriately expressed in terms of a critical degree of overlap between the characteristic $P(U_*)$ and $P(U_{*T})$ probability distributions for the boundary layer and the sediment, respectively.

   (a) A new experimental technique to obtain the $P(U_{*T})$ distribution associated with sediments in air is described.

   (b) Attention is drawn to the lack of detailed information on airflow characteristics on granular boundaries.

   It is thought that with detailed laboratory and field measurements of the $P(U_*)$ distribution, it may be possible to develop an objective probablistic model of aeolian entrainment by atmospheric winds.

3) The spatial distribution of threshold shear stresses associated with a turbulent boundary layer on a granular surface was found to be semi-organised. Such organisation may arise from organised sweep passage in the bursting cycle or from flow disturbances under the particular conditions of the experiments. Evidence that entrainment is largely a stochastic process initiated by sweeps is presented.

4) Aeolian entrainment was found to be an inverse exponential function of time and free stream windspeed. The rate of entrainment was found to increase in response to an increase in flow turbulence and is interpreted as reflecting differences in $P(U_*)$ distributions associated with different flow regimes and the ways in which they interact with the $P(U_{*T})$ distribution of a sediment. Experimental results imply that the more frequent, lower intensity U_{*T} values associated with a given $P(U_*)$ distribution are responsible for the bulk of aeolian entrainment.

5) Spatial differences in aeolian threshold conditions in the natural environment are likely to be brought about by: (a) differences in the $P(U_*)$ distribution arising from differences in surface geometry; and (b) differences in the $P(U_{*T})$ distribution for a sediment caused by differences in grain size distribution and shape, exposure and inter-particle cohesion.

6) Mean shear velocity is thought to be an unsuitable parameter by which to express aeolian threshold conditions if the positive skewness of the local $P(U_*)$ distribution is less than the maximum possible value for that surface, (i.e. if the boundary layer is not 'fully turbulent').

7) Comparisons between published and experimental data using both 'restricted' and 'universal' empirical threshold curves show that discrepancies between $\bar{U}_{*T}$ values result largely from: (a) differences in the local flow regime; (b) ambiguous definition of the aeolian threshold condition and inconsistent experimental identification of incipient grain motion; (c) use of insufficiently

uniform test materials; and (d) the use of different test bed configurations and different techniques to measure bed shear velocity.

8) Aeolian entrainment is characterised by a progressive rolling and bouncing process. No evidence of an initial vertical rise of particles was recorded.

9) Grain oscillation at the threshold is considered to result from vortex shedding processes from alternate grain faces. In certain circumstances, this motion may be reinforced by air turbulence.

10) Bed permeability was found to have no detectable effect on aeolian threshold conditions in these experiments.

APPENDICES

A1 Computer program to calculate wind velocities

The program given below was written to calculate wind velocities from pitot-static pressure measurements arising from arrays 1 and 2, using a Casio FX-700P programmable calculator.

```
 10  PRINT "WIND VELOCITY CALCULATION"
 20  VAC: SET E4
 30  INPUT "AIR TEMPERATURE (°C) =", T
 40  INPUT "BAROMETRIC PRESSURE (mmHg) =", B
 50  M = (0.80634 + ((-8.4E^-4)*T))*1000
 60  A = (1.2929*(273.13/(T+273.13)))*((760 - (0.3783*B))/760)
 70  INPUT "NUMBER OF PITOT PRESSURE READINGS", N
 80  INPUT "STATIC PRESSURE (m, alcohol) =", S
 90  INPUT "MANOMETER INCLINATION ANGLE (degrees)", a
100  FOR I = 1 TO N
110  INPUT "PITOT PRESSURE (m, alcohol) =", P
120  H = (S-P)
130  U = SQR ((A*H*9.81*SIN Z)/(0.5*M)
140  PRINT "WIND VELOCITY (m/s) ="; U
150  NEXT I
160  END
```

Description of the program

Line 20 clears the memory and instructs the calculator to round off all the calculations to four decimal places. The air temperature T and barometric pressure B are entered in lines 30 and 40 respectively. Using the air temperature value T, the manometer fluid density M is

calculated at line 50. The density of air, A is then calculated at line 60 using T and B values. Line 70 provides the option of relating a number of pitot pressure measurements N to a single static pressure measurement S. In the case of the pitot-tube arrays described in 3.4.1, N=7. The static pressure, S, and manometer inclination angle, Z, are input at lines 80 and 90. In the loop between lines 100 and 150, wind velocity is calculated using the relationship described by equation 3.2. The number of times this calculation is repeated is specified at line 70.

A2 Preparation of test strips

To study the entrainment of material from different positions on the surface of the plate it was necessary to develop a technique for laying strips of loose particles, one grain diameter in thickness, across the surface of the experimental plate at the required distance downwind from Station A (Figure 4.2(a)).

In the method finally evolved, a large steel rule, 4cm wide, was placed across the surface of the plate in the required position and loose granular material was poured along its downwind edge. The rule was then removed and the grains were spread out using a circular motion to produce a wide flat strip. Light application of a rubber print roller was used to spread the strip out further until a smooth, well-packed surface approximately one grain diameter in thickness was produced. The rule, acting as a guide, was then laid across the strip and all the loose material not covered was carefully brushed aside. Use of a soft brush ensured that no damage was done to the surface of the plate. When the rule was removed a neat strip of test grains, 4cm in width, remained on the surface of the plate. Further light rolling often caused the strip to spread slightly. The rule and brush were then used again to produce a neat strip of test grains. Great care was taken to ensure that any loose particles brushed aside during preparation of the strip were swept downwind so as not to interfere with the subsequent experiment.

A3 Photographic processing techniques

In the investigations of aeolian entrainment reported in Chapters 4, 6 and 7, the erosion of strips and beds of test material was recorded photographically using a range of black and white films rated at ASA/ISO values appropriate for the local illumination and camera shutter speed/aperture requirements. The processing used gave medium contrast, medium grained negatives suitable for mid-format enlargement using a diffuser enlarger system. In certain instances, however, the contrast of the negative image was poor and it was not possible to discriminate accurately between the test material and the plate base layer. In such circumstances, it was necessary to contact print these negatives on to 'kodalith' orthochromatic high contrast film (lith film). This technique produced a high contrast negative in which the eroding strip or bed of test material was clearly visible. A summary of the film processing data is given in Table A3.1. The quality of the photographic image was closely monitored by nightly film processing. Occasionally, incorrect film exposure resulted in an unusable batch of negatives. In such circumstances the appropriate experiment was repeated on the following day.

A Philips PCS 2000 enlarger, equipped with a tri-colour head, was used to print the negatives on to Ilford multi-grade, resin coated black and white paper. This variable contrast paper gave prints with similar contrast from a range of negative densities simply by altering the blue and green filtration settings on the enlarger head. This eliminated the need for a range of different photographic paper grades and greatly simplified the printing process. The prints were processed in 'Ilfospeed' developer (Table A3.2) and were number coded for later

analysis. The life of the developer and processing efficiency was maximised by developing prints in batches of at least 100. Print washing time was reduced by using warm water and, after drying, the resulting prints were inspected to assess the final image contrast.

As the resulting prints were used to calculate the percentage of test material uneroded during the printing of strip and bed erosion sequences, it was essential that the enlargement ratio remained constant. The initial configuration of the strip or bed was traced on to the enlarger baseboard and all subsequent projected negatives associated with a given erosion sequence were compared directly with the dimensions of the initial configuration. On only a very few occasions were adjustments of the enlargement ratio necessary as a consistent image to film plane distance was set during photography of the erosion sequences. Further, the sturdy clamping mechanism between the enlarger column and head ensured no movement occurred once the enlargement ratio had been set.

Film	DESCRIPTION	FORMAT	ASA/ISO	DEVELOPER	DILUTION	TANK/DISH DEVELOPMENT TIMES, 20 C,(min)	STOP BATH 1+30 SOLUTION (Paterson 'Acustop') Time (sec)	FIXER 1+3 SOLUTION ILFORD 'HYPAM' FIXING TIME (min)
ILFORD FP4	Medium speed, Panchromatic, black & white negative film	35mm	160	ILFORD 'ILFOSOL'	1+9	6.5 (TANK)	20	15
ILFORD HP5	High speed, Panchromatic, black & white negative film	35mm	500 800 1600	ILFORD 'MICROPHEN'	1+1 STOCK STOCK	11 (TANK) 8.5 (TANK) 28 (TANK)	20	15
KODALITH ORTHO-TYPE 3 (2556)	Extremely high contrast, ortho-chromatic black & white film	Sheets (20.3x 25.4cm	6	'KODALITH' Super Liquid	STOCK	2.5 to 4 (DISH) (actual time determined by exposure and contrast requirements	20	15

Table A3.1 Summary of film processing stages

NEGATIVE CONTRAST, (determined from contact prints)	TRI-COLOUR FILTRATION (Kodak scale)			PRINT DEVELOPER	DEVELOPMENT TIME (MIN)	STOP BATH Paterson 'acustop' 1+19	FIXER Ilford 'Ilfofix' 1+3	WASH TIME at 25°C
	BLUE	GREEN	RED					
HIGH	40	0	0		1			
HIGH-MEDIUM	15	15	0	Ilford	1			
MEDIUM	0	40	0	'Ilsospeed	1	30 secs	5 mins	15 mins
MEDIUM-LOW	0	70	0	Multigrade'	1.25			
LOW	0	180	0		1.50			

Table A3.2 Summary of print processing

A4 Determination of porosity and permeability of treated and untreated ballotini

(a) Porosity of ballotini

The porosity of ballotini was determined by a total infiltration method (i.e. the pore spaces in a given sample were completely filled with water). Initially the weight (in grammes) of a large oven-dried petri-dish (w_d) was recorded using a sensitive electric balance. The dish was then filled with de-aired distilled water and a flat glass lid of weight w_l was carefully slid across the rim so that the water occupied the entire volume of the dish. The weight of the petri-dish, water and glass lid (w_q) were then recorded. The volume of the petri-dish (v_d) was then determined using

$$v_d = w_q - (w_d+w_l) \qquad \text{A4.1}$$

To ensure accuracy, this procedure was repeated twice. A sample of loose ballotini was then poured into the petri-dish and the top surface was carefully levelled by sliding the glass plate across the dish rim. The weight of the dish, lid and ballotini (w_{tb}) was then recorded and the weight of the ballotini sample (w_b) was determined from

$$w_b = w_{tb} - (w_d+w_l) \qquad \text{A4.2}$$

The lid was then removed and de-aired distilled water was slowly added on to the sample using a burette. Great care was taken to ensure that no loose grains were lost during this operation. When the water level in the sample had risen approximately 5mm, the petri-dish was

sealed inside a glass vacuum desiccator. The air pressure within the desiccator was then reduced to 20mm Hg using a vaccuum pump and the sample was left for 10 minutes. After this time, the pressure inside the desiccator was allowed to equalize slowly with that of the atmosphere. The petri-dish was then removed and more water was carefully poured on to the sample until the water level had risen a further 5mm. The sample was again evacuated for a further 10 minutes. This process ensured the removal of any entrapped air and was repeated until the sample was completely saturated. The glass lid was then slid across the rim of the dish and the combined weight of the dish, lid, ballotini and water (w_{ts}) was recorded. The weight of water held in the pore spaces of the sample (w_w) was determined using

$$w_w = w_{ts} - (w_b+w_d+w_l) \qquad \text{A4.3}$$

and hence the volume of water in the pore spaces (v_p) was obtained from

$$v_p = w_w \qquad \text{A4.4}$$

The porosity of ballotini was defined in 7.2.3 as the ratio of total voids volume to total sediment volume. Thus knowing the volume of the petri-dish holding the ballotini sample (v_d) and the volume of pore water within that sample (v_p), ballotini porosity (P_n), expressed as a percentage, was obtained from

$$P_n = (v_p/v_d) \times 100 \qquad \text{A4.5}$$

Using this technique it was also possible to determine the porosity of the non-erosive ballotini beds described in 7.2.2(a) and (b). In this

case the test beds were prepared inside the petri-dish using the techniques described in 7.2.2. In all cases the above procedure was repeated five times so as to obtain an arithmetic mean porosity value for a given test material. This value was considered to account for unavoidable differences in bed packing associated with the various test beds studied.

(b) Permeability of ballotini

Before disposing of a particular sample in the petri-dish, the water was carefully drained away and the dish was placed in a cool oven for approximately 1 hour. When thoroughly dry, these samples were then used in a comparative visual assessment of bed permeability for both non-erosive and loose ballotini samples in situ. Water was coloured using green food dye and relative differences in permeability were assessed subjectively by observing the rate of infiltration through a test bed when coloured water was poured on to the surface. This simple test showed clearly that the permeability of ballotini was virtually unaffected by the bonding lacquer.

Normally the permeability of a substance is expressed by Darcy's (1856) equation

$$k_{(perm)} = Q_d / A_s(P/l_s) \qquad \text{A4.6}$$

where

$k_{(perm)}$	= permeability	ms^{-1}
Q_d	= discharge	ms^{-1}
A_s	= cross sectional area of a sample	m^2
P	= pressure	Nm^{-2}
l_s	= thickness of sample	m

A number of experimental techniques based on this expression are available to determine accurately the permeability of porous substances. However, in the context of the investigations reported in Chapter 7, further assessment of test bed permeability using more objective techniques was considered to be unnecessary.

BIBLIOGRAPHY

Adriani, M.J. and Terwindt, J.H., 1974. 'Sand stablization and dune building'. Rijkswaterstaat communications, 19, 68pp.

Allen, J.R.L., 1985. 'Loose-boundary hydraulics and fluid mechanics: selected advances since 1961'. In: P.J. Brenchley and B.P.J. Williams, (eds.), 'Sedimentology: recent developments and applied aspects', Blackwell Scientific Publications, London.

Antonia, R.A., 1981. 'Conditional sampling in turbulence measurement'. Ann. Rev. Fluid Mech., 13, 131-56.

Askoy, S., 1973. 'Fluid forces acting on a sphere near a boundary'. Paper A29, Proc. 15th Congress Int. Ass. Hydraul. Res., 1, 212-24.

Armitt, J. and Counihan, J., 1968. 'The simulation of the atmospheric boundary layer in a wind tunnel'. Atmos. Environ., 2, 49-71.

Arvidson, R.E., 1972. 'Aeolian processes on Mars: erosive velocities, settling velocities and yellow clouds'. Bull. Geol. Soc. Am., 83, 1503-8.

Azizov, M.T., 1977. 'Influence of soil moisture on the resistance of soil to wind erosion'. Soviet Soil Sci., 9(1), 105-8.

Bacharov, A.P., 1972. 'Instruments and their application in the study of the wind erosion of soils'. Alma-Ata, Kaynar.

Bagnold, R.A., 1941. 'The Physics of Blown Sand and Desert Dunes'. Methuen, London.

Bagnold, R.A., 1963. 'Sedimentation: beach and nearshore processes'. In: M.N. Hill, ed., 'The Sea', Vol. 3, Interscience Publishers, New York, 507-28.

Bagnold, R.A., 1974. 'Fluid forces on a body in shear flow; experimental use of 'stationary flow'. Proc. R. Soc. Lond. A340, 147-71.

Baines, W.D., 1950. 'An exploratory investigation of boundary layer development on smooth and rough surfaces'. PhD Dissertation, State Univ. Iowa.

Baines, W.D., 1951. 'A literature survey of boundary layer development on smooth and rough surfaces at zero perssure gradient'. Rept. Iowa Inst. Hydraul. Res.

Bairstow, L., 1925. 'Skin Friction'. J.R. Aero. Soc., 19(3), 197-203.

Bakewell, H.P., 1966. 'An experimental investigation of the viscous sublayer in turbulent pipe flow'. Dept. Aerospace Engrn., Pennsylvania State Univ., Sept., 1966.

Bakewell, H.P. and Lumley, J.L., 1967. 'Viscous sublayer and adjacent wall region in turbulent pipe flow'. Physics Fluids, 10, 1880-94.

Beard, D.C. and Weyl, P.K., 1973. 'Influence of texture on porosity and permeability of unconsolidated sand'. Bull. A.A.P.G., 51, 349-69.

Beavers, G.S. and Daniel, J.D., 1967. 'Boundary conditons at a naturally permeable wall'. J. Fluid Mech., 30(1), 197-207.

Bellhouse, B.J. and Schultz, D.L., 1966. 'Determination of mean and dynamic skin friction, separation and transition in low-speed flow with a thin-film heated element'. J. Fluid Mech., 24, 379-86.

Belley, P.Y., 1964. 'Sand movement by wind'. Tech. memo. 1, U.S. Army Coastal Engineering Research Centre, 5201 Little Falls Road, NW, Washington, DC 20016.

Benedict, P.C., Bondurant, D.C., Mckee, J.E., Priest, R.F., Smallshaw, J. and Vanoni, V.A., 1966. 'Sediment transport mechanics: Initiation of motion'. J. Hydraul. Div., Proc. Am. Soc. Civ. Engr., 92 (HY2), 293-313.

Benedict, B.A. and Christensen, B.A., 1972. 'Hydrodynamic lift on a stream bed'. In: H.W. Shen, ed., 'Sedimentation', Dept. Civ. Engnr., Colorado State Univ., 5, 1-5. 17.

Berg, N.H., 1983. 'Field evaluation of some sand transport models'. Earth Surf. Proc. and Landforms, 8, 101-14.

Bernal, J.D. and Mason, J., 1960. 'Co-ordination of randomly packed spheres'. Nature, 188, 910-11.

Bisal, F., 1973. 'Initiation of movement of soil aggregates'. Canad. J. Soil Sci., 53(4), 481-2.

Bisal, F. and Hsieh, J., 1966. 'Influence of moisture on erodibility of soil by wind'. Soil Sci., 102(3), 143-6.

Bisal, F. and Nielsen, K.F., 1962. 'Movement of soil particles in saltation'. Canad. J. Soil Sci., 42(1), 81-6.

Black, T.J., 1966. 'Some practical applications of a new theory of wall turbulence'. Proc. Heat Transfer and Fluid Mech. Inst., Stanford Univ. Press.

Black, T.J., 1968. 'An analytical study of the measured wall pressure field under supersonic turbulent boundary layers'. NASA CR - 888.

Blackwelder, R.F., 1978. 'The bursting process in turbulent boundary layers'. In: C.R. Smith and D.E. Abbott, (eds.), 'Lehigh Workshop on Coherent Structure in Turbulent Boundary Layers', Lehigh Univ., 211-27.

Blackwelder, R.F. and Eckelman, H., 1979. 'Streamwise vortices associated with the bursting phenomenon'. J. Fluid Mech., 94, 577-94.

Blake, W.K., 1970. 'Turbulent boundary layer wall pressure fluctuations on smooth and rough walls'. J. Fluid Mech., 44, 637-46.

Blasius, H., 1908. 'Grenzschichten in Flussigkeiten mit Kleiner Reibung', (Boundary layers in liquids at low Reynolds number), Diss. Gottinger 1907; Z. Math. und Phys., 56, 1-37. English translation in NACA TM 1256.

Blinco, P.H. and Simmons, D.B., 1974. 'Characteristics of turbulent boundary shear stress'. J. Engrn. Mech. Div., Am. Soc. Civ. Engrs., 100(EM2), 203-20.

Blinco, P.H., 1975. 'Turbulent structure near a smooth boundary'. J. Engrn. Mech. Div., Am. Soc. Civ. Engrs., 101, 241-55.

Blom, J. and Wartena, L., 1969. 'The influence of changes in surface roughness on the development of the turbulent boundary layer in the atmosphere'. J. Atmos. Sci., 26, 255-65.

Boly, B.A. and Friedman, M.B., 1959. 'On the viscous flow around the leading edge of a flat plate'. J. Aero/Space Sciences, 26, 453-4.

Boughey, A.S., 1957. 'Ecological studies of tropical coastlines'. J. Ecol., 45, 665-87.

Bressolier, C. and Thomas, Y.F., 1977. 'Studies on wind and plant interactions on French Atlantic coastal dunes'. J. Sedim. Petrol., 47, 331-8.

Brahms, A., 1757. 'Elements of dam and hydraulic engineering'. Aurich, Germany. 1, 105.

Browand, F.K., Oster, D., Plocher, D. and Mclaughlin, D., 1983. 'Sediment entrainment by a turbulent spot: a progress report'. In. B.M. Sumer and A. Muller (eds.), Proc. of Euromech 156, 'Mechanics of Sediment Transport', Istanbull, 12-14 July, 1982, Balkema, 27-32.

Brown, G.L. and Thomas, A.S.W., 1977. 'Large scale motions in a turbulent boundary layer'. Phys. Fluids Suppl., 20, 243-52.

Brunt, D., 1934. 'Physical and Dynamical Meterology', Cambridge.

Burgers, J.M., 1924. 'The motion of a fluid in the boundary layer along a plane smooth surface'. In: C.B. Biezeno and J.M. Burgers, (eds.), Proc. 1st Int. Cong. Appl. Mech., Delft, 1925, 113-28.

Cantwell, B.J., 1979. 'Coherent turbulent structures as critical points in unsteady flow'. Arch. Mech., Stosow., 31, 707-21.

Cantwell, B.J., 1981. 'Organized motion in turbulent flow'. Ann. Rev. Fluid Mech., 13, 457-515.

Cantwell, B.J., Coles, D.E. and Dimotakis, P.E., 1978. 'Structure and entrainment in the plane of symmetry of a turbulent spot'. J. Fluid Mech., 87, 641-72.

Carrier, G.F. and Lin, C.C., 1948. 'On the nature of the boundary layer near the leading edge of a flat plate'. Q. Appl. Math., 6, 63-8.

Carson, M.A., 1971. 'The mechanics of erosion'. Pion Ltd.

Casey, H.J., 1935. 'Über Geschiebebewegung'. (About the critical drag force). Mitt. Preuss. versuchsant. Wasses-, Erd-, Schiffsban, Berlin.

Cermak, J.E. and Arya, S.P.S., 1970. 'Problems of atmospheric shear flows and their laboratory simulation'. Bound. Lay. Meterol., 1, 40-60.

Chambers, A.J., Antonia, R.A., Brown, L.W.B. and Raupach, M.R., 1983. 'Studies of the large structure in a turbulent boundary layer over a rough surface'. In B.M. Sumer and A. Muller (eds.), Proc. of Euromech 156, 'Mechanics of Sediment Transport', Istanbul, 12-14 July, 1982, Balkema,

Chanda, B., 1958. 'Turbulent boundary layer over heated and unheated, plane and rough surfaces'. Dept. Civ. Engr., Colorado State Univ., Rept. 1, AFCRC TN-58-428.

Cheng, E.D.H. and Clyde., C.C., 1971. 'Instantaneous hydrodynamic lift and drag forces on large roughness elements in turbulent open channel flow'. 'Sediment symposium in honour of H.A. Einstein'. H.W. Shen, (ed.), Colorado State Univ.

Chepil, W.S., 1945(a). 'Dynamics of wind erosion I: Nature of movement of soil by wind'. Soil Sci., 60, 305-20.

Chepil, W.S., 1945(b) [or 1945°, Figures 5.5 and 5.6]. 'Dynamics of wind erosion II: Initiation of soil movement'. Soil Sci., 60, 397-411.

Chepil, W.S., 1945(c). 'Dynamics of wind erosion III: The transport capacity of the wind'. Soil Sci., 60, 475-80.

Chepil, W.S., 1956. 'Influence of moisture on erodibility of soil by wind'. Soil Sci. Soc. Am. Proc., 20, 288-92.

Chepil, W.S., 1958(a). 'The use of evenly spaced hemispheres to evaluate aerodynamic forces on a soil surface'. Trans. Am. Geophys. Union, 39, 397-403.

Chepil, W.S., 1958(b). 'Soil conditions that influence wind erosion'. U.S. Dept. Agric., Tech. Bull. No. 1185.

Chepil, W.S., 1959. 'Equilibrium of soil grains at the threshold of movement by wind'. Soil Sci. Soc. Am. Proc., 23, 422-28.

Chepil, W.S. and Milne, R.A., 1939. 'Comparative study of soil drifting in the field and in the wind tunnel'. Sci. Agric., 19, 249-57.

Chepil, W.S. and Milne, R.A., 1941. 'Wind erosion of soils in relation to size and nature of the exposed area'. Sci. Agric., 21(8), 413-22.

Chepil, W.S. and Woodruff, N.P., 1963. 'The physics of wind erosion and its control'. Advances in Agronomy, U.S. Dept. Agric., 15, 211-302.

Chiu, T.J., 1967. 'Sand transport by wind'. Tech. Rept., Dept. Coastal Engrn. Univ. Florida.

Chu, Y. and Gelhar, L., 1972. 'Turbulent flow with granular permeable boundaries'. MIT, Dept. Civ. Engr., Rept. No. 148, Cambridge, Mass.

Clark, J.A., 1968. 'A study of incompressible turbulent boundary layers in channel flow'. J. Basic Engng., D90, 455-68.

Clyde, C.G. and Einstein, 1966. 'Fluctuating total head in a viscous sublayer'. J. Eng. Mech. Div., Trans. Am. Soc. Civ. Engrs., 92(EM2), 251-75.

Collins, R.E., 1961. 'Flow of fluids through porous materials'. Chapman and Hall Ltd., London.

Coleman, N.L., 1967. 'A theoretical and experimental study of drag and lift forces acting on a sphere resting on a hypothetical stream bed'. Proc. 12th Congress. Int. Ass. for Hydraul. Res., 185-92, Fort Collins, Colorado.

Coleman, N.L., 1972. 'The drag doefficient of a stationary sphere on a boundary of similar spheres'. La Houille Blanche, No. 1, 17-21.

Coleman, N.L. and Ellis, W.M., 1976(a). 'Model study of the drag coefficient on a streambed particle'. Proc. 3rd. Federal Interagency Sedimentation Conf., Denver, Colorado, 4-12.

Coleman, N.L. and Ellis, W.M., 1976(b). 'A stream bed - particle model - study facility using hydroxyethylcellulose solutions as a fluid'. USDA, Agric. Res. Service, ARS-S-147, 8pp.

Coles, D.E., 1978. 'A model for flow in the viscous sublayer'. In: Smith, C.R. and Abbott, D.E., (Eds.), Lehigh Workshop on Coherent Structure in Turbulent Boundary Layers', 462-69.

Coles, D.E. and Barker, S.J., 1975. 'Some remarks on a synthetic turbulent boundary layer'. In: S.N.B. Murthy, (ed.), Turbulent mixing in non-reactive and reactive flows', 285-92.

Compte-Bellot, G., 1963. 'Coefficients des Dessymetrie et d'Aplatissement, Spectres et Correlations en Turbulence de Condiute'. J. de Mechanique, Vol. III (2), 96-105.

Cooke, R.U., Brunsden, D., Doornkamp, J.C. and Jones, P.K.C., 1982. 'Urban Geomorphology in Drylands'. OUP, Oxford.

Corino, E.R. and Brodkey, R.S., 1969. 'A visual investigation of the wall region in turbulent flow'. J. Fluid Mech., 37, 1-30.

Corn, M., 1966. 'Adhesion of particles'. In: C.N. Davies, (Ed.), Aerosol Science, Academic Press, London.

Darcy, H., 1856. 'Les fontaines publiques de la ville de Dijon'. Dalmont, Paris.

Davies, P.O.A.L., 1950. 'The behaviour of a pitot-tube in transverse shear'. J. Fluid Mech., 3(5), 441-56.

Davies, T.R.H. and Samad, M.F.A., 1978. 'Fluid dynamics lift on a bed particle'. J. Hydraul. Div., proc. Am. Soc. Civ. Engr., 104(HY8), 1171-82.

Dhawan, S. and Narasimha, R., 1957. 'Some properties of boundary layer flow during transition from laminar to turbulent motion'. J. Fluid Mech., 3, 418-36.

Dinkelacker, A., 1979. 'Play tornado-like vortices: a role in the generation of flow noise?'. IUTAM Symp. Mech. Sound generation in flows, Springer, 217-21.

Dinkelacker, A., Hessel, M., Meier, G. and Schewe, G., 1977. 'Investigations of pressure fluctuations beneath a turbulent boundary layer by means of an optical method'. Phys. Fluids, 20(10), 216-24.

Dolgilevich, M.I. and Vasili'yev, Y.I., 1974. Wind tunnel for simulating the wind erosion of soils. Soviet Soil Sci., 6(3), 340-5.

Dryden, H.L., 1934. 'Boundary layer flow near flat plates'. Proc. 4th. Intern. Cong. Appl. Mech., Cambridge, Endland, 175-86.

Dryden, H.L., 1936. 'Airflow in the boundary layer near a plate'. NACA Rep. 562.

Dryden, H.L., 1939. 'Turbulence and boundary layers'. J. Aeronautical Sci., 6, 85-100 and 101-5.

Dryden, H.L., 1956. 'Recent investigations of the problem of transition', Zeitschrift fur Flugwissenschaft, 4, 89-95.

Duncan, W.J., Thom, A.S. and Young, A.D., 1970. 'Mechanics of Fluids', 2nd Ed., Edward Arnold, London.

Dyunin, A.K., 1963. 'Mechanisms of blowing snow'. Novosibirsk, Izd., SD AN SSSR.

Eckelman, H., 1974. 'The structure of the viscous sublayer and the adjacent wall region in a turbulent channel flow'. J. Fluid Mech., 65, 439-50.

Eckelman, H. and Reichardt, H., 1972. 'An experimental investigation in a turbulent channel flow with a thick viscous sublayer'. Proc. Symp. on Turbulence in Liquids, Univ. Missouri-Rolla.

Einstein, H.A., 1950. 'The bedload function for sediment transportation in open channel flows'. U.S. Dept. Agric., Tech. Bull. 1026.

Einstein, H.A. and El-Samni, E.A., 1949. 'Hydrodynamic forces on a rough wall'. Rev. Modern Phys., 21, 520-4.

Einstein, H.A. and Li, H., 1956. 'The viscous sublayer along a smooth boundary'. J. Hydraul. Div. Proc. Am. Soc. Civ. Engr., 123, 293-313.

Elder, J.W., 1960. 'An experimental investigation of turbulent spots and breakdown to turbulence'. J. Fluid Mech., 9(2), 235-42.

Ellis, A.J. and Lee, C.H., 1919. 'Geology and ground waters on the western part of San Diego County, California'. U.S. Geol. Surv. Water Supply Paper 446, 121-3.

Emmons, H.W. and Bryson, A.E., 1952. 'The laminar-turbulent transition in a boundary layer: Part 1, J. Aeronautical Sci., 18, 490-8: Part 2, Proc. 1st US Nat. Cong. Appl. Mech., 859-68.

Fage, A., Falkner, V.W., 1930. 'An experimental determination of the intensity of friction on the surface of an aerofoil'. Proc. Roy. Soc. Lond. A129, 378-86.

Fage, A. and Preston, J.H., 1941. 'On transition from laminar to turbulent flow in the boundary layer'. Proc. Roy. Soc. Lond. A178, 201-27.

Falco, R.E., 1977. 'Coherent motions in the outer region of turbulent boundary layers'. Phys. of fluids, 20(10), II, S124-32.

Favre, A., Dumas, R., Verollet, E. and Coantic, 1966. 'Couch limite turbulente sur Paroi Poreuse avec Aspiration'. J. Mechan., 5, 3-28.

Feindt, E.G., 1957. 'Untersuchungen über die Abhangigkeit des Umschlanges laminar-turbulent von der Oberflachenrauhigkeit und der Druckverteilung'. (Transition from laminar to turbulent flow on a rough surface in zero pressure gradient). Diss. Braunschweig 1956: Jb 1956 Schiffbautechn. Gesellschaft 50, 180-203.

Fenton, J.D. and Abbott, J.E., 1977. 'Initial movement of grains on a stream bed: the effect of relative intrusion'. Proc. Roy. Soc. Lond. A352, 523-37.

Fiedler, H. and Head, M.R., 1966. 'Intermittency measurements in a turbulent boundary layer'. J. Fluid Mech., 25, 719-35.

Ford, E.F., 1957. 'The transport of sand by wind'. Trans. Am. Geophys. Union, 38(2), 186-97.

Francis, J.R.D., 1969. 'A Textbook of Fluid Mechanics'. Edward Arnold, London.

Fraser, H.J., 1935. 'Experimental study of the porosity and permeability of clastic sediments'. J. Geol., 43, 910-1010.

Garde, R.J. and Sethuraman, S., 1969. 'Variation of the drag coefficient of a sphere rolling on a boundary'. La Houille Blanche, 7,

Gerety, K.M. and Slingerland, R.L., 1982. '"Saltation equivalence" in aeolian sand transport'. IAS Cong., Hamilton, Ontario.

Gerety, K.M. and Slingland, R.L., 1983. 'Nature of the saltating population in wind tunnel experiments with heterogenous size-density sands'. In: M.E. Brookfield and T.S. Ahlbrandt, (eds.), 'Eolian Sediments and Processes, (Developments in Sedimentology 38)', Elsevier, Amsterdam, 115-31.

Gessler, J., 1971. 'Beginning and ceasing of sediment motion'. In 'River mechanics', H.W. Shen (ed.), 1(7), Fort Collins, Colorado.

Gilbert, K.G. and Murphy, E.C., 1914. 'The transportation of debris by running water'. U.S. Geol. Surv. Prof. Papers, 86, 263-74.

Gillette, D., 1978(a). 'Tests with a portable wind tunnel for determining wind erosion threshold velocities'. Atmos. Environ., 12, 2309-13.

Gillette, D., 1978(b). 'A wind tunnel simulation of the erosion of soils: Effect of soil texture, sand-blasting, wind speed and soil consolidation on dust production'. Atmos. Environ., 12, 1735-43.

Gillette, D., Adams, J., Endo, A., Smith, D. and Kihl, R., 1980. 'Threshold velocities for input of soil particles into the air from desert soils'. J. Geophys. Res., 85, 5621-30.

Gillette, D., Adams, J., Muhs, D. and Kihl, R., 1982. 'Threshold friction velocities and rupture moduli for crusted desert soils for input of soil particles into air'. J. Geophys. Res., 87, 9003-15.

Gimmingham, C.H., 1955. 'A note on water table, sand movement and plant distribution in a North African oasis'. J. Ecol., 43, 22-5.

Goldman, A.R., Cox, R.G. and Brenner, 1967. 'Slow viscous motion of a sphere parallel to a plane wall'. Chem. Engnr. Sci., 22, 653-60.

Goldstein, S., 1930. 'Concerning some solutions of the boundary layer equations in hydrodynamics'. Proc. Camb. Phil. Soc., 26, 1-30.

Goldstein, S., 1936. 'A note on roughness'. Aeronautical Res. Council, Repts. and Memo., 1763.

Graf, W.H., 1971. 'Hydraulics of sediment transport'. McGraw-Hill, New York.

Grass, A.J., 1970. 'Initial instability of fine bed sand'. J. Hydraul. Div. Proc. Am. Soc. Civ. Engrs., 96(HY3), 619-32.

Grass, A.J., 1971. 'Structural features of turbulent flow over smooth and rough boundaries'. J. Fluid Mech., 50, 233-55.

Grass, A.J., 1983. 'The influence of boundary layer turbulence on the mechanics of sediment transport'. In: B.M. Sumer and A. Muller (eds.), Proc. of Euromech 156, 'Mechanics of Sediment Transport', Istanbul, 12-14 July, 1982, Balkema, 3-17.

Granton, L.C. and Fraser, H.J., 1935. 'Systematic packing of spheres - with particular reference to porosity and permeability'. J. Geol., 43, 785-909.

Greeley, R., Iversen, J.D., Pollack, J.B., Udovich, N. and White, B.R., 1974. 'Wind tunnel studies of Martian eolian processes'. Proc. R. Soc. Lond. A341, 331-60.

Greeley, R., White, B.R., Leach, R., Iversen, J.D., and Pollack, J.B., 1976. 'Mars: Wind friction speeds for particle movement'. Geophys. Res. Lett., 3, 417-20.

Greeley, R., White, B.R., Pollack, J.B., Iversen, J.D. and Leach, R.N., 1977. 'Dust storms on Mars: considerations and simulation', NASA TM-78423.

Greeley, R. and Leach, R., 1978. 'A preliminary assessment of the effect of electrostatics on aeolian processes'. Rept. Planetary Geol. Prog., 1977-1978. NASA TM 79729, 236-7.

Greeley, R., Leach, R., White, B.R., Iversen, J.D. and Pollack, J.B., 1980(a). 'Threshold wind speeds for sand on Mars: Wind tunnel simulations'. Geophys. Res. Lett., 7, 121-4.

Greeley, R., White, B.R., White, R.N., Leach, R., Leonard, R., Pollack, J.B. and Iversen, J.D., 1980(b). 'Venus aeolian processes: saltation studies and the Vernusian wind tunnel'. NASA TM-82385, 275-7.

Greeley, R., Williams, R.H. and Marshall, J.R., 1983. 'Velocities of windblown particles in saltation: preliminary laboratory and field measurements'. In: M.E. Brookfield and T.S. Albrandt, (Eds.), 'Eolian Sediments and Processes, (Developments in Sedimentology 38)', Elsevier, Amsterdam, 133-48.

Greeley, R., Iversen, J.D., Leach, R., Marshall, J.R., White, B.R. and Williams, S.H., 1984. 'Windblown sand on Venus: preliminary results of laboratory simulations'. Icarus, 57, 112-24.

Greeley, R. and Marshall, J.R., 1985. 'Transport of Venusian rolling "stones" by wind?' Nature, 313, 771-3.

Greeley, R. and Iversen, J.D., 1985. 'Wind as a Geological Process'. Cambridge Planetory Science Ser., CUP.

Griggs, D.T., 1936. 'The factor of fatigue in rock exfoliation'. J. Geol., 44, 781-96.

Gupta, A.K., Lauger, J. and Kaplan, R.E., 1971. 'Spatial structure in the viscous sublayer'. J. Fluid Mech., 50, 493-512.

Gyr, A., 1983. 'Towards a better definition of the three types of sediment transport'. J. Hydraul. Res., 21(1), 1-15.

Hama, F., 1954. 'Boundary layer characteristics for smooth and rough surfaces'. Trans. Soc. Naval. Arch. Marine Engrs., 62, 333-9.

Hansen, M., 1930. 'Die Geschwindigkeitsverteilung in der Grenzschicht an einer eingetauchten Platte'. (Boundary layer velocity profiles on a flat plate in water). NACA TM 585.

Head, M.R., 1978. 'Combined flow visualization and hot-wire measurements in turbulent boundary layers'. In: C.R. Smith and D.E. Abbott., (eds.), 'Lehigh Workshop in Coherent Structure in Turbulent Boundary Layers', Lehigh Univ., 98-109.

Head, M.R., 1979. 'Flow visualization of turbulent boundary layer structure'. AGARD Conf. Proc., 271, 25-39.

Head, M.R. and Bandyophadyay, P., 1981. 'New aspects of turbulent boundary layer structure'. J. Fluid Mech., 107, 297-338.

Hinze, J.O., 1975. 'Turbulence'. 2nd ed., McGraw-Hill, New York.

Hjulstrom, F., 1935. 'Studies of the morphological activities of rivers as illustrated by the River Fyris'. Bull. Geol. Inst. Univ. Uppsala, 25, 221-527.

Horikawa, K., 1959. 'Sand movement by wind action: on the characteristics of sand traps'. Ser. 72, Issue 4, Wave Res. Lab., Univ. Calif., Berkeley.

Horikawa, K. and Shen, H.W., 1960. 'Sand movement by wind action - on the characteristics of sand traps'. Beach Erosion Board, Tech. Memo. 119, (51pp).

Howard, A.D., 1977. 'Effect of slope on threshold of motion and its application to orientation of wind ripples'. Bull. Geol. Soc. Am., 88, 853-6.

Howarth, L., 1938. 'On the solution of the laminar boundary layer equations'. Proc. Roy. Soc. Lond., A164, 547-79.

Hsu, S.A., 1971. 'Wind stress criteria in eolian sand transport'. J. Geophys. Res. 76, 8684-86.

Imai, I., 1957. 'Second approximation to the laminar boundary layer flow over a flat plate'. J. Aeronautical Sci., 24, 155-6.

Imaki, K., 1968. 'The structure of the turbulent boundary layer's "superlayer"'. Bull. Inst. Space Aeronaut. Sci., Univ. Tokyo, 4, 448-536.

Inman, D.L., 1952. 'Measures for describing the size distribution of sediments'. J. Sedim. Petrol., 22, 125-45.

Ishihara, T. and Iwagaki, Y., 1952. 'On the effect of sand storms in controlling the mouth of the Kiku river'. Kyoto Univ., Disaster Prevention Res. Inst., Bull. 2.

Iversen, J.D., Greeley, R., Pollack, J.B. and White, B.R., 1973. 'Simulation of Martian eolian phenomena in the atmospheric wind tunnel'. Space Simulation, NASA Spec. Publ., 36, 191-213.

Iversen, J.D., Greeley, R., White, B.R. and Pollack, J.B., 1975. 'Estimates of saltation threshold and erosion rates on Mars'. AIAA paper No. 75, 1144-9.

Iversen, J.D., Pollack, J.B., Greeley, R. and White, B.R., 1976. 'Saltation thresholds on Mars: The effect of interparticle force, surface roughness and low atmospheric density'. Icarus, 29, 318-93.

Iversen, J.D. and White, B.R., 1982. 'Saltation thresholds on Earth, Mars and Venus'. Sedimentology, 29, 111-19.

Jackson, R.G., 1976. 'Sedimentological and fluid dynamics implications of the turbulent bursting phenomenon in geophysical flows'. J. Fluid Mech., 77, 531-60.

Janour, Z., 1951. 'Resistance of a flat plate at low Reynolds number'. NACA TM 1316.

Jeffreys, H., 1929. 'On the transport of sediments by streams'. Camb. Phil. Soc. Proc., 25, 272-6.

Jensen, J.L. and Sørensen, M., 1982. 'A model for saltation trajectories - evaluated by means of trap data'. Dept. Theoretical Statistics, Aarhus Univ. Denmark, Res. Rept. 85.

Jensen, J.L. and Sørensen, M., 1983. 'On mathematical modelling of aeolian saltation'. In B.M. Sumer and A. Muller (eds), Proc. of Euromech 156, 'Mechanics of Sediment Transport', Istanbul, 12-14 July, 1982, Balkema, 65-72.

Johnson, J.W., 1963. 'Sand movement on coastal dunes'. In: Proc. Fed. Inter-Agency Sedimentation Conf., USDA, 747-55.

Jones, D.P., 1981. 'Particle vibration at the boundary in turbulent shear flow'. Unpub. MSc Thesis, Univ. British Columbia, Canada.

Jones, W.M. and Mills, D., 1961. 'Porosity and surface area of a granular bed from measurements of the flow of air through the bed and measurements of the granular shape factor'. Brit. J. Appli. Phys., 12, 172-4.

Kadib, A.A., 1965. 'A function for sand movement by wind'. Univ. Calif. Hydraul. Engnr. Lab. Tech. Rept., HEL-2-12, 91-129.

Kalinske, A.A., 1942. 'Criteria for determining sand transport by surface creep and saltation'. Trans. Am. Geophys. Union, 23(2), 64-90.

Kaplan, R.E. and Laufer, J., 1969. 'Further measurements in the intermittent region of a turbulent boundary layer'. Boing Symp. Turbulence, Seattle, Washington.

Karahan, E., 1975. 'Initiation of motion for uniform and non-uniform materials'. PhD Thesis, Tech. Univ., Istanbul, Turkey.

Kawamura, R., 1951. 'Study of sand movement by wind'. Inst. Sci. and Tech., Tokyo, Rept. 5, 95-112.

Kemp, P.H. and Grass, A.J., 1967. 'The measurement of turbulent velocity fluctuations close to a boundary in open channel flow'. Proc. 12th Cong. of Int. Assoc. Hydraul. Res., Vol. 2.

Keulegan, G.H., 1938. 'Laws of turbulent flows in open channels'. J. Res. natn. Bur. Stand., 21, 707-41.

Kim, H.T., Kline, S.J. and Reynold, W.C., 1968. 'An experimental study of turbulence production near a smooth wall in a turbulent boundary layer with zero pressure gradient'. Thermosciences Div., Stanford Univ., Rept. MD-20.

Kind, R.J., 1976. 'A critical examination of the requirements for model simulation of wind-induced erosion/deposition phenomena such as snow drifting'. Atmos. Environ., 10, 219-27.

Klebanoff, P.S., 1956. 'Characteristics of turbulence in a boundary layer with zero pressure gradient'. NACA TM 3178.

Klein, S.J., Reynolds, W.C., Schraub, F.A. and Rundstadler, P.W., 1967. 'The structure of turbulent boundary layers'. J. Fluid Mech., 30, 741-73.

Knottnerus, D.J.C., 1978. 'Relative humidity of the air and critical wind velocity in relation to erosion'. In: M. De Boodt and D. Gabriels, (eds.), 'Assessment of Erosion', Wiley and Sons, Chichester.

Knottnerus, D.J.C., 1980. 'Relative humidity of the air and critical wind velocity in relation to erosion'. In: M. De Boodt and D. Gabriels, (eds.), 'Assessment of Erosion', Wiley and Sons, chichester.

Kolbuszewskie, J., 1948. 'An experimental study of the maximum and minimum porosities of sands'. Proc. 2nd Int. Conf. Soil Mech., Rotterdam, 1, 158-65.

Kolbuszewskie, J., Nadolski, L. and Dydacki, Z., 1950. 'Porosity of wind deposited sands'. Geol. Mag., 87, 433-5.

Kolbuszewskie, J., 1953. 'Note on factors governing the porosity of wind deposited sands'. Geol. Mag., 90, 48-56.

Komar, P.D. and Miller, M.C., 1973. 'The threshold of sediment movement under oscillatory water waves'. J. Sedim. Petrol., 43, 1101-10.

Kovasznay, L.S.G., 1970. 'The turbulent boundary layer'. Ann. Rev. Fluid Mech., 2, 95-112.

Kovasznay, L.S.G., Kibens, V. and Blackwelder, R., 1970. 'Large scale motion in the intermittent region of a turbulent boundary layer'. J. Fluid Mech., 41, 283-325.

Kraichnan, R.H., 1956. 'Pressure fluctuations in turbulent flow over a flat plate'. J. Acoust. Soc. Am., 28, 378-88.

Kramer, H., 1935. 'Sand mixtures and sand movement in fluvial levels'. J. Hydraul. Div., Trans. Am. Soc. Civ. Engrs., 100, 798-838.

Kuchemann, D., 1965. 'Report on the IUTAM symposium on concentrated vortex motions in fluids'. J. Fluid Mech., 21, 1-20.

Kuhn, W.E., 1961. 'Ultrafine particles'. Wiley, New York.

Kuhlman, H., 1958. 'Quantitative measurements of aeolian sand transport'. Geografisk Tidsskrift, 57, 51-74.

Kuo, Y.H., 1953. 'On the flow of an incompressible viscous fluid past a flat plate at moderate Reynolds numbers. J. Math. and Phys., 32, 83-100.

Landahl, M.T., 1967. 'A wave-guide model for turbulent shear flow'. J. Fluid Mech., 29, 441-59.

Lane, E., 1955. 'Design of stable channels'. J. Hydraul. Div., Proc. Am. Soc. Civ. Engr., 120, 1234-60.

Laufer, J., 1954. 'The structure of fully developed pipe flow'. NACA Rept. TN 2954.

Laufer, J., 1975. 'New trends in experimental turbulence research'. Ann. Rev. Fluid Mech., 7, 307-26.

Lee, M.K., Eckelmann, L.D. and Hanratty, T.J., 1974. 'Identification of turbulent wall eddys through the phase relation of the componants of the fluctuating velocity gradient'. J. Fluid Mech., 66, 17-34.

Leeder, M.R., 1985. 'Sedimentology - Process and product'. George Allen and Unwin, London.

Lettau, K. and Lettau, H.H., 1978. 'Experimental and micro-meterological field studies of dune migration'. In: H.H. Lettau and K. Lettau, (eds.), 'Exploring the World's Driest Climates', Univ. Wisconsin-Madison, Inst. Environ. Studies, IES Rept., 101, 110-47.

Lewis, W.V. and Miller, M.M., 1955. 'Kaolin model glaciers'. J. Glaciol., 2, 417-22.

Liepmann, H.W. and Skinner, G., 1954. 'Shearing-stress measurements by means of a heated element'. NACA TN 3268.

Lighthill, M.J., 1963. 'Laminar boundary layers'. In L. Rosenhead, (ed.), Clarendon Press, Oxford.

Lloyd, A., 1967. 'The generation of shear flow in a wind tunnel'. Quart. J.R. met. Soc., 93, 79-96.

Logie, M., 1981. 'Wind tunnel experiments on dune sands'. Earth Surf. Proc. and Landforms, 6, 365-74.

Logie, M., 1982. 'Influence of roughness elements and soil moisture on the resistance of sand to wind erosion'. Aridic soils and Geomorphic Processes, Catena Supplement 1, Braunschweig, 161-73.

Lu, S.S., and Willmarth, W.W., 1973. 'Measurements of the Reynolds stress in a turbulent boundary layer'. J. Fluid Mech., 60, 481-511.

Ludwieg, H. and Tillmann, W., 1949. 'Investigations of the wall shearing stress in turbulent boundary layers'. Ing. Arch., 17, 207-288. (English translation in NACA TM 1285 (1950)).

Lyles, L. and Krauss, R.K., 1971. 'Threshold velocities and initial particle motion as influenced by air turbulence'. Trans. Am. Soc. Agric. Engrs., 14, 563-6.

Lyles, L. and Schrandt, R.L., 1971. 'Wind erodibility as influenced by rainfall and soil salinity'. Soil Sci., 114(5), 367-72.

Lyles, L. And Woodruff, N.P., 1971. 'Boundary layer flow structure: Effects on detatchment of non-cohesive particles'. In: H.W. Shen, (Ed.), 'Sedimentation', Dept. Civ. Engr., Colorado State Univ., 2.1-2.16.

Lyles, L. Schrandt, R. and Schmeidler, N., 1974. 'How aerodynamic roughness elements control sand movement'. Trans. Am. Soc. Agric. Engrs., 17(1), 134-9.

Lynch, R.A. and Brackley, E.F., 1974. 'Shearing stress meter'. J. Appl. Met., 13, 588-91.

MacRae, J.C. and Gray, W.A., 1961. 'Significance of the properties of materials in the packing of real spherical particles'. Brit. J. Applied Phys., 12, 164-72.

Maegley, W.J., 1976. 'Saltation and Martian sandstorms'. Geophys. Space Phys., 14, 135-42.

Marshall, J.K., 1971. 'Drag measurements in roughness arrays of varying density and distribution'. Agric. Meterol., 8, 269-92.

McCormick, M.E., 1968. 'An analysis of the formation of turbulent patches in the transition boundary layer'. J. App. Mech., 35, 216-19.

McGee, W.G., 1897. 'Sheetflood erosion'. Bull. Geol. Soc. Am., 8, 87-112.

Merceret, F.J., 1972. 'An experimental study of wind velocity profiles over a wavy surface'. Coll. of Maritime Studies, Delaware Univ., Publ. 2MS065.

Messiter, A.F., 1970. 'Boundary layer flow near the trailing edge of a flat plate'. SIAM J. Appl. Math., 18, 241-57.

Miller, M.C. and Komar, P.D., 1977. 'The development of sediment threshold curves for unusual environments (MARS) and for inadequately studied materials (Foram sands)'. Sedimentology, 24, 709-21.

Miller, M.C., McCave, I.N. and Komar, P.D., 1977. 'Thresholds of sediment motion under unidirectional currents'. Sedimentology, 24, 507-27.

Monin, A.S., 1962. 'Empirical data on turbulence in the surface layer of the atmosphere'. J. Geophys. Res., 67(8), 3103-9.

Moore, W.L., 1951. 'An experimental investigation of the boundary layer development along a rough surface'. PhD Dissertation, Univ. Iowa.

Morton, J.K., 1957. 'Sand dune formation on a tropical shore. J. Ecol., 45, 495-7.

Mueller, A. and Studerus, X., 1979. Proc. 18th IAHR-Congress, Cagliari, Italy, B.A.3, 19.

Mulhearn, P.J., 1978. 'A wind tunnel boundary layer study of the effect of a roughness change: rough to smooth'. Bound. Lay. Met., 15, 9-30.

Mulhearn, P.J. and Finnigan, J.J., 1978. 'Turbulent flow over a very rough, random surface'. Bound. Lay. Met., 15, 109-32.

Mutlu-Sumer, B., 1984. 'Lift forces on moving particles near boundaries'. J. Hydraul. Div., Proc. Am. Soc. Civ. Engrs., 110(9), 1272-8.

Nakagawa, H. and Nezu, I., 1977. 'Predictions of the contributions to Reynolds Stress from bursting events in open channel flows'. J. Fluid Mech., 80, 99-128.

Nakagawa, H. and Nezu, I., 1980. 'Turbulent behaviours of open channel flow with permeable beds'. Proc. Intern. Conf., Water Res. Developments, Taipei, China.

Narayanan, B. and Marvin, J., 1978. 'On the period of the coherent structure in boundary layers at large Reynolds numbers'. In: C.R. Smith and D.E. Abbott, (eds.), 'Lehigh Workshop on Coherent Structures in Turbulent Boundary Layers', Lehigh Univ.

Nath, J.H. and Yamamoto, T., 1974. 'Forces from fluid flow around objects'. Proc. 14th Conf. on Coastal Engineering, Copenhagen, Denmark.

Neill, C.R., 1967. 'Mean velocity criterion for scour of coarse, uniform bed material'. Int. Assoc. Hydraul. Res., 12th Cong. Proc., Fort Collins, Colorado, 3, 46-54.

Neill, C.R. and Yalin, M.S., 1969. 'Quantitative definition of beginning of bed movement'. J. Hydraul. Div., Proc. Am. Soc. Civ. Engrs., 95(HY1), 585-7.

Nemenyi, P., 1940. 'The different approaches to the study of propulsion of granular materials and the value of their coordination'. Trans. Am. Geophys. Union, 21st Ann. Meeting, 633-42.

Nemoto, S., Mitsudera, M., Takahashi, K., Uotso, H. and Kobayaski, S., 1969. 'On the thresold velocity for the saltation of sand'. Papers in Meterol. and Geophys., 20(4), 365-84.

Nickling, W.G., 1984. 'The stabalising role of bonding agents on the entrainment of sediment by wind'. Sedimentology, 31, 111-17.

Nickling, W.G. and Ecclestone, M., 1980. 'A technique for detecting grain motion in wind tunnels and flumes'. J. Sedim. Petrol., 50, 652-4.

Nickling, W.G. and Ecclestone, M., 1981. 'The effect of soluable salts on the threshold shear velocity of fine sands'. Sedimentology, 28, 505-10.

Nikuradse, J., 1933. 'Stromungsgesetz in rauhen Rohren'. (Flow in rough pipes). Forschg. Arb. Ing. Wes. No. 361.

Nikuradse, J., 1942. 'Laminare Reibungsschichten an der Langsangeströmten Platte'. (The laminar boundary layer on a flat plate at low Reynolds numbers). Monograph. Zentrale f. wiss. Berichtswesen, Berlin.

Nychas, S.G., Hershey, H.C. and Brodkey, R.S., 1973. 'A visual study of turbulent shear flow'. J. Fluid Mech., 61(3), 513-40.

O'Brian, M.P. and Rindlaub, B.D., 1936. 'The transportation of sand by wind. Civ. Eng., 6, 325-7.

Offen, G.R. and Kline, S.J., 1974. 'Combined dye-streak and hydrogen - bubble visual observations of a turbulent boundary layer'. J. Fluid Mech., 62(2), 223-39.

O'Loughlin, E.M. and Annambhotla, V.S.S., 1969. 'Flow phenomena near rough boundaries'. J. Hydraul. Res., 7, 231-50.

O'Neil, M.E., 1968. 'A sphere in contact with a plane wall in a slow linear shear flow'. Chem. Engrn. Sci., 23, 1293-8.

Oldaker, D.K. and Tiederman, W.G., 1977. 'Spatial structure of the viscous sublayer in drag reducing channel flows'. Phys. Fluids, 20(10), 133-44.

Owen, P.R., 1964. 'Saltation of uniform grains in air'. J. Fluid Mech., 20, 225-42.

Owen, P.R., and Zienkieuvicz, H.K., 1957. 'The production of uniform shear flow in a wind tunnel'. J. Fluid Mech., 2, 521-31.

Painter, D., 1985. 'Wowee! A workshop'. Soil and Water, 2, 34-36.

Panofsky, H.A., 1974. 'The atmospheric boundary layer below 150 metres'. Ann. Rev. Fluid Mech., 6, 147-77.

Patel, V.C., 1965. 'Calibration of the Preston tube and limitations on its use in pressure gradients'. J. Fluid Mech., 23, 185-208.

Perry, A.E., Lim, T.T. and Teh, E.W., 1981. 'A visual study of turbulent spots'. J. Fluid Mech., 104, 387-405.

Peterson, S.T. and Junge, C.E., 1971. 'Sources of particulate matter in the atmosphere'. In: W.H. Matthews, W.W. Kellogg and G.D. Robinson, (Eds.), 'Man's Impact on the Climate', MIT Press, Cambridge, Massachusetts, 310-20.

Pettijohn, F.J., Potter, P.E. and Siever, R., 1972. 'Sand and sandstone'. Springer-Verlag, New York.

Phillips, O.M., 1967. 'The maintenance of Reynolds stress in turbulent shear flow'. J. Fluid Mech., 27(1), 131-44.

Pitty, A.F., 1977. 'Introduction to Geomorphology'. Methuen and Co., London.

Plate, E.J., 1971. 'Aerodynamic characteristics of atmospheric boundary layers'. U.S. Dept. Energy Tech. Inf. Centre, Washington D.C.

Pollack, J.B., Haberle, R., Greeley, R. and Iversen, J.D., 1976. 'Estimates of windspeeds required for particle motion on Mars'. Icarus, 29, 395-417.

Prandtl, L., 1905. 'Über Flussigkeits-bewegung bei sehr Kleiner Reibund'. (The flow of liquid with very little friction). Proc. 3rd. Int. Math. Congr., Heidelberg, 484-91. English Translation: NACA TM 452 (1928).

Praturi, A.K. and Brodkey, R.S., 1978. 'A sterioscopic visual study of coherent structures in turbulent shear flow'. J. Fluid Mech., 89, 251-72.

Preston, J.H., 1954. 'The determination of turbulent skin friction by means of pitot tubes'. J.R. Aero. Soc., 58, 109-21.

Pye, K., 1980. 'Beach salcrete and eolian sand transport: evidence from North Queensland'. J. Sedim. Petrol., 50, 257-61.

Rao, K.N., Narasimha, R. and Narayanan, M.A.B., 1971. 'Bursting in a turbulent boundary layer'. J. Fluid Mech., 48, 339-52.

Rathburn, R.E. and Guy, H.P., 1967. 'Measurement of hydraulic and sediment transport variables in a small recirculating flume'. Water Resour. Res., Ann. Geophys. Union., 3, 107-22.

Raupach, M.R., 1981. 'Conditional statistics of Reynolds Stress in rough-wall and smooth-wall turbulent boundary layers'. J. Fluid Mech., 108, 363-82.

Reynolds, O., 1883. 'An experimental investigation of the circumstances which determine whether the motion of water shall be direct or sinuous, and the law of resistance in parallel channels'. Phil. Trans. R. Soc., 174, 935-82.

Robertson, J.M. and Martin, J.D., 1966. 'Turbulence structure near rough surfaces'. AIAA J., 4(12), 2242-45.

Rubinow, S. and Keller, J., 1961. 'The transverse force on a spinning sphere moving in a viscous fluid'. J. Fluid Mech., 11, 447-59.

Rundstadler, P.W., Kline, S.J. and Reynolds, W.C., 1963. 'An experimental investigation of flow structure of the turbulent boundary layer'. Thermosciences Div., Mech. Engrn. Dept., Stanford, Rept. MD-8.

Ryan, J.A., 1964. 'Notes on the Martian yellow clouds'. J. Geophys. Res., 69, 3759-70.

Sabot, J., Saleh, I. and Compte-Bellot, G., 1977. 'Effect of roughness on the intermittent maintenance of Reynolds shear stress in pipe flow'. Phys. Fluids, 20(10), 150-5.

Saffman, P.G., 1965. 'The lift on a small sphere in slow shear flow'. J. Fluid Mech., 22, 385-98.

Saffman, P.G., 1977. 'Problems and progress in the theory of turbulence'. In: 'Structure and mechanisms of turbulence II', H. Fiedler, (ed.), Lecture notes in physics, 76, 273, Springer.

Sagan, C. and Bagnold, R.A., 1975. 'Fluid transport on Earth and aeolian transport on Mars'. Icarus, 26, 209-18.

Sagan, C. and Pollack, J.B., 1969. 'Windblown dust on Mars'. Nature, 223, 791-4.

Savas, O., 1979. 'Some measurements in synthetic turbulent boundary layers'. PhD Thesis, Calif. Inst. Tech., Pasadena, Calif.

Scheidegger, A.E., 1957. 'The physics of flow through porous media'. Univ. Toronto Press.

Schiller, L., 1932. 'Handbuch der Experimental Physik'. 4, (1-207), Leipzig.

Schlichting, H., 1979. 'Boundary Layer Theory'. 6th ed., Pergamon Press, New York.

Schmidt, R.A., 1982. 'Properties of blowing snow'. Rev. of Geophys. and Space Phys., 20, 39-44.

Schraub, F.A., Kline, S.J., Henry, V., Rundstadler, P.W. and Little, A., 1964. 'Use of hydrogen bubbles for quantitative determination of time dependent velocity fields in low-speed water flows'. Rept. MD-10., Thermosciences Div., Mech. Engr. Dept., Stanford Univ., U.S.A.

Schraub, F.A. and Kline, S.J., 1965. 'Study of the structure of the turbulent boundary layer with and without longitudinal pressure gradients'. Thermosciences Div., Mech. Engnr. Dept., Standford Univ., Rept. MD-12.

Schubauer, G.B. and Klebanoff, P.S., 1955. 'Contributions on the mechanics of boundary layer transition'. NACA TN 3489.

Schumm, S.A., 1973. 'Geomorphic thresholds and complex response of drainage systems'. In: M. Morisawa, (ed.), 'Fluvial Geomorphology', Publications in Geomorphology, State Univ. New York, Binghampton, New York, 299-309.

Scott, G.D., 1960. 'Packing of spheres'. Nature, 188, 908-9.

Seppala, M. and Linde, K., 1978. 'Wind tunnel studies of ripple formation'. Geografiska Annaler, 60, 29-42.

Shen, H.W. and Wand, J.S., 1970. 'Incipient motion in the limiting deposit condition of solid-liquid pipe flow'. Proc. Hydrotransport 1, Cong. Brit. Assoc. Hydraul. Res., London.

Shields, A., 1936. 'Anwendung der Aehnlichkeitsmechanic und der Turbulemforschung auf die Geschiebewegung'. Mitt. Preuss. Versuchsant. Wasserbaw Schiffbaw, 26. Translated in: W.P. Ott and J.C. Van Uchelen as 'Application of similarity principles and turbulence research on bed-load movement', Calif. Inst. Tech., Pasadena, Calif.

Smalley, I.J., 1970. 'Cohesion of soil particles and the intrinsic resistance of simple soil systems to wind erosion'. J. Soil Sci., 21, 154-61.

Smerdon, E.T. and Beasley, R.P., 1961. 'Critical tractive forces in cohesive soils'. Agric. Engnr., St. Joseph, Mich., 26-29.

Smith, C.R., 1978. 'Visualization of turbulent boundary layer structure using a moving hydrogen bubble wire probe. In: C.R. Smith and D.E. Abbott, (eds.), 'Lehigh Workshop on Coherent Structures in Turbulent Boundary Layers', Lehigh Univ., 48-97.

Smith, C.R. and Metzler, S.P., 1983. 'The characteristics of low-speed streaks in the near-wall region of a turbulent boundary layer'. J. Fluid Mech., 129, 27-54.

Smith, W.O., Foote, P.D. and Busang, P.F., 1929. 'Packing of homogeneous spheres'. Phys. Rev., 34, 1271-74.

Stanton, T.E., Marshall, D. and Bryant, C.N., 1920. 'On the conditions at the boundary of a fluid in turbulent motion'. Proc. Roy. Soc. Lond., A97, 413-34.

Sternberg, R.W., 1972. 'Predicting initial motion of bedload transport of sediment particles in the shallow marine environment'. In: D.J. Swift, (ed.), 'Shelf Sediment Transport'. Dowden, Hutcheson and Ross, 21-59.

Stewartson, K., 1974. 'Multistructural boundary layers on flat plates and related bodies'. Adv. Appl. Mech., 14, Academic Press, New York.

Strouhal, V., 1878. 'Uber eine besondere Art der Tonerregung'. (About a special type of sound agitation). Ann. Phys. und Chemie, New Series, 5, 216-51.

Sumer, B.M., 1974. 'Mean velocity and longitudinal dispersion of heavy particles in turbulent open-channel flow'. J. Fluid Mech., 65, 11-28.

Sumer, B.M. and Deigaard, R., 1981. 'Particle motions near the bottom in turbulent flow in an open channel'. Part 2. J. Fluid Mech., 109, 311-37.

Sundborg, A., 1956. 'The river Klaralven; a study in fluvial processes'. Geog. Ann. Stockholm, 38, 125-316.

Sutherland, A.J., 1966. 'Entrainment of fine sediments by turbulent flows'. Rept. KH-R-13, W.M. Keck Lab. of Hydraulics and Water Research, Calif. Inst. Tech.

Sutton, O.G., 1949. 'The applications to micrometerology of the theory of turbulent flow over rough surfaces'. Q.J.R. met. Soc., 75, 342-58.

Svasek, J.N. and Terwindt, J.H., 1974. 'Measurements of sand transport by wind on a natural beach'. Sedimentology, 21, 311-22.

Tabler, R.D., 1980. 'Geometry and density of drifts formed by snow fences'. J. Glaciology, 26, 405-19.

Tani, I., Hama, R. and Mituisi, S., 1940. 'On the permissible roughness in the laminar boundary layer'. Aero. Res. Inst., Tokyo Imp. Univ., Rept. 199.

Theodorsen, T., 1952. 'Mechanisms of turbulence'. Proc. 2nd. Midwestern Conf. on Fluid Mech., Ohio State Univ.

Thwaites, B., 1960. 'Incompressible Aerodynamics'. Clarendon Press, Oxford.

Tillman, W., 1946. 'Investigations of some particularities of turbulent boundary layers on plates'. Kaiser-Wilhelm Inst. fur Stromungsforschung, UM 6227 (Gottingen). Translated in: M.A.P. Volkenrode, Joint Intellegence Objectives Agency File B.1.G.S.-19, MPA-VG-457.

Tison, L.J., 1953. 'Studies of the critical tractive force of entrainment of bed material'. Proc. Int. Ass. Hydraul. Res., Minnesota Int. Hydraul. Conv., Minneapolis, Minn., 21-35.

Townsend, A.A., 1949. 'Momentum and energy diffusion in the turbulent wake of a cylinder'. Proc. R. Soc. Lond., A197, 124-38.

Townsend, A.A., 1956. 'The structure of turbulent shear flow'. C.U.P., Cambridge.

Townsend, A.A., 1961. 'Equilibrium layers and wall turbulence'. J. Fluid Mech., 11, 97-20.

Townsend, A.A., 1970. 'Entrainment and the structure of turbulent flow'. J. Fluid Mech., 41, 13-46.

Tsuchiya, Y., 1970. 'Successive saltation of a sand grain by wind'. Proc. 12th Conf. Coastal Engrn., 3, 1417-27.

Tsuchiya, Y. and Kawata, Y., 1972. 'Characteristics of saltation of sand grains by wind'. Proc. 13th Conf. Coastal Engrn., 12, Vancouver, 1617-25.

Tu, B.J. and Willmarth, W.W., 1966. 'An experimental study of turbulence near the wall through correlation measurements in a thick turbulent boundary layer'. Tech. Rept. No. 02920-3-T, Dept. Aerospace Engrn., Univ. Michigan, ANN Arbor.

Uil'Yams, G., 1963. 'Problems of the effect of eolian sand transport at various heights on the particle size composition of the sand'. Dokl. Akad. nauk SSSR, 149(2), 137-49.

Uzkan, T. and Reynolds, W.C., 1967. 'A shear-free turbulent boundary layer'. J. Fluid Mech., 28(4), 803-821.

Van Burkalow, A., 1945. 'Angle of repose and angle of sliding friction: an experimental study'. Bull. Geol. Soc. Am., 56, 669-707.

Van der Hegge-Zijnen, B.G., 1924. 'Measurements of the velocity distribution in the boundary layer along a plane surface'. PhD Thesis, Delft, Netherlands.

Vanoni, V.A., 1964. 'Measurements of critical shear stress entraining fine sediments in a boundary layer'. Calif. Inst. Tech., Pasadens, Rept. No. KH-R-7, Calif, 1-49.

Vanoni, V.A., 1975. 'Sedimentation Engineering'. Am. Soc. Civ. Engrs., Manuals and Reports on Engineering Practices, 54.

Von Kármán, T., 1921. 'Über laminare und turbulente Reibung'. Z. Angew. Math. Mech., 1, 237.

Warren, A., 1979. 'Aeolian Processes'. In: C. Embleton and J. Thornes, (eds.), 'Process in Geomorphology', Edward Arnold, London, 325-51.

Watters, G.Z. and Rao, M.V.P., 1971. 'Hydrodynamic effect of seepage on bed particles'. J. Hydraul. Div., Am. Soc. Civ. Engrs., 97(HY3), 421-39.

Weinberger, R.K. and Adlon, G.L., 1971. 'Particle dislodgement and entrainment by a low density airstream flowing over a surface'. NASA CR 111924.

Wentworth, C.K., 1922. 'A scale of grade and class terms for clastic sediments'. J. Geol., 30, 377-92.

White, B.R., 1979. 'Soil transport by winds on Mars'. J. Geophys. Res., 84, 4643-51.

White, B.R. and Schultz, J.D., 1977. 'Magnus effect in saltation'. J. Fluid Mech., 81, 497-512.

White, C.M., 1940. 'The equilibrium of grains on the bed of a stream'. Proc. R. Soc. Lond. A174, 322-38.

White, F.M., 1974. 'Viscous Fluid Flow'. McGraw-Hill, New York.

White, S.J., 1970. 'Plane bed threshold of fine grained sediments'. Nature, 228, 152-3.

Willetts, B.B. and Murray, C.G., 1981. 'Lift exerted on stationary spheres in turbulent flow'. J. Fluid Mech., 105, 487-505.

Willetts, B.B., 1983. 'Transport by wind of granular materials of different grain shapes and densities'. Sedimentology, 30, 669-79.

Willmarth, W.W., 1971. 'Unsteady force and pressure measurements'. Ann. Rev. Fluid Mech., 3, 147-70.

Willmarth, W.W., 1975. 'Pressure fluctuations beneath turbulent boundary layers'. Ann. Rev. Fluid Mech., 7, 13-38.

Willmarth, W.W. and Wooldridge, C.E., 1962. 'Measurements of the fluctuating pressure at the wall beneath a thick turbulent boundary layer'. J. Fluid Mech., 14, 187-210.

Willmarth, W.W. and Bogar, T.J., 1977. 'Survey and new measurements of turbulent structures near walls'. Physics of Fluids, 20(10), II, S9-21.

Willmarth, W.W. and Yang, C.S., 1970. 'Wall pressure fluctuations beneath turbulent boundary layers on a flat plate and a cylinder'. J. Fluid Mech., 41, 47-80.

Williams, G., 1964. 'Some aspects of the aeolian saltation load'. Sedimentology, 3, 357-87.

Williams, P.B. and Kemp, P.H., 1971. 'Initiation of ripples on flat sediment beds'. J. Hydraul. Div., Am. Soc. Civ. Engrs., 97(HY4), 505-20.

Wilson, I.G., 1972. 'Aeolian bedforms - their development and origins'. Sedimentology, 19, 173-210.

Wilson, S.J. and Cooke, R.U., 1980. 'Wind Erosion'. In: M.J. Kirkby and R.P.C. Morgan, (eds.), 'Soil Erosion'. John Wiley, London, 217-51.

Winant, C.D. and Browand, F.K., 1974. 'Vortex pairing: the mechanism of turbulent mixing layer growth at moderate Reynolds number'. J. Fluid Mech., 63, 237-55.

Wood, G.P., Weaver, W.R. and Henry, R.M., 1974. 'The minimum free stream wind velocity for initiating motion of surface material on Mars'. Langley Research Centre, NASA TMX-71959.

Wooding, R.A., Bradley, E.F. and Marshall, J.K., 1973. 'Drag due to regular arrays of roughness elements of varying geometry'. Bound. Lay Meterol., 5, 258-308.

Woodruff, N. and Siddoway, F.H., 1965. 'A wind erosion equation'. Proc. Soil Sci. Sec. Am., 29, 602-8.

Wygnanski, I., 1981. 'Transition and turbulent spots'. In: G.K. Patterson and J.L. Zakin, eds., Turbulence Symp. Proc., Dept. Chem. Engrn., Univ. Missouri-Rolla.

Wygnanski, I.J. and Champagne, F.H., 1973. 'On transition in a pipe. Part. I. The origin of puffs and slugs and the flow in a turbulent slug'. J. Fluid Mech., 59, 281-335.

Wygnanski, I., Sokolov, M. and Frieman, D., 1976. 'On a turbulent 'spot' in a laminar boundary layer'. J. Fluid Mech., 78, 785-819.

Yalin, M.S., 1972. 'Mechanics of sediment transport'. Pergamon Press, Oxford.

Yalin, M.S. and Karahan, E., 1979. 'Inception of sediment transport'. J. Hydraul. Div., Am. Soc. Civ. Engrs., 105(HY11), 1433-43.

Yang, C.T., 1973. 'Incipient motion and sediment transport'. J. Hydraul. Div., Am. Soc. Civ. Engrs., 99(HY10). 1679-1704.

Yasso, W.E., 1966. 'Heavy mineral concentration and Sastugi-like deflation furrows in a beach salcrete at Rockaway Point, New York'. J. Sedim. Petrol., 36, 836-8.

Zagni, A. and Smith, K., 1976. 'Channel flow over permeable beds of graded spheres'. J. Hydraul. Div., Am. Soc. Civ. Engrs., 102 (HY2), 207-22.

Zakkay, V., Barra, V. and Wang, C.R., 1978. 'Coherent structure of turbulence at high subsonic speeds'. In: C.R. Smith and P.E. Abbott, (eds.), 'Lehigh Workshop on Coherent Structure in Turbulent Boundary Layers', Lehigh Univ., 387-95.

Zilberman, M., Wygnanski, I. and Kaplan, R., 1977. 'Transitional boundary layer spot in a fully turbulent environment'. Phys. Fluids, 20(10), 258-71.

Zingg, A.W., 1952. 'Wind tunnel studies of the movement of sedimentary material'. Proc. 5th Hydraul. Conf., Iowa State Univ., Publ. No. 54.

Zingg, A.W., 1953. 'Some characteristics of aeolian sand movement by saltation process'. Editions du Centre National de la Recherche, Sci. 13, Quai Anatole France, Paris (7e), France, 197-203.

Zingg, A.W. and Chepil, W.S., 1950. 'Aerodynamics of wind erosion'. Agric. Engrs., 31, 279-82.

Zippe, H.J. and Graf, W.H., 1983. 'Turbulent boundary layer flow over permeable and non-permeable rough surfaces'. J. Hydraul. Res., 21(1), 51-65.

Znamenskiy, A.I., 1958. 'Experimental investigations of the wind erosion of sands and problems in the control of sand drifts'. Materialy Issledovaniy v Pomoshch' Proyektirovaniya i Stroitel' stua Kara Kumskogo Kanala, Ashkhabad.